

Biological applications of multimodal imaging  
involving Raman and 4Pi Raman  
microscopy

**Dmitry Khalenkow**

2021

Thesis submitted in fulfillment of the requirements for the  
degree of *Doctor of Philosophy* (Ph.D.) in  
**Applied Biological Sciences at Ghent University**



**Nederlandse vertaling van de titel:**

**Biologische toepassingen van multimodale  
beeldvorming met Raman en 4Pi Raman  
microscopie**

**Dmitry Khalenkow**

**2021**

**Funding**

This work was supported by the project grant from the Special Research Fund BOF of Ghent University, grant #: BOF14/IOP/003; (project number: 24J201400010).

**Copyright**

The author and the promoter do not give the permission to put this thesis to disposal for consultation and to copy parts of it for personal use.

*“The substructure of life regresses infinitely towards smaller and smaller components. Behind tissues we find cells, and behind cells, molecules. Each unraveled layer reveals new secrets, but also new questions.”*

Academician Prokhor Zakharov, Datalinks

**Promoter: Prof. Dr. Andre G. Skirtach**

Department of Biotechnology

Faculty of Bioscience Engineering

Ghent University, 9000 Ghent, Belgium

**Dean: Prof. Dr. Ir. Marc Van Meirvenne**

**Rector: Prof. Dr. Ir. Rik Van de Walle**

## **Members of the examination committee**

### **Prof. Dr. Guy Smagghe (Chair)**

Department of Plants and Crops  
Faculty of Bioscience Engineering  
Ghent University, 9000 Ghent, Belgium

### **Prof. Dr. Daisy Vanrompay (Secretary)**

Department of Animal Sciences and Aquatic Ecology  
Faculty of Bioscience Engineering  
Ghent University, 9000 Ghent, Belgium

### **Prof. Dr. Andre G. Skirtach (Promotor)**

Department of Biotechnology  
Faculty of Bioscience Engineering  
Ghent University, 9000 Ghent, Belgium

### **Prof. Dr. Nico Boon**

Department of Biotechnology  
Faculty of Bioscience Engineering  
Ghent University, 9000 Ghent, Belgium

### **Prof. Dr. Nicolas Le Thomas**

Department of Information Technology  
Faculty of Engineering and Architecture  
Ghent University, 9000 Ghent, Belgium

### **Prof. Dr. Christian Vanhove**

INFINITY Laboratory  
Faculty of Engineering and Architecture  
Ghent University, 9000 Ghent, Belgium

### **Prof. Dr. Christoph Krafft**

Raman and infrared Histopathology Group  
Leibniz Institute of Photonics Technology  
07745 Jena, Germany







## **Acknowledgments**

First, and most important, I would like to express my deepest and sincere gratitude to my promotor Prof. Andre Skirtach for giving me the opportunity to conduct the research in his team. This project was successful because of his continuous support and advices he provided during my Ph.D. He taught me what is really meant to be a scientist and the true value of academic freedom in pursuit of knowledge.

I would like to express my gratitude to the Prof. Nicolas Le Thomas for his help in designing and building the Raman 4Pi. His technical expertise and advices were priceless and allowed us to solve a number of difficult problems.

Alejandro (Tormo Diaz): you were always ready to rush ahead bravely and stubbornly to solve numerous technical problems we encountered. You taught me a lot about how to approach the difficulties from engineering point of view. For me, as a person with biological background, it was a very interesting experience).

I would like also to thank the Department of Molecular Biotechnology, the Nano-biotechnology group members, and my colleagues: Dr. Bogdan Parakhonskiy, Dr. Timothy Douglas, Anatolii Abalymov, Ekaterina Lengert, Irina Vidiyasheva, Louis Van der Meeren, Joost Verduijn. Planning and conducting experiments together with you was fun and I will miss our lunches in cafeteria.

Last, but not the least, I want to thank all people, who were willing to spend their time helping with the samples, measurements and analysis: Prof. Daisy Vanrompay, Prof. Nico Boon, Prof. Christian Vanhove, Prof. Eric Boschker, Prof. Filip Meysman, Prof. Bart Braeckman, Joanna, Sam, Cristina, Benjamin, Aleksandra, Tim, Tobias. Thank you all for allowing me to work together with you.



## Table of Contents

<b>List of abbreviations</b> .....	<b>14</b>
<b>Abstract (EN)</b> .....	<b>20</b>
<b>Abstract (NL)</b> .....	<b>22</b>
<b>1 Introduction to microscopy, Raman microscopy, and multimodal imaging</b> .....	<b>26</b>
1.1 MICROSCOPY: HISTORICAL DEVELOPMENTS .....	27
1.2 INTRODUCTION TO FUNDAMENTALS OF VIBRATIONAL SPECTROSCOPY .....	29
1.2.1 Infrared absorption spectroscopy .....	29
1.2.2 Raman spectroscopy .....	30
1.2.3 Role of absorption coefficient of water in vibrational spectroscopy .....	34
1.2.4 Advantages and disadvantages of Raman microscopy and spectroscopy .....	35
1.3 SURFACE-ENHANCED RAMAN SCATTERING (SERS), COHERENT ANTI-STOKES RAMAN SCATTERING (CARS) AND STIMULATED RAMAN SCATTERING (SRS).....	36
1.3.1 SERS .....	36
1.3.2 Multiphoton Raman spectroscopy: CARS, SRS .....	37
1.3.3 Polarized and Resonance Raman spectroscopy .....	38
1.4 RECENT DEVELOPMENTS IN RAMAN MICROSCOPY.....	39
1.4.1 Advances in biological applications of Raman microscopy .....	39
1.4.2 Reference databases for Raman peak assignment and analytical calculations .....	41
1.4.3 Raman labels .....	41
1.4.4 Superresolution fluorescence and Raman microscopy .....	42
1.4.5 Other applications of Raman microscopy .....	43
1.5 MULTIMODAL IMAGING AS AN EMERGING TREND.....	44
1.6 GOALS OF THIS THESIS WORK .....	46
<b>2 Added value of brain tissue analysis using Raman microscopy and magnetic resonance imaging (MRI)</b> .....	<b>50</b>
2.1 INTRODUCTION .....	51
2.2 MATERIALS AND METHODS .....	53
2.2.1 Experimental layout .....	53
2.2.2 mTBI induction .....	54
2.2.3 <i>In vivo</i> longitudinal MRI imaging .....	54
2.2.4 Sample preparation, Raman microscopy data acquisition, and pre-processing.....	55
2.3 RESULTS AND DISCUSSION .....	57
2.3.1 Scanning tissue samples with Raman microscope .....	57

2.3.2	Construction of Raman molecular images of tissue samples.....	59
2.3.3	MRI results.....	64
2.3.4	Analysis of Raman molecular images of the corpus callosum .....	64
2.3.5	Analysis of corpus callosum molecular fingerprints before and after mTBI .....	65
2.3.	CONCLUSION .....	67
<b>3</b>	<b>Localization of bovine lactoferrin inside calf cells by fluorescence and Raman microscopy .....</b>	<b>70</b>
3.1	INTRODUCTION .....	71
3.2	MATERIALS AND METHODS .....	73
3.3	RESULTS AND DISCUSSION .....	74
3.3.1	Analysis of Fluorescent images .....	74
3.3.2	Lactoferrin localization with Raman.....	76
3.4	CONCLUSION .....	78
<b>4</b>	<b>Molecular analysis of conductive fibers in cable bacteria by Raman microscopy, X-ray, and mass spectrometry-based methods .....</b>	<b>82</b>
4.1	INTRODUCTION .....	83
4.2	MATERIALS AND METHODS .....	86
4.2.1	Sample preparation.....	86
4.2.2	Raman microscopy .....	87
4.2.3	X-ray and mass spectrometry methods .....	88
4.3	RESULTS AND DISCUSSION .....	89
4.3.1	Localization of fibers inside the intact cable bacteria with confocal Raman .....	89
4.3.2	Analysis of extracted conductive fibers.....	92
4.4	CONCLUSION .....	96
<b>5</b>	<b>Drug delivery systems with SERS functionality <i>in vitro</i> and <i>in vivo</i>.....</b>	<b>100</b>
5.1	CHARACTERIZATION OF CALCIUM CARBONATE DRUG CARRIERS WITH SERS FUNCTIONALITY.....	101
5.1.1	Introduction.....	101
5.1.2	Materials and methods .....	104
5.1.3	Results and discussion.....	106
5.2	DRUG CARRIER DETECTION AND RELEASE INDUCTION <i>IN VIVO</i> USING SERS.....	108
5.2.1	Introduction.....	108
5.2.2	Material and methods.....	110
5.2.3	Results and discussion.....	113
5.3	CONCLUSION .....	119

<b>6</b>	<b>4Pi Raman microscopy and atomic force microscopy investigation of <i>Chlamydia</i> infected cells.....</b>	<b>122</b>
6.1	INTRODUCTION .....	123
6.2	THE 4Pi RAMAN MICROSCOPE SETUP AND CHARACTERIZATION .....	125
6.3	APPLICATION OF 4Pi RAMAN AND AFM FOR ANALYSIS OF INTRACELLULAR BACTERIA .....	131
6.3.1	Introduction.....	131
6.3.2	Materials and methods .....	134
6.3.3	Molecular imaging with 4Pi Raman microscopy .....	136
6.3.4	Analysis of Raman scattering data .....	138
6.3.5	AFM topographical imaging .....	141
6.4	CONCLUSION .....	144
<b>7</b>	<b>General discussion, conclusions and perspectives .....</b>	<b>147</b>
7.1.	GENERAL DISCUSSION .....	147
7.2.	GENERAL CONCLUSIONS .....	155
7.3.	PERSPECTIVES AND FUTURE DIRECTIONS .....	158
	<b>REFERENCES .....</b>	<b>162</b>
	<b>APPENDIX .....</b>	<b>176</b>
	Supplementary Information for Chapter 1.....	177
	Supplementary Information for Chapter 2.....	180
S2.1	Basics of Raman data processing and analysis.....	181
S2.2.	Raman data preprocessing in R.....	193
S2.3	Raman molecular images .....	205
	References to Supplementary Information for Chapter 2 .....	206
	Supplementary Information for Chapter 4.....	208
	Supplementary Information for Chapter 5.....	210
	Supplementary Information for Chapter 6.....	214
	Summary .....	220
	Samenvatting.....	224
	<b>CV and the publication list of the author .....</b>	<b>228</b>



## List of abbreviations

### A

AC	Acoustic mode of Atomic Force Microscopy
AFM	Atomic Force Microscopy
AFM-IR	Atomic Force Microscope – Infra-Red
Alexa Fluor	Alexa Fluorophore

### B

BGM	Buffalo Green Monkey
bLF	Bovine Lactoferrin

### C

CaF <sub>2</sub>	Calcium Fluoride
CARS	Coherent Anti Stokes Raman
C-AFM	Conductive Atomic Force Microscopy
CCD	Charge-Coupled Device
CCKM	Complete <i>C. psittaci</i> culture medium
<i>C. elegans</i>	<i>Caenorhabditis elegans</i>
<i>C. psittaci</i>	<i>Chlamydia psittaci</i>
CT	X-ray Computed Tomography

### D

DIC	Differential Interference Contrast
DNA	Deoxyribonucleic Acid

### E

EB	Elementary Body
EDTA	Sodium ethylenediaminetetraacetate

EHEC	Enterohemorrhagic <i>Escherichia coli</i>
EM	Electron Microscopy
EMCCD	Electron Multiplying Charged-Coupled Device
<b>F</b>	
FCS	Fluorescence Correlation Spectroscopy
FRAP	Fluorescence Recovery After Photobleaching
FRET	Fluorescence Resonance Energy Transfer
FWHM	Full Width at Half Maximum
<b>I</b>	
IR	Infrared
<b>L</b>	
LASER	Light Amplification by Stimulated Emission of Radiation
LC-MS	Liquid Chromatography-Mass Spectrometry
LED	Light Emitting Diode
LEXRF	Low Energy X-ray Fluorescence
<b>N</b>	
NA	Numerical aperture
Nano-SIMS	Nanoscale Secondary Ion Mass Spectrometry
NIR	Near infra-red
NGM	Nematode growth medium
Ni	Nickel
NPs	Nanoparticles
NCBI SRA	The National Center for Biotechnology Information Sequence Read Archive



## **M**

MALT	Mucosa-Associated Lymphoid Tissue
MEM	Eagle's Minimal Essential Medium
mTBI	Mild Traumatic Brain Injury
MRI	Magnetic Resonance Imaging
MilliQ	Millipore Water purified with a resin filter with resistivity of 18.2 MΩ•cm

## **P**

PBS	Phosphate Buffered Saline
PSF	Points Spread Function
PALM	Photoactivated Localization Microscopy

## **Q**

QI	Quantitative Imaging
----	----------------------

## **R**

RARE	Rapid Acquisition with Refocused Echoes
RB	Reticulate Body
RNA	Ribonucleic Acid
RPM	Revolutions Per Minute
RT-PCR	Reverse Transcription Polymerase Chain Reaction

## **S**

SDS	Sodium Dodecyl Sulfate
SEM	Scanning Electron Microscopy
SERS	Surface-Enhanced Raman Spectroscopy
SIM	Structured Illumination Microscopy
SRG	Stimulated Raman Gain

SRL	Stimulated Raman Loss
SRS	Stimulated Raman Scattering
STED	Stimulated Emission Depletion
STEM-EDX	Scanning Transmission Electron Microscopy Energy-Dispersive X-ray spectroscopy

## T

TBI	Traumatic Brain Injury
TEM	Transmission Electron Microscopy
TERS	Tip Enhanced Raman Scattering
TIRF	Total Internal Reflection Fluorescence
TRITC-BSA	Tetramethylrhodamine Bovine Serum Albumin
Trp	Tryptophan

## U

UV	Ultraviolet
----	-------------

## NUMERIC, LATIN

2D	2-dimensional
3D	3-dimensional
4Pi	the solid angle of a complete sphere (steradians)
$\Delta$ LF	Delta-lactoferrin
$\pi$	mathematical constant (equal to 3.14159)
a.u.	arbitrary unit
$\mu$ L	microliter
mL	milliliter
pm	picometer
nm	nanometer
$\mu$ m	micrometer

mm	millimeter
cm	centimeter
m	meter
$\mu\text{s}$	microsecond
mW	milliWatt



## Abstract (EN)

Raman microscopy is becoming an increasingly important label-free imaging technique. It proved to be a viable tool for life science applications allowing to analyze bacteria, cells, and tissues at the molecular level. Combining Raman microscopy with complementary imaging modalities and techniques is explored here to: (1) analyze mild traumatic brain injury (mTBI) in a combination with magnetic resonance imaging (MRI) for detecting mild, and invisible to medical imaging techniques, brain tissue damage; (2) reveal complementarity of Raman and fluorescence microscopy approaches for investigating and tracking bovine lactoferrin inside calf rectal epithelial cells in the presence of enterohemorrhagic *Escherichia coli* (EHEC); (3) apply Raman microscopy along-side the molecular analysis approaches (such as scanning transmission electron microscopy-energy dispersive X-ray (STEM-EDX), low energy X-ray fluorescence (LEXRF), nanoscale secondary ion mass spectrometry (Nano-SIMS)) to uncover the origin of the long-range conductance in cable bacteria; (4) develop multifunctional surface enhanced Raman scattering (SERS) platform based on calcium carbonate particles for enhancing a weak Raman scattering signal of biomolecules as well as to apply Raman microscopy for particle detection *in vivo* in *Caenorhabditis elegans* (*C. elegans*) worms; and (5) combine Raman microscopy and atomic force microscopy (AFM) to track *Chlamydia psittaci* in cells. Analysis of described above samples and phenomena is based on Raman molecular fingerprint images, where, similarly to fluorescence light microscopy, the resolution is limited by diffraction of light. Therefore, efforts are also put to enhance the resolution of Raman microscopy-based imaging by adding a 4Pi configuration to a confocal Raman microscope. As a result, a possibility to enhance the axial (also called longitudinal) resolution is investigated by constructing a 4Pi confocal Raman microscope, which is also applied to study bacteria inside cells. Results presented in this work emphasize the added value of multimodal microscopy approaches, particularly involving Raman microscopy, in a broad range of applications in bioengineering, biomedicine, and biology.



## Abstract (NL)

Raman microscopie is een belangrijke labelvrije beeldvormingstechniek voor de biowetenschappelijke toepassingen om bacteriën, cellen en weefsels te analyseren op het moleculaire niveau. Het combineren van Raman microscopie met complementaire beeldvormingsmodaliteiten en technieken wordt hier onderzocht om: (1) het analyseren van mild traumatisch hersenletsel (mTBI) in een combinatie met magnetische resonantie beeldvorming (MRI) voor het detecteren van mild hersenweefsel schade; (2) het onthullen van de complementariteit van Raman en fluorescentiemicroscopie benaderingen voor het onderzoeken en volgen van runderlactoferrine in kalf rectaal epitheelcellen in de aanwezigheid van enterohemorragische *Escherichia coli* (EHEC); (3) de Raman microscopie toe te passen samen de moleculaire analyse benaderingen (zoals scanning transmissie elektronenmicroscopie-energie-dispersieve röntgenstraling (STEM-EDX), lage energie röntgenfluorescentie (LEXRF), nanoschaal secundaire ionenmassaspectrometrie (Nano-SIMS)) om de oorsprong van de lange-afstandsgeleiding in kabelbacteriën aan het licht te brengen; (4) het ontwikkelen van een multifunctioneel oppervlakte-versterkte Raman verstrooiing (SERS) platform op basis van calciumcarbonaatdeeltjes voor de versterking van een zwak Raman-verstrooiingssignaal van de biomoleculen en het toepassen van de Raman microscopie voor de *in vivo* detectie van deeltjes in *Caenorhabditis elegans* (*C. elegans*) wormen; en (5) het combineren van Raman microscopie en atoomkrachtmicroscopie (AFM) om *Chlamydia psittaci* in cellen op te sporen. De analyse van de hierboven beschreven stalen en fenomenen is vaak gebaseerd op Raman moleculaire “vingerafdrukbeelden” waarbij, net als bij de fluorescentie lichtmicroscopie, de resolutie beperkt is door de diffractie van het licht. Daarom worden er ook inspanningen ingezet om de resolutie van de op Raman microscopie-gebaseerde beeldvorming te verbeteren door een 4Pi configuratie toe te voegen aan een confocale Raman microscoop. Op die manier wordt de mogelijkheid onderzocht om de axiale (zogenaamde longitudinale) resolutie te verbeteren door het construeren van een 4Pi confocale Raman microscoop, die wordt ook toegepast om bacteriën in cellen te bestuderen. De gepresenteerde in dit werk resultaten benadrukken de meerwaarde van multimodale microscopische benaderingen met betrekking tot de Raman microscopie in toepassingen in bio-ingenieur wetenschappen, geneeskunde en biologie.

•





# Chapter 1

Introduction to microscopy, Raman microscopy, and multimodal imaging



# **1 Introduction to microscopy, Raman microscopy, and multimodal imaging**

The first applications of microscopes in life science were revolutionary and led to the discovery of cells and bacteria. This discovery played a special role in development of human civilization. Evolution of microscopy led to advancements, among which is Raman microscopy. This technique permits label-free imaging of molecules. In this chapter, we describe brief history of microscopy, basic principles of Raman microscopy, its advantages and disadvantages, and its biological applications. We also discuss multimodal imaging, where Raman microscopy plays an important role.

## 1.1 MICROSCOPY: HISTORICAL DEVELOPMENTS

Contemporary microscopy is becoming multimodal. In multimodal imaging, different techniques are used on the same or similar samples to obtain complementary structural or functional information. It is now used not only in medicine but also in biology, bioscience engineering, and life sciences. In all these application areas, molecular imaging has become a key attribute covering a broad range of scales from microscopic (mostly used in biology) to macroscopic (predominantly used in medicine) levels. Developments in biomedical imaging were broadly stimulated by advances in microscopy.

The origin of microscopy can be traced back to the end of the XVI<sup>th</sup> century (around 1590-1595). Then, Hans Lippershey and Zacharias Janssen discovered that a larger magnification than that of a single magnifying glass can be obtained by placing several lenses in a tube. It is not fully known if they really were the first who discovered this phenomenon, but they were the first who tried to patent it. This invention (which is also linked to telescopes) not only made the revolution in sea navigation but also led to amazing scientific findings. For example, Galileo used a telescope to discover the moons around Jupiter. It was also realized that several lenses produce a magnifying effect that can be used not only to observe big objects far away but also to study tiny objects nearby. Such a device was named – a “microscope.” Application of microscopes in research grew exponentially in the XVII<sup>th</sup> century leading to groundbreaking scientific discoveries. Interestingly, applications of microscopes in biology began when a Dutch trader, Antoni van Leeuwenhoek, invented a method of creating high-quality lenses, which allowed him to obtain a magnification of up to 275 times. When observing various objects, such as a drop of water or a sample from his tooth plaque, van Leeuwenhoek has found with his hand-made microscope that such samples were populated by small living organisms invisible to the naked eye. He called them “animalcules.” In modern terminology, we know those animalcules as bacteria and protista. Besides being the founding father of microbiology and bacteriology, van Leeuwenhoek also made contributions to other life science fields. For example, he discovered spermatozoa, bands in muscle tissue, nematode worms, and vacuoles in plant cells. The discovery of cells, however, is attributed to Robert Hooke and his famous “Micrographia”. The more mysteries of life were discovered with the help of microscopes - the more questions appeared; in turn, that drove the need for better microscopes. However, even with perfect lenses, conventional light microscopes have the fundamental limit in their

spatial resolution <sup>1</sup> of 0.2  $\mu\text{m}$ , as it was introduced by Ernst Abbe. The Abbe diffraction limit equation allows calculation of the theoretically possible resolution (for non-coherent light) for a microscopic system <sup>2</sup>:

$$d = \frac{\lambda}{2n \sin \theta} \quad (1)$$

where  $d$  is the minimum resolving distance for light with wavelength  $\lambda$ , which propagates in a medium with refractive index  $n$ ,  $\theta$  - is an angular aperture of the optical system. According to the Abbe's equation, it is not possible to observe individual molecules in conventional microscopy using visible light. However, scientists have developed various techniques allowing to obtain information at the molecular level: fluorescence, superresolution microscopy, spectroscopy, etc. Spectroscopy is based on analysis of how light interacts with matter and how such interaction induces changes in light and/or in molecules. Information about molecules can be obtained by measuring those changes.

Light can interact with matter in various ways. Here, we focus on absorption, scattering, and electron transition processes resulting from the interaction of a photon with molecular bonds, Figure 1.1.

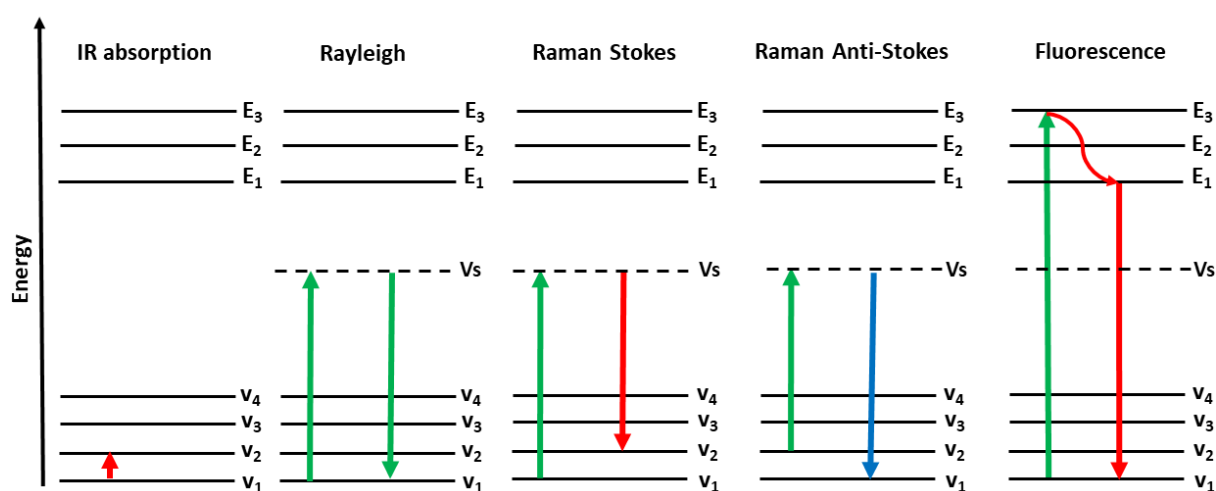


**Figure 1.1.** Absorption, scattering, and fluorescence processes are illustrated by the Jablonski energy diagram.  $V_1$ - $V_4$  – vibration energy states,  $V_s$  – virtual energy state,  $E_1$ - $E_3$  – higher energy vibration and excited states.

## 1.2 INTRODUCTION TO FUNDAMENTALS OF VIBRATIONAL SPECTROSCOPY

### 1.2.1 Infrared absorption spectroscopy

The interaction of incident photons with a molecule can result in absorption of photons. If the frequency of an incident photon corresponds to that required for an internal transition between electron states in a molecule, then that photon is absorbed, and an electron is excited to a higher energy state. Information about the chemical composition of the molecule can be obtained by analyzing which frequencies of incident source are absorbed. In this regard, infrared (IR) spectroscopy measures absorption of energy required for transitions between different vibration states, because each molecule has its own set of vibration modes, as it is presented in Figure 1.2 on an example of a CO<sub>2</sub> molecule.

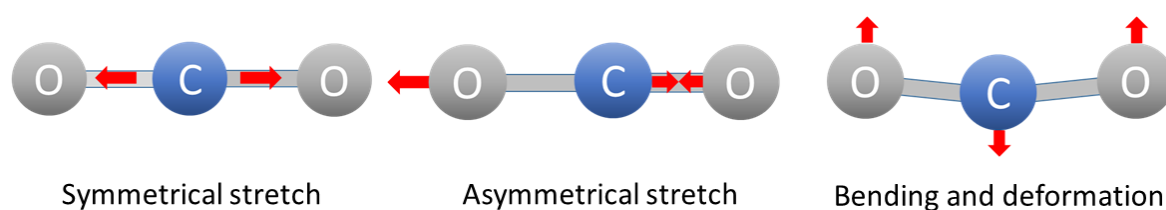


**Figure 1.2.** *Vibration modes of a CO<sub>2</sub> molecule.*

The number of vibrational degrees of freedom for a linear molecule with  $N$  atoms is  $3N-5$ . For example, carbon dioxide (CO<sub>2</sub>) is a linear molecule; therefore, it has 4 possible vibration states. A non-linear molecule will have  $3N-6$  potential vibrational modes<sup>3</sup>.

Vibration modes are IR active when there is a change in the dipole moment. In the case of carbon dioxide molecule, the asymmetric stretching and bending/deformation are IR active, while symmetric stretching is detectable in scattering of molecules, referred to as Raman scattering. The selection mechanisms, which allow predicting IR or Raman active modes, will be discussed further in this chapter. But first, we provide an overview of basic principles of Raman spectroscopy.

### 1.2.2 Raman spectroscopy

The basic principles of Raman spectroscopy can be described as follows. When light impinges on a sample, it can either go through the sample without any interaction, it can be absorbed, or it can be scattered by the sample. In the process of scattering, the energy exchange occurs between the incident photons and molecules of the sample. This interaction leads to vibrations of atoms in the molecule. The energy levels in vibration states are quantized, while energy brought by incident photons allows excitation of molecules from their ground vibration energy level to the so-called virtual excited state. It is important to note that the so-called “virtual state” has no physical meaning. This concept is used to describe a transient state after incident photon absorption and before energy emission in the form of a scattered photon. After the molecule is brought into the virtual excited state, three scenarios are possible:

1. Because the virtual energy state is unstable, electrons may fall back to the same vibration level (of the electronic ground state) emitting photons with the same frequency as the incident photons. This is the elastic scattering process, and it is called Rayleigh scattering.
2. There exists a small but finite possibility that a part of energy carried by the incident photon would be used to transfer a molecule into a higher vibrational level of the ground state. The energy of the emitted photon would be lower than that of the incident photon. This process is referred to as Stokes scattering.
3. In a situation, where a molecule is already in a higher vibrational state, the energy exchange can go in the opposite direction than that in the Stokes scattering process. This would cause the scattered photon to be emitted with higher energy than the incident photon. This effect is called anti-Stokes scattering.

Let us examine those three scattering processes from the point of view of classical theory of light scattering. Here, light-matter interaction can be described as the interaction between an incident oscillating electromagnetic field and electron clouds of molecules. Such interaction will disturb the electronic charge distribution and induce the dipole moment to the molecule. The induced oscillating dipole moment will act as an antenna emitting secondary electromagnetic radiation (scattered light).

The induced dipole moment in an irradiated molecule can be written as <sup>4</sup>:

$$\vec{\mu} = \tilde{\alpha}\vec{E} \quad (2)$$

where  $\vec{\mu}$  is the molecular dipole induced by an external electric field  $\mathbf{E}$ , and  $\tilde{\alpha}$  is the polarizability tensor. Since we are interested in linear scattering processes, the nonlinear components of the polarizability tensor can be neglected.

The external electromagnetic field can be described as:

$$\vec{E} = \vec{E}_0 \cos(\omega_0 t) \quad (3)$$

here  $\mathbf{E}_0$  is a vector amplitude of the electromagnetic wave and  $\omega_0$  is its oscillation angular frequency.

Polarizability is a proportionality factor between an external electromagnetic field and the induced dipole moment. It is related to how easily the external electromagnetic field can deform electron orbitals of the molecule from their equilibrium position. It is important to note that polarizability is not constant. The motions, such as vibrations of atoms, will change the polarizability of a molecule since electron clouds adjust for the nuclear geometry to minimize energy of the system.

Assuming that displacement of atoms from the equilibrium position is relatively small, the polarizability for an individual normal mode  $\mathbf{q}$  can be described using a static term and a displacement-dependent term:

$$\alpha = \alpha_0 + \frac{\partial \alpha}{\partial q} q \quad (4)$$

The normal mode  $\mathbf{q}$  of oscillation of the molecule at the characteristic frequency  $\omega_q$  can be written as follows:

$$q = q_0 \cos(\omega_q t) \quad (5)$$

Combining equations (2), (3), (4), and (5) results in <sup>4</sup>:

$$\mu(t) = \left[ \alpha_0 + \frac{\partial \alpha}{\partial q} q_0 \cos(\omega_q t) \right] E_0 \cos(\omega_0 t) \quad (6)$$

By applying the trigonometric formula for the product of two cosines, equation (6) can be reformulated as follows:



$$\mu(t) = \alpha_0 E_0 \cos(\omega_0 t) + \frac{1}{2} \left( \frac{\partial \alpha}{\partial q} \right)_{q_0} q_0 E_0 \cos[(\omega_0 - \omega_q)t] + \frac{1}{2} \left( \frac{\partial \alpha}{\partial q} \right)_{q_0} q_0 E_0 \cos[(\omega_0 + \omega_q)t] \quad (7)$$

The frequency in equation (7) is important in vibrational spectroscopy since it points at vibrations of atoms in a molecule, and it can be expressed in wavenumbers as follows:

$$\nu = \frac{1}{2\pi c} \sqrt{\frac{K}{\mu}} \quad (8)$$

where  $K$  is the spring constant,  $c$  is the speed of light in vacuum,  $\mu = m_1 * m_2 / (m_1 + m_2)$  is the so-called reduced mass, and  $m_1$  and  $m_2$  are masses of atoms.

Equation (7) shows that Raman scattering can be viewed as a limited case of a general light scattering process <sup>4</sup>. The induced dipole moment, which is the source of scattered light, is described by three terms:

1. The first term:  $\alpha_0 E_0 \cos(\omega_0 t)$  describes the oscillation with the same frequency  $\omega_0$  as that of incident light, and, therefore, scattered light will also have the frequency  $\omega_0$ . This is referred to as elastic Rayleigh scattering.
2. The second term illustrates the oscillation with the frequency  $\omega_0 - \omega_q$ . This means that the frequency of emitted light will be decreased, or red-shifted, in respect to the incident light frequency. This is called Stokes scattering.
3. The third term represents emitted light, which has higher energy than that of the excitation beam, and it is named anti-Stokes scattering.

The second and third terms of equation (7) explain why Stokes and anti-Stokes scatterings modes form symmetrical, relative to excitation light frequency, patterns in Raman spectra. But it is important to note that intensities of emitted Stokes and anti-Stokes light differ. The distribution of electrons on different energy levels follows the Boltzmann law. At room temperature, most of the electrons will be in the lowest vibrational level of the ground electronic state. Anti-Stokes photons are emitted when incident light interacts with electrons in a higher vibrational energy level of the ground electronic state. Therefore, most of the Raman scattered photons will be Stokes photons, making them easier to detect than anti-Stokes photons. That is why in subsequent chapters of this dissertation, Raman spectra

(scattering intensity as a function of frequency shift in wavenumbers) are referred to and plotted as spectra corresponding only to Stokes photons, while the weaker anti-Stokes part of the spectrum will be discarded and not shown on spectral plots.

The power emitted by the induced dipole is given by <sup>4</sup>:

$$P = \frac{q_0^2}{12\pi\epsilon_0 c^3} \left( \frac{\partial \alpha}{\partial q} \right)_{q_0}^2 (\omega_0 - \omega_q)^4 E_0^2 \quad (9)$$

It can be seen from equation (9) that vibration is Raman active if a change in the polarizability of a molecule does not equal zero ( $\frac{\partial \alpha}{\partial q} \neq 0$ ). In contrast, a vibration is IR active if this vibration involves a change of the dipole moment. For a small linear molecule, the polarizability can be schematically represented as an ellipsoid drawn around the molecule <sup>5</sup>. Using such a representation, it is possible to visually demonstrate why for carbon dioxide a symmetrical stretching is Raman active ( $\frac{\partial \alpha}{\partial q} \neq 0$ ) and an asymmetric stretching vibration is IR active ( $\frac{\partial \mu}{\partial q} \neq 0$ ), Figure 1.3.

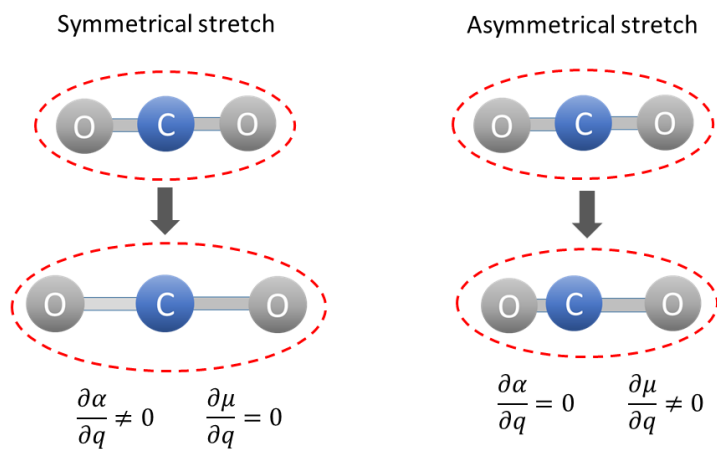


**Figure 1.3.** Polarization changes in a carbon dioxide molecule during symmetric and asymmetric stretching.

The intensity of Raman scattering is proportional to the overall power <sup>4</sup>:

$$I_{Stokes} \propto \left( \frac{\partial \alpha}{\partial q} \right)_{q_0}^2 (\omega_0 - \omega_q)^4 E_0^2 \quad (10)$$

In equations (9) and (10), terms  $\omega_q$  and  $\left( \frac{\partial \alpha}{\partial q} \right)_{q_0}$  are intrinsic properties of measured molecules, while  $\omega_0$  and  $E_0$  are experimental parameters, which can be modified to affect intensity of

scattered light. Equation (10) explains why an increase of laser power and frequency leads to an increase of the Raman scattering intensity.

### 1.2.3 Role of absorption coefficient of water in vibrational spectroscopy

Water can be a problem for analyzing life science samples with IR spectroscopy. Figure 1.4 shows the absorption coefficient of liquid water, from where one can see why water causes a problem for IR spectroscopy: a relatively high absorption coefficient of water in the IR range. And this problem is even more pronounced in the biologically relevant fingerprint spectral area between 1000 and 3000  $\text{cm}^{-1}$ , inset in Figure 1.4 (red curve).

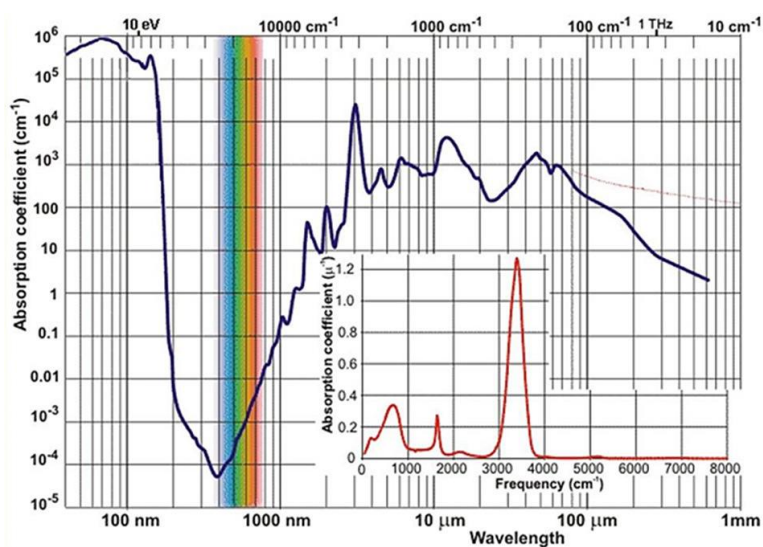


**Figure 1.4.** The absorption coefficient of liquid water (reproduced from Bec et al. <sup>6</sup>).

On the other hand, excitation light sources with wavelengths in the visible part of spectrum (and sometimes ultraviolet (UV) and near-IR) are used in Raman spectroscopy. For those excitation light sources, a clear absorption minimum situated in the visible range of the electromagnetic spectrum can be seen in Figure 1.4. Therefore, Raman spectroscopy can be used for characterizing samples in water. However, challenges in this area still exist: one has to avoid autofluorescence, which is originated in the visible spectral range (that prompts to increase the wavelength of the excitation source). But, at the same time, one should not increase too much the wavelength of the excitation source (increasing wavelength decreases the scattered intensity according to equation (10)). Overall, water poses a problem for IR but not for Raman spectroscopy.

#### 1.2.4 Advantages and disadvantages of Raman microscopy and spectroscopy

Raman microscopy, where spectroscopy is applied for spatial mapping and imaging, has the following advantages.

1. Raman microscopy is label-free. This means that, in contrast to fluorescence microscopy, no external label-molecules are required to obtain information about a sample. This is very relevant for cell biology, where the presence of labels can alter the molecular state of cells.
2. Water molecules produce a very weak Raman scattering. Therefore, the presence of water does not pose a problem (in contrast to infrared spectroscopy). This makes Raman microscopy particularly interesting for analysis of biological samples.
3. In most cases, Raman spectroscopy is non-destructive, which is essential, because that allows development of *in vivo* applications. Raman measurements do not often alter the sample at the molecular level in any detectable way, samples can be subsequently analyzed with other techniques.
4. Compared to alternative analytical microscopy techniques, like immunofluorescence, no special sample preparation techniques are required.
5. Implementation of the confocal principle (which is often done by connecting an optical fiber between a Raman microscope and spectrometer and using the fiber core as the pinhole) and focusing the excitation light through a high NA objective allows acquiring Raman spectral information from a specifically selected volume of a sample.

On the other hand, Raman microscopy has the following disadvantages.

1. Raman scattering produces very weak signals, which may lead to long measurement times. It may cause problems if, for example, the analyzed samples can degrade and/or change their molecular composition over time. Also, sample damages may occur in cases of long laser exposures.
2. Weak Raman signals may lead to long measurement times making it difficult to analyze many samples in a reasonably short period of time.
2. Autofluorescence from samples may oversaturate the detector and mask the Raman signal.

3. Complex organic molecules, such as proteins consist of similar atoms: hydrogen, oxygen, nitrogen, carbon, sulfur, and phosphorus. Therefore, it is challenging to identify specific organic molecules inside cells.

4. Sophisticated data analysis is often required to extract information from spectral datasets.

5. Raman microscopy has a similar resolution limit as that of fluorescence light microscopes.

Development of specialized Raman-based techniques, such as CARS, SERS, and Raman labels, allowed to solve some of the above-mentioned issues by enhancing Raman signals, improving the sensitivity, the resolution, and signal acquisition time. In the next section, we briefly discuss those techniques.

### **1.3 SURFACE-ENHANCED RAMAN SCATTERING (SERS), COHERENT ANTI-STOKES RAMAN SCATTERING (CARS) AND STIMULATED RAMAN SCATTERING (SRS)**

#### **1.3.1 SERS**

Surface-Enhanced Raman scattering (SERS) technique allows for a significant enhancement of Raman signals. There are two mechanisms, which contribute to signal enhancement: chemical and electromagnetic. Electromagnetic enhancement is the result of a localized nanoplasmon excitation within a SERS substrate. Noble metal nanoparticles with sizes smaller than the excitation wavelength of light are often used as SERS substrates. Such nanoparticles act as dipoles by creating strong local electromagnetic fields. Such fields act as an excitation source for molecule located near the nanoparticles, thus enhancing the Raman scattering. Additionally, Raman scattered light from a molecule is further amplified by a localized surface nanoplasmon resonance, leading to an even stronger Raman signal enhancement. Chemical enhancement can result from the resonance Raman effect induced by physicochemical interactions of a molecule with the metal surface. This interaction causes a charge transfer between the molecule and the surface, modifying its polarizability and thus enhancing the Raman scattering process.

### 1.3.2 Multiphoton Raman spectroscopy: CARS, SRS

Multiphoton Raman spectroscopy includes both coherent anti-Stokes Raman scattering (CARS) and stimulated Raman scattering (SRS) and allows for molecular imaging <sup>7</sup>.

Conventional CARS microscopy is based on irradiating a sample with two laser beams with different frequencies: a pump beam at the frequency  $\omega_p$  and a Stokes beam at  $\omega_s$ , Figure 1.5 (A). The pump beam is used for the excitation of electrons from the ground level into the virtual state  $V_{s1}$ , Figure 1.5 (A). Next, illumination by the Stokes beam forces electrons to fall into a higher vibrational energy state of the ground energy level, red arrow in Figure 1.5 (A). The pump beam can be adjusted so that the residual differences  $\Delta\omega = \omega_p - \omega_s$  would correspond to the desired vibrational energies of the molecule. The result of this double beam illumination is a higher population of electrons in a certain vibrational energy state of the ground electron level. Then, the pump beam can be used to excite those electrons into the second virtual energy state,  $V_{s2}$  in Figure 1.5 (A). From there, electrons relax back into the ground state emitting anti-Stokes photons with frequency  $\omega_{cars} = \omega_p + \Delta\omega$ , blue arrow in Figure 1.5 (A). As a result, a strong Raman signal with the frequency  $\omega_{cars} = 2\omega_p - \omega_s$  can be detected. The intensity of this signal can be up to five orders of magnitude higher than the signal from conventional (spontaneous) Stokes Raman scattering <sup>8</sup>.

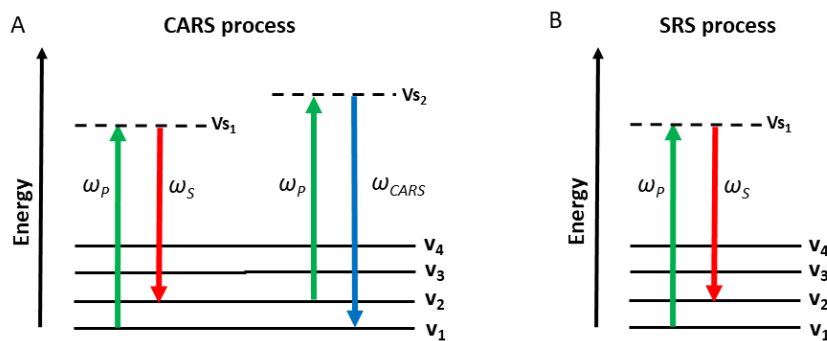


**Figure 1.5.** Schematics of: (A) coherent anti-Stokes Raman scattering (CARS) and (B) stimulated Raman scattering (SRS) processes.

Such strong signals in CARS processes allow for a decrease of signal acquisition times up to 10  $\mu$ s per datapoint. (As it will be shown in subsequent chapters, slow signal acquisition is one of the limiting factors of conventional Raman microscopes during analysis of biological samples). The additional benefit of CARS is that the autofluorescence background, commonly present in a conventional Raman spectrum, does not pose a problem. This is because anti-Stokes

photons, detected in CARS microscopes, are blue-shifted (i.e., possessing higher energies), while photons emitted through fluorescence are red-shifted. Therefore, the latter photons can be easily discarded during the measurement.

Developed in 1962<sup>9</sup>, stimulated Raman scattering (SRS) is similar to CARS. Two laser beams are used in SRS: a pump beam at  $\omega_p$  and a Stokes beam at  $\omega_s$ , Figure 1.5 (B). When the frequency difference ( $\omega_p - \omega_s$ ) matches the frequency of a particular molecular vibration, an amplification of Raman signal is achieved. This results in a decrease of the pump beam intensity, called stimulated Raman loss (SRL), and an increase in the Stokes beam intensity, called stimulated Raman gain (SRG). When ( $\omega_p - \omega_s$ ) does not match any of the molecular vibrational frequencies, SRL and SRG cannot occur. The spectral fingerprint of a molecule can be obtained by maintaining the pump beam frequency constant and using Stokes beam to scan at various frequencies<sup>10</sup>. SRS differs from CARS in that SRG as well as SRL in SRS do not exhibit a non-resonant background<sup>10</sup>.

### 1.3.3 Polarized and Resonance Raman spectroscopy

Polarized Raman spectroscopy allows obtaining additional information about the symmetry of vibration modes. Raman scattering is sensitive to the polarization of incident light. If linearly polarized light is used, then the majority of Raman scattered signals will be aligned in the same plane as that of incident light. It is possible to measure two orthogonally polarized components of Raman spectra by using a polarizer, an optical filter that only allows light of a specific polarization to pass through it. The depolarization coefficient of a particular peak can be obtained by calculating the ratio between intensities of parallel and orthogonal components of the scattered signal. The depolarization coefficient provides information about the symmetry of vibrational modes. Polarized Raman microscopy can be used to analyze isotropic and anisotropic samples. In anisotropic samples the changes in polarization or sample orientation will result in changes in relative intensities of scattering signals with different polarizations, allowing to obtain additional information about the sample. For example, such an approach was used to investigate the molecular orientation distribution in cellulose fibers<sup>11</sup>.

Raman scattered signal is weak. But when energy of incident light is close to energy of an electronic transition of a molecule, the resulting resonance leads to an increase of Raman

signal by several orders of magnitude <sup>12</sup>. The smaller the difference between the frequency of incident light and the electronic transition is, the stronger the resulting resonance Raman intensity will be. In large molecules, only those vibration modes coupled to the chromophore molecular groups can be enhanced by the resonance Raman scattering <sup>13</sup>. The main challenge of resonance Raman spectroscopy is the influence of strong fluorescence, Figure 1.6.

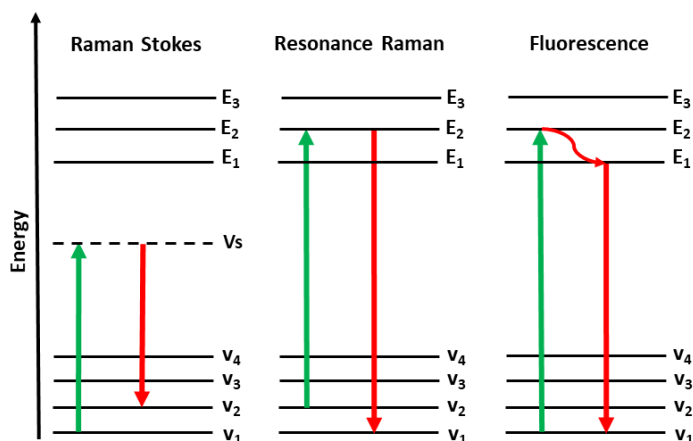


**Figure 1.6.** Raman Stokes scattering, resonance Raman and fluorescence processes illustrated by Jablonski energy diagram.

## 1.4 RECENT DEVELOPMENTS IN RAMAN MICROSCOPY

### 1.4.1 Advances in biological applications of Raman microscopy

Even though significant attention is devoted now to fluorescence microscopy due to the resolution revolution, Raman microscopy is steadily becoming a popular tool in molecular biology and histopathology <sup>14</sup>. It is widely used in cancer research to identify malignant cells. For example, discrimination between osteosarcoma cells and mesenchymal stromal cells was recently shown <sup>15</sup>, where the differentiation between cells was based on comparing their Raman molecular fingerprints. A similar approach is also used in tissue engineering. Recently, Raman molecular fingerprints were used to identify different stages of stem cell differentiation <sup>16 17</sup>. A comparison of Raman molecular fingerprints also enabled a fast and label-free identification of bacterial species <sup>18</sup>. In addition, Raman spectroscopy not only allowed for discrimination between bacteria species, but also permitted identification of variations in phenotypes of bacteria at a single cell level <sup>19</sup>. Also, Raman spectra can be used



to analyze the molecular composition of the sample, for example, to evaluate the bone mineral crystallinity<sup>20</sup>.

Raman microscopy also proved to be a useful tool to study cells and tissue biochemistry<sup>21</sup>. Here, research is often based on using Raman molecular images. Typical Raman molecular images are constructed based on multiple molecular fingerprints collected from an area of interest. The principles of Raman molecular imaging are discussed in detail in Chapter 2. Raman molecular imaging was used to analyze the extracellular matrix arrangement of engineered articular cartilage<sup>22</sup>. It was also shown that Raman imaging can be applied for histopathological studies<sup>23</sup> and in rheumatology<sup>24</sup>. In cancer research, Raman molecular images were used to compare biochemistry of eosinophils versus leukemia cells<sup>25</sup>.

The cell metabolism of such molecules as glucose<sup>26</sup>, cholesterol<sup>27</sup>, and drugs<sup>28</sup> has been studied with coherent Raman scattering in live cells. A possibility to detect the protease activity was also shown using waveguide-based SERS<sup>29</sup>.

Raman microscopy is often used for qualitative analysis in cells and tissue studies. However, a possibility to obtain quantitative information about the molecular composition of cells and cell organelles was recently shown<sup>30</sup>. The presented approach relies on data mining and previously acquired reference databases containing spectra of basic molecular components measured at various concentrations but under the same conditions. The quantification is based on fitting a measured spectrum of a sample to the reference spectrum generated based on the weighted spectra of the molecular components and acquired under the same conditions as those used for investigation of the sample<sup>30</sup>.

Furthermore, developments in treating the autofluorescence background of Raman spectra should be mentioned. Background removal is a standard practice in Raman spectroscopy because this procedure can significantly improve the downstream analysis. At the same time, background removal can result in information loss, because the autofluorescence background may carry information about the sample. Specifically, it was shown that the autofluorescence part of the Raman spectrum can be used to obtain information about the cell differentiation state<sup>31</sup>. It was also demonstrated as a part of the emerging multimodal microscopy concept that a combined application of autofluorescence and Raman spectroscopy allows achieving 97.3 % accuracy in skin cancer diagnostics, while the accuracy determined separately for each spectroscopic method was less than 79 %<sup>32</sup>.

### 1.4.2 Reference databases for Raman peak assignment and analytical calculations

Biological molecules are complicated and many of them consist of similar atoms. That represents a challenge in the identification of molecules, especially in cells. Therefore, precise and extensive databases<sup>33</sup> are particularly desirable in this area. In fact, dedicated databases are also necessary for many fields, for example, pharmaceutical<sup>34</sup>.

In addition, modeling of the frequencies of Raman vibrational peaks is a desired feature that can help to confirm the peak assignment and analyze the structure of molecule<sup>35</sup>. Even when the structure of a molecule is known, as it was shown for phthalocyanine<sup>36</sup>, modeling allows investigating the influence of the environment on atomic vibrations (Supplementary Information for Chapter 1, Appendix, Figure S1.1). Different methods for performing calculations have been recently overviewed<sup>6</sup> and a good comparison between the modeled data provided additional insights (Supplementary Information for Chapter 1, Appendix, Figure S1.2).

### 1.4.3 Raman labels

Raman microscopy is a label-free technique. However, it is possible to enhance the detection sensitivity of Raman microscopy by applying Raman labels in, for example, surface enhanced Raman scattering (SERS). Similarly to fluorescent labels, Raman labels can be used to mark and detect molecules inside the complex organic medium. There are different categories of Raman labels: SERS labels, chemical labels, and isotopes.

SERS labels can be used as labels in immunofluorescent techniques, with the only difference that instead of a fluorescent tag, antibodies are attached to a SERS label. Such label can be created by covering the SERS substrate, like a gold particle, with a reporter molecule and then conjugated with an antibody against the molecule of interest<sup>37</sup>. There is a great variety of molecules that can be used as reporters: Rhodamine 6G, tetramethylrhodamine, 2-bromo-4-mercaptobenzoic acid, *etc.* There is also an ongoing effort in developing new SERS platforms<sup>38</sup>. Numerous novel SERS nanoparticles were synthesized by material scientists, for example, star-like nanoparticles<sup>39 40</sup>, nanocubes<sup>41 42</sup>, *etc.*

An advantage of SERS labels is a possibility to use many different types of labels simultaneously, and thus detect various target molecules. Additionally, all labels can be

detected with a single laser. So, there is no need for multiple lasers with different wavelengths like in fluorescence microscopy. The disadvantage of such SERS labels is that their size is much bigger than that of conventional fluorescent labels.

The idea behind chemical labels is based on direct tagging of a molecule with that having a distinct molecular fingerprint. Alternatively, one can chemically modify molecules for facilitating the detection of its molecular fingerprint. One of the promising reporters for chemical labeling is an alkyne tag. Besides its small size, another advantage of alkyne tagging is that alkynes have a strong Raman peak at  $\sim 2120\text{ cm}^{-1}$ , outside of typical biologically relevant Raman spectrum regions ( $600\sim 1800\text{ cm}^{-1}$  and  $2800\sim 3200\text{ cm}^{-1}$ ). It was demonstrated that alkyne tagged thymidine analogs can be used to monitor DNA synthesis in live cells using a Raman microscope <sup>43</sup>.

Isotope labeling is based on the substitution of certain atoms in a molecule with their isotopes. Isotope substitution results in a characteristic downshift in the Raman spectrum of the molecule due to the replacement of light atoms with heavier and more stable isotopes. Isotope labels can be used to find the presence of atoms in a biological structure or to study and quantify the metabolic activity of microorganisms <sup>44</sup>. It was also recently demonstrated that general metabolic activity of bacteria can be probed by simple addition of deuterium oxide ( $\text{D}_2\text{O}$ ), also called heavy water, to the growth medium <sup>45</sup>. Metabolically active microorganisms would then incorporate deuterium into cells forming a C-D bond with a distinct peak around  $2040\text{--}2300\text{ cm}^{-1}$ .

#### **1.4.4 Superresolution fluorescence and Raman microscopy**

Although fluorescence microscopy is not the focus of this study, it is not possible to discuss superresolution without mentioning superresolution microscopy, which was developed to overcome the diffraction limited resolution of light microscopes. Superresolution provides a possibility to push the resolution beyond the half-wavelength diffraction limit set by Abbe: imaging of cellular organelles, structures, and even molecules is now possible with an unprecedented level of details, even comparable with that obtained in electron microscopy <sup>46</sup>. 4Pi fluorescence microscopy is one of the earliest additions to the growing number of such superresolution methods. It is based on the interference of two coherent light sources, focused on the same spot on the sample plane, allowing a great improvement in axial

resolution <sup>47</sup>. Another superresolution technique, which utilizes light interference, is structured illumination microscopy (SIM) <sup>48</sup>. In SIM, a sample is illuminated with structured light in the form of a specific pattern (often strips) and information is collected in the reciprocal frequency space. The interaction between the excitation pattern, produced by phase-shifting, and the sample results in large-scale interference patterns (the so-called Moiré fringes), which contain information about the sample and illumination patterns (shifted by phase). Analysis of resulting image datasets involves reverse Fourier transform and enables reconstruction of the original image with a higher lateral resolution by approximately a factor of two. An essential advantage of SIM is that no special fluorophores are needed. Besides 4Pi fluorescence microscopy and SIM, there is a growing number of other superresolution techniques: stimulated emission depletion microscopy (STED) <sup>49</sup>, photoactivated localization microscopy (PALM) <sup>50</sup>, total internal reflection fluorescence (TIRF) <sup>51</sup> microscopy, *etc.*

In analogy to what is performed in fluorescence microscopy, in Raman microscopy several solutions to achieve superresolution were developed. One of such techniques is tip-enhanced Raman scattering (TERS) <sup>52</sup>. In TERS, SERS active nanoparticles or coating are mounted on a tip of an atomic force microscope (AFM); scanning the tip over the sample area allows to achieve a high spatial resolution (at the nanometer scale). A possibility to measure live cells in an aqueous medium using TERS was demonstrated <sup>53</sup>. In addition, it was shown that TERS allows obtaining sequence information of DNA molecules <sup>54</sup> because the surface is scanned with a sub-molecular precision. An interesting approach to achieve superresolution in Raman microscopy is to transfer concepts of superresolution methods used in fluorescence microscopy. One of such superresolution methods, inspired by STED, involves specially shaping the laser beam to selectively excite and detect signals from specific points <sup>55</sup>. Another recently implemented superresolution Raman microscope is based on the structural illumination approach, in analogy to SIM in fluorescence; there, using a mice brain slice, 1.4 fold lateral resolution improvement was achieved in comparison to conventional Raman microscopes <sup>56</sup>.

#### **1.4.5 Other applications of Raman microscopy**

The range of applications of Raman spectroscopy and microscopy is extremely large, so only selected applications are highlighted here.

Relevant for Belgian history and culture, medieval paintings have been investigated with Raman spectroscopy to determine pigments and dyes<sup>57</sup>. In addition, Raman spectroscopy has been broadly applied in geology, where experiments are performed in remote places, for example in plains in Patagonia, Argentina, necessitating portable Raman instruments<sup>58</sup>.

Besides biology and geology, Raman spectroscopy is a popular tool in food science. Recently, the portable Raman in combination with SERS was applied for detecting food contamination<sup>59</sup>. SERS was also used to study specific food components, such as food colorants<sup>60</sup> and to investigate the interaction of food packing with food<sup>61</sup>.

### **1.5 MULTIMODAL IMAGING AS AN EMERGING TREND**

Complementarity of different microscopy modalities means that different (but complementary) information about samples can be obtained using those approaches. In this regard, a special term, the so-called correlative microscopy, has been used to cross-compare results obtained from scanning the same areas of samples by using different microscopy modalities. Some examples of such correlative microscopy include a combination of light and electron microscopy to investigate infectious cell cultures<sup>62</sup>; correlative light and electron microscopy to investigate biological samples<sup>63</sup>; atomic force microscopy (AFM) and electron microscopy (EM) to investigate the structure of actin cytoskeleton<sup>64</sup>. Interesting results are also expected by adding X-ray analysis, where X-rays with small wavelengths, 10 pm to 10 nm, are used to obtain information about the atomic structure of a sample. Very detailed atomic-level information can be obtained by combining different microscopy techniques<sup>65</sup>. It can be noted that in medical imaging and clinical practice, multimodal imaging has been also at the forefront of research<sup>66</sup>.

Addition of X-ray scattering methods to Raman spectroscopy provides particularly important structural information, because X-ray methods use a much smaller wavelength of the excitation source and can provide essential structural information about samples. For example, a combination of Raman microscopy with X-ray fluorescence, electron dispersive X-ray spectroscopy, and gas chromatography-mass spectrometry has been applied to study beads from archaeological excavations in the Democratic Republic of Congo<sup>67</sup>, where a gap in history has been filled by discovering new details. Furthermore, a combination of Raman and energy dispersive X-ray (EDX) analysis was applied to investigate dentin and tooth

enamel in dentistry, where the mineralization depth has been measured <sup>68</sup>. Within Raman microscopy area itself, various approaches were developed combining different modalities: SERS, SRS, CARS, TERS.

Combining medical and microscopy multimodal imaging is particularly attractive <sup>69</sup> and Raman microscopy has a special place in such application due to its inherently label-free nature of image acquisition. Research has been already carried out combining Raman microscopy and other types of imaging. For example, fluorescence microscopy has been combined with Raman microscopy to investigate biofilms <sup>70</sup>, where it was identified that a combination of these techniques allows for a deeper understanding of complex biological events than made possible by either of these techniques.

We hypothesize that combining Raman microscopy with other imaging modalities, including medical imaging, would enable uncovering important information relevant for various bioscience applications.

We hypothesize also that development of new approaches in Raman microscopy, including superresolution (achieved by interfering two coherent beams in the direction of their propagation, i.e., 4Pi microscopy) would be an important tool in many fields, including bioscience and bioengineering.

## 1.6 GOALS OF THIS THESIS WORK

The goals of this work are focused on developing **biological applications of multimodal imaging techniques** involving Raman microscopy and exploration of complementarity of such analytical and microscopic techniques for analysis of biological and biomedical samples.

Investigation of biomedical and biological samples is organized here starting from large-scale objects (tissue) and followed by smaller objects (cells and bacteria) as well as biomolecules (the molecular level). While investigating objects with sizes close to the resolution limit of a confocal Raman microscope, a new approach, namely 4Pi Raman confocal microscopy, is developed and applied for investigation of bacteria inside cells.

Specifically, these goals are described as follows.

- 1) Brain tissues: exploration of complementarity of Raman microscopy with magnetic resonance imaging (MRI) based on an example of pathological changes in brain tissues after mild traumatic brain injury (mTBI), (Chapter 2).
- 2) Cells: investigation of complementarity of Raman and fluorescence microscopy for detection and intercellular localization of bovine lactoferrin inside calf rectal epithelial cells in the presence/absence of a bacterial infection, (Chapter 3).
- 3) Inter-bacterial molecular substructures: application of Raman microscopy along-side X-ray and mass spectrometry methods for establishing the molecular composition of conductive fibers inside cable bacteria exhibiting long-distance electron transport, (Chapter 4).
- 4) Development of multifunctional SERS (surface enhanced Raman scattering) particles for molecular detection and drug delivery. Testing a possibility to localize multifunctional particles and induce drug release *in vivo* inside *Caenorhabditis elegans* (*C. elegans*) worms using SERS, (Chapter 5).
- 5) Development of a 4Pi Raman confocal microscope and its application, together with atomic force microscopy (AFM), to study *Chlamydia psittaci* bacteria inside mammalian cells, (Chapter 6).





# Chapter 2

Added value of brain tissue analysis using Raman microscopy and magnetic resonance imaging (MRI)

**Chapter 2** is based on the following publication:

**Added value of microscale Raman chemical analysis in mild traumatic brain injury (TBI): A comparison with macroscale MRI.** D. Khalenkow, S. Donche, K. Braeckman, C. Vanhove, AG. Skirtach. *ASC Omega* **2018**, 3, 12.

## **2 Added value of brain tissue analysis using Raman microscopy and magnetic resonance imaging (MRI)**

In this chapter, we investigate the capability of Raman confocal microscopy to analyze biological samples at the tissue level. In addition, we combine Raman microscopy with magnetic resonance imaging (MRI). The latter technique is widely used in medicine for tissue analysis, but it lacks the resolution of microscopy techniques and provides limited molecular information. Therefore, a combination of MRI with histological microscopy techniques, such as Raman microscopy, can be a valuable tool to better understand the structural and molecular changes in the brain after an injury, particularly when the injury is not very pronounced, as it is the case in mild traumatic brain injury (mTBI). In this work, we analyze brain tissue samples before and after traumatic brain injury using both MRI and Raman microscopy. Furthermore, we have developed protocols for sample preparation, scanning, and analysis of the resulting data with a confocal Raman microscope. This chapter discusses how to analyze biological tissue samples using Raman microscopy when no prior information about its state was known.

## 2.1 INTRODUCTION

The definition of traumatic brain injury (TBI) is the following: it is a pathological change in brain structure and function caused by an impact of an object or brain rapid acceleration/deceleration <sup>71</sup>. TBI is, unfortunately, a frequently occurring trauma in military and other conflicts. Besides, it is also common in everyday life since TBI can also be a result of sport activities, particularly in American football or boxing, or a car, motorcycle, or bicycle accident <sup>72</sup>. TBI is divided into several categories: mild, moderate, and severe. Gradation is based on the Glasgow Coma Scale and the severity of symptoms <sup>73</sup>. In this work, we study the mild TBI (mTBI), which is diagnosed in 80 % of head trauma patients in the US (CDC 2010) <sup>74</sup>. It is considered the least severe and dangerous form of TBI. However, at least 30 % of mTBI patients were not able to achieve full neurologic recovery and have developed prolonged behavior and cognitive changes <sup>75</sup>.

Magnetic resonance imaging (MRI) is a conventionally used method to study TBI <sup>76</sup> and it provides a possibility for non-invasive *in vivo* visualization of tissue. MRI uses strong magnetic field that forces the spins of protons in the sample to align with magnetic field <sup>77</sup>. Next, an intense radio frequency radiation causes the spins out of alignment with magnetic field. After the radiofrequency radiation is turned off, protons realign with magnetic field, emitting the radio pulses. These pulses are detected and used to construct the MRI image. The analysis of resulting MRI images allows the detection of damage caused by TBI, such as brain white matter shearing, foci of axonal injury, and small subacute hemorrhages <sup>78</sup>. These brain lesions were observed with MRI in patients with moderate and severe TBI <sup>79</sup>. However, the MRI scans of the patients with mild TBI often show no abnormalities since conventional MRI is not sensitive enough to detect the micro-bleedings and diffuse/traumatic axonal injuries, which are the common complication of mTBI. Therefore, little is known about mTBI underlying causes and mechanisms <sup>80 81</sup>. That is why we have decided to test whether Raman confocal microscopy would be a viable addition to conventional neuroimaging tools for uncovering pathological changes in the brain tissue caused by mTBI.

There are two reasons why Raman microscopic molecular images can have an added value to MRI. The first reason: while it is possible to perform deep in-tissue imaging with a conventional MRI scanner, its spatial resolution is not as high as that of an optical microscope (100  $\mu\text{m}$  versus under 1  $\mu\text{m}$  for MRI and light microscopy, respectively). The second reason: MRI misses

specificity to detect the underlying biological changes in the brain after mTBI <sup>80</sup>, where Raman spectroscopy, with its ability to obtain data on a molecular level <sup>82</sup>, might provide a valuable and complementary addition in this case. It may be possible to use MRI to locate the damaged spot and then use Raman microscopy to obtain information about molecular changes in this area. It should be noted that advanced forms of MRI, such as diffusion-weighted MRI, are more sensitive than conventional MRI. It was shown that diffusion-weighted MRI could detect changes in brain after mTBI invisible by conventional MRI <sup>83 84</sup>. Diffusion MRI image analysis based on white matter tract integrity metrics allows studying changes in axons after mTBI <sup>85</sup>. But even advanced forms of MRI in a combination with sophisticated data analysis lack the specificity of histological techniques. For example, it was possible to detect changes in mTBI rat brains after a cognitive training program using diffusion tensor MRI, but it was not possible to link those changes to specific region of the brain or to understand the molecular nature of those changes <sup>84</sup>. Here Raman microscopy can be particularly attractive.

Raman spectroscopy has been already used in neuroscience for analysis of biochemical changes in peripheral nerves after an injury <sup>86</sup> and to track molecular changes on the surface of the brain hemispheres after TBI <sup>87</sup>. Raman spectroscopy was also used to study the lipid content of the brain and brain tumors <sup>88</sup>. Recently, it was shown that TBI can be diagnosed with SERS by detecting specific biomarkers in blood <sup>89</sup>.

The studies mentioned above were focused on either individual neurons, biomarkers in body fluids, brain surface or the molecular composition of brain lipids, while, to the best of our knowledge, no analysis of changes in corpus callosum after mTBI has done to-date using Raman microscopy. That is why the primary goal of our study was to investigate whether any changes in brain regions can be observed after mTBI using a simultaneous application of MRI and Raman microscopy. We have chosen the corpus callosum region of the brain as the main focus of our study, because significant changes in volume and morphology in the corpus callosum areas were reported in humans after severe TBI <sup>90</sup>.

## 2.2 MATERIALS AND METHODS

### 2.2.1 Experimental layout

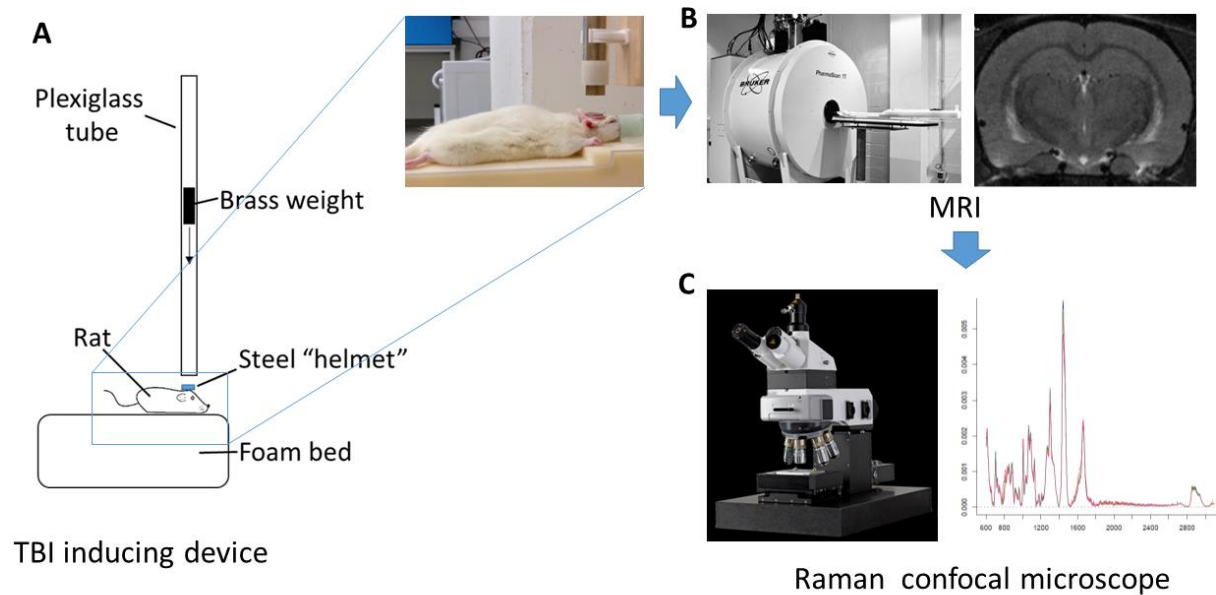


**Figure 2.1.** Schematics of the experiment studying mTBI impacts on mice brain.

(A) Marmarou's setup for mTBI induction in rats: a rat in the device is shown in the insert. (B) MRI scans were done before and after mTBI induction to detect the damaged brain region. (C) Raman scans were conducted to obtain information about the molecular changes after mTBI in the corpus callosum region of the brain.

The experimental layout is shown in Figure 2.1. First, mTBI is induced in a rat by controllable force impact of a brass weight. Next, we have performed MRI scans to analyze the impact of this injury *in vivo*, Figure 2.1 (B). The brains of the rats were scanned with conventional T2-weighted MRI (a) before, (b) one day after, and (c) one week after mTBI to identify and image the damaged areas. Subsequently, the brains were extracted and subjected to Raman histological analysis with the focus on the corpus callosum region, Figure 2.1 (C). Raman and MRI scans were done by applying both techniques to similar areas in the brain before and after mTBI.

### 2.2.2 mTBI induction

To induce mTBI in a controllable and, most important, repetitive way, the replica of the Marmarou weight-drop model<sup>91</sup> was built (Figure 2.1 (A)). In such a device, the severity of the TBI can be controlled by adjusting the mass of the weight and the drop height. The experiments were carried on eight adult female Wistar rats (n=8, weight 265±16 g), purchased from Janvier Labs (Le Genest-Saint-Isle, France). Studies were approved by the Animal Ethics Committee at Ghent University (ECD 17/96), and experiments were conducted in accordance with the guidelines of the European Commission (Directive 2010/63/EU).

All rats were anesthetized with a mixture of isoflurane and O<sub>2</sub> (5% induction, 2% maintenance). This was done not only to immobilize rats during TBI induction but also to reduce the stress and suffering of the animals. Additionally, rats were injected with 0.05 mg/kg buprenorphine (Temgesic, Indivior) subcutaneously. Buprenorphine is an opioid drug that is used to relieve pain in human TBI patients.

After 30 minutes, the rat's head was shaved, 100 µL of 2% xylocaine (AstraZeneca) was locally injected into the scalp and an incision was made to expose the skull. A metallic disc with a diameter of 10 mm and 3 mm thickness, which served as a helmet, was glued onto the skull 1/3 before and 2/3 behind bregma. Next, five rats have received a mild traumatic brain injury with varying severity by dropping the 450 g brass weight. One rat received the impact from the weight dropped from 1.0 meter (TBI100), two from 1.30 meters (TBI130), and two from 1.45 meters (TBI145). The last three rats did not receive the impact and were used as a reference control group (sham). 1 mL of physiological solution (0.9 % NaCl) was injected through a catheter inserted in the lateral tail vein, to reduce the hemodynamic shock.

Subsequently, the helmet was removed, and the incision was stitched. Additionally, the rats were imaged with a CT scan (X-Cube, Molecubes, Ghent, Belgium) to rule out any skull fractures because this is a criterion for euthanasia and the sign of severe TBI. To minimize the radiation dose, a general-purpose low dose one-bed position scan was performed. One day post impact the rats received an extra dose of 0.05 mg/kg buprenorphine.

### 2.2.3 *In vivo* longitudinal MRI imaging

MRI scans were conducted to analyze the impact of induced brain injury *in vivo*. MRI data were acquired on a 7T MRI scanner (BioSpin Pharmascan 70/16, Bruker, Ettlingen, Germany) using a volume rat brain/mouse whole-body RF coil. The brains of all rats participating in the

experiment were scanned with conventional T2-weighted MRI before, one day after, and one week after TBI. The purpose of the scans was to identify and image the damaged areas. Control rats were subjected to similar scans and drug treatment as mTBI rats. During imaging, the animals were under 2% isoflurane anaesthesia, their body temperature was kept constant using circulating warm water heated blanket and bubble wrap, and respiration rate was monitored with a pressure pad. For each time point, a whole-brain anatomical T2-weighted scan was done using a Rapid Acquisition with Refocused Echoes (RARE) sequence: TR=5.5 seconds, TE=37 milliseconds, RARE factor=8, FOV=2.5 x 2.5 cm. There were 45 slices scanned with a thickness of 600  $\mu\text{m}$  per slice and with an in-plane resolution of 109 x 109  $\mu\text{m}$ . The acquisition time was 12 minutes.

#### **2.2.4 Sample preparation, Raman microscopy data acquisition, and pre-processing**

Unfortunately, in contrast to MRI, it is not possible to access the deep brain structures *in vivo* with a confocal Raman microscope. The solution we found was to extract the brain, cut it into slices, which then can be scanned with Raman. The main challenge here is how to cut the brain in a repeatable way with minimum changes in molecular or histological structures. The conventional way in life science and pathological anatomy for microscopic tissue slice preparation is to embed the sample tissue in paraffin or plastic and then cut it with a microtome. We found that such methods cannot be used for Raman microscopy for two reasons:

1. Raman spectra of both plastic and paraffin contain intense peaks that overlap and oversaturate the cellular peaks;
2. the embedment procedure requires heating and/or dehydration of samples, which may influence its molecular or structural composition.

Therefore, we developed the protocol for tissue slides preparation for confocal Raman microscopy, which is based on deep freezing of the tissue. Such a procedure gives it the necessary hardness to be cut with a microtome. This step is particularly relevant for such soft tissue as the brain. Tissue freezing was followed by cutting it with cryo-microtome and immediate fixation during the de-freezing. We opted to do fixation after cutting and not before, because it was not possible, without sacrificing more rats, to evaluate how good fixation would work on the whole brain, in particular, how deep and how fast formaldehyde



would penetrate in the brain. Also, there was a danger that the whole brain fixation would create a formaldehyde concentration gradient, where surface brain proteins would undergo more cross-linking than proteins in deep brain regions<sup>92</sup>. The sample preparation was done as follows: one week post mTBI induction, all rats were euthanized with 100 mg/kg of sodium pentobarbital (20%) (Kela NV, Hoogstraten, Belgium). Brains were extracted from the skulls and immediately snapped frozen in liquid nitrogen-cooled 2-methylbutan (Reagent-Plus<sup>®</sup> 99%, Sigma Aldrich). Next, brains were cut into 20  $\mu\text{m}$  thick slices with a cryo-microtome (CM3050 S, Leica Microsystems, Belgium). Three tissue slices per animal were produced. The obtained tissue slices were placed on quartz slides (Ted Pella, Inc.) fixed for 10 minutes with 4% formaldehyde (4078-9001, Klinipath) and scanned with a Raman confocal microscope.

The Raman microscope (Alpha300R+, WITec, Ulm, Germany) was equipped with a 785 nm laser (Toptica, Munich, Germany) and an UHTS 300 spectrometer with a charged coupled device (CCD) camera (ANDOR iDus 401 BR-DD, Belfast, Great Britain) cooled to -72 °C.

The same microscope, laser, and CCD camera were used for all research described in this thesis. Therefore, information about microscope setup will not be repeated in subsequent chapters. Only relevant experimental details, such as laser power, integration time, objectives will be described in the following chapters.

All tissue studies were conducted with laser power of 225 mW. A water immersive 20x/0.6 NA objective (Nikon) was used for scanning. Tissue areas of 400  $\mu\text{m}$  x 200  $\mu\text{m}$  were mapped with the step size of 10  $\mu\text{m}$ /pixel and an integration time of 1.5 seconds per data point. Three area scans per slice were performed. Brain slices were kept in the Hanks' Balanced Salt solution (14025050, ThermoFisher) during the whole scan to avoid tissue detachment from the quartz slide, dehydration, and osmotic damage.

Spectral datasets were pre-processed in R.3.4 using the *HyperSpec* package<sup>93</sup>. Background subtraction and baseline correction were done by applying the *Asymmetric Least Squares* function, and normalization by applying *the area-under-curve* method using the *Baseline*<sup>94</sup> and *MALDIquant*<sup>95</sup> packages, respectively. The detailed information about the basics of Raman datasets pre-processing and analysis can be found in Appendix (Supplementary Information for Chapter 2 (Appendix), S1).

## 2.3 RESULTS AND DISCUSSION

### 2.3.1 Scanning tissue samples with Raman microscope

Tissue slices were prepared similar to the protocol presented by Bergner *et al.*<sup>96</sup> Next, a step-by-step approach to optimize sample handling and scan acquisition was carried out with the aim to investigate and minimize all external factors which could interfere with the scans.

Initially, a possibility of discriminating between different rat tissue types in the Raman datasets described in literature on mice<sup>97</sup> and rat<sup>98</sup> was investigated. Subsequently, a procedure was developed to apply such protocols for MRI-Raman microscopy-based approach. First, we have measured and compared Raman spectra of brain, heart, and kidney rat tissues. As it can be seen from Figure 2.2 (A), each tissue type produces a distinct molecular fingerprint highlighted with grey rectangles.

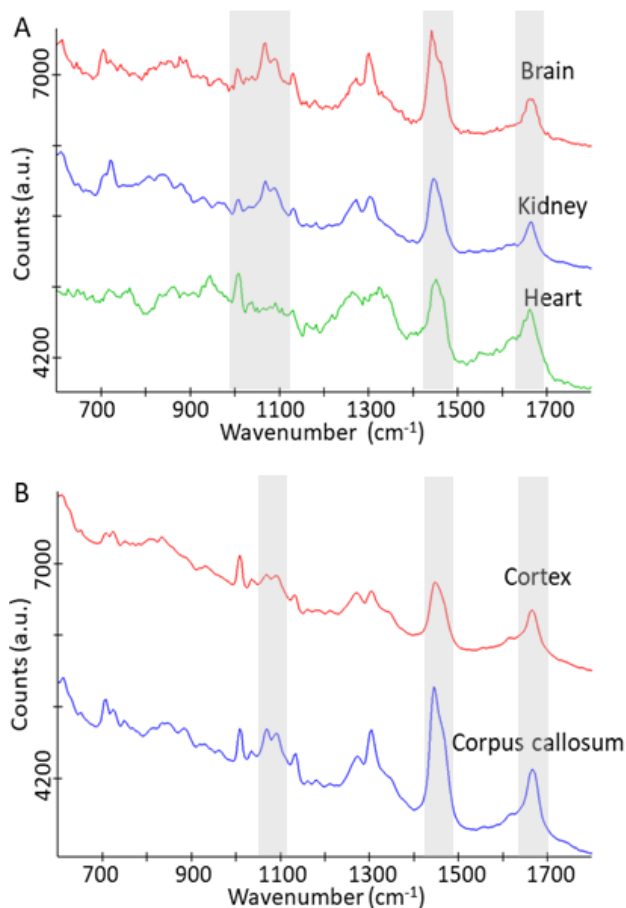


**Figure 2.2.** Comparison of molecular fingerprints of tissues of rats. (A) Raman scattering spectra from brain, kidney, and heart tissues. (B) Raman scattering spectra from the brain cortex and corpus callosum regions.

Next, we have tested if Raman confocal microscopy is sensitive enough to discriminate between different structures inside brain tissue slices. It was found that the cortex and corpus callosum areas have distinct molecular fingerprints, Figure 2.2 (B). After we had confirmed that confocal Raman microscopy allows obtaining spectra with a high enough resolution to discriminate between tissue types, we have moved to identification and removal of possible sources of external noise, which can potentially influence the measurements.

It was found that the main factor in this case is the structural integrity of the tissue slice over time. It is important to remember that tissue slices in our case were only 25  $\mu\text{m}$  thick and they were not fixed to the surface of the slide (quartz slides were used). It was also found that water currents produced by stage and microscope objective movement during scans can cause detachment and degradation of the sample around its edges. For the brain tissue, this effect started to be noticeable only after 3 hours of active scanning and moving the stage. While the corpus callosum area situated in the center of the slice is not affected, the detached pieces of brain tissue can be captured by the scanning laser beam and cause distortions on the molecular image.

The next step was to find an optimal integration time per measured spot in an area scan. Integration time can be defined as the amount of time the Raman signal is measured by a CCD camera to obtain the single spectrum. At a low integration time, small peaks can be masked by noise. Therefore, higher integration times lead to an improved resolution of the peaks. However, this trend is not always applicable: at a certain point, an increase in the integration time would produce no measurable increase in spectrum quality. The second factor to consider is that each area scan can consist of hundreds of individual Raman spectra, and because of that, the measurement of a single area can take hours. If the sample is not structurally stable, then long multi-hour scans may affect it. That is why, it is crucial to find the optimal integration time, since it allows decreasing the overall scanning time. It was done by taking multiple Raman spectra at the same spot, gradually increasing the integration time after each scan, until no improvement in peaks resolution was detected.

The last factor to consider is whether the confocal volume, from which the Raman signal is measured, is the same for all points of the dataset. Because we use a confocal microscope to collect the Raman scattering signal, the diffraction limited focal area of the microscope will affect the peak resolution. The scanned samples were placed on a thick quartz slide, which

was then mounted inside a Petri dish. Both quartz and plastic Petri dish bottom sides are not perfectly flat, and this induces a slight tilt of the sample. The average brain slice length was around 4000  $\mu\text{m}$  in the largest dimension. The difference in the axial position of the optimal focus was found to be offset by up to 100  $\mu\text{m}$  compared to the position at the opposite edge of the sample. The solution to this potential problem was to divide a sample in a set of rectangular areas with average dimensions of 400  $\mu\text{m}$  x 200  $\mu\text{m}$  and calibrate the microscope to have the optimal focus at the center of each area.

### **2.3.2 Construction of Raman molecular images of tissue samples**

Each area scan produces in a large dataset of 800 entries, where each entry is a single spectrum consisting of 1024 data points. After pre-processing steps were performed, entries in the dataset were grouped based on how similar their spectra were. Because different tissue types have their unique molecular fingerprints, the dataset entries containing spectra from, for example, the cortex can be separated from the datapoints belonging to the corpus callosum area. Such clustering can be done using both supervised and un-supervised data mining.

In data processing, no pre-processed and annotated brain Raman datasets were available, which could have been used as a training set for supervised data mining. Therefore, unsupervised hierarchical clustering has been applied to select those data points belonging to the corpus callosum region. This method also allowed detecting structural and molecular abnormalities of the scanned tissue. The main disadvantage of unsupervised clustering is that it is necessary to make an intelligent guess about the number of groups, into which datasets need to be divided. Splitting the dataset into a low number of groups leads to losing valuable information, while dividing the obtained data into too many groups would lead to separation of the datasets based on slight differences generated by the background noise or laser power fluctuations. Therefore, such separation will provide no useful information. In our case, we have used the silhouette plot method and preliminary knowledge of what types of tissues we expected to find in the investigated area to determine the optimal number of clusters. The silhouette plot can be constructed by plotting the measure of how close each point in one cluster is to points in the neighboring clusters versus the number of clusters. The histological optical images of the scanned area, Figure 2.3 (A), can also provide important information on

the number of clusters. It is possible to use the following approach: start with two clusters and then gradually increase the number of clusters, while comparing the resulting molecular images with those obtained by an optical microscope and performing the manual inspection of each cluster. By giving each cluster of data points a unique color, and plotting each data point as a single pixel, we can create a molecular image of the scanned area, Figure 2.3 (B), where various tissues and structural abnormalities can be also visualized. After background subtraction, normalization, and clustering – information about the anatomical and molecular composition can be extracted from the resulting pre-processed datasets.

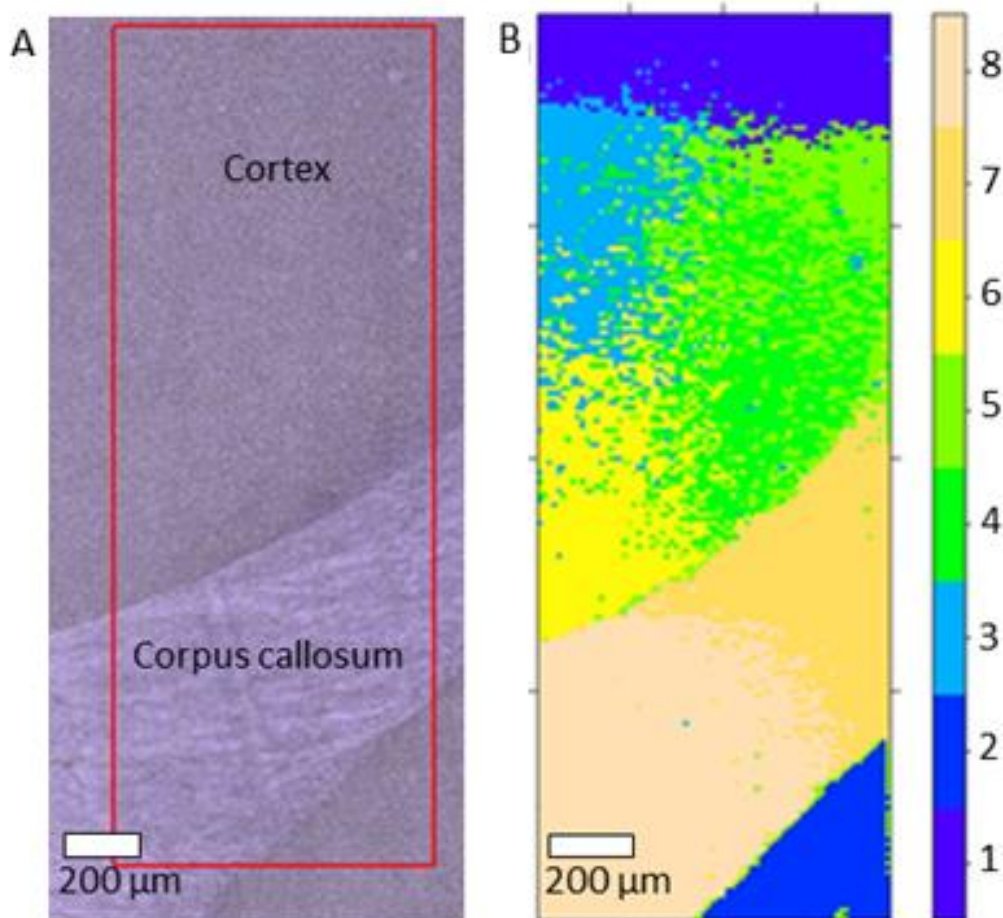


**Figure 2.3.** (A) Light microscopy image of cortex and corpus callosum, and (B) the corresponding Raman spectroscopic image produced by the hierarchical clustering analysis. Numbering of colors corresponds to clusters.

It is important to note that the resulting molecular images can contain artifacts and distortions, which may introduce bias into the image interpretation and analysis. The nature of such artifacts may depend on the structure and topography of analyzed tissue. If the tissue

slice is not flat, if it has a rough surface with significant variations in height between points, then that can result in molecular image distortion. Because of a rough surface, the number of molecules in the confocal volume varies between the points, translating into variations in peak intensities, Figure 2.4 (A, B).

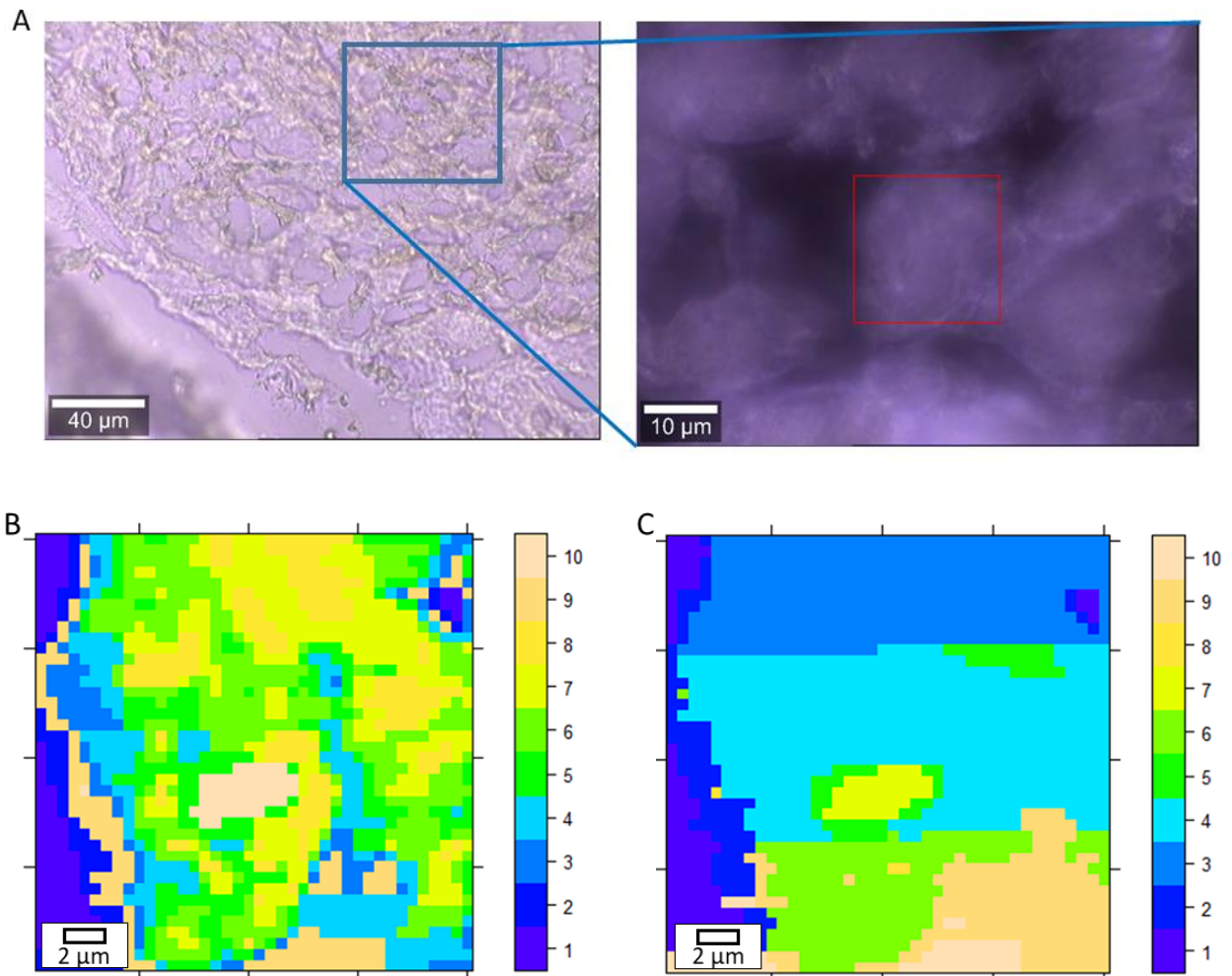


**Figure 2.4.** (A) Light microscope images of rat heart tissue. The red rectangle marks the area scanned with Raman microscopy. (B) Raman molecular image constructed based on the clustering analysis. No data normalization was done. (C) Raman molecular image, constructed based on the clustering analysis performed on a normalized dataset. Numbering of colors corresponds to clusters.

On heatmaps and clustering images, such variation results in the appearance of false substructures, which are not actually present in the tissue. The problem can be partially solved with intensity normalization across the dataset. However, normalization itself may introduce additional artifacts on the image or remove actual substructures, Figure 2.4 (C). This creates

certain challenges for samples with a rough surface, such as heart tissue slices. Because it is not possible to conclude with a high degree of certainty if the identified substructure on the molecular image is a scanning artifact or if it is present in the sample. Additionally, samples with a rough surface may pose the challenge of reproducing the results using conventional confocal Raman microscope scanning due to obstacles associated with precisely focusing on the same plane. This problem may be solved by scanning a high number of samples and by scanning the same area at different confocal planes. However, such an approach extensively increases the scanning time. Combining Raman microscopy with atomic force microscopy (AFM) is useful for interpreting Raman molecular images of samples with a rough surface. The complementarity of Raman and AFM will be discussed in detail in **Chapter 6**.

As it is already mentioned in section 2.3.1, the second problem encountered during measurements was sample degradation. The degradation was noticeable in a microscope: small particles of organic material appeared in the sample due to tissue degradation. Peculiarly, these small particles can be captured by a laser beam and distort the image. Such distortions manifest themselves in the form of parallel lines on the image. The lines can be present both on the heatmap and the clustering image. The problem of particle detachment was especially relevant during the imaging of rat's kidney tissue slices, Figure 2.5 (A, B). Such artifacts, caused by captured particles, cannot be removed with normalization, Figure 2.5 (C). The lines were present not only when the scan was performed at the edge of the slice, but also in the central regions of the sample (Supplementary Information for Chapter 2 (Appendix), Figure S2.6). The fast degradation of kidney tissue slices makes it challenging to image such a sample with Raman microscope.

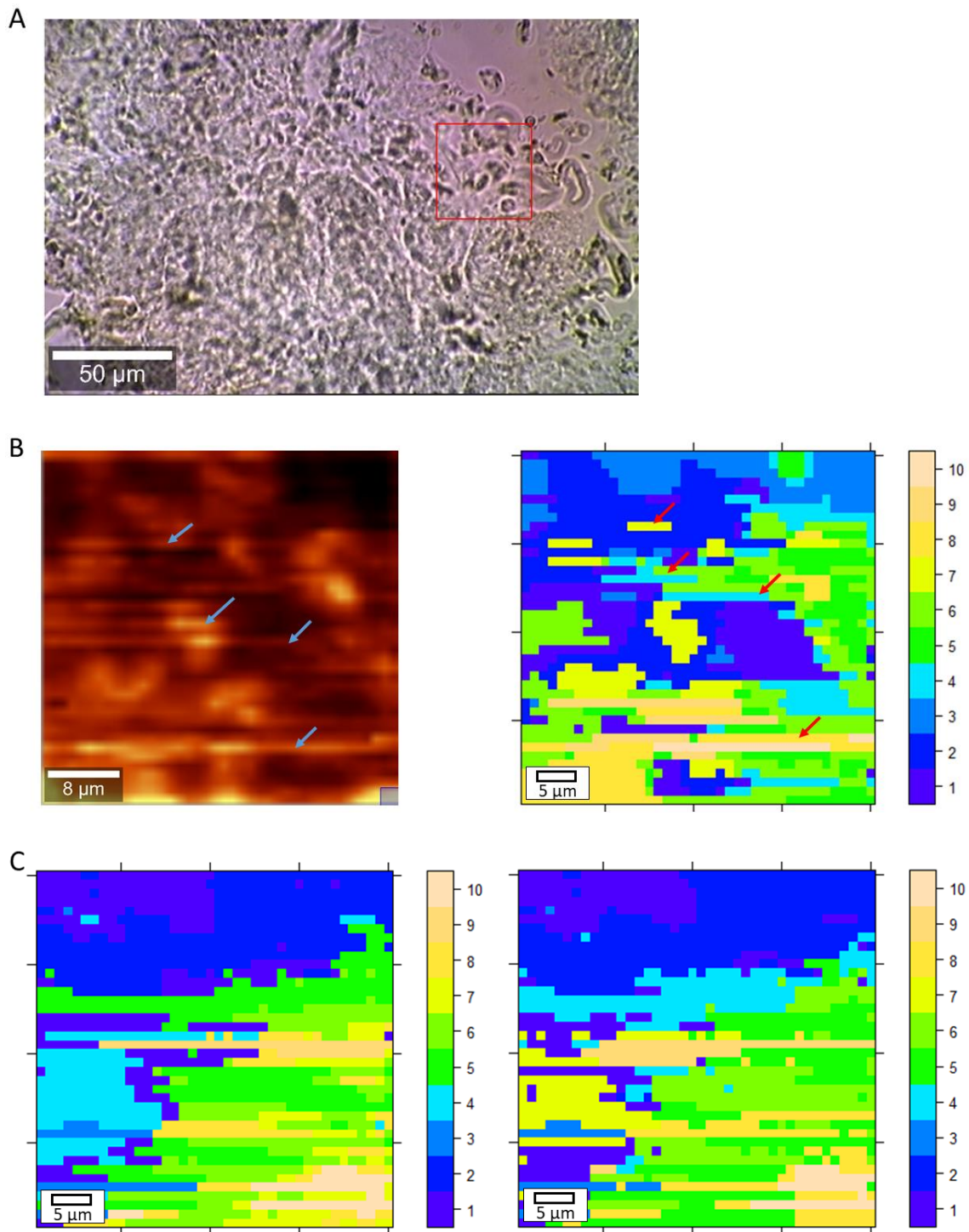


**Figure 2.5.** (A) Transmission light microscopy images of rat kidney tissue. The red rectangle marks the area at the edge of the slice scanned with Raman microscopy. (B) Raman scattering heatmap of the rat kidney tissue based at the  $1004\text{ cm}^{-1}$  peak; red and blue arrows mark image artifacts caused by detached tissue debris. Clustering analysis is shown on the right-hand side of panel (B). (C) Comparison of non-normalized (left) and normalized (right) Raman clustering image. Numbering of colors corresponds to clusters.



### 2.3.3 MRI results

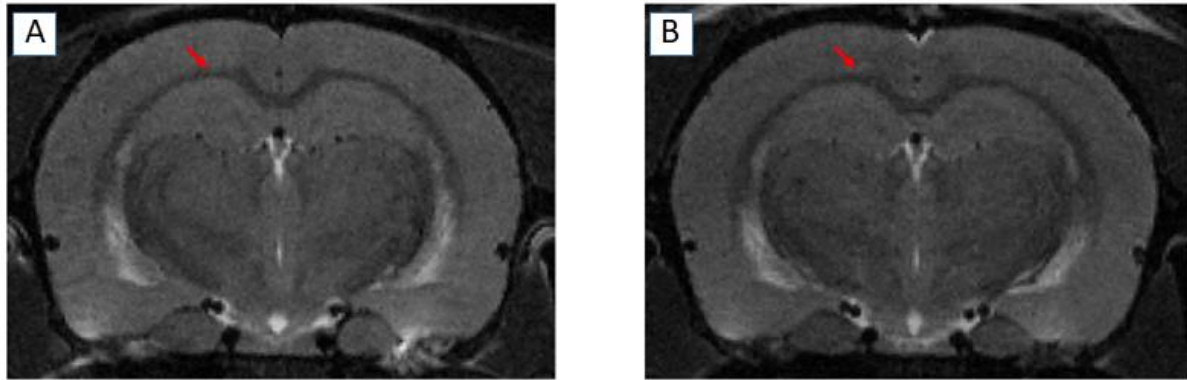


**Figure 2.6.** T2-weighted MRI brain images (A) before mTBI, and (B) 1 week after impact. Arrows point to the corpus callosum area.

The anatomical T2-weighted MRI scans (with distinct sequences of pulses) of the brain of a rat were obtained in the next step. In Figure 2.6, the scans are shown before (A) and one week after (B) the impact. Anatomical T2-weighted images were very similar in all animals; therefore, Figure 2.6 is representative of all animal brains analyzed in this experiment. The MRI scan resulted in a dataset of images, from which we have chosen the slices, where the corpus callosum and the lobes of the hippocampus are clearly visible. No significant changes were observed in these regions on slices obtained one day and one week after the TBI; these scans were also compared to those from the control rats. This supports the evidence that the produced impact induces only a mild TBI.

### 2.3.4 Analysis of Raman molecular images of the corpus callosum

After analysis of 54 molecular images, we have found a histologically abnormal area (15-20  $\mu\text{m}$  in size) in a brain slice obtained from a rat in 1 week after the medium force TBI, Figure 2.7 (A). This area had two times higher Raman signal intensity compared to the signal from the surrounding tissues, Figure 2.7 (B). A similar signal pattern was noticed in molecular fingerprint from dried rat blood, suggesting that the observed abnormal area may be the result of micro-hemorrhages common in mTBI<sup>81</sup>.

Blood in the corpus callosum area was found only in one animal. Two factors can explain the absence of such areas in other TBI samples. The first possible explanation is that because the slices were very thin, blood could be washed away during the fixation or scanning.

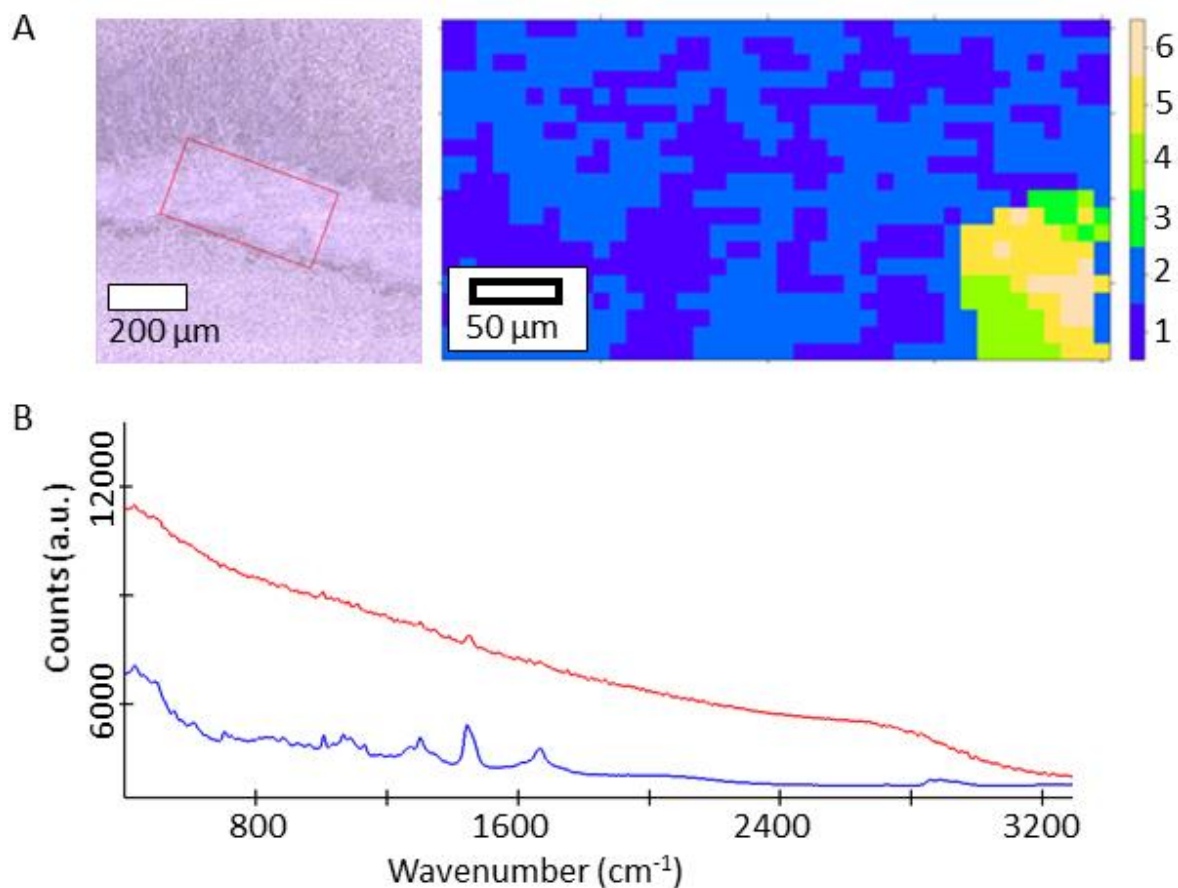


**Figure 2.7.** (A) Light microscopy image of the corpus callosum and corresponding Raman molecular image of the corpus callosum with an abnormal region. (B) The mean Raman spectra of the corpus callosum (blue) and high-intensity spectrum of the abnormal region (red) from the image in the panel (A). Numbering of colors corresponds to clusters.

The second explanation is that an insufficient number of brain slices was analyzed in this experiment or that observed micro-hemorrhages were present only in a limited number of mTBI cases.

### 2.3.5 Analysis of corpus callosum molecular fingerprints before and after mTBI

Data points corresponding to the corpus callosum of rats were compared between control (rats with no impact) and mTBI affected rats with the focus on the 2800-3000 cm<sup>-1</sup> Raman spectral region, Figure 2.8 (A). We have focused on this part of the spectrum because of the existence of neurological interpretation for the peaks in this region. It was found that in the peripheral nerves, the peak intensity in the 2940 cm<sup>-1</sup> region of Raman neuronal spectrum is proportional to the neurofilament protein concentration, and the peak in the 2855 cm<sup>-1</sup> region

corresponds to myelin lipids concentration, respectively <sup>99</sup>. A comparison of peak ratios between the samples was done using average spectra calculated from each scanned area. In total, 54 areas were scanned. A comparison of spectra between the control rats and mTBI rats has shown a significant decrease of the 2940 cm<sup>-1</sup> to 2855 cm<sup>-1</sup> peak ratios after mTBI with p= 0.001299 for TBI130 versus control rats. A decrease in peak ratios was also observed for TBI145 rat versus the control rats with p= 0.00076, Figure 2.8 (B).

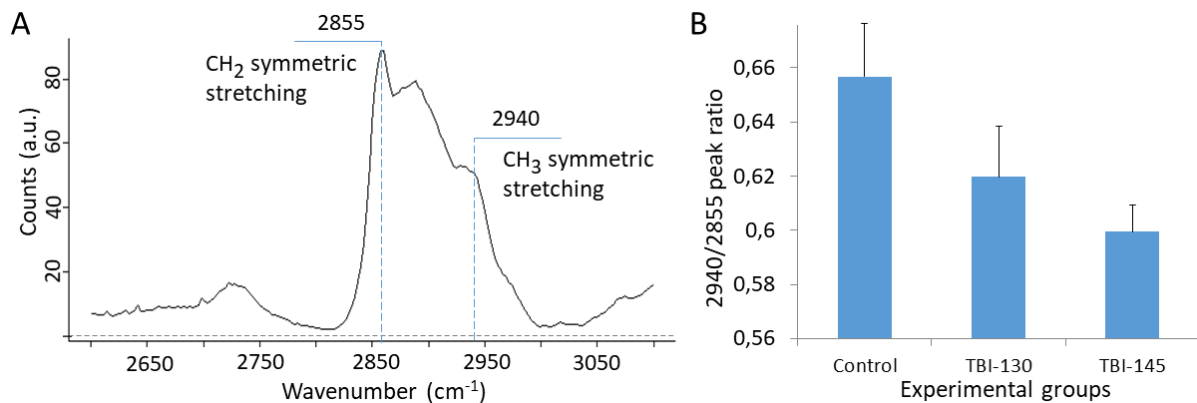


**Figure 2.8.** (A) Raman spectrum of the CH stretching region used for peak intensity analysis. (B) Changes in the Raman scattering intensity peak ratio at 2940 cm<sup>-1</sup> to that at 2855 cm<sup>-1</sup> after the mTBI. The control column in the plot shows the peak ratio obtained from the corpus callosum area of a rat not exposed to TBI. The TBI 130 and TBI 145 columns are the peak ratios from rats, in which the mild TBI was induced by the weight drop from 1.30 m and 1.45 m heights, respectively. Error bars show the standard deviation between the data points.

There was observed a larger change in peak ratios in TBI145 compared to control than in TBI130, Figure 2.8 (B). But it is important to note that only one brain from the TBI145 group was scanned with Raman microscopy, as the second rat was found dead the next day after the impact. Due to ethical consideration, it was decided not to subject additional animals for 1.45 m weight drop impact. That is why it is not possible to conclude with high certainty whether the larger difference in peak ratios observed in TBI145 compared to TBI130 is caused by individual differences between animals or is the result of more severe brain damage by the weight drop from 1.45 m.

Because our analysis was based on the mean spectrum of the scanned areas, it was challenging to deduce whether the observed differences in molecular fingerprint between control and TBI130 present in all axons in the corpus callosum area or only in a limited number of them.

### 2.3. CONCLUSION

A combination of MRI and Raman imaging is demonstrated to be a viable approach to study mTBI on macro- and micro- scales. TBI caused by an impact of dropping a 450 g weight from 1.30 m and 1.45 m heights did not produce lesions detectable with conventional MRI, measured one day and one week after the impact. The absence of lesions in MRI images was a good reference that the applied force did not cause a severe TBI in rats. However, no damage could be detected with MRI. On the other hand, analysis of corpus callosum regions revealed detectable changes in brain tissue using Raman microscopy, even under conditions of mTBI. This is evidenced by analyzing the decrease in the ratio of axon proteins to myeloid lipids as detected in the corpus callosum region after mTBI. The hierarchical clustering analysis allowed discriminating between different anatomical regions of the brain, detecting structural and molecular abnormality inside the corpus callosum region, which is presumably the result of micro bleeding caused by mTBI. The addition of Raman microscopy to brain study provides the means to track changes in the brain, undetectable by conventional MRI. However, it was necessary to cut the brain to get access to the corpus callosum region. Invasiveness and associated with it challenging for *in vivo* scans are the main disadvantages of the presented protocol of tissue analysis with Raman microscopy. However, Raman spectroscopy itself is nondestructive for tissue slices. It is essential to mention here that even more detailed analysis is possible, for example, an area of a sample can be cut-off from a slice, scanned with Raman microscopy, and used for further analysis, such as genomic sequencing or immunostaining.

# Chapter 3

Localization of bovine lactoferrin inside calf cells by fluorescence and Raman microscopy

**Chapter 3** is based on the following publication:

**Lactoferrin translocates to the nucleus of bovine rectal epithelial cells in the presence of *Escherichia coli* O157: H7.** J. Rybarczyk (\*), D. Khalenkow (\*), E. Kieckens, AG. Skirtach, E. Cox, D. Vanrompay. *Veterinary Research* **2019**, 50, 75 (\* - equal first-author contribution).

### **3 Localization of bovine lactoferrin inside calf cells by fluorescence and Raman microscopy**

In this chapter, we investigate samples on a significantly lower scale, where each spectrum is obtained from an area of around one micrometer in diameter. Such an acquisition enables the identification of the position of molecules inside cells and bacteria. Also, similarly to previous chapters, we continue the investigation of a combination of Raman microscopy with various analytical techniques to obtain additional information about samples. We aim to achieve this goal by investigating complementarity of Raman and fluorescence microscopy for localizing molecules (bovine lactoferrin) with known molecular composition inside cells. Translocation of bovine lactoferrin to cell nuclei is investigated after cellular uptake; the influence of bacteria on the bovine lactoferrin translocation is also studied.

### 3.1 INTRODUCTION

It was already shown how to perform the analysis on the tissue level (this was described in **Chapter 2**). Next, we test the capability of conventional confocal Raman microscopy to analyze samples at the cell level. To achieve this goal, we have carried out research to identify the position of lactoferrin inside bovine rectal epithelium cells. Lactoferrin is a member of transferrin family of iron-binding glycoproteins. One of the main roles of transferrin is to supply iron to the cell. Transferrin can reversibly chelate iron ions with a high affinity ( $K_d=10^{-20}$  M) <sup>100</sup>. Iron-loaded transferrin binds to cell surface transferrin receptor 1 <sup>101</sup>. Next, transferrin/receptor complex is taken inside the cell via endocytosis. The endosome with transferrin inside undergoes acidification, mediated by the ATPase proton pump. The drop of pH to 5.5 inside the endosome triggers the release of iron ions from transferrin. Transferrin is then either degraded or released from the cell for another iron transport cycle <sup>101</sup>.

Besides iron transport, lactoferrin can also modulate the immune response and it is known to possess antimicrobial properties <sup>102</sup>. Lactoferrin is secreted by epithelial cells and can be found in milk, tears, sweat, gastrointestinal, and other exocrine fluids<sup>103 104 105</sup>. It is also present in serum and secondary granules of neutrophils <sup>106</sup>. It was recently found that the administration of bovine lactoferrin (bLF), extracted from milk, allows removal of *Enterohemorrhagic Escherichia coli* (EHEC) from rectal mucosa in cattle<sup>107</sup>. *Enterohemorrhagic Escherichia coli* is a foodborne pathogenic bacterium. The gastrointestinal tract of cattle acts primarily as reservoirs for this microorganism <sup>108 109</sup>. Typically, infected cattle hosts show no symptoms of illness. However, EHEC can infect humans via contaminated water, food, or direct contact with the animals. In humans, those bacteria colonize the colon and cause a broad range of pathologies: hemorrhagic colitis, hemolytic uremic syndrome, watery or bloody diarrhea, and hemolytic uremic syndrome <sup>110</sup>. The additional danger of EHEC infection is that the treatment with conventional antibiotics triggers the SOS response in these bacteria, which leads to the release of Shiga toxin and therefore resulted in an increase in the mortality rate of the patients <sup>111</sup>. That is why the possibility to remove EHEC infection in cattle would provide significant benefits for healthcare by decreasing the chances of human contact with those bacteria. The anti-EHEC property of bLF are especially interesting because it may allow clearing EHEC by modulating of native immune response of the animal and without the use of antibiotics.



In humans exist various isoforms of lactoferrin. One of the isoforms, called delta-lactoferrin ( $\Delta$ LF), is known to be able to translocate to the nucleus and act there as a transcription factor<sup>112 113,114</sup>. No  $\Delta$ LF or its analog, to the best of our knowledge, was found in animals up to date. Therefore, we aimed to find if the bLF can be uptaken by calf rectal epithelium cells and whether it is translocated then to the nucleus, similar to  $\Delta$ LF in humans. Additionally, we aimed to find how the presence of EHEC influence the uptake and translocation of bLF.

The Raman spectroscopy was already used to study bovine lactoferrin<sup>115</sup>. Nevertheless, to the best of our knowledge, no Raman studies describing the changes caused by bLF in the molecular fingerprint of bovine rectal epithelium cells were done. The absence of such information brought an additional challenge to localizing bovine lactoferrin inside the cell. The bovine lactoferrin is a glycoprotein. Therefore, its peaks may be masked by the peaks originated from other proteins and glycoproteins inside cells. However, Raman is a very sensitive technique. If we scan the cell, which was incubated in the presence of bLF, and compare the spectrum of this cell with the spectrum of untreated control cells – we may detect the difference in the spectra between those cells. If we compare the spectra of the nuclear region between the treated and untreated cells – we may also observe the changes in the Raman spectrum. However, it is not possible with a significant degree of certainty to conclude that the found differences in molecular fingerprints were caused by bovine lactoferrin presence in the nucleus. The observed differences may be the result of biochemical processes caused by bLF in the growth medium or the cytoplasm or by the presence of EHEC or by other factors. This problem can be solved by using fluorescent microscopy as a complementary tool to confirm that changes in the molecular fingerprint in a particular region inside the cell can be attributed to the bovine lactoferrin.

### 3.2 MATERIALS AND METHODS

The first problem we faced was that the bovine rectal epithelial cell culture was not commercially available. This was solved by developing the primary cell culture from a sample of calf rectum. All subsequent experiments were done using the cells from this culture. The isolation of bovine rectal crypt was performed according to protocols described in other studies<sup>116 117 118 119</sup> with minor modifications<sup>120</sup>.

Rectal epithelial cells were seeded on CaF<sub>2</sub> Raman grade 75 × 25, 1 mm polished slides (Crystran Ltd., UK) and grown till a monolayer was formed. The nalidixic acid-resistant Shiga-toxin negative *Escherichia coli* O157: H7 (EHEC) strain NCTC 12 900<sup>121</sup> was grown overnight at 37 °C in 10 mL Luria–Bertani broth medium (Becton–Dickinson, Claix, France).

Next, the cells were washed with PBS and inoculated with EHEC (10<sup>7</sup> CFU/mL, diluted in DMEM). Then, inoculated cells were incubated for 5 hours at 37 °C, allowing EHEC to attach to the cells. In the following step, the inoculated cells were washed with PBS and treated with 100 µL (1 mg/mL DMEM) of Alexa Fluor 488-labelled bLF or Alexa Fluor 488 dye or unlabeled bLF and incubated for 2 hours (37 °C, 5 % CO<sub>2</sub>). All treatment conditions were tested in triplicates, with two biological replications. bLF was fluorescently labelled with Alexa Fluor 488, using Alexa Fluor® 488 Protein Labeling Kit. Labeling was done according to the standard protocol provided by the manufacturer (Molecular Probes, Eugene, OR, USA).

After two hours of incubation, cells were washed with PBS (4 °C) and fixed with 4 % paraformaldehyde (30 minutes, at room temperature). In samples allocated for only fluorescence microscopy analysis, nuclei were additionally stained using the Hoechst 33258 nucleic acid dye (Sigma). This was done to visualize the nuclei of the cells on fluorescent images. Staining was done for 10 minutes at room temperature.

Fluorescence imaging was performed using a Nikon Ti confocal laser scanning microscope (Nikon, Belux, Brussels, Belgium) with a Nikon Plan Apo VC 60x Oil DIC N2 objective (1.40 NA). Two types of images were obtained: high-resolution axial imaging of a single cell with subsequent three-dimensional (3D) cell reconstruction, Figure 3.1, and wide-scale lateral mapping of multiple cells, Figure 3.2. Next, cells, where the presence of bLF was confirmed by fluorescent microscopy, were mapped with a Raman microscope. Laser power was set to 180 mW. A 100x/0.9 NA (Nikon, Japan) objective was used. The mapping resolution was 2 points

per  $\mu\text{m}$ . Integration time was 1 second. The cells treated with Alexa 488 dye were used as control. The heatmaps were generated with Project FOUR v.4.0 (WITec 2014).

### 3.3 RESULTS AND DISCUSSION

#### 3.3.1 Analysis of Fluorescent images

The overlapping of nuclei stained with Hoechst 33258 and bLF-Alexa-stained region confirms that bLF is translocated to the nucleus of the cell, Figure 3.1. Interestingly, the axial scan of the bLF-Alexa positive cells and the following 3D reconstruction showed that all lactoferrin is localized in the nucleus area and nearly absent in the cytoplasm. The concentration of lactoferrin in one spot inside the cell was also observed in Raman images.

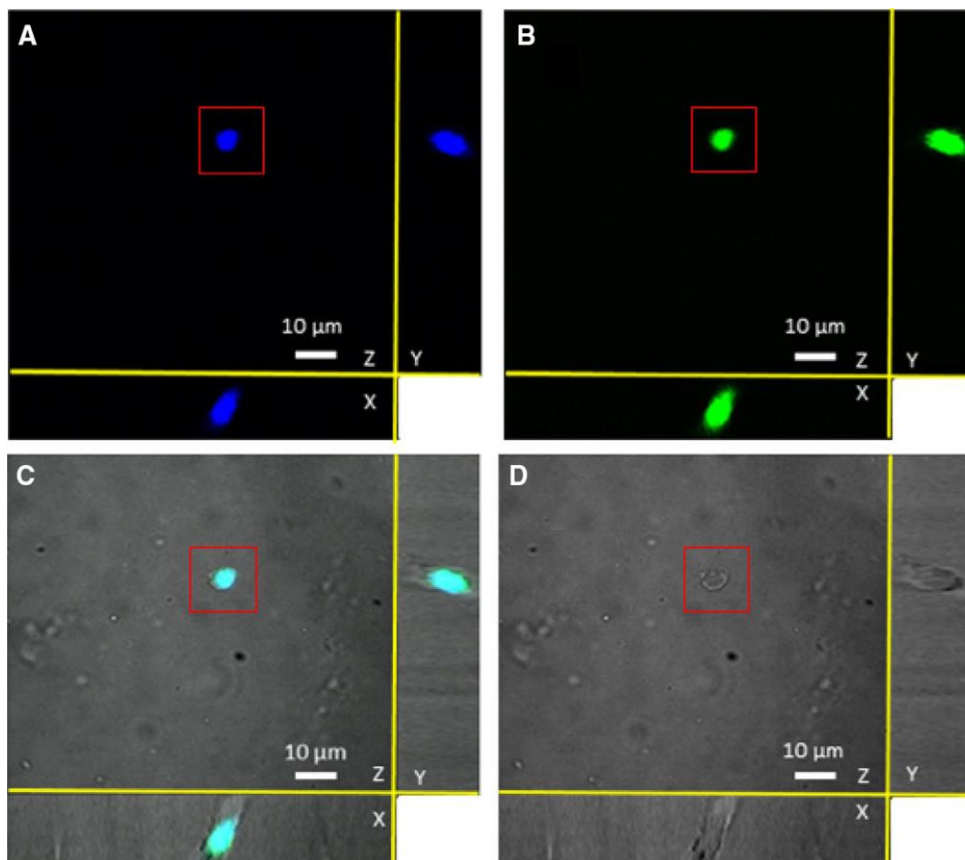


**Figure 3.1.** Three-dimensional fluorescence confocal microscopy images of a calf rectal epithelium cell. (A) Fluorescent image of the nucleus stained with the Hoechst dye. (B) Fluorescence microscopy image of the region inside the cell with bLF- Alexa- Fluor 488. (C) Merged image of A, B, and transmission. (D) The corresponding transmission microscopy image.

Next, cells with or without fluorescent marked bLF in the nuclei were counted using the *Cell counter* plugin from the ImageJ v.150b. The counting results showed that the presence of EHEC O157:H7 leads to a significant increase ( $p < 0.5$ ) of bLF translocation rate. In samples inoculated with EHEC, on average 480 cells (38.5 %) from 1248 were bLF-Alexa Fluor positive, Figure 3.2 (D, E, F). However, in the absence of EHEC, only 17 cells (1.34 %) from 1270 showed the presence of bLF in the nucleus Figure 3.2. (A, B, C).

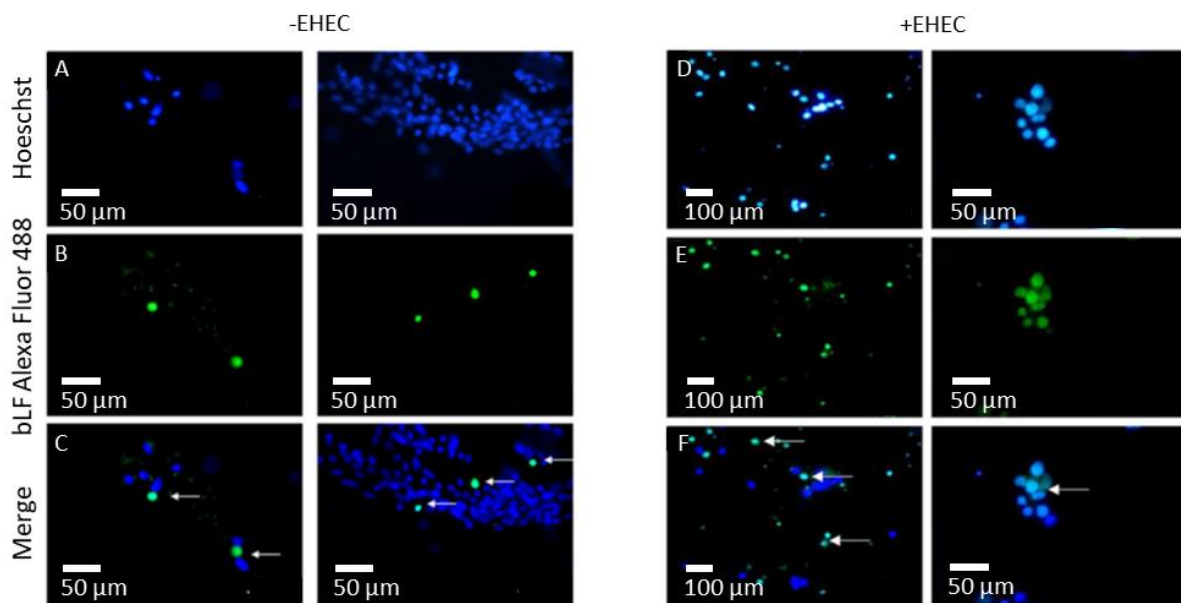


**Figure 3.2.** Fluorescence microscopy images of bovine rectal epithelial cells. Cells were stained with bLF-Alexa Fluor 488 and Hoechst 33258. -EHEC panel shows images of the cells grown in the absence of EHEC. +EHEC panel shows the images of the cells grown in the presence of EHEC. (A), (D) show cell nuclei stained with the Hoechst nuclear dye. (B), (E) show cells with bLF-Alexa Fluor 488 inside. (B) The localization of bLF-Alexa Fluor 488 without the EHEC infection is depicted. (C), (F) – merged images of A and B, or D and E respectively, show the cells, marked with arrows, with bLF-Alexa in the nuclei.

Such upregulation of bLF translocation can be explained by activation of cellular innate defense mechanism, caused by EHEC presence, where bLF may act as an immunomodulator. An alternative explanation can be that bacterial uptake of iron resulted in its deficiency inside the cell. The iron deficit leads to the rise of bLF receptor numbers on the plasma membrane and, therefore, to increase of lactoferrin uptake by the cell and its subsequent translocation to the nucleus.

### 3.3.2 Lactoferrin localization with Raman

The Raman molecular fingerprint of pure unlabeled bLF in PBS (35 mg/mL) was used to localize the bLF inside the cell. The fluorescent image was used to localize the region where the bovine lactoferrin was present. Comparing this region Raman spectrum with the spectrum of pure unlabeled bLF revealed that the  $1555\text{ cm}^{-1}$  peak can be used for lactoferrin localization inside the cell, Figure 3.3 (A, B, D). The shape of the area with an intense  $1004\text{ cm}^{-1}$  peak, assigned to phenylalanine<sup>33</sup>, correlates with the shape of the cell visible on a light microscopic image, Figure 3.3 (A, C). On the other hand, the region with a highly intense  $1555\text{ cm}^{-1}$  peak was found only in an area where according to fluorescent imaging, lactoferrin is present. The strong  $1555\text{ cm}^{-1}$  peak in the lactoferrin molecular fingerprint was observed before<sup>115</sup>. In this study, a  $1555\text{ cm}^{-1}$  peak was assigned to the tryptophan (Trp) indole ring<sup>115</sup>. Interestingly, the peptides rich in Trp are known to have a high antimicrobial activity<sup>122</sup>. The  $1555\text{ cm}^{-1}$  intense peak was absent in scans of control cells. After the molecular fingerprint of bLF inside the cell was identified, Raman can be used in subsequent studies to identify the bLF cellular localization, and in contrast to fluorescent microscopy, no labels are required. However, it is essential to note that the evaluation of many cells with conventional Raman was extremely time-consuming. The recording of a single spectrum from one cell took us approximately 1 minute. Minimum 20 minutes were required to obtain the molecular image of a single cell with Raman, while fluorescent microscopy allowed us to image more than 1000 cells in 10 minutes. The low throughput of Raman was the result of the technical limitations of the microscope we were using. The performance of Raman can be significantly improved with more sensitive detectors. This can be done, for example, by changing the CCD camera to an Electron Multiplying CCD (EMCCD) camera. A higher sensitivity of EMCCD would allow us to process a larger number of cells in a shorter time frame.

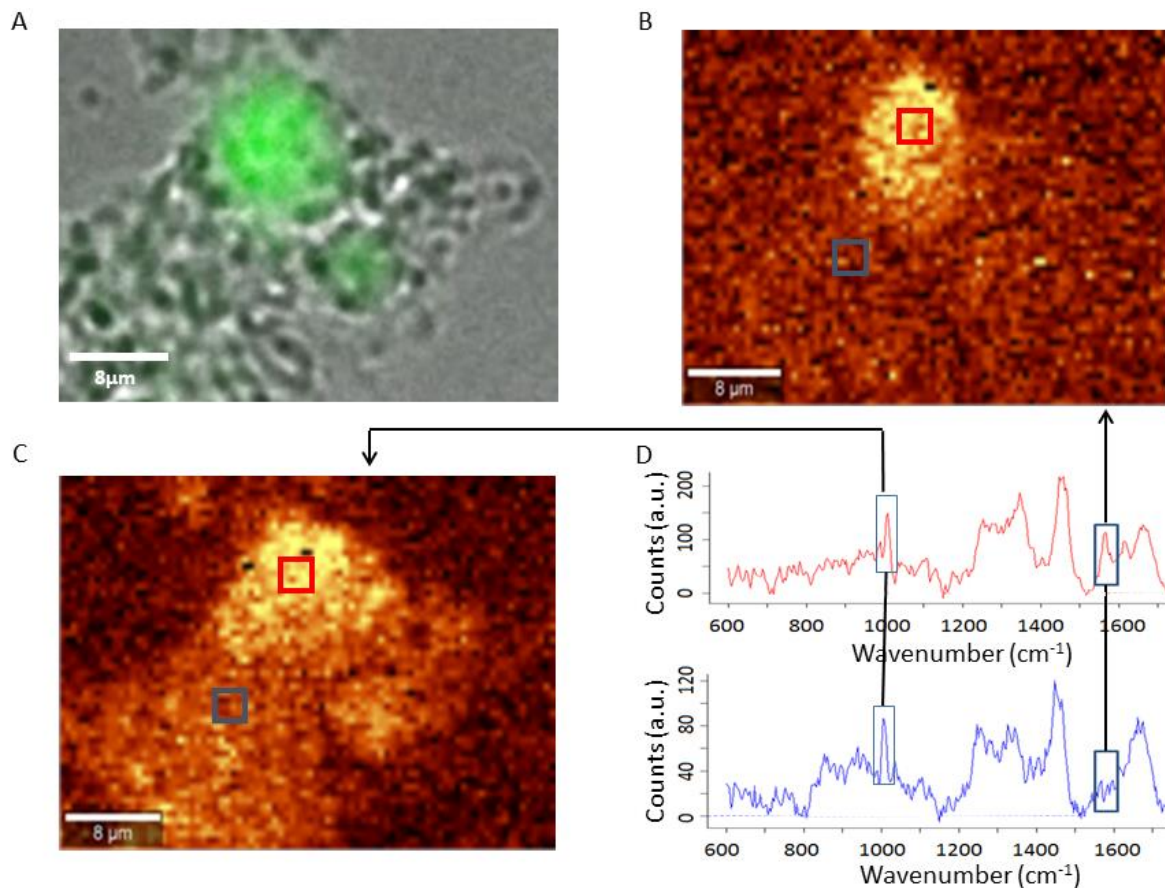


**Figure 3.3.** Fluorescence and Raman microscopy images of a calf rectal epithelial cell with bLF-Alexa 488. (A) Fluorescence microscopy image of bLF-Alexa Fluor 488 inside a rectal epithelial cell. (B) The heat map of the cell is generated using the  $1555\text{ cm}^{-1}$  peak assigned to tryptophan in bLF. (C) The heat map of the cell is generated using the  $1004\text{ cm}^{-1}$  peak. This heatmap reveals the protein distribution inside the cell <sup>123</sup>. (D) Raman scattering spectra show peaks used for the generation of the heat maps in (B) and (C). The upper spectrum (the red curve), taken inside the nucleus in the area marked with the red rectangle on (B) and (C), contains the peak at  $1555\text{ cm}^{-1}$ . In the bottom spectrum (the blue curve), obtained outside the nucleus in the area marked with the blue rectangle in (B) and (C), the  $1555\text{ cm}^{-1}$  peak is absent.

### 3.4 CONCLUSION

In this chapter, it is demonstrated how to use Raman microscopy to identify the position of a molecule inside a cell. Here, the structure of the molecule (lactoferrin) was known before the experiment. Additionally, it was possible to obtain the molecular fingerprint of pure lactoferrin. However, it was challenging to visualize lactoferrin inside the cell due to the cellular fluorescence background. Additionally, the peaks originated from lactoferrin were masked by the overlapping peaks originating from other molecules inside the cell. Because of this, it was challenging to predict which peaks from bovine lactoferrin molecular fingerprint would be visible inside the cell. The challenge was solved by using fluorescent microscopy, which showed to be a viable complementary tool. Fluorescent labels allowed localization of lactoferrin and tracing its translocation to the nucleus of calf rectal epithelium cells. The rate of lactoferrin uptake and subsequent translocation increased in the presence of EHEC. Analysis of the Raman scattering spectrum measured inside the nucleus allowed identification of the unique lactoferrin-related peak. After the molecular fingerprint of the chosen molecule (bovine lactoferrin) was identified, it was possible to study intracellular translocation of lactoferrin with a Raman microscope, without using fluorescent labels. It is important to note that, if a molecule does not possess peaks distinct from its environment, it would be difficult to localize it with a conventional Raman microscope, especially at low concentrations. Such lack of specificity is a disadvantage of Raman microscopy.





# Chapter 4

Molecular analysis of conductive fibers in cable bacteria by Raman microscopy, X-ray, and mass spectrometry-based methods

**Chapter 4** is based on the following manuscript:

**Efficient long-range conduction in cable bacteria through nickel protein wires.** H.T.S. Boschker, P.L.M. Cook, L. Polerecky, R. Thiruvallur Eachambadi, H. Lozano, S. Hidalgo-Martinez, D. Khalenkow, V. Spampinato, N. Claes, P. Kundu, D.A. Wang, S. Bals, K.K. Sand, F. Cavezza, T. Hauffman, J. Tataru Bjerg, A.G. Skirtach, K. Kochan, M. McKee, B. Wood, D. Bedolla, A. Gianoncelli, N.M.J. Geerlings, N. Van Gerven, H. Remaut, J. S. Geelhoed, R. Millan-Solsona, L. Fumagalli, L.-P. Nielsen, A. Franquet, J.V. Manca, G. Gomila, F.J. R. Meysman

*Nat. Commun.* (in revision).

## **4 Molecular analysis of conductive fibers in cable bacteria by Raman microscopy, X-ray, and mass spectrometry-based methods**

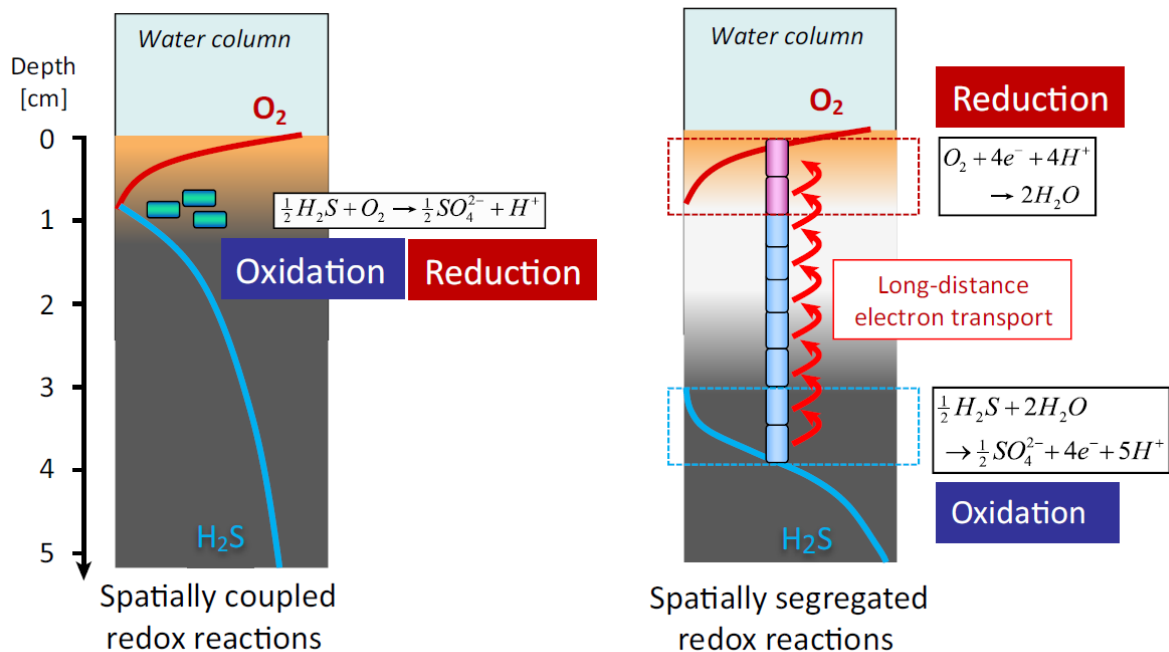
In the previous chapter, we have investigated the translocation of bovine lactoferrin to calf cell nuclei using Raman and fluorescent microscopy. The molecular composition of bovine lactoferrin was known, and the goal was to localize it inside the cell. In this chapter, an example of a different situation is presented, where the position of certain structures is known, their molecular composition is unknown. The previously unknown molecular composition of long conductive fibers inside the so-called cable bacteria is thus investigated using Raman microscopy in a combination with mass spectrometry and X-ray analytical methods. Such fibers have important value for molecular electronics due to their unique electrochemical properties: long-distance electron transport.

## 4.1 INTRODUCTION

In the previous chapter, we have demonstrated application of molecular fingerprinting for a localization of a molecule inside cells; there, the chemical composition of the chosen molecule (bovine lactoferrin) was known before the experiment. Next, we discuss here how to use Raman scattering to obtain information about the chemical composition of unknown molecules and nano-scale structures. Fibers inside the filamentous cable bacteria of the *Desulfobulbaceae* family were chosen as a sample for proof-of-concept analysis. Cable bacteria are multicellular microorganisms, known for their unique property to generate and conduct electric current over centimetre-scale distances<sup>124 125 126 127</sup>.

Cable bacteria are unique as their existence challenges the established dogma that each cell individually generates the energy for its existence by using electron donors and acceptors from the surrounding media<sup>127</sup>. This rule applies not only to microorganisms such as sulfur oxidation bacteria, but also to complex multicellular life forms. Here, the specialized cells supply the energy-rich molecules, which are then transported to distant cells to keep them alive. For example, in humans, metabolically active cells are supplied through the bloodstream with the electron donors, such as glucose, and electron acceptors, such as oxygen. The reduction-oxidation of those molecules produces the energy necessary to keep the cell alive. Those reactions are based on electron transport over nanometre scale distance and are performed by each cell individually.

Cable bacteria use a very different strategy. Here, the cooperation between specialized cells is not based on the exchange of energy-rich molecules but on the generation of electric current to supply the electrons to distant cells and produce the energy. The ability to transport the electrons over centimetre long distances allows the cable bacteria to spatially separate between the cells the oxidation and reduction parts of the single metabolic reaction of energy production. The anode cells generate electrons by sulfur oxidation. Then, the resulting electrons are transported to cathode cells and used for oxygen reduction. The ability to transport electrons over long distance allowed the cable bacteria to use the sulfur-rich deep layers of the sea bottom, inaccessible for other organisms. Long distance separation of oxidation and reduction parts of metabolic reaction is the tremendous evolutionary advantage over single-cell sulfur oxidation bacteria, which can exist only in a small niche in the seafloor, in the interface between sulfur-rich and oxygen-rich mediums, Figure 4.1.



Trends in Microbiology

**Figure 4.1.** (Left) Sulfur oxidation bacteria use sulfur and oxygen to produce energy. The oxidation and reduction reaction occurs in the same location. (Right) Cable bacteria separate the process of oxidation and reduction by using long-distance electron transport. This allows cable bacteria to use sulfur stored in deep layers of the seafloor (reproduced from Meysman *et al*<sup>127</sup>).

In cable bacteria, electrons are channelled internally from cell to cell via a network of parallel fibers<sup>128 129</sup>. Fibers (~ 50 nm diameter) are formed inside of the periplasmic space, which is shared by all cells. They run along the whole length of bacteria filament and demonstrate interesting electric properties. The conductivity of fibers was found to be higher than 20 S/cm<sup>130</sup>. That means that fibers are more conductive than currently produced synthetic organic conductive polymers. At the same time, bacterial fibers can support the electric current density of ~ 100 A m<sup>-2</sup>. This value is comparable to that of conventional household copper wire. Such extraordinary properties of naturally occurring biomaterial have an excellent potential for advancing the field of bioelectronics, offering the possibility for developing new devices and technology. However, before moving to the direct technological application, we must learn about the chemical composition and structure of the conductive fibers. Such knowledge would allow one to build a deeper understanding of the working of electron transport through the fibers. Currently, these aspects are poorly understood.

The conductive properties of the filaments were confirmed with direct electrical measurements and Conductive Atomic Force Microscopy (C-AFM) <sup>131</sup>. The analysis of the filaments with Resonance Raman approach shows the presence of cytochrome associated molecular fingerprints in the intact filaments spectra, but it was found that cytochromes play no role in electron transport<sup>125 130</sup>. These facts allowed us to conclude that the electron transport mechanism in cable bacteria differs from the electron transport through conductive nanowires in other bacteria species, such as *Shewanella* <sup>132 133</sup>. Up to date, the chemical structure of the conductive fibers in cable bacteria remained unresolved.

## 4.2 MATERIALS AND METHODS

### 4.2.1 Sample preparation

Cable bacteria, used for analysis, were collected from natural sediments obtained from the Rattekaai salt marsh (The Netherlands). This sediment was chosen because of the size of bacteria inhabiting this area. They consistently formed thick 4  $\mu\text{m}$  diameter cables. The relatively big size facilitates easier (compared to other bacteria) handling during collection and fiber sheath extraction. Additionally, higher mass per cell resulted in a stronger Raman signal during analysis. Sediment was homogenized, packed in PCV core liner tubes, and incubated in aerated artificial seawater.

Next, using a stereo microscope, the intact cable bacteria were picked up from the top sediment layer. They were washed at least six times with MilliQ water to remove the sediment microparticles and transferred to a glass microscope coverslip.

One of the challenges we faced during fibers analysis with Raman microscope was the problem of sample immobilization. If the scans were conducted in air, the extracted fibers and intact bacteria could be damaged by prolonged laser exposure. The heat problem can be solved by conducting all the scans in the liquid, such as PBS or artificial seawater. However, it was challenging to conduct the area scans because bacteria, in contrast to adherent cell cultures, were not attached to the bottom of the glass. Therefore, the liquid microcurrents from the objective and stage movement resulted in a semi-random shift of bacteria from its original position. Several solutions to this problem were developed. The first approach was to cover cable bacteria with low-density agar. This was done by first finding the density of agar, which produces minimal interference with the samples' molecular fingerprints. At the same time, the agar layer should be dense enough to prevent the sample movements. Next, the time required for the agar with the chosen density to start the solidification was determined. The agar should be applied to the sample as close to the solidification time point as possible to avoid heat damage of the sample.

The sample was immobilized in 100  $\mu\text{L}$  of agar. The agar was delivered via a pipette. The deposition was done by deploying the agar solution from the pipet by performing circular motion with the pipet tip around the sample. This allows us to form a flat, thin, and homogeneous agar layer. The developed agar-based sample immobilization procedure was also successfully applied in subsequent research projects for other types of samples, such as

cells, worms, and algae. However, this method was time-consuming and incorrect timing can result in loss of the sample. Additionally, because of the small size of cable bacteria, it was problematic to localize them inside the agar layer. Therefore, it was used for cross-section scans, while for single spectrum and line scans – an alternative immobilization procedure was developed. The custom made ultrathin (100  $\mu\text{m}$  thick)  $\text{CaF}_2$  cover slides were produced. Bacteria were deposited on the  $\text{CaF}_2$  slide inside the 20  $\mu\text{L}$  droplet of PBS or artificial seawater. Ultrathin  $\text{CaF}_2$  cover slide was gently set on the top of the droplet. Then the glass was immobilized with nail polish (Essence, Luxembourg) delivered with a thin brush. After the nail polish solidifies, the sample was scanned with Raman. Additionally, it was controlled that nail polish did not dissolve and contaminate the sample. The solidified droplet of nail polish was set in PBS for 3 hours and scanned with Raman microscopy. No traces of nail polish were detected in PBS.

#### 4.2.2 Raman microscopy

Cable bacteria were scanned with a confocal Raman microscope equipped with near-IR 785 nm laser. The laser power was set to 180 mW (measured before the objective). A 100x/0.9 NA objective (Nikon) was used, while the integration time was set to 10 seconds. Axial profiles were generated with the step of 0.1  $\mu\text{m}$  per point. Obtained Raman spectra were pre-processed in R.3.4. as described in Supplementary Information for Chapter 2 (Appendix), S2.1 and S2.2, resulting in the removal of cosmic rays and baseline correction. Baseline adjustments were made using the Asymmetric Least Squares method from the *baseline* package. Additionally, the background was measured next to each filament and subtracted from filament spectra.

Spectra were recorded from various points inside bacteria. Besides molecular imaging described in **Chapter 2**, we have also performed the line scans to profile the nanowires distribution inside the bacterial filament segment. The line scans were made by taking Raman scattering measurements every 0.3  $\mu\text{m}$  across the sample and combining the resulted spectra in one dataset. The distribution of molecules in the sample can be visualized by plotting the peak intensity versus the axial coordinates. This method is less time consuming than the area scan and can be used in situations when molecular imaging is not required.



### 4.2.3 X-ray and mass spectrometry methods

Intact cable bacteria and extracted fibers were characterized by STEM-EDX using Tecnai Osiris microscope (Thermo Fischer Scientific). The acceleration voltage was 200 kV. Measurements were done using ChemiSTEM system. The resulting data was analyzed by Bruker ESPRIT software.

LEXRF measurements were done using TwinMic Beamline in the Elettra Sincrotrone (Trieste, Italy). Excitation energy was 2 keV and the beam spot size was 570 nm. The acquisition time was 20 seconds per pixel. The resulting LEXRF datasets were processed with PyMCA multiplatform software to obtain LEXRF maps.

Extracted fiber sheaths were also characterized by Nano-SIMS using NanoSIMS 50L (Cameca). The high-energy Cs<sup>+</sup>-ion beam (16 keV, 0.5 pA) was used for detection of secondary ions: <sup>12</sup>C<sup>-</sup>, <sup>12</sup>C<sup>14</sup>N<sup>-</sup>, <sup>16</sup>O<sup>-</sup>, <sup>31</sup>P<sup>-</sup>, and <sup>32</sup>S<sup>-</sup>. The beam size was ~ 50 nm. The area of 10 μm x 10 μm was mapped with the lateral resolution of 30 nm per pixel. The dwell time was 1 ms per pixel. 600 frames of the mapped area were collected. The same area was also mapped using the primary O<sup>-</sup>-ion beam (2 pA) to detect positive secondary ions <sup>56</sup>Fe<sup>+</sup>, <sup>58</sup>Ni<sup>+</sup>, <sup>60</sup>Ni<sup>+</sup>, <sup>63</sup>Cu<sup>+</sup> and <sup>66</sup>Zn<sup>+</sup>. The beam size was beam size ~ 100 nm. The dwell time was 5 ms per pixel. 168 frames were collected.

## 4.3 RESULTS AND DISCUSSION

### 4.3.1 Localization of fibers inside the intact cable bacteria with confocal Raman

Single spectrum, line scan, and area scans of cable bacteria were done using a near-IR laser. Line scans were performed across the bacteria filaments, as it is shown in Figure 4.2(A, B). The averaged spectra showed the typical bands found in the majority of cell and bacteria spectra: 1004  $\text{cm}^{-1}$  band from phenylalanine ring deformation, lipid-associated  $\text{CH}_2$  bending at 1462  $\text{cm}^{-1}$ , amide I protein peak at 1672  $\text{cm}^{-1}$ , and C-H stretching at 2950  $\text{cm}^{-1}$ <sup>134</sup>, Figure 4.2 (C).

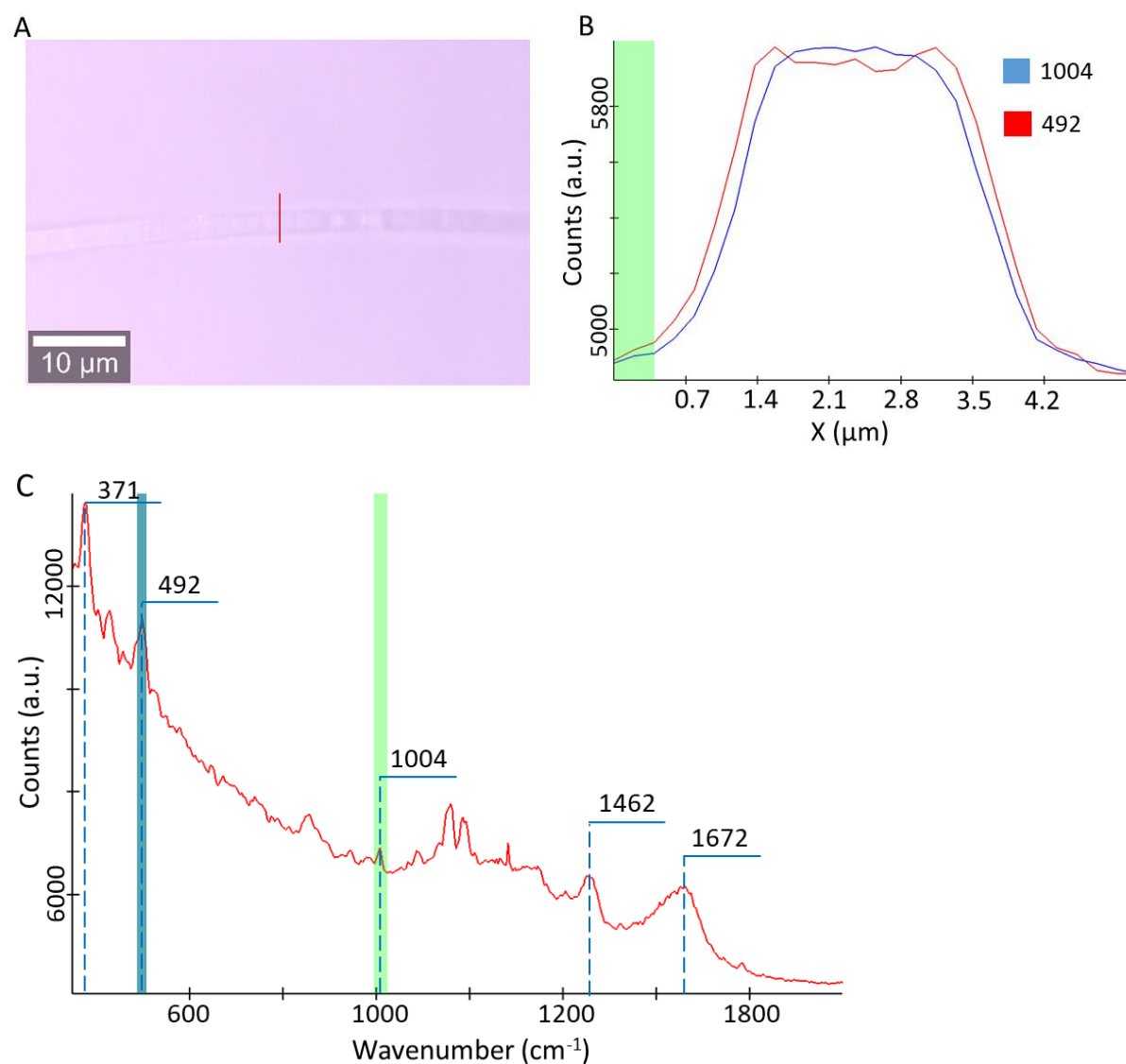


**Figure 4.2.** Application of Raman microscopy to study cable bacteria. (A) Light microscopy image of a cable bacteria; the red line marked the scanned area. (B) Peak intensity profiles across the scanned area. (C) Raman scattering spectrum of the cable bacteria.

The cable bacteria spectrum contained two low-frequency bands at  $371\text{ cm}^{-1}$  and  $492\text{ cm}^{-1}$ . The analysis of the line scans revealed that  $1004\text{ cm}^{-1}$ ,  $1462\text{ cm}^{-1}$ ,  $1672\text{ cm}^{-1}$  peaks show a similar uniform distribution across the bacteria. The low-frequency bands have different distribution patterns, showing the increase in signal at the edges of bacteria, Figure 4.2 (A, B).

Such an increase suggests that  $371\text{ cm}^{-1}$  and  $492\text{ cm}^{-1}$  bands can be associated with the conductive fibers, which are situated as parallel bundles around bacteria. Because of the low axial resolution of confocal Raman at the edges of bacteria, the volume from which the Raman signal is acquired contains more fibers than measured volume in the center. This leads to an increase in low bands intensity around the edges, Figure 4.3.

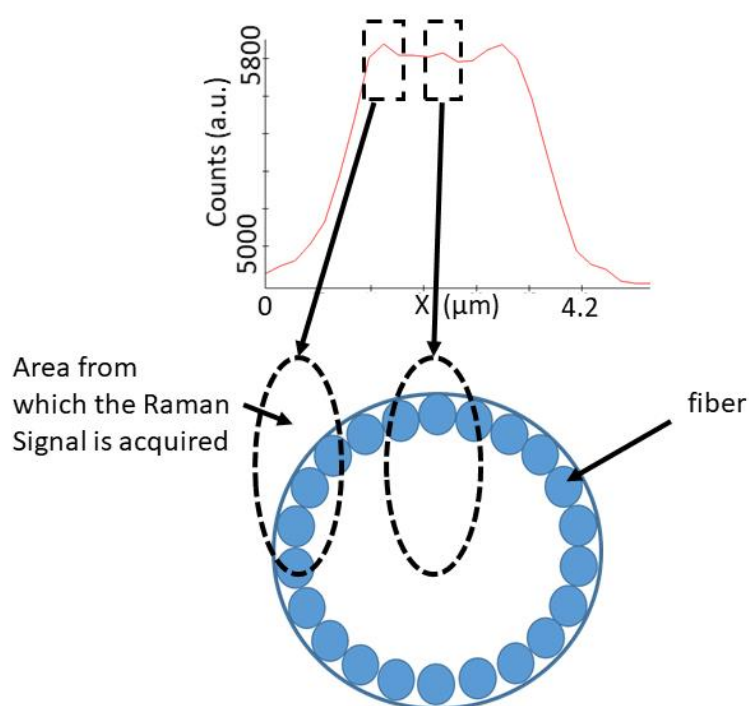


**Figure 4.3.** Correlation between the number of fibers in the scanned area and the corresponding  $492\text{ cm}^{-1}$  peak intensity profile.

To confirm this hypothesis, we have conducted a cross-section scan. The intact cable bacteria were immobilized in agar. Next, the multiple line scans were done. After each line scan, the axial position of the sample was changed by  $0.1\text{ }\mu\text{m}$  with a high precision stage. The resulted line scans were combined in one dataset, and the molecular images of the bacteria cross-section were constructed. Images were generated as heatmaps, based on  $371\text{ cm}^{-1}$ ,  $492\text{ cm}^{-1}$ ,  $1004\text{ cm}^{-1}$  and  $1672\text{ cm}^{-1}$  peaks intensities, Figure 4.4 and (Supplementary Information for Chapter 4 (Appendix), Figure S4.1), respectively.

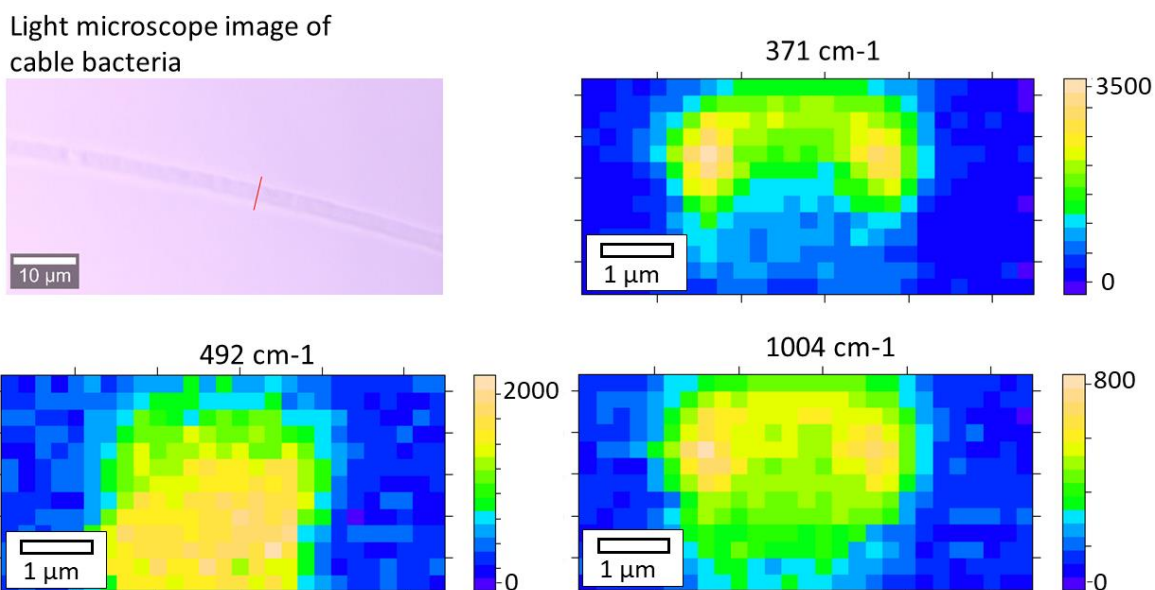


**Figure 4.4.** Raman heatmap images of a cross-section of a cable bacterium. Colors in molecular images correspond to counts in arbitrary units.

The heatmaps of the  $1004\text{ cm}^{-1}$  and  $1672\text{ cm}^{-1}$ , Figure 4.4 and (Supplementary Information for Chapter 4 (Appendix), Figure S4.1), respectively, have similar uniform intensity distribution to what was observed during the line scans. However, the  $371\text{ cm}^{-1}$  and  $492\text{ cm}^{-1}$  heatmaps showed that molecules associated with these peaks are primarily concentrated in periplasmic space and/or cell wall of bacteria. According to the heatmaps of the  $371\text{ cm}^{-1}$  and  $492\text{ cm}^{-1}$  peaks, the molecules associated with those low bands are not evenly distributed. There are two hot spots at the edges of the bacteria. However, those two high concentration spots at the axial heatmaps are, probably, the artefacts caused by a low axial resolution, similar to the edge peaks observed in line scan bacterial profile. The alternative hypothesis is that indeed these molecules are concentrated in two spots around the edges. The cross-section profiling of other cable bacteria does not show the presence of two hot spots of  $371\text{ cm}^{-1}$  and  $492\text{ cm}^{-1}$  peaks associated molecules. However, a comparison of  $371\text{ cm}^{-1}$  and  $1004\text{ cm}^{-1}$  heatmaps showed the  $371\text{ cm}^{-1}$  associated molecules are present in highly concentrated only in the upper periplasmic space of bacteria, Figure 4.4 and Figure 4.5. The first conclusion which can be drawn from axial molecular images is that those molecules are concentrated in the form of half-circle on only one side of bacteria. However, it is highly improbable that all scanned bacteria were randomly deposited on  $\text{CaF}_2$  slide in such a way that the observed half-circle is oriented parallel to the surface of the glass on all images. Also, the observed distribution pattern contradicts the electronic microscopy data according to which the fibres

are spread around the whole bacteria. Therefore, the observed image may be the artefact coming from low transparency of the fibres to a specific wavelength, where the signal from the lower part of bacteria is blocked and cannot reach the detector. The observed molecular imaging artefacts illustrate the need to critically analyse the microscopic data while taking into consideration all the factors that could influence the measured Raman signal.

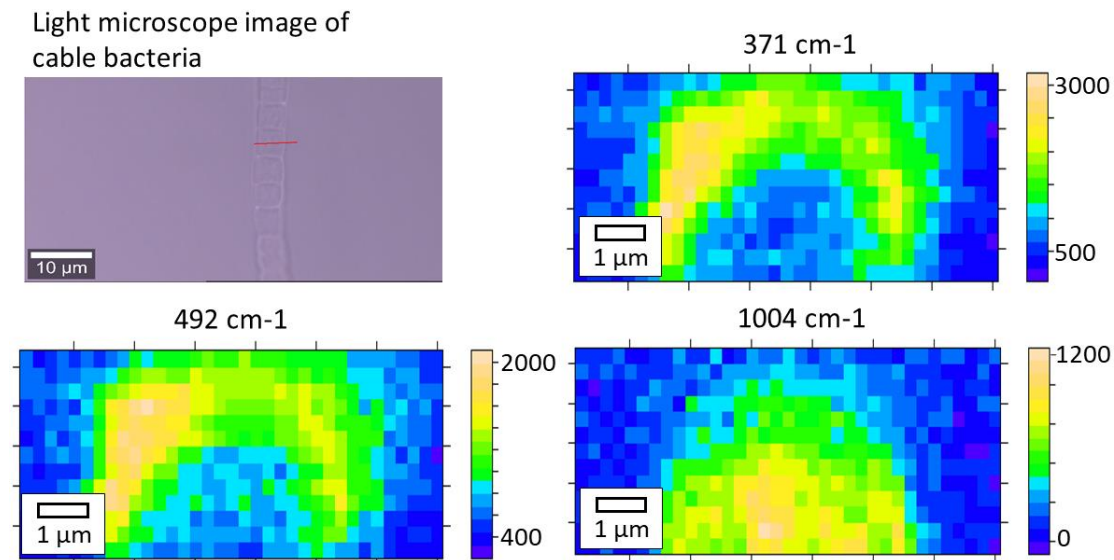


**Figure 4.5.** Raman heatmap images of a cross-section of a cable bacterium. Colors in molecular images correspond to counts in arbitrary units.

#### 4.3.2 Analysis of extracted conductive fibers

Next, the fibers were extracted by incubating bacteria in 1 % (w/w) sodium dodecyl sulfate (SDS) for 10 minutes and then washed with MilliQ water. To remove the traces of SDS, which may be absorbed by the fibers, filaments were treated with 1 mM sodium ethylenediaminetetraacetate (EDTA), pH 8 for 10 minutes. Finally, the fibers were washed six times with MilliQ and analyzed with an atomic force microscope – infrared spectroscopy (AFM-IR). The recorded spectra showed the presence of amide I  $1643\text{ cm}^{-1}$ , amide II  $1562\text{ cm}^{-1}$ , and amide III  $1290\text{ cm}^{-1}$  peaks, suggesting that the fibres mainly consists of proteins<sup>135 136</sup>. The relatively intense peak at  $3056\text{ cm}^{-1}$  (C-H stretching) indicates that fibre protein is rich in aromatic amino acids. The spectra also contained the peaks at  $1765\text{ cm}^{-1}$  (from C=O stretching) and  $1398\text{ cm}^{-1}$  (from C=O bending) associated with polysaccharides<sup>136</sup>. Most likely, the source of polysaccharide peaks were the remains of peptidoglycan layer. Such peptidoglycan layer is present in periplasmic space of all Gram-negative bacteria. Probably, the peptidoglycan molecules were not completely removed during fibers extraction.

Subsequent scanning of extracted fibers with NIR confocal Raman provided additional insights into filament structure. The resulted Raman spectrum contained bands at a low wavenumber range:  $371\text{ cm}^{-1}$  and  $492\text{ cm}^{-1}$ , analogous to the spectrum of intact bacteria, Figure 4.6.

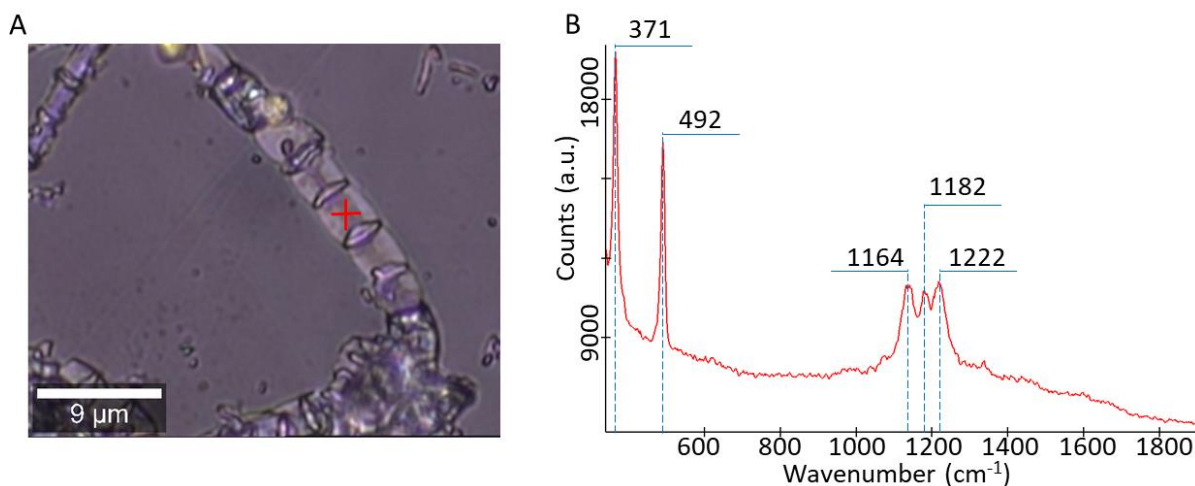


**Figure 4.6.** Raman microscopy study of fibers extracted from cable bacteria. (A) Light microscopy image of the fibers. The point, where the Raman spectrum (presented in (B)) was taken, is marked with the red cross. (B) Raman scattering spectrum of extracted cable bacteria fibers.

This confirms the hypothesis that fibers are the source of  $371\text{ cm}^{-1}$  and  $492\text{ cm}^{-1}$  peaks. The low wavenumber of those peaks suggests that they may be originated from metal ion<sup>137</sup>, present in the fibers. One of the possible candidates for the metal was Nickel (Ni). The Raman spectra of extracted fibers showed similarities with Ni diethylene ligand<sup>138</sup>. In this case, the  $492\text{ cm}^{-1}$  peaks may be originated from the breathing of diethylene containing an aromatic ring. The central peaks at  $1164\text{ cm}^{-1}$ ,  $1182\text{ cm}^{-1}$ , and  $1222\text{ cm}^{-1}$  may be the results of C-N and C-C stretching in aromatic rings. The alternative possibility was that low bands are originated from Ni-S found in S-ligated Ni-metalloproteins. Here, the  $371\text{ cm}^{-1}$  peak is assigned to the Ni-S stretching<sup>139 140</sup>, while  $492\text{ cm}^{-1}$  is assigned to the S-S stretching<sup>137</sup>.

The presence of sulphur (S) was later confirmed using the isotope labelling method<sup>141</sup>. Sulfate, which contained  $^{34}\text{S}$  isotope, was added to the bacteria growth media. Then the Raman spectrum of cable bacteria incubated in the presence of S isotope was obtained using a green laser<sup>138</sup>. The resulting spectra were compared with bacteria grown under normal conditions. The isotope labelling method is based on the fact that the substitution of the atom with

isotope leads to a change of vibration energy and the small shift of corresponding Raman peaks position <sup>142</sup>. The shift to low wavelength numbers was indeed observed for both low bands in isotope-labelled bacteria. This provides strong evidence that sulfur is present in the fibers and suggests that it is ligated with the metal ion.

The theory that nickel is a part of conductive fibres, deduced from the analysis of Raman spectra, was confirmed using scanning transmission electron microscopy-energy dispersive X-ray (STEM-EDX), low energy X-ray fluorescence (LEXRF), and nanoscale secondary ion mass spectrometry (Nano-SIMS).

In STEM-EDX, a sample is irradiated with a highly focused electron beam, which causes atoms within the beam path to emit characteristic X-rays. X-rays are measured in order to determine the atomic composition of sample <sup>143</sup>. STEM-EDX analysis showed the presence of metalloproteins, such as Fe, Ni, and Cu, both in intact filaments and in extracted fiber sheaths, Figure 4.7 (A-B). The amount of Fe decreased after fiber sheaths extraction, while Ni was enriched by a factor of 2-4 compared to that in intact bacteria. The decrease in the Fe signal can be explained by cytochrome loss because of the extraction procedure. Intact cable bacteria and extracted sheaths were also analyzed with low energy X-ray fluorescence (LEXRF) to confirm the results obtained with STEM-EDX. LEXRF uses soft X-ray (X-ray with the energy below 5 keV) beam to cause the characteristic low energy X-ray fluorescence emission from atoms in a sample. This low energy X-ray fluorescence approach is particularly suited to obtain information about elements with a low atomic number <sup>144</sup>. Data from LEXRF analysis confirm that Ni is primarily concentrated in the fiber sheath, Figure 4.7 (C-E). Here, again the Fe counts decreased in extracted fibers, in accordance to what was observed in the STEM-EDX analysis. In contrast, Cu levels exceeded the STEM-EDX values. This can be explained by a contamination during the LEXRF analysis. Next, extracted fibers were analyzed with Nano-SIMS. Nano-SIMS is an analytical technique based on secondary ion mass spectrometry (SIMS). In SIMS, ion beam illuminates the sample and ejected secondary ions are analyzed <sup>145</sup>. In Nano-SIMS, high-resolution microscopy is linked with secondary ion mass spectrometry analysis to provide information about the molecular and isotopic composition of samples at a high spatial resolution. This technique is obtaining increasing attention in regard with biological applications <sup>146</sup>. The high-resolution Nano-SIMS analysis showed the presence of parallel line pattern on the images of extracted fibers sheaths, Figure 4.7 (F). Those lines were rich in Ni

and S. The spacing between the lines was 150-200 nm, similar to the spacing expected to exist between the fibers <sup>147</sup>.

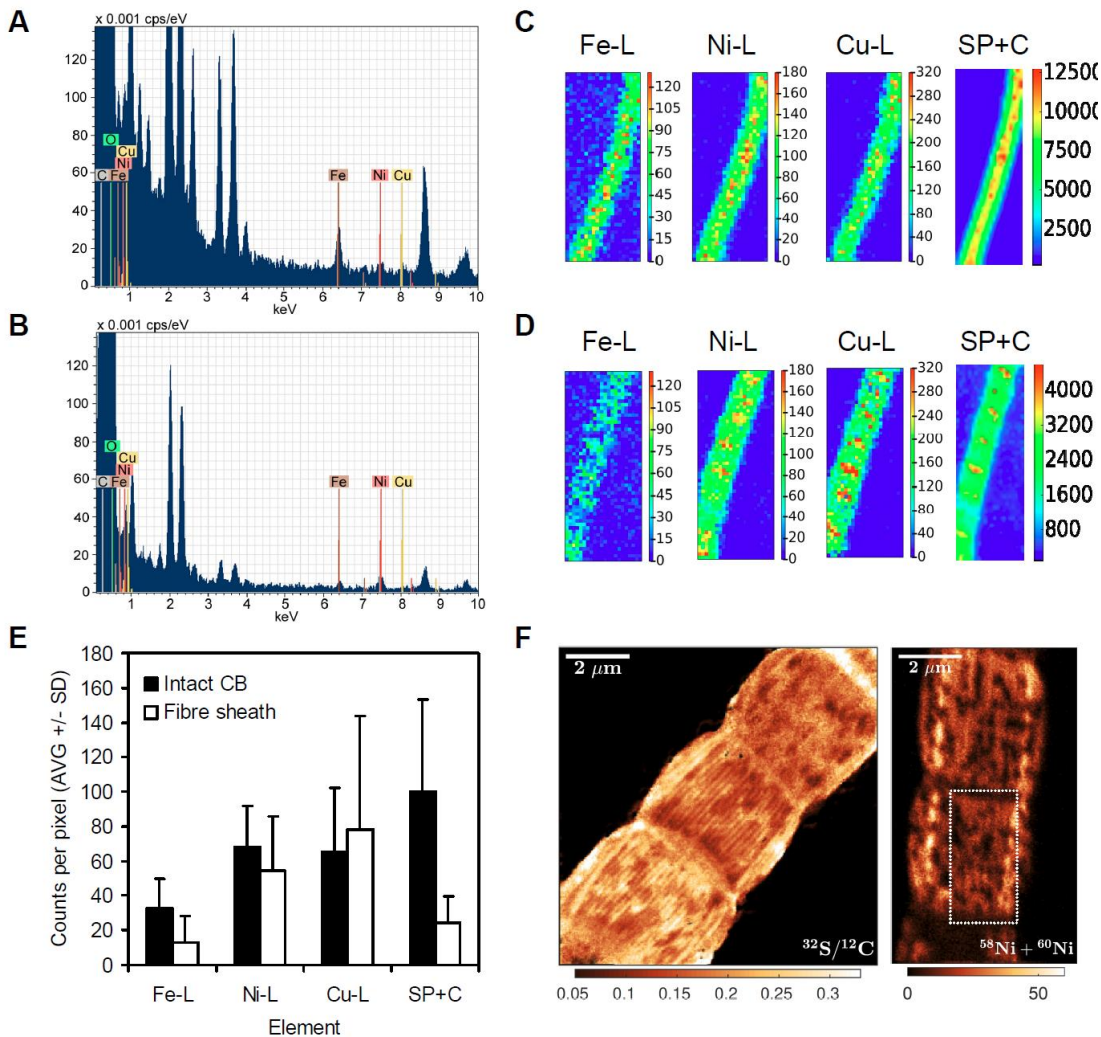


**Figure 4.7.** Analysis of molecular composition of intact cable bacteria and extracted fiber sheaths. (A) STEM-EDX spectra of intact cable bacteria. (B) STEM-EDX spectra of extracted fiber sheaths. (C) Synchrotron low energy X-ray fluorescence (LEXRF) maps of intact cable bacteria (SP+C is Scatter Peak plus Compton). (D) Synchrotron LEXRF maps of fiber sheaths. (E) Comparison of average counts per pixel for detected transition metals between intact cable bacteria and extracted fiber sheaths. SP+C data was scaled by changing the average of the intact counts to 100. (F) Nanoscale Secondary Ion Mass Spectrometry (Nano-SIMS) images of fiber sheath. The figure is adapted from Boschker et al. <sup>141</sup> Colors in molecular images correspond to counts in arbitrary units.



#### 4.4 CONCLUSION

In this chapter, we have investigated a situation opposite to that discussed in **Chapter 3**. Specifically, the localization of a structure inside bacteria was known, but its molecular composition was unknown. That is why the aim was to understand the molecular structure of conductive fibers situated inside cable bacteria. Using the line scans and cross-section mapping, we have localized two peaks, the position of which overlaps with the position of the fibers. The connection between those peaks and fibers was confirmed by the filament extraction procedure using a destructive chemical treatment. The analysis of spectra of fibers hints for the presence of nickel ions inside the fibers. The presence of nickel ions inside the fiber structure was confirmed by subsequent analysis with electron microscopy, X-ray and mass spectrometry analytical methods. Such a finding is remarkable, because the presence of nickel in conductive fibres proposes the existence of yet unknown form of long-range electron transport in bacteria.

In analogy to lactoferrin study, the identification of the fiber-related molecules was possible due to the presence of unique peaks in molecular fingerprints. The “unique peak” in this context means that it is not ordinarily present in the cytoplasm of cells or bacteria.

Confocal Raman microscopy provided insights into molecular composition of the fibres. However, because of the complex nature of biological samples and the sensitivity of Raman spectroscopy, multiple interpretations of the measured molecular fingerprints are possible. Therefore, the findings deduced from the Raman analysis was confirmed with alternative techniques such as isotope labelling, time-of-flight secondary ion mass spectrometry, *etc.*

The cross-section scans of the cable bacteria also revealed that a low axial resolution of conventional confocal Raman can produce artefacts in the images. This only augments the need for multimode imaging approach.



# Chapter 5

Drug delivery systems with SERS  
functionality *in vitro* and *in vivo*

**Chapter 5** is based on the following publications:

**Magnetic and silver nanoparticle functionalized calcium carbonate particles—Dual functionality of versatile, movable delivery carriers which can surface-enhance Raman signals.** B.V. Parakhonskiy, A. Abalymov, A. Ivanova, D. Khalenkow, and A.G. Skirtach *Journal of Applied Physics* **2019**, 126, 203102.

**Laser-induced remote release *in vivo* in *C. elegans* from novel silver nanoparticles-alginate hydrogel shells.** E. Lengert, B.V. Parakhonskiy, D. Khalenkow, A. Zečić, M. Vangheel, J.M. Monje Moreno, B.P. Braeckman, A.G. Skirtach. *Nanoscale* **2018**, 10, 17249-17256.

## **5 Drug delivery systems with SERS functionality *in vitro* and *in vivo***

In the first part of this chapter, a novel SERS platform is developed and evaluated. The platform is based on silver-coated calcium carbonate microparticles designed with dual functionality: a drug carrier and a SERS sensor for molecular detection *in vitro*. The particles are also functionalized with magnetite, giving them the ability for controllable movement in a magnetic field. In the second part of this chapter, the calcium carbonate microparticles are used for the development of alginate-based drug delivery platform for *in vivo* applications. The built-in SERS functionality of alginate microparticles allowed their localization inside *C. elegans* worms and controllable initiation of drug release. Peculiarly, the presence of a high Raman background, which is usually attempted to be removed from the signal, is used here for particle localization.

## 5.1 CHARACTERIZATION OF CALCIUM CARBONATE DRUG CARRIERS WITH SERS FUNCTIONALITY

### 5.1.1 Introduction

One of the goals in drug delivery research field is to find the carriers capable of delivering the drugs at the desired site of action, while at the same time avoiding the premature drug release<sup>148</sup>. An untargeted drug release can occur because of the diffusion of active substance before the carrier reaches the site of interest or because of premature degradation of the carrier. Up to date, a number of drug delivery carriers were proposed: liposomes, silica, polymeric particles, carbon-based carriers, inorganic particles such as calcium carbonate, *etc.*<sup>149</sup> Liposomes are small vesicles build from lipid bilayers. They are attractive for drug delivery because of their ability to fuse with the cell membrane, providing an efficient intercellular drug delivery. Nevertheless, liposomes have some disadvantages<sup>150</sup>. For example, sterilization is challenging due to their sensitivity to heat. The other problem is the physicochemical instability of liposomes since hydrolysis of the ester bond in phospholipids can take place, leading to aggregation of liposomes and drug escape. Porous silica-based particles are versatile drug carriers, possessing several beneficial characteristics such as biodegradability, porosity, and high surface area<sup>151</sup>. The disadvantage of silica-based drug carriers is that their interaction with phospholipids can lead to potential hemolysis of red blood cells. It was also found that porous silica nanoparticles can promote metabolic changes in cells leading to cancer.

Calcium carbonate-based microparticles present an attractive alternative to the above-mentioned drug delivery systems. They pose several advantages, such as versatility, high loading volume, and lack of cellular toxicity<sup>152</sup>. They also are shown to be applicable in regenerative medicine and tissue engineering<sup>153 154 155</sup>. The degradation products of calcium carbonate are non-toxic  $\text{Ca}^{2+}$  and  $\text{CO}_3^{2-}$  ions, naturally present in blood. It was shown that a local increase of an extracellular  $\text{Ca}^{2+}$  concentration could promote bone tissue regeneration<sup>156</sup>. Calcium carbonate can exist in three anhydrous crystalline forms: vaterite, calcite, and aragonite. The most stable form in water is calcite, while vaterite is the least stable crystalline form of calcium carbonate<sup>157 158</sup>. Although vaterite is thermodynamically unstable, because of its high solubility in water, it can be stabilized with metal ions or organic molecules. In addition, polycrystalline vaterite spheres are attractive as drug carriers because of their high

surface area to volume ratio, due to their porous nature, and as a result – a high loading capacity<sup>152</sup>. Calcium carbonate drug carriers can be modified to get additional functionality by covering their surface with organic or inorganic molecules. Magnetic nanoparticles can be used for functionalization of calcium carbonate. The modification of a drug carrier with magnetic nanoparticles provides the ability to control carrier motion using a magnetic field. Such control was shown to be possible not only in cells and tissues<sup>153</sup> but also *in vivo* in a living body<sup>159</sup>.

Silver nanoparticles (NPs) can be also used for vaterite functionalization due to their unique thermal, optical, and electrical properties. Silver NPs have antibacterial properties<sup>160</sup>: a desired feature in wound bandages, cosmetics, and textile products. Silver NPs possess high thermal and electrical conductivity and can efficiently absorb and scatter light<sup>161</sup>. Light absorption and scattering for a specific wavelength are dependent on the diameter and shape of NPs. The aggregation of the silver particles can produce surface plasmon resonance effect in the near-IR part of the spectrum which can be used for SERS<sup>162</sup>. The SERS was first discovered in 1974 by Fleischmann *et al*, who described a substantial increase in Raman signal from pyridine after it was absorbed on a rough surface of silver electrode<sup>163</sup>. Since then, SERS found its application in such areas as medical testing<sup>164</sup>, forensic analysis<sup>165</sup>, drug discovery<sup>166</sup>, biological and chemical sensors<sup>167</sup>.

SERS properties of silver NPs make them an attractive candidate for Raman-based biosensors. It was shown that SERS platforms can be applied for a pathogen detection<sup>168</sup>. Both magnetic and silver NPs can be adsorbed on drug carriers adding them complementary functionalities. It was even demonstrated that silver on magnetic nanoparticles could be used for analyte molecules separation, and such a process can be monitored by SERS<sup>169</sup>. It should be also noted that elaborate novel platforms are now under development, including optical waveguides for more stable SERS detection<sup>170</sup>.

In this study, porous vaterite calcium carbonate particles were designed and tested as multifunctional drug carriers. The schematic of the experiments is shown in Figure 5.1. The multifunctionality of the particles was achieved by modifying them with two types of nanoparticles: (a) magnetite nanoparticles for providing magnetic field-controlled motion capability, and (b) silver nanoparticles for enabling molecule detection on the surface of particles with SERS. The possibility of utilizing silver/magnetite functionalized calcium carbonate particles as a SERS platform was demonstrated using Rhodamine 6G as a model

system. Subsequently, the cytotoxicity of silver/magnetite calcium carbonate particles and the speed of their motion in a magnetic field were tested <sup>171</sup>. Nevertheless, to stay within the boundaries of the topic of the thesis, in this chapter, we will focus primarily on the label-free SERS molecular detection functionality of the developed silver/magnetite drug delivery platform.

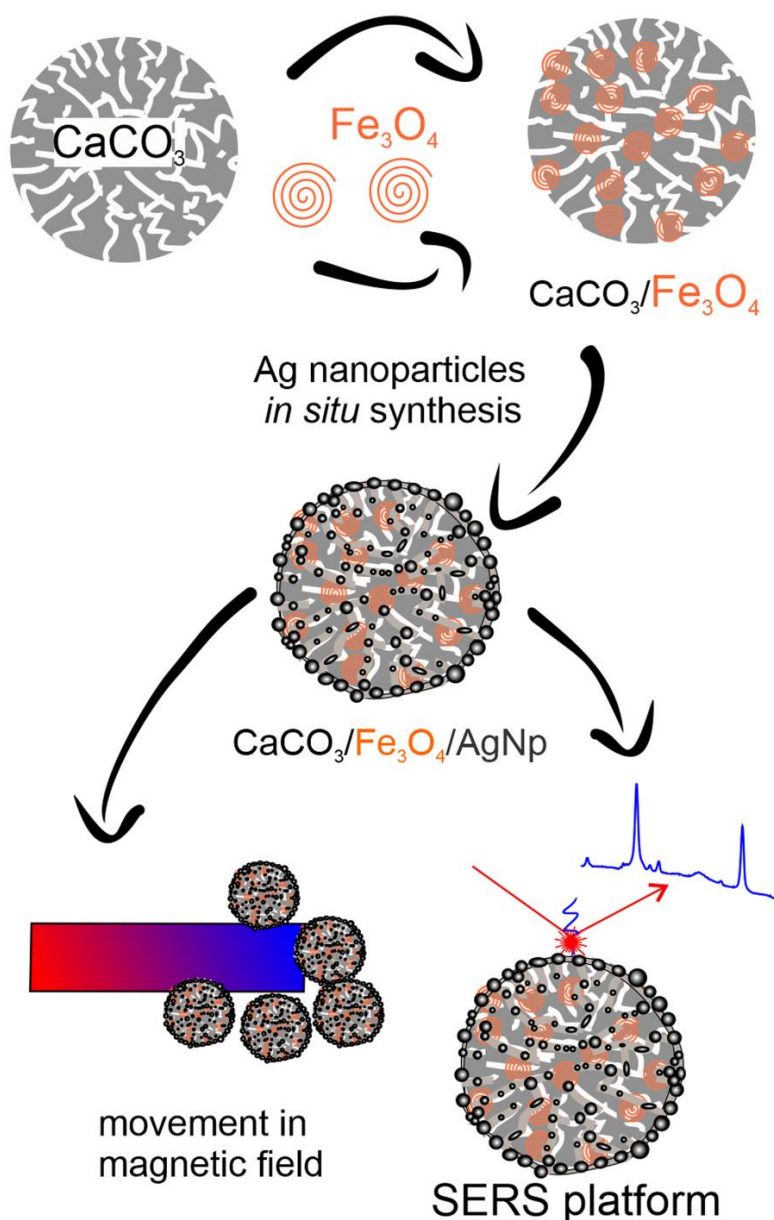


**Figure 5.1.** Schematics of experiments. The synthesized  $\text{CaCO}_3$  microparticles were modified with magnetic and silver nanoparticles. Then, their capabilities to move in a magnetic field and feasibility as SERS biosensor platform were tested.



### 5.1.2 Materials and methods

#### Synthesis of CaCO<sub>3</sub> particles and coating them with 30 nm silver nanoparticles

Spherical CaCO<sub>3</sub> microparticles, 4 μm in diameter, were synthesized according to the protocol described by Volodkin *et al.*<sup>172</sup>. The solutions of sodium carbonate NaCO<sub>3</sub> (1 mL, 0.2 M) and calcium chloride CaCl<sub>2</sub> (1 mL, 0.2 M) were mixed in equal volumes and stirred for 1 minute at room temperature at a rotation speed of 500 revolutions per minute (RPM). The participated particles were separated from the solvent by centrifugation (3000 RPM, 3 minutes) and washed with pure ethanol. The centrifugation and washing steps were repeated three times. The obtained micrometer vaterite particles were dried in an oven for 1 hour at 70 °C and stored in a freezer (- 10 °C). The magnetite was absorbed on the micrometer particles by adding 10 mg of vaterite into 1 mL of magnetite solution. Ultrasound was used to avoid large aggregations of magnetite. The resulting suspension was vortexed for 30 minutes and was cooled afterward for 15 minutes in a freezer (10 °C). The deposition of silver 30 nm nanoparticles on vaterite was done based on the protocol described in Kamyshinsky *et al.*<sup>173</sup> using a silver mirror reaction. First, equal volumes of 0.5 M AgNO<sub>3</sub> and 0.5 M NH<sub>4</sub>OH were mixed. Next, NH<sub>4</sub>OH was added to the solution until it became transparent. This reaction resulted in the formation of [Ag(NH<sub>3</sub>)<sub>2</sub>]OH, called the Tollens' reagent. 1.5 mL of water, 150 μL of Tollens' reagent, and 20 μL of 5 % dextrose were added to particle suspension to absorb silver NPs (nanoparticles) onto the vaterite carrier. The resulting solution was then shaken for 10 minutes. The functionalized particles were separated by centrifugation (3000 RMP, 3 minutes) and stored in water.

#### SERS enhancement factor evaluation

The evaluation of microparticles, functionalized with silver and magnetite nanoparticles, as possible SERS platform was done by estimation of the SERS enhancement factor. The calculations were based on the Raman spectral data. The particles were divided into groups and incubated with various concentrations (10<sup>-3</sup> M, 10<sup>-4</sup> M, and 10<sup>-5</sup> M) of Rhodamine 6G. Then, particles were deposited on the surface of a quartz slide, and the spectrum of Rhodamine 6G was measured with Raman microscopy for each dilution. Laser power was set to 15 mW, and the integration time was 3 seconds. Next, the reference solution of Rhodamine

6G ( $10^{-3}$  M) without the particles was deposited on the quartz surface, and the Raman spectrum was obtained. For this measurement, the laser power was set to 130 mW, and the integration time was 3 seconds. All measurements were done using a Nikon 40×/0.6 NA objective. Spectra were obtained by conducting  $100\ \mu\text{m} \times 100\ \mu\text{m}$  area scans with the step of  $10\ \mu\text{m}$  per datapoint, and the average spectrum of the scanned area was calculated. All measurements were done in triplicates. The signal intensity of three characteristic peaks of Rhodamine 6G ( $1319\ \text{cm}^{-1}$ ,  $1375\ \text{cm}^{-1}$ , and  $1514\ \text{cm}^{-1}$ ) was compared between spectra of Rhodamine 6G from the measured reference sample and Rhodamine 6G adsorbed on the particles to evaluate the SERS enhancement factor.

The SERS enhancement factor can be experimentally determined by measuring an analyte with a conventional Raman microscope and with SERS. If the same laser frequency is used for both measurements and collection geometry is similar, then (after normalization by laser power and integration time) the enhancement factor can be given as <sup>174</sup>:

$$\text{Enhancement factor} = \frac{\frac{I_{\text{sers}}}{N_{\text{sers}}}}{\frac{I_{\text{ref}}}{N_{\text{ref}}}} \quad (11)$$

where **I** – Intensity of analyte peak measured with SERS or conventional Raman spectroscopy,  
**N** – number of molecules in volumes measured with SERS or with conventional Raman.

Equation (11) describes the overall enhancement of Raman signal intensity for molecules near the surface of a SERS active nanostructure. It should be noticed that it is often challenging to estimate the number of molecules responsible for the measured Raman signal. And it is particularly difficult to estimate the number of molecules in close proximity to multifunctional microparticles, because of the porous nature of calcium carbonate and a random amount and distribution of silver nanoparticles on the surface of calcium carbonate particles. Additionally, it is challenging to precisely estimate the total number of multifunctional microspheres in the measured volume. Therefore, we normalize the measured SERS and Raman intensities based on the concentration of an analyte instead of the number of molecules. Here, we assume that the change in the concentration of analyte molecules in the solution will result in a proportional change in the number of molecules near the SERS sensor. This allows estimating the enhancement factor, which was calculated as follows: <sup>175</sup>

$$\text{Enhancement factor} = \frac{\frac{I_{\text{sers}}}{P_{\text{sers}} \cdot C_{\text{sers}}}}{\frac{I_{\text{ref}}}{P_{\text{ref}} \cdot C_{\text{ref}}}} \quad (12)$$

where **I** – Raman scattering intensity, **C** – the concentration of the analyte, **P** – laser power during measurement.

### 5.1.3 Results and discussion

To evaluate properties of composite silver/magnetite functionalized microparticles as a SERS sensor platform, we have calculated the SERS enhancement factor using data measured for Rhodamine 6G, as a model molecule. Figure 5.2 (A) depicts Raman spectra of Rhodamine 6G measured in a solution and adsorbed on the surface of calcium carbonate particles. The measured spectra contain characteristic peaks of Rhodamine 6G at  $1375 \text{ cm}^{-1}$ ,  $1514 \text{ cm}^{-1}$ , and  $1319 \text{ cm}^{-1}$ , in agreement with data reported in literature<sup>35,176</sup>. These three peaks were present both in the reference spectrum obtained with a conventional Raman microscope and in the spectrum measured that with SERS; therefore, they were used for calculation of the enhanced factor. The results show that the presented SERS platform can enhance the Raman signal by a factor of 10 at the concentration of  $10^{-3} \text{ M}$ , but the enhancement factor can be as high as 1000 for the concentration of analyte of  $10^{-5} \text{ M}$ , Figure 5.2 (B).

Figure 5.2 (B) reveals also that the enhancement factor is decreasing with increasing concentration of the analyte (Rhodamine 6G), which was somewhat unexpected. But it can be explained by a high absorbing capability of vaterite particles, which results in an oversaturation of the surface of microparticles with Rhodamine 6G. That is why the amount of measured Rhodamine 6G molecules is not directly proportional to the concentration of Rhodamine 6G in the solution. While such a property of the tested platform makes the task of precise quantification of analyte concentration challenging, the experimental results show that the presented vaterite SERS platform can be utilized for detection of a low quantity of analytes in a solution. Additionally, the high absorption capability of the calcium carbonate particles allows using them for the development of specialized drug delivery systems. Such a system is discussed in the next section of this chapter.

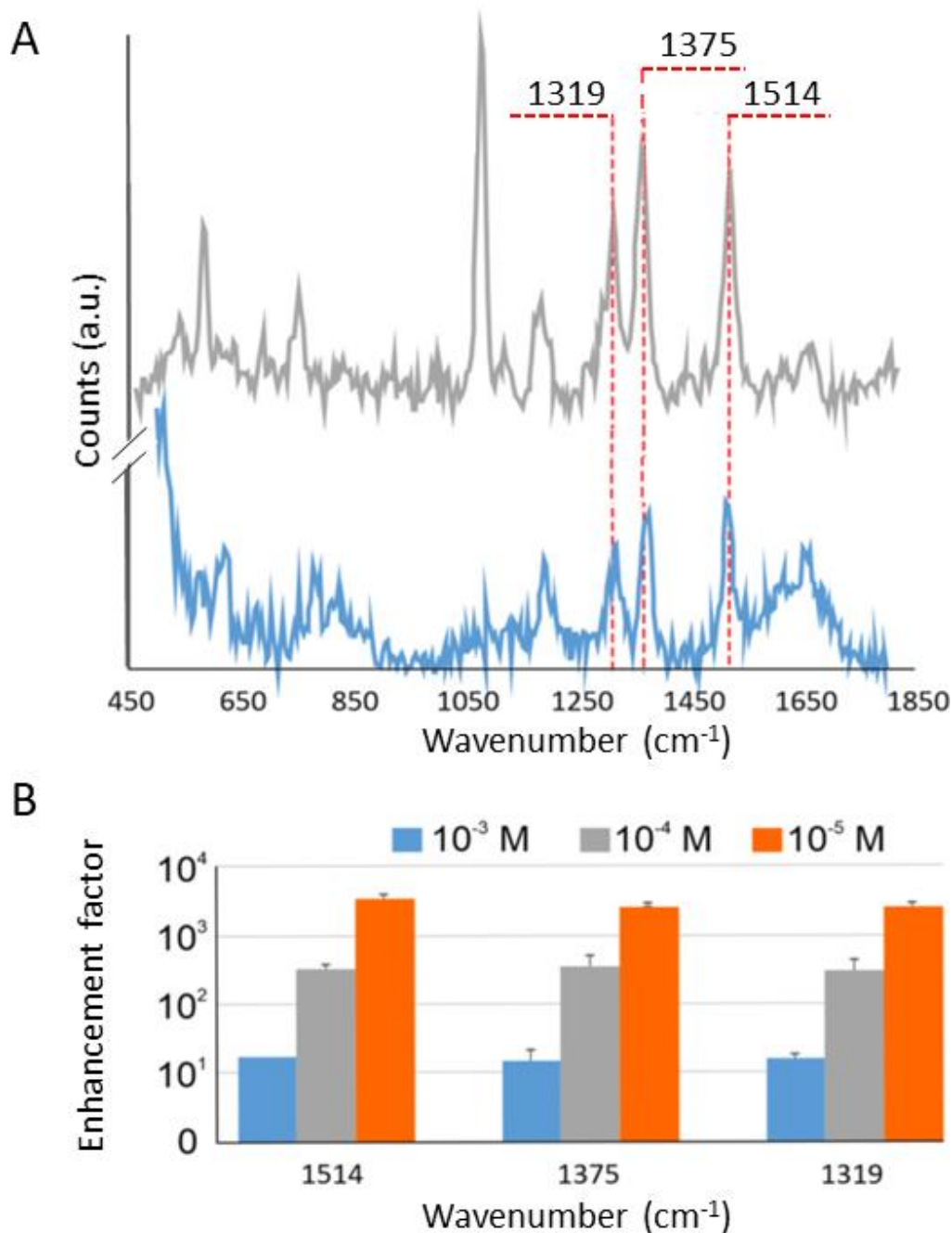


**Figure 5.2.** (A) Raman spectra of Rhodamine 6G. (Top grey spectrum) SERS spectrum of the Rhodamine 6G ( $10^{-5}\text{M}$ ) adsorbed onto calcium carbonate particles functionalized with magnetic and silver nanoparticles, measured with 15 mW of laser power. (Bottom blue spectrum) The reference spectrum of Rhodamine 6G in a solution measured with laser power of 130 mW. (B) Comparison of enhancement factors for various Rhodamine 6G concentrations obtained by dilution. Calculations were based on the intensity of  $1514\text{ cm}^{-1}$ ,  $1375\text{ cm}^{-1}$ , and  $1319\text{ cm}^{-1}$  peaks.

## 5.2 DRUG CARRIER DETECTION AND RELEASE INDUCTION *IN VIVO* USING SERS

### 5.2.1 Introduction

In the first part of this chapter, we have discussed the various drug carriers and their advantages and disadvantages. However, drug transportation is only the first part of the drug delivery process. Drug release from carriers is the next crucial subsequent step in drug delivery and it can be induced by a broad range of stimuli: chemical (dissolution)<sup>177</sup>, biological (targeting and biodegradability)<sup>178</sup>, or physical (remote action)<sup>179</sup>. The delivery system based on chemical or biological release mechanisms has several problems. In the case of biological stimuli, it is difficult to control the onset of release, while release based on a chemical dissolution of the carrier can be used in biology only under certain conditions, such as change of pH inside the target tissue or cell.

On the other hand, the release system activated by physical stimuli is well suited for controllable intracellular drug delivery, and it can be implemented using a broad range of physical effects: heating nanoparticles with light<sup>180</sup>, heating<sup>181</sup>, and deformation as a result of magnet-magnetic nanoparticle interaction<sup>182</sup>, mechanical action and cavitation with ultrasound<sup>183</sup>. A light-induced release can be done using of polymer-photoresponsive linker-drug conjugates<sup>184</sup>, polymers with the capability to undergo light-dependent structural changes<sup>185</sup> or by heating nanoparticles with a laser<sup>186</sup>. In the case, where the release is based on laser-nanoparticle interaction on polymeric capsules, it can be conducted in two different ways. Depending on the nanoparticle density in the microcapsule wall, release can be either non-disruptive<sup>187</sup> or explosive<sup>188</sup>. The latter is not always a disadvantage. It was shown that explosive release could be used in photo-thermal therapy of cancer cells, where cells are destroyed through excessive heat accumulation around nanoparticles<sup>189</sup>. On the other hand, non-destructive, light-controlled release of biomolecules from polymeric capsules inside a living organism or a single cell provides the possibility to study biological processes with optimized time control. Therefore, we aimed to develop such kind of capsules and test them *in vivo*. We have chosen *C. elegans* for *in vivo* testing, because it is one of the best-established animal model<sup>190</sup>, which is widely used in a broad range of life science fields such as neurotoxicology, disease study, and anti-aging research. It is a small non-parasitic nematode with a short life cycle, which is approximately three days at 20 °C. It has a high reproduction rate (>300 eggs per nematode) and the ability to self-fertilize<sup>191</sup>.

In contrast to cell culture, the drug delivery method based on diffusion from the culture medium can be challenging in the case of *C. elegans* because of the worm's thick cuticle. Uptake by *C. elegans* can take place via ingestion by pharyngeal pumping. The problem is that such a drug delivery strategy does not allow massive controllable uptake of compounds that are solubilized in the medium, although uptake does occur in low quantity. Nematodes have a specialized filter feeder that (with every pumping cycle of the pharynx) takes up a small amount of microbial suspension and spits out the liquid while retaining the bacteria, which are then further transported to the intestine <sup>192</sup>. It is possible to load compounds in microparticles to increase uptake rates. Particles must be compatible in size with the *C. elegans* feeding apparatus. Such particles must also be stable in a dry state. This can be a problem for some types of drug carriers, such as polyelectrolyte capsules. They may collapse in air, because they are produced and designed to be applied exclusively in an aqueous solution.

In this study, micro alginate shells, stable in a dry state, were synthesized using calcium carbonate as a core template and modified with silver nanoparticles allowing shells detection with SERS and a controllable drug release. The mechanism of the release was based on localized heating of plasmonic nanoparticles sitting in the walls of alginate capsules. For such a drug delivery/release system, the use of Raman microscopy is particularly attractive because it allows drug carrier detection inside nematodes with SERS, enabling localization of the carriers upon controllable drug release at the desired location. It should be noted that Raman microscopy has already been proved to be a useful tool to study *C. elegans* metabolism since it was already used to investigate glycogen content<sup>193</sup>, fat metabolic pathways<sup>194</sup>, and image the distribution of lipids <sup>195</sup>.

## 5.2.2 Material and methods

### Synthesis of hollow silver alginate hydrogel shells from calcium carbonate template

The synthesis procedure of silver alginate hydrogel shells is shown in Figure 5.3, showing that molecules can be absorbed in CaCO<sub>3</sub> microparticle. Then, drug-containing particle is used as a core, Figure 5.3 (A), which is subsequently covered with alginate, Figure 5.3 (B).

Further, CaCO<sub>3</sub> particles were loaded with tetramethylrhodamine bovine serum albumin (TRITC-BSA), which was chosen here as a model system due to its size (comparable to other biomolecules in the case of BSA) and a possibility of visualization in fluorescence microscopy (due to fluorescence of TRITC). This dye was used as a model drug delivery molecule. TRITC fluorescence allows using fluorescence microscope images of the particles to confirm the particle localization. Then, silver nanoparticles were formed in the alginate walls, and calcium carbonate core was dissolved, leaving alginate shells filled with TRITC-BSA Figure 5.3 (C). The described above synthesis was done according to the following procedure: first, 40 mg of CaCO<sub>3</sub> microparticle powder was prepared according to the protocol by Lengert *et al.*<sup>196</sup> Next, microparticles were placed in a 2 mL Eppendorf tube and suspended in 1 mL of sodium alginate (5 mg/mL). This suspension was vortexed (2000 RPM) for 10 minutes. The resulting sodium alginate coated CaCO<sub>3</sub> microparticles were washed three times with deionized water. Next, 0.5 mL of 0.75 M AgNO<sub>3</sub> was added to previously prepared sodium alginate CaCO<sub>3</sub> microparticles to initiate cross-linking of sodium alginate. The mixture was agitated for 10 min in a shaker and then washed with deionized water. In the last step, the CaCO<sub>3</sub> core was dissolved by the addition of 0.5 mL of ascorbic acid (0.1 M) leaving the alginate shell filled with TRITC-BSA. Ascorbic acid also induced the formation of silver nanoparticles in the walls of alginate shells. Finally, silver alginate microspheres were precipitated by centrifugation, and the supernatant was removed. The microspheres were washed three times with MilliQ water and stored in the water for further use.

Scanning electron microscopy (SEM) was used to visualize 3D surface of the particles. SEM was done after each synthesis using MIRA II LMU (Tescan). The operating voltage of SEM was set to 30 kV.

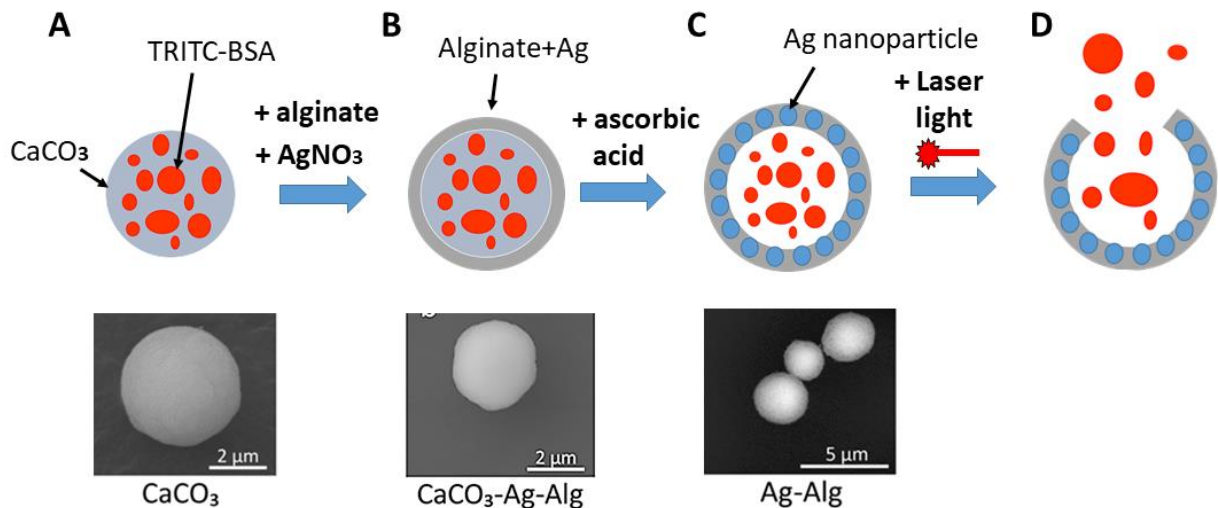


**Figure 5.3.** Synthesis of silver alginate hydrogel microspheres loaded with TRITC-BSA for laser-induced release inside *C. elegans* worms. (A)  $\text{CaCO}_3$  particles loaded with TRITC-BSA. (B)  $\text{CaCO}_3$  particles covered with alginate and functionalized with Ag nanoparticles. (C) Alginate microspheres with incorporated Ag nanoparticles and loaded with TRITC-BSA. (D) Laser irradiation results in destruction of alginate microspheres and release of TRITC-BSA.

### Uptake of shells by *C. elegans*

The *C. elegans* worms were grown according to the standard protocol: the wild-type strain N2 was cultured on nematode growth medium (NGM) agar plates, seeded with the *Escherichia coli* strain OP50 as a food source for the worms. Plates were incubated at 20 °C.

The silver alginate microspheres were loaded with fluorescent TRITC-BSA molecules. Then, 0.1 mL of 20 mg/mL microspheres were mixed with 0.1 mL *Escherichia coli* suspension. The resulting mixture was added to the plate with the worms and incubated for 20 hours. For controllable drug release experiments, worms were paralyzed with levamisole (100 mM) in S-basal buffer (50 mM potassium phosphate, 100 mM NaCl, pH 6). It was added directly to the agar plate with nematodes. Then, the nematodes were investigated using fluorescent, confocal, Raman, and Nomarski differential interference contrast microscopes. *C. elegans* motility before and after experiments served as the vitality test.

### Evaluation of focused laser beam exposure on the viability of *C. elegans* worms

We have tested whether exposure to 785 nm laser would harm the worms. The *C. elegans* worms were grown according to the standard protocol: the wild-type strain N2 was cultured



on nematode growth medium (NGM) agar plates, seeded with the *Escherichia coli* strain OP50 as a food source for the worms. Plates were incubated at 20 °C. To test the effect of laser irradiation worms were divided into four groups, with a minimum of ten worms per group:

1. The positive control group: worms in this group were not treated with levamisole and were not irradiated with a laser.
2. The second control group: worms were treated with levamisole but were not exposed to a laser.
3. The third control group: worms were treated with levamisole and exposed to 15 mW of laser radiation (similar to the power required to open the capsules).
4. The fourth group: worms were treated with levamisole and exposed to 160 mW of laser radiation.

The worms were first grown on NGM plates with *Escherichia coli* OP50 until they reach the day two adult stage. Next, they were transferred onto bacteria-free NGM plates. The groups 2, 3 and 4 were paralyzed with levamisole (100 mM final concentration) in S-basal buffer (50 mM potassium phosphate, 100 mM NaCl, pH 6). Levamisole is an acetylcholine receptor agonist. The continuous muscle activation by levamisole leads to temporary muscle paralysis in nematodes. Levamisole solution was added directly to the agar plate with nematodes. The laser exposure was done by focusing the 785 nm laser beam for 10 seconds on the head region, tail region, and the middle section of each worm in groups 3 and 4. A 100x/0.9 NA objective (Nikon) was used for laser focusing, and laser power was measured before the objective.

After the laser exposure, all worms were transferred onto new NGM plates, seeded with *Escherichia coli*, for recovery and subsequent vitality evaluation. The evaluation was done after 2 hours and 20 hours after the laser exposure.

### **Alginate shells localization inside *C. elegans* and drug release activation**

The alginate capsule localization inside *C. elegans* and subsequent drug release was done using a home-build setup, which combined Raman and fluorescent microscope. It was created by adding a CCD camera and an excitation LED source to the Alpha300R+ confocal Raman microscope. The alginate shell was localized inside the *C. elegans* by conducting the area scans with Raman. The laser power was set to 1 mW (measured before the objective). A 100x/0.9

NA (Nikon) objective was used for all types of scans. To conduct anatomical molecular imaging, laser power, measured before the objective, was set to 165 mW, and the integration time was 1 second per point. The Head region of the worm was mapped with a resolution of 2 spectra per  $\mu\text{m}$ . For particle detection, worms were mapped with a resolution of 1 spectrum per  $\mu\text{m}$ . The laser power was 1 mW, and scans were done with 1 second and 0.1 second integration time. The laser power of 15 mW was used for the induction of drug release. The release of fluorescent dye from the shell was confirmed by comparing fluorescence microscopic images of the region around the shell before and after laser irradiation.

### **Raman data analysis**

The heatmaps based on  $1665\text{ cm}^{-1}$  peak were generated with Project FOUR v.4.0 (WITec 2014). The spectra preprocessing and analysis was done in R.3.4. using the *hyperspec* package. The preprocessing was conducted using the pipeline and Rscripts described in Appendix (Supplementary Information for Chapter 2 (Appendix), S2.2). The background was removed with the *als* algorithm from the package *baseline*. Intensity heat maps and anatomical molecular images were constructed using a biological relevant spectral region between  $600$  and  $1800\text{ cm}^{-1}$ . For visualization of the spatial arrangement of anatomical features inside the *C. elegans*, the datasets were first normalized using vector normalization, and then data points were grouped based on their spectral similarity using hierarchical clustering.

## **5.2.3 Results and discussion**

### **Evaluation of the effect of laser irradiation on *C. elegans* viability**

The preliminary tests showed that irradiation of *C. elegans* with 160 mW laser for 20 seconds could lead to worm death because of the destructive explosion, Figure 5.4. Such effect can be explained by the fact that worms were dried on  $\text{CaF}_2$  slides and scanned in the air; therefore, laser heat was not diffused fast enough, causing the temperature increase inside the worm and its subsequent destruction.

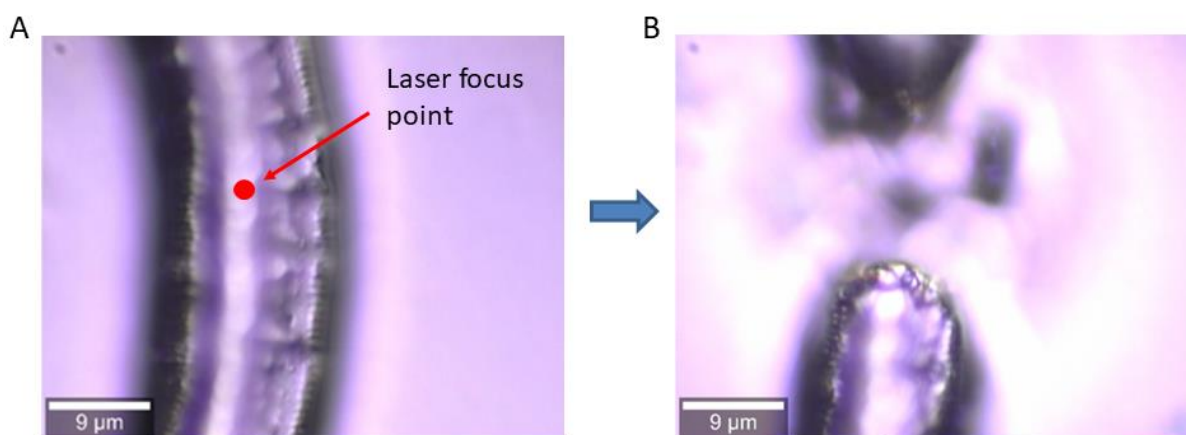


**Figure 5.4.** Effect of laser irradiation on *C. elegans*. (A) Intact worm on a  $\text{CaF}_2$  slide before laser exposure. The red dot marks the spot, where laser (power of 160 mW) will be focused. (B) The destroyed worm's body segment around the laser spot.

All further laser scans of *C. elegans* were done on agar. Additionally, worms were covered with  $\sim 50 \mu\text{m}$  thin layer of S-buffer to solve the problem of heat accumulation.

Next, we have tested whether laser exposure under such conditions is not destructive for the worms, Table 5.1.

Group 1	Group 2	Group 3	Group 4
- levamisole - laser exposure	+ levamisole - laser exposure	+ levamisole + 15 mW laser exposure	+ levamisole + 160 mW laser exposure

**Table 5.1.** Experimental setup for testing the effect of laser exposure on the vitality of *C. elegans*.

Worms were divided into four groups, Table 5.1., where group 1 served as control. Group 2 was the second control group and was used to validate that paralyzing effect of levamisole had no long-term negative effect on worm's viability. Groups 3 and 4 were used to evaluate the effect of laser irradiation. Group 3 was exposed to 15 mW of laser light. Such laser power setting was chosen because the preliminary tests showed that similar power is required to open the alginate shells. Group 4 was irradiated with 160 mW: this power is commonly used to measure cells with Raman microscopy. This laser power allowed obtaining cellular spectra with a good resolution and a relatively short integration time.

No explosive worm's death or structural damage was observed in groups 3 and 4, proving that a combination of agar with liquid solved the heat dissipation problem.

The motility of the worms was used to evaluate whether levamisole or laser affected their viability. The evaluation was done 2 hours after the exposure. Worms from groups 2, 3, and 4 showed very low motility compared to control group 1. After gentle touching with a platinum wire probe, a small movement was observed only in the head region. The viability evaluation was repeated after 20 hours. All worms from groups 2, 3, and 4 showed the same motility as the control group 1. This leads to the conclusion that low motility observed 2 hours after exposure can be explained by the paralyzing effect of levamisole. No difference in viability was observed in 20 hours between worms with and without laser exposure. This observation suggests that 15 mW and 160 mW laser irradiation had no significant effect on *C. elegans* viability under tested experimental conditions.

#### **SERS functionalized alginate micro-shell localization and release induction inside *C. elegans***

Next, we aimed to demonstrate the possibility of a controllable laser-induced release of TRITC-BSA from the shells inside the *C. elegans*. Nematodes were fed with silver functionalized alginate shells and paralyzed with levamisole. Each alginate shell was loaded with TRITC-BSA. Fluorescence of TRITC-BSA was used to track the particle position inside the nematode with fluorescent microscopy, Figure 5.5 (A, B). Additionally, we have used Raman microscopy for verification of the particle position and to obtain molecular images based on the biochemical composition of the tissue Figure 5.5 (C). In contrast to the method discussed in **Chapter 3**, we did not use molecular fingerprint features, such as the presence of a unique peak in spectra of the particle or the TRITC-BSA, to discriminate between tissue and particle data points on Raman area scans. Instead, our detection method was based on the contrast between the high Raman signal intensity in the proximity to silver-functionalized shells and the relatively weak average Raman signal of the surrounding tissue.

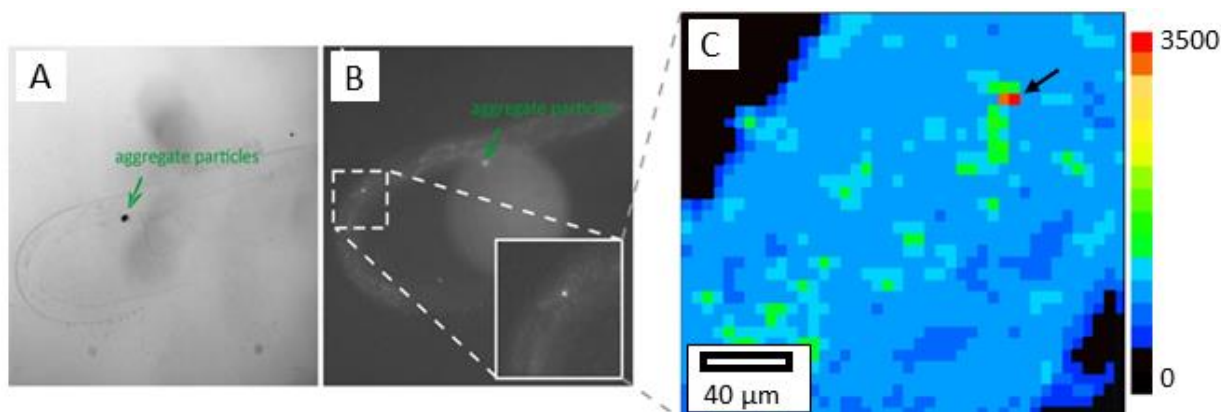


**Figure 5.5.** (A) Transmission microscopy image of a *C. elegans* worm on agar. (B) Fluorescence microscopy image of the same worm. (C) The heatmap of the *C. elegans* worm's segment is shown with the alginate silver-functionalized shell. The heatmap is constructed based on the average Raman signal intensity in the  $600\text{ cm}^{-1}$  -  $1800\text{ cm}^{-1}$  spectral region. Because of the SERS signal amplification, the shell can be localized due to the highest signal intensity (red and orange pixels) relative to other points in the dataset. Colors in the molecular image in (C) correspond to counts in arbitrary units.

The high signal intensity was the result of the SERS effect caused by the presence of silver nanoparticles in the walls of shells. The particle on the fluorescent image obtained from *C. elegans* correlates with the particle position was on Raman the heatmap image, identified due to the highest Raman signal intensity relative to the other spectra in the dataset, Figure 5.5 (C). The Raman area scans were made with 1 mW of power and with 1 second integration time. Such scan settings allowed to localize the particle without inducing the release of the loaded compound. In the next experiment, the integration time of the Raman microscope was decreased ten times: from 1 to 0.1 seconds. The particles can be still localized inside the worms Figure 5.6 (A) and (B). At such low laser power settings and short integration time, the worms tissue produces no detectable Raman signal, Figure 5.6 (D), while the particles still can be detected because of Raman background, due to the SERS signal amplification Figure 5.6 (C). Typically, background is removed from a Raman spectrum to improve the quality of the dataset. Nevertheless, in this approach, we demonstrate that the presence of the background itself can be beneficial and can be utilized for the detection of the particle position on the spectral image.

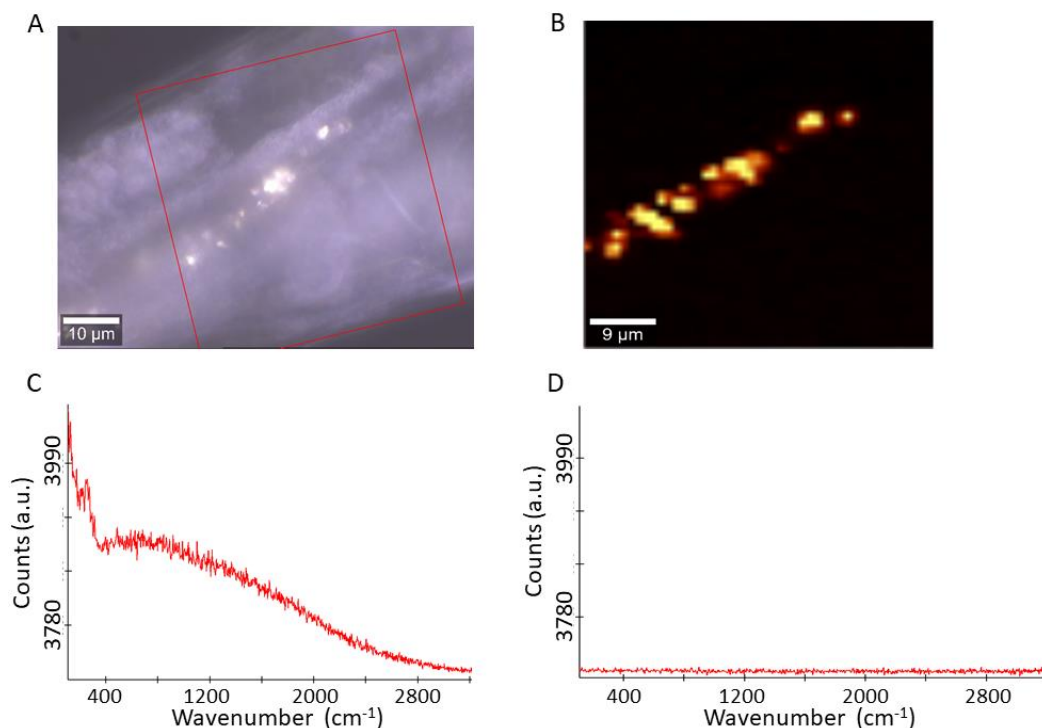


**Figure 5.6.** (A) Transmission microscopy image of a *C. elegans* segment functionalized with Ag nanoparticles. (B) The Raman scattering heat map generated using the average Raman signal intensity in the  $600\text{ cm}^{-1}$  -  $1800\text{ cm}^{-1}$  spectral region. Particles are visible as yellow dots. (C) Spectrum of the particle inside the worm. (D) Spectrum of *C. elegans*' tissue (with no features).

The “built-in” SERS detection functionality in the tested particles allows for label-free particle location without additional SERS-tagging molecules. A strong SERS signal provides the possibility to decrease the scanning time significantly. Ultrafast scanning not only lowers the chance of unintentional drug release but also decreases the possibility that the worm's metabolism would be influenced by a laser. A disadvantage of the detection approach based on background in SERS signal is that, in contrast to conventional SERS-labels, only one type of particles can be detected simultaneously.

It is essential to note that in general, Raman microscopy can be used not only to localize the shell with the drug inside nematodes but also to obtain information about the biochemical composition of tissues and organs inside *C. elegans* without dissecting or adding fluorescent labels before and after internalization of particles, Figure 5.7 (A-D), (Supplementary Information for Chapter 5 (Appendix), Figure S5.1, Figure S5.2). The heatmaps based on selected bands allow studying the distribution of such biomolecules as proteins and lipids inside a living nematode, Figure 5.7 (C).

Hierarchical clustering analysis based on a spectral similarity between data points was used to group data points from similar tissues together. By giving each group a unique pseudo color label, it was possible to visualize such anatomical structures as pharynx and intestine inside the worm, Figure 5.7 (D).

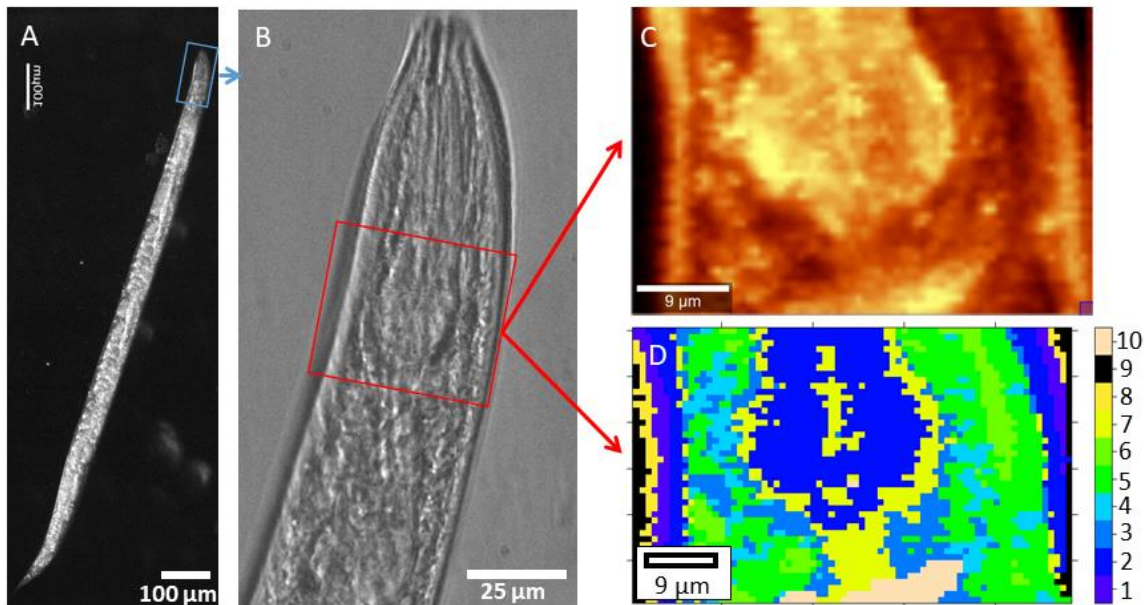


**Figure 5.7.** (A) Optical microscopy image of a *C. elegans* worm. (B) DIC image of the head region of the same *C. elegans* worm. The area scanned with Raman microscopy is marked with the red rectangle. (C) Raman heatmap constructed based on intensity of the  $1665\text{ cm}^{-1}$  peak showing the alpha-helix proteins and unsaturated fatty acids distribution. (D) Molecular image is generated by clustering analysis, where pixels with similar molecular fingerprints are depicted with the same false colors. Numbering of colors corresponds to clusters.

It can be seen in Figure 5.7 that positions of anatomical structures on the image generated by clustering analysis of datapoints with similar Raman molecular fingerprint, Figure 5.7 (C), correlate with those on differential interference contrast (DIC) microscopy image, Figure 5.7 (B). The body wall of the worm in the scanned area was found to consist of 3 types of datapoints marked with grey, dark purple, and pseudo blue colors. The data points marked with yellow and blue color form the pharynx (metacarpus and isthmus), the orange marked data points form the nerve ring. The mean Raman spectra of each cluster in Figure 5.7 (C) can be found in Supplementary Information for Chapter 5 (Appendix), Figure S5.3.

### 5.3 CONCLUSION

New drug delivery carriers based on calcium carbonate particles are developed and functionalized with SERS active silver nanoparticles and with magnetite. Such an assembly was found to provide a SERS enhancement factor of up to  $10^3$ . Calcium carbonate particles have been also functionalized with magnetic nanoparticles. A possibility to control the movement of the particles with a magnetic field may be desirable for cellular studies because it may allow moving particles to a specific region in a cell, where Raman scattering signals can be measured specifically from that area. However, it is essential to note that a high absorbing capability of the particles has made the quantification of analyte concentration with SERS challenging.

The high absorption capability of calcium carbonate particles was used to create alginate shells, which were functionalized with silver nanoparticles for SERS signal enhancement in Raman microscopy. In contrast to the first part of the work carried out in this chapter, SERS was not used for molecular detection. The SERS was applied here for precise localization of the alginate-based drug carriers inside *C. elegans*. Furthermore, temperature increase on silver nanoparticles induced by illuminating laser was used for controllable light-induced drug release. The fabricated drug carriers were tested *in vivo* in *C. elegans* worms. The SERS functionality of the particles allowed detecting them inside worms with very fast area scans using only 1 mW of laser power. The detection method was based on using the strong background in the SERS signal for drug carrier localization.



# Chapter 6

4Pi Raman microscopy and atomic force microscopy investigation of *Chlamydia* infected cells

**Chapter 6** is based on the following publication and manuscript:

**Superresolution  $4\pi$  Raman microscopy.** A. Diaz Tormo, D. Khalenkow, K. Saurav, A.G. Skirtach, N. Le Thomas. *Opt Lett.* **2017**, 42, 4410-4413.

**Complementary multimodal microscopy study of *Chlamydia psittaci* infected cells:  $4\pi$  Raman and atomic force microscopy.** D. Khalenkow, A. Diaz Tormo, J. Rybarczyk, J. Verduijn, L. Van Der Meeren, D. Vanrompay, N. Le Thomas, A.G. Skirtach, *submitted*.

## **6 4Pi Raman microscopy and atomic force microscopy investigation of *Chlamydia* infected cells**

In this chapter, the 4Pi Raman microscope and its basic working principles are described. System calibration and 4Pi Raman microscopy data acquisition and processing are illustrated by constructing axial profiles of polystyrene nanoparticles. Subsequently, 4Pi Raman microscopy in a combination with an atomic force microscope (AFM) is applied to investigate *Chlamydia psittaci* inside eukaryotic cells.

## 6.1 INTRODUCTION

Understanding structures and interactions between molecules, cells, tissues, and organisms is the goal of biological sciences, where transmission and fluorescence microscopy remain the most used visualization techniques.

After invention of Fluorescence Recovery After Photobleaching (FRAP), Fluorescence Resonance Energy Transfer (FRET), and Fluorescence Correlation Spectroscopy (FCS) techniques, development of novel approaches in microscopy has paused, only to be vigorously rekindled again with the invention of superresolution microscopy techniques<sup>197</sup>. In the area of superresolution microscopy, novel molecular localization algorithms, new fluorophores for superresolution microscopy as well as instrument development, for example, the STED microscopy approach have led to an increase of the resolution in the lateral plane of a microscope by a staggering amount of almost an order of magnitude<sup>198</sup>. This would not have been particularly essential if not for the fact that such a resolution becomes comparable with the sizes of single molecules. This ultimately sparked substantial interest and brought together scientists from optics, photonics with those working in cell biology and medicine to further develop and optimize superresolution microscopy techniques.

Another superresolution technique is 4Pi fluorescence microscopy, which leads to a significant improvement of the axial resolution<sup>47</sup>. The development was seen to be essential since the axial resolution of a microscope is about  $\sim$  three times worse than the lateral resolution. The improvement of lateral resolution in 4Pi microscopy (4Pi effect) is achieved through the interaction of two coherent laser beams focused on the same point. The resulting interference between the light waves produces the pattern where the area of maximum light intensity is narrower than that produced by a single beam, Figure 6.1.

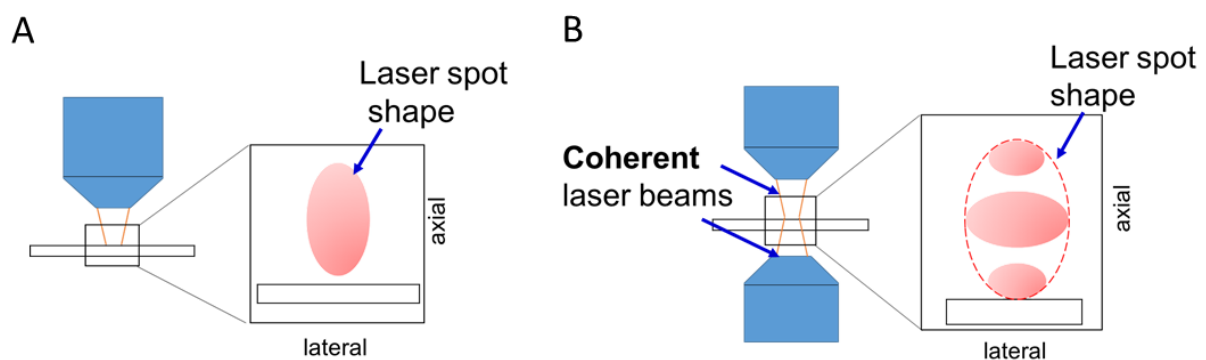


**Figure 6.1.** A comparison of (A) confocal, and (B) 4Pi microscopes.

The described above principle of 4Pi axial resolution improvement in fluorescence microscopy can be applicable to Raman microscopy. Indeed, just as in fluorescence microscopy, a combination of Raman spectroscopy with confocal microscopy allows obtaining high-resolution Raman molecular images of the tissues, cells, and cellular components but in this case without using any labels. Furthermore, just as in fluorescence microscopy, the axial resolution of a conventional Raman microscope is about three times lower than the lateral resolution. The limitation in the axial resolution is overcome by combining the confocal Raman microscopy approach with the 4Pi Raman technique. We have shown that such a technique allowed us to resolve nanometer-thick structures<sup>199</sup>. Here we applied 4Pi Raman microscopy for nanolayer analysis. The nanolayers are used in a broad range of fields, such as energy storage<sup>200</sup>, optics<sup>201</sup>, and drug delivery<sup>202</sup>. We have demonstrated that 4Pi Raman microscopy can be used for non-destructive and simultaneous characterization of each nanolayer in nanolayers stack<sup>114</sup> (Supplementary Information for Chapter 6 (Appendix), Figure S6.1), providing information about its chemical composition, optical properties, and microstructure. Such an analysis of multiple properties at the same time is challenging with techniques commonly used for nanolayers characterization like ellipsometry, X-ray, and electron microscopy.

Application of the developed 4Pi Raman microscopy to analysis of different samples, including those in cell biology, is an interesting topic. However, it is essential first to discuss basic principles of 4Pi Raman microscopy developed in the course of this work. First, we discuss the microscopy setup pointing out the interaction and interference of the interacting beams. An important detail of the setup is a possibility to control phases of the interacting beams. Subsequently, we discuss measurement procedure, peculiarities of the setup and data processing.

## 6.2 THE 4Pi RAMAN MICROSCOPE SETUP AND CHARACTERIZATION

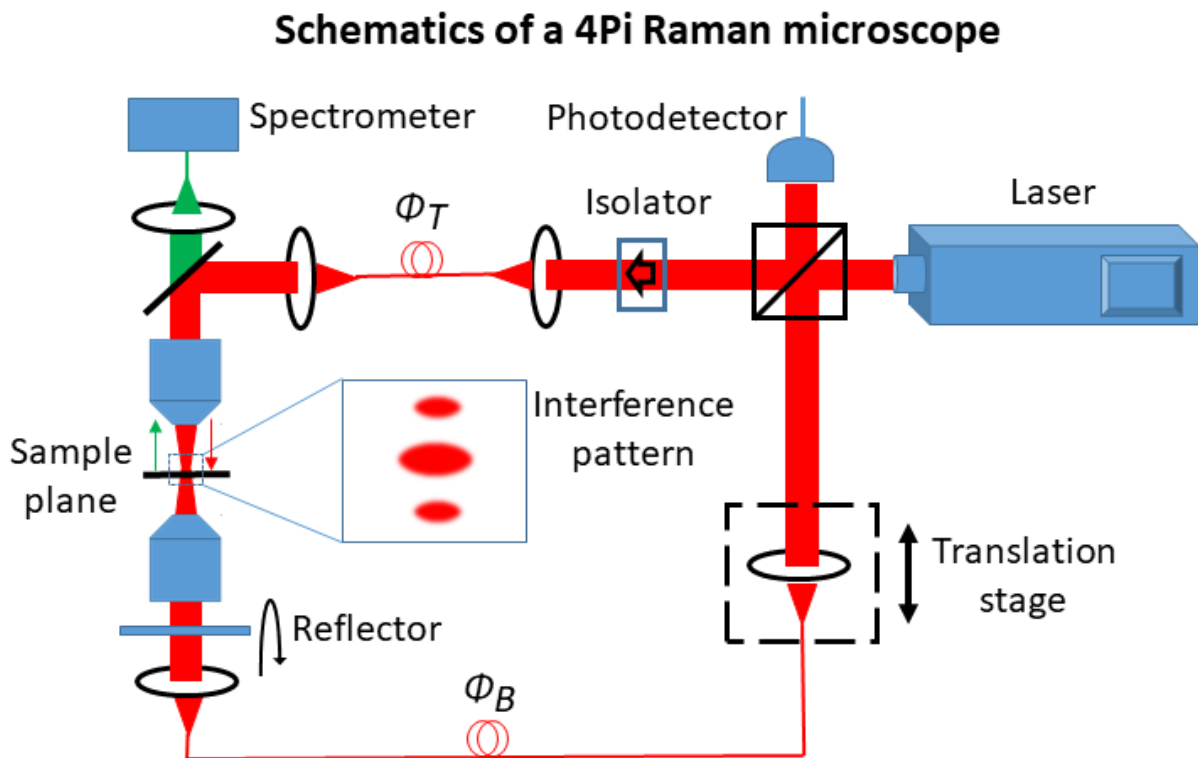


**Figure 6.2.** Schematics of a 4Pi Raman microscope showing two beams impinged on a sample and the generated interference pattern.

The 4Pi Raman microscopy setup was built on the basis of a custom-made confocal Raman microscope (Alpha300R+, WITec), which provides the possibility for both top and bottom sample excitation with a laser. Similar to the measurements performed with a conventional confocal Raman microscope described in previous chapters, we have used a laser source (Toptica, Munich, Germany) operating at 785 nm as a light source to minimize potential fluorescence in the visible spectral range.

The schematics of the 4Pi Raman microscopy setup is shown in Figure 6.2. The laser beam from a single laser source is split into two beams, which are then focused back on the sample through the objective lens. The interaction of the beams can result in constructive or destructive interference. The resulting interference pattern on the sample plane is dependent on the beam phases. Light in both beams undergoes the phase shifts relative to the phase of the original laser beam. The  $\Phi_T$  is the phase shift in the arm connected to the top objective, and  $\Phi_B$ , phase shift is the phase shift in the arm connected to the bottom objective. The

photodetector provides information about the phases of the beams to the controller of the translation stage. The translation stage is then used to modify the phase relationship between the beams by changing the length of the optical pathway of one of the arms. That creates a feedback loop, which allows us to stabilize and change the interference pattern on the sample plane. The main challenge in this approach was that we could not measure the phases of the beams directly at the sample plane. To solve this problem, we installed the partial reflector to one of the arms. By measuring the beam, which was the result of interference between the reflected light from one arm and transmission light from the second arm, we were able to obtain the phase information indirectly. The resulting phase, measured by the photodetector, can be described by the following formula:

$$\Phi = (\Phi_{Tr} + \Phi_{Sample} - \Phi_{Ref} - \Phi_S) \quad (13)$$

where  $\Phi_{Tr}$  – phase of the transmission beam before the sample,  $\Phi_{Sample}$  – phase change caused by sample,  $\Phi_{Ref}$  – phase of reflected light from the second beam,  $\Phi_S$  – shift introduced by an optical path to detector.

To evaluate the presented 4Pi microscope setup and demonstrate the possibility of resolution improvement, a single 500 nm monodisperse polystyrene nanoparticle was measured in the 4Pi mode, and the axial particle's profile was constructed using the obtained data. The light microscope image of the scanned particle and its molecular fingerprint, recorded with a convention Raman microscope, is shown in Figure 6.3. The 1005  $\text{cm}^{-1}$  peak was used for system calibration and axial profile construction. This peak was chosen because it was the most intense peak on the spectrum.

For 4Pi measurements, the following objectives were used: a 100x/0.95 NA objective (Zeiss) was mounted in the top arm (the top objective), and a 20x/0.5 NA (Nikon) objective was used in the bottom arm (the bottom objective). The laser power at fiber output before interferometer was 260 mW. However, only 35 mW was recorded before the objectives in both arms. For all measurements in the 4Pi mode, the Raman signal was collected through the top objective. The collected signal was sent to spectrograph through multimode fiber with 100  $\mu\text{m}$  core-diameter. Measurements were done with 7 seconds integration time.

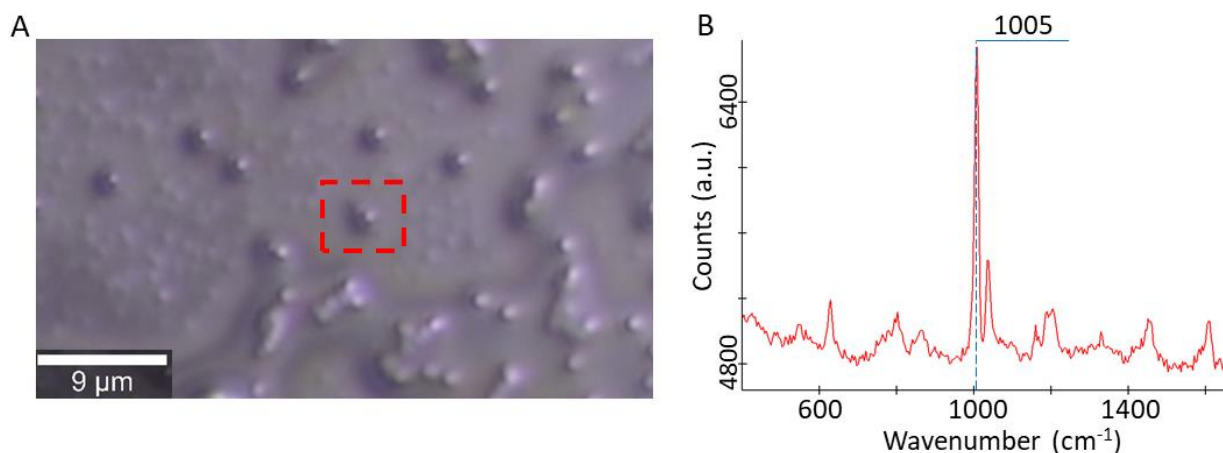


**Figure 6.3.** (A) A transmission light microscope image of 500 nm polystyrene nanoparticles. The particle measured with Raman microscopy is marked with the red dashed rectangle. (B) The Raman scattering spectrum of the measured particle.

Before measurements, the laser power in both beams was calibrated to produce an equal contribution to the Raman signal intensity. This was done by blocking the upper or lower arm and measuring the Raman signal of the particle.

Next, we have confirmed that the change in the beam's interference pattern in the sample plane influences the measured Raman signal. The configuration of the assembled microscope allows altering the phase of one of the beams relative to the other one. As expected, the change in phase translated to the change in the peak intensity, Figure 6.4.

It can be seen from Figure 6.4 that intensity of the peak of 4Pi Raman microscopy scanning (the red line) is higher compared to the trace corresponding the confocal scanning (the black dashed line). Further, the size distribution of the particle in the axial plane was measured. During axial profiling, both laser beams remained stationary focused on one point, while the particle was moved in an axial direction by high precision piezo stage with the step of 100 nm. It should be noted that the chosen commercially available particles were very monodisperse – that allowed not only choosing any particle on the slide, but also provided a solid reference in regard with the diameter of particles. In addition, the molecular composition of the particles was also controlled by the manufacturer (Micromod Partikeltechnologie GmbH, Germany).



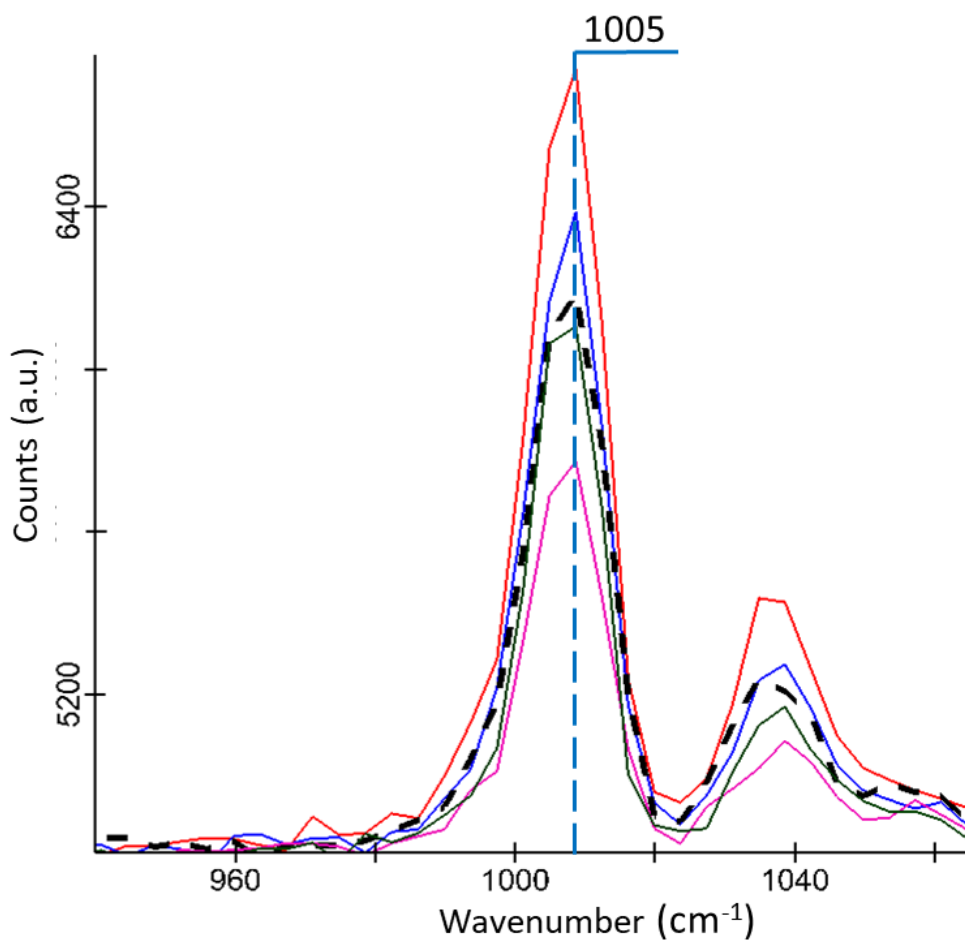


**Figure 6.4.** Effect of the phase change on Raman peak intensity. Spectra drawn with solid lines are Raman spectra of a polystyrene particle taken in the 4Pi mode under different phase interferences. The spectrum drawn with the dashed line is that obtained with a conventional Raman microscope.

For each axial coordinate point, 4Pi Raman spectra were recorded with different phase interactions and as a result different Raman peak intensities. Because we do not measure the phase directly in the sample plane – it is challenging to determine the position of the translation stage, which would allow obtaining the phase configuration with the maximum positive or negative laser beams interference. To solve this problem we were recording multiple Raman spectral datapoints, each with a different phase configuration. This allows application of a non-linear regression based on the measured peak intensities to interpolate the profile of the phase interference. Peak intensities with maximum constructive interference can be extracted from the resulted cosine curves. By plotting intensity of the obtained peak versus the axial coordinate - the profile of the particle was constructed.

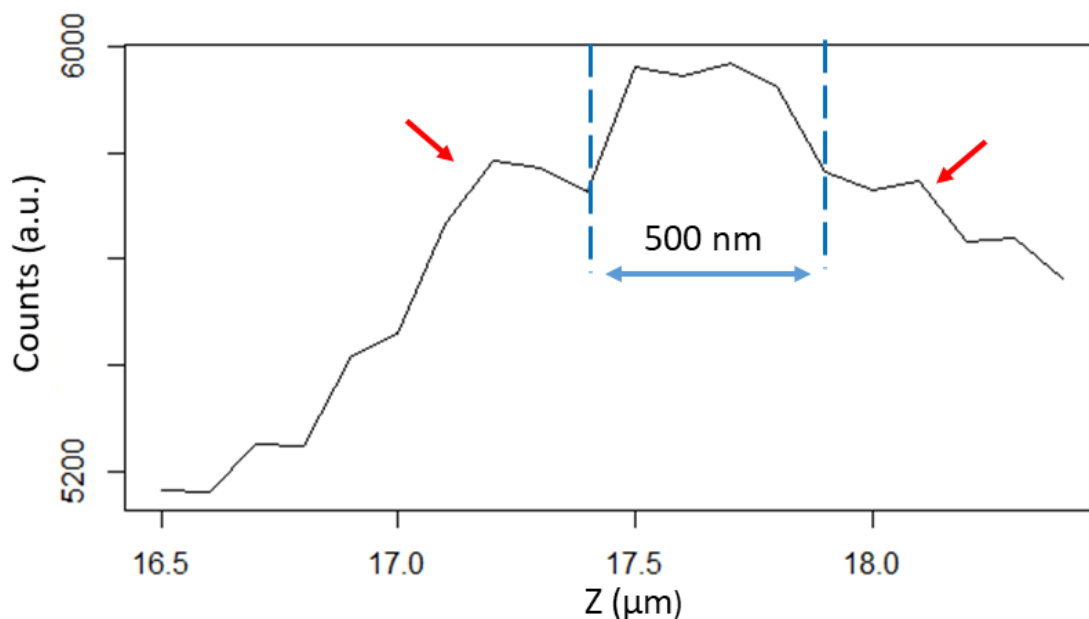


**Figure 6.5.** The axial profile of a 500 nm polystyrene particle constructed using the built 4Pi Raman microscope. The side lobes are marked with red arrows. The central lobe is marked with dashed lines.

The size of the central lobe in the resulted profile corresponds to the size of the particle. The smaller side lobes are visible in Figure 6.5 near the central lobe. This is expected because of the interference pattern in the 4Pi mode, which consists of a large central and two smaller side fringes, Figure 6.5. Because the reflections used for phase control are collected before the objectives, the fringe position was independent of the sample movement.

The resulted polystyrene particle profile is a combination of the size distribution of the measured particle and the points spread function (PSF) of the microscope system. To obtain a better approximation of the PSF, the measurements were repeated using smaller (100 nm) particles. Besides the challenge to localize such particle on the surface of CaF<sub>2</sub> and to discriminate between single particle and conglomerate of two or three particles, the main problem was that the Raman signal from a single particle was too weak to be detected. Therefore, we used 250 nm particles to estimate the PSF, Figure 6.6 (A-C). An atomic force microscope was used to additionally confirm the size of the particle, Figure 6.6 (B).

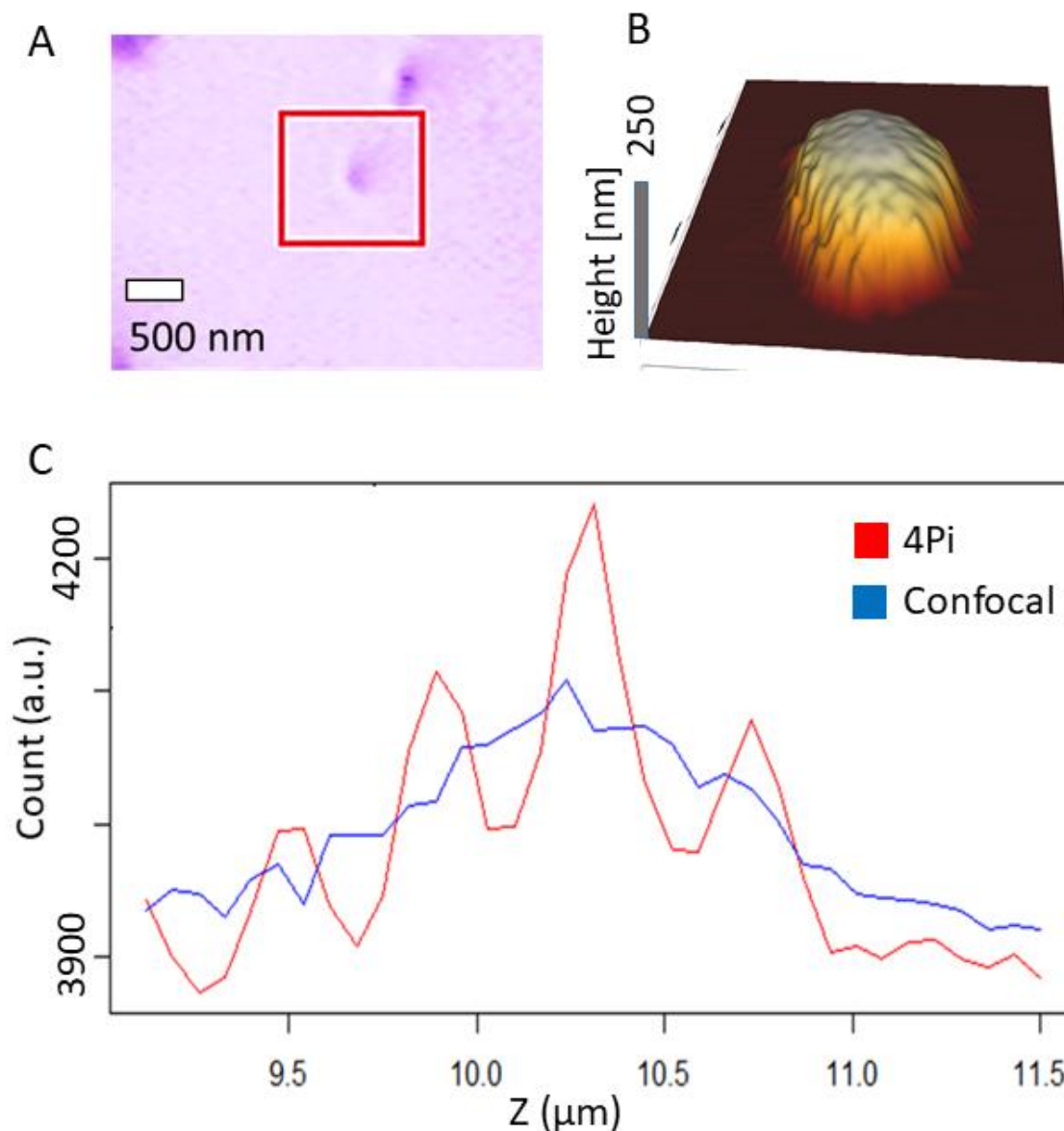


**Figure 6.6.** (A) A light microscopy image of nanoparticles. (B) A 3D image of a nanoparticle obtained using an atomic force microscope. (C) The point spread function (PSF) of 4Pi Raman and confocal microscopy scans (scaled on the Y-axis).

The resulting PSF profiles, shown in Figure 6.5 and Figure 6.6, demonstrate a possibility of an axial resolution improvement in the 4Pi Raman microscopy mode (similar to that in fluorescence microscopy). Nevertheless, to achieve such a resolution improvement, the side lobes must be eliminated or suppressed from the PSF profiles. This can be done digitally and by improving the hardware part of the microscope and interferometer.

## 6.3 APPLICATION OF 4Pi RAMAN AND AFM FOR ANALYSIS OF INTRACELLULAR BACTERIA

### 6.3.1 Introduction

Next, we have tested the 4Pi Raman microscope capability to image mammalian cells. In this regard, it was shown that a cell could significantly influence the beam phase<sup>203</sup>. Therefore, imaging of mammalian cells with a 4Pi Raman microscope was expected to be a challenging task, because of difficulties to obtain a stable interference between the two laser beams caused by phase fluctuations. For such an optically highly inhomogeneous object as a cell (with intracellular bacteria), this problem may be particularly essential. On the other hand, such testing provides an opportunity to demonstrate the feasibility of application of 4Pi Raman microscopy for imaging of complex biological samples. Therefore, we have chosen two types of cells for 4Pi Raman microscopy (axial imaging): HeLa cells - a well-established model of research in cell biology, and monkey lung cells infected with *Chlamydia psittaci* (*C. psittaci*), which is a Gram-negative bacterium. Similarly to other *Chlamydia* species, *C. psittaci* is an obligate intracellular parasite. It cannot grow and reproduce outside of the host cell. After *C. psittaci* is taken inside the cell, it forms inclusions in the cellular membrane<sup>204</sup>. Inside the inclusion, *C. psittaci* replicates, taking the nutrients from the host cell, while avoiding the destruction of its membrane compartment by lysosomes. The exact mechanism of how *Chlamydia* escapes the intercellular defense mechanism is not fully understood<sup>205</sup>. Upon finishing the development cycle, *C. psittaci* leaves the host cell and infects the neighboring cells, repeating the cycle<sup>206</sup>, Figure 6.7. More detailed overview of *Chlamydia* life cycle in the light of host cell membrane interaction can be found in Supplementary Information for Chapter 6 (Appendix), Figures S6.2.

*C. psittaci* proliferates inside the avian species and therefore represents a significant economic risk to the poultry industry<sup>207</sup>. More important, it can also infect humans via zoonosis causing so-called "parrot fever", which is atypical pneumonia with a broad range of symptoms such as difficulty breathing and nonproductive cough, high fever, low pulse, chills, and headache<sup>208</sup>. Because of its relatively small size (from 0.3 to 1 micrometer, depending on the stage of the life cycle) and significant importance to industry and healthcare, *C. psittaci* constitutes an exciting but challenging subject to study, where it is difficult to obtain information about intercellular organisms *in vivo* without destroying the host cell<sup>209</sup>. This problem can be solved

with Raman microscopy, since it allows obtaining information about the metabolic state of intercellular bacteria in a label-free and non-destructive way.

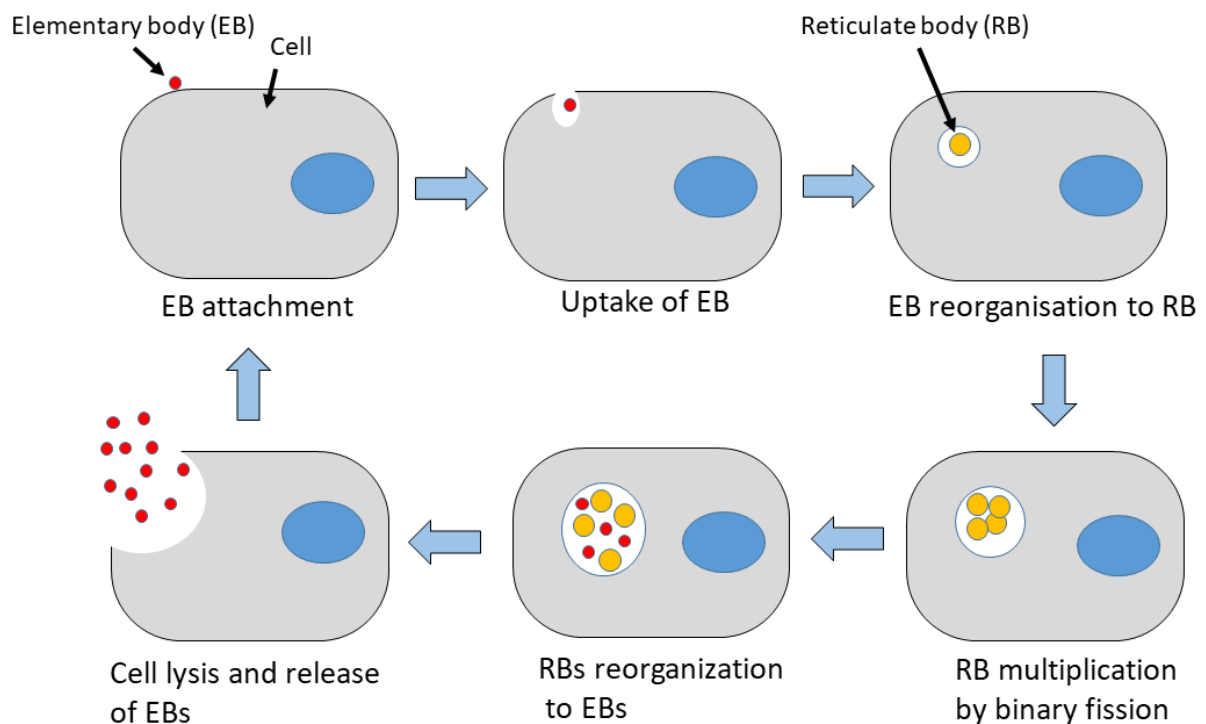


**Figure 6.7.** Life cycle of *Chlamydia psittaci*. Elementary body (EB) of *C. psittaci* is taken inside the cell. It forms the inclusion inside the cellular membrane. Next, EB transition into reticulate body (RB) inside the inclusion. RB is a metabolically active form of *C. psittaci* which is capable to multiply through binary fission. After several multiplications, RBs reorganize back into EBs and leave the cell to repeat the cycle (a comprehensive schematics is shown in Supplementary Information for Chapter 6 (Appendix), Figure S6.2).

An increased axial resolution of 4Pi Raman microscopy would be thus a very desired feature to precisely localize bacteria inside cells. In addition, this would allow for a more accurate discrimination of spectral information coming from bacteria and from surrounding cellular cytoplasm.

Another high-resolution technique applied in this study is atomic force microscopy (AFM). It allows imaging and characterizing cells infected with *C. psittaci* in a label-free and non-destructive way. In this case, the surface is scanned with a sharp tip attached to the cantilever. Upon approaching the surface, the cantilever bends due to the interaction of the tip with it. By measuring the cantilever deformation, it is possible to reconstruct the topography and

even measure mechanical properties of samples <sup>210</sup>. However, in contrast to Raman microscopy, this technique permits imaging only the surface of cells. Therefore, AFM would be an attractive complementary to 4Pi Raman microscopy technique for characterization of the surfaces. We aimed thus to implement the multimodal microscopy approach to study *Chlamydia* infected cells using both 4Pi Raman microscopy and AFM, Figure 6.8.

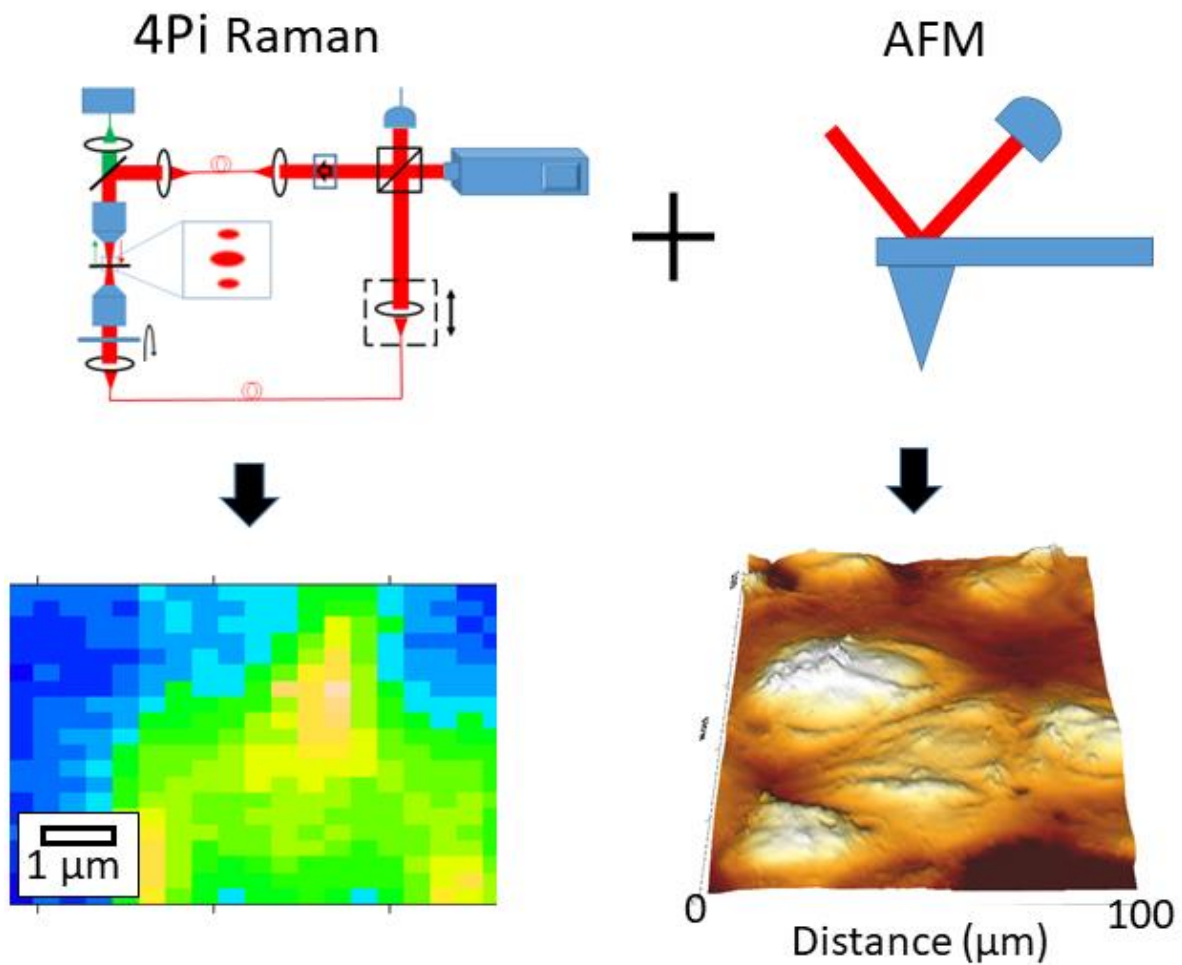


**Figure 6.8.** Schematic setup of experiments conducted in multimodal microscopy approach combining Raman microscopy and AFM. 4Pi Raman microscopy is used therein to characterize cells infected with *C. psittaci*, while AFM is used to scan the surface of infected cells.

### 6.3.2 Materials and methods

To scan biological samples with 4Pi Raman microscopy, we have designed custom-made Petri dishes, where a part of the bottom surface was substituted with an ultrathin (0.1  $\mu\text{m}$  thick)  $\text{CaF}_2$  slide. Bringing  $\text{CaF}_2$  slide is necessary to avoid additional background from silica glass or plastic if 785 nm laser is used. And such a laser allows avoiding the autofluorescence from biological samples, while still providing a relatively strong Raman signal. However, it scatters strongly on glass and plastic. This represents a particular problem in our case of 4Pi Raman microscopy, because the laser from the bottom arm must go through the Petri dish before reaching the sample. Therefore, substituting plastic with  $\text{CaF}_2$  slide grants the possibility to obtain spectra of cell adhered to the bottom. The low thickness of the  $\text{CaF}_2$  slide allows minimizing the effect of the substrate on the phase of propagating beams.

Experiments were conducted using HeLa and Buffalo Green Monkey (BGM) cells, which were cultured with DMEM (Lonza, catalog number: 12-604F) supplemented with 10 % FBS (ThermoFisher, catalog number: 10500-064) and 1 % PenStrep (Lonza, cat no DE17-602E) and seeded upon the custom-made Petri dish (with  $\text{CaF}_2$  slide) and incubated for 24 hours at 37 °C and 5%  $\text{CO}_2$ . BFM cells were cultured using the Eagle's minimal essential medium (MEM) supplemented with 10 % heat-inactivated fetal bovine serum (Greiner Bio-one, Vilvoorde, Belgium), 1 % L-glutamine (Gibco®, Merelbeke, Belgium), 1 % vitamins (Gibco®), 2 % vancomycin (Sandoz®, Vilvoorde, Belgium) and 1 % streptomycin sulfate (Gibco®). The virulent *C. psittaci* strain 92/1293 (ompA genotype D), isolated from diseased turkey broilers on a turkey farm in the Netherlands, was used to inoculate the BGM cells as described by Vanrompay *et al.*<sup>211</sup> Briefly, BGM cells were seeded into a custom-made Petri dish with  $\text{CaF}_2$  bottom and incubated until they formed a monolayer. After 24 hours, the culture medium was removed, and 75  $\mu\text{L}$  of the bacterial inoculum was added to the cells, followed by adding a complete *C. psittaci* culture medium (CCKM). The inoculated cells were incubated for 3 days at 37 °C and 5%  $\text{CO}_2$ . After incubation, the complete culture medium was removed, and cells were washed with sterile PBS and fixed for 10 minutes with 4 % formaldehyde. Next, formaldehyde was removed, and cells were kept in PBS at 4 °C until further analysis with AFM and 4Pi Raman microscopes.

Topographical AFM images were acquired using a Nanowizard 4™ BioAFM (Bruker/JPK Instruments) in the JPK Quantitative imaging (QI®) mode using ATEC-CONT cantilevers. These

sharp-tip cantilevers (the radius of the curvature  $< 10$  nm) have an increased tip height ( $15 \mu\text{m}$ ) to avoid contact of the cantilever beam and the cells during imaging. JPK QI™ (or quantitative imaging) mode is a unique alternative to acoustic (AC) mode AFM also known as the tapping mode AFM. This mode represents a combination of the contact mode AFM and AC mode. For each pixel, a force curve is acquired, thus allowing to gather high-resolution images without having the lateral drag often observed in the contact mode, and contrary to tapping mode, the vertical force exerted upon the sample can be controlled, which allows for much richer data analysis.

In addition to AFM, cells were also scanned using 4Pi Raman microscopy. The 4Pi Raman spectra were recorded on the microscope setup described in the first part of the chapter. The only difference was that instead of the  $100\times/0.95$  NA (Zeiss) objective in the top arm, a  $63\times/1.0$  NA (Zeiss) water immersive objective was used. The cytoplasmic part of the BGM cell with *C. psittaci* and the cytoplasmic part of the HeLa cell with lipid droplet were selected for analysis with 4Pi Raman, Figure 6.9 (A). The 4Pi measurements were made using a similar pipeline as for polystyrene nanoparticle profiling - each point in the area of interest was measured four times, and the Raman scattering intensity was interpolated. The distance between the points was  $0.2 \mu\text{m}$  on both axes. Integration time and laser power were 10 seconds and 35 mW, respectively. The resulting 4Pi datasets were used to construct molecular images. Molecular images were constructed based on the intensity of the following peaks: the peak at  $1004 \text{ cm}^{-1}$  is associated with proteins, the peaks at  $1453 \text{ cm}^{-1}$  and  $1662 \text{ cm}^{-1}$  are associated with lipids, Figure 6.9 (B). The pseudo-color was assigned to each pixel based on the calculated Raman scattering intensity of the peaks at this point. Next, hierarchical clustering analysis of 4Pi dataset was used to calculate average Raman spectra of *C. psittaci* inside BGM cell and lipid droplet inside HeLa cell, Figure 6.9 (C).



### 6.3.3 Molecular imaging with 4Pi Raman microscopy

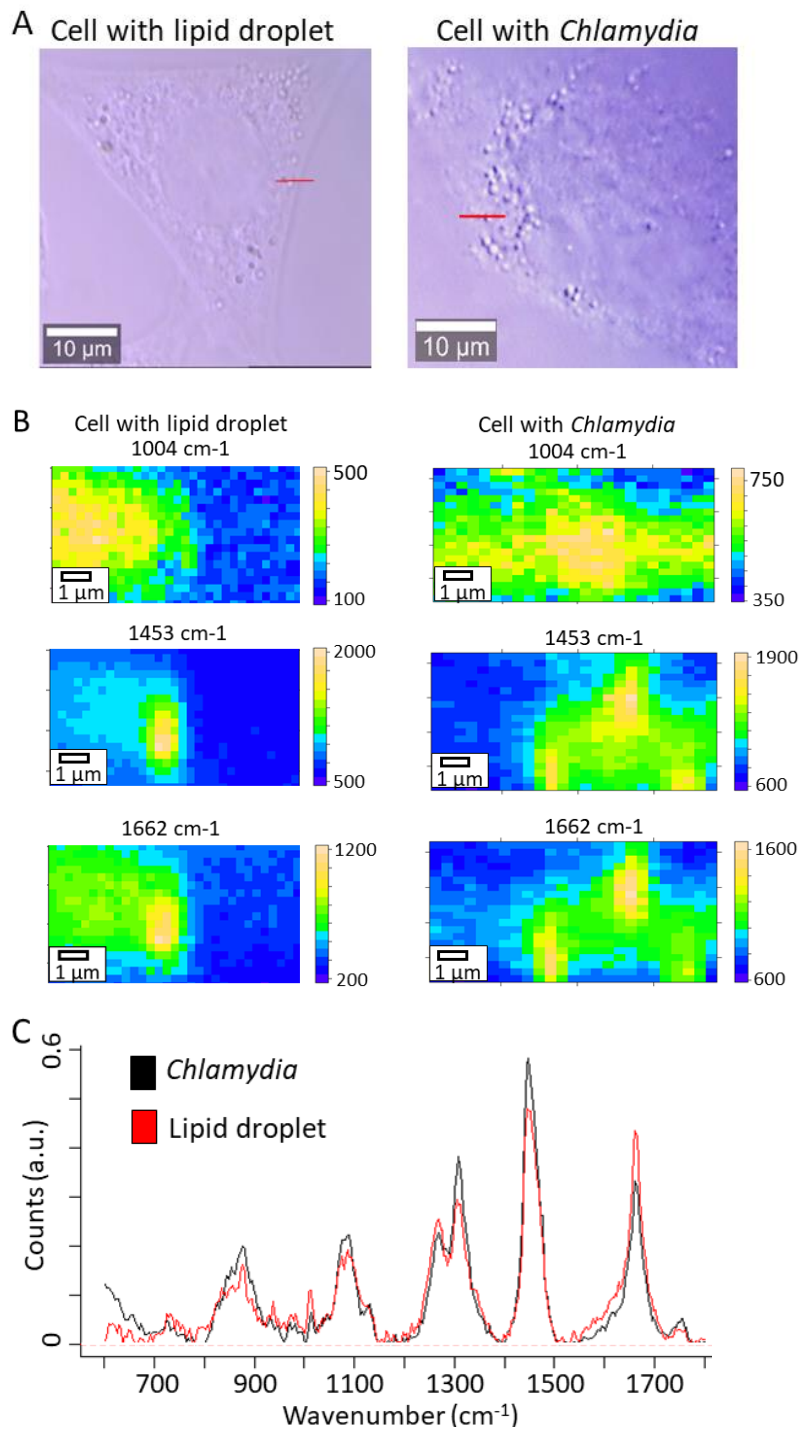


**Figure 6.9.** (A) (Left) Optical microscopy image of HeLa cell with lipid droplets. Cytoplasmic cellular parts along the red line were analyzed with a Raman microscope. (Right) Optical microscopy images of a Buffalo Green Monkey (BGM) cell infected with *C. psittaci*. (B) The resulting heatmaps obtained from intensities of  $1004 \text{ cm}^{-1}$ ,  $1453 \text{ cm}^{-1}$  and  $1662 \text{ cm}^{-1}$  peaks. (C) The average Raman spectra of *C. psittaci* and lipid droplet inside the cell. Colors in molecular images correspond to counts in arbitrary units.

The presented setup allowed us to obtain a stable beam interference during axial molecular imaging despite the phase changes induced by cellular substructures. The resulted dataset was used to generate 4Pi Raman molecular images of lipid droplets in the cytoplasm of HeLa cell and *C. psittaci* inside the BGM cell, Figure 6.9. However, it took over 10 hours to generate a single molecular image. Such a long time acquisition is due to multiple image recordings (four times) with a different phase configuration; additionally, it required at least 10 seconds to change and stabilize the phase configuration before each of those four measurements. The main challenges to work with living cells and bacteria are substantially long scanning times. In experiments, it was not possible to detect an increase of the axial resolution in axial 4Pi Raman microscopy images. In contrast, an increase in axial resolution in fluorescence 4Pi microscopy has been achieved by deconvolution, i.e. by removing (digitally) the secondary lobes from the PSF of each pixel.

In the case of 4Pi Raman microscopy, if developing the deconvolution algorithms for 4Pi Raman microscopy is pursued, then, the following factors should be taken into consideration.

1. During the axial imaging, it was found that all molecules influence the Raman signal intensity of every pixel along the laser pathway both in the confocal and 4Pi mode. If the molecule produces an intense Raman signal, a strong Raman signal from this molecule would be detected even when it is present outside of the actual confocal volume. This effect is illustrated in Figure 6.10.
2. In fluorescent microscopy, the signal is originated only from isolated points where the fluorescent labels are present. In contrast, in Raman microscopy, it is more challenging to distinguish the pixels, because every point inside the cell can produce similar Raman scattering signals. This is particularly relevant for the C-H molecular vibrations, which are omnipresent in cells. It is also essential to note that a Raman peak in organic samples can be a sum of scattering signals originated from different molecules possessing similar molecular vibrations <sup>212</sup>.

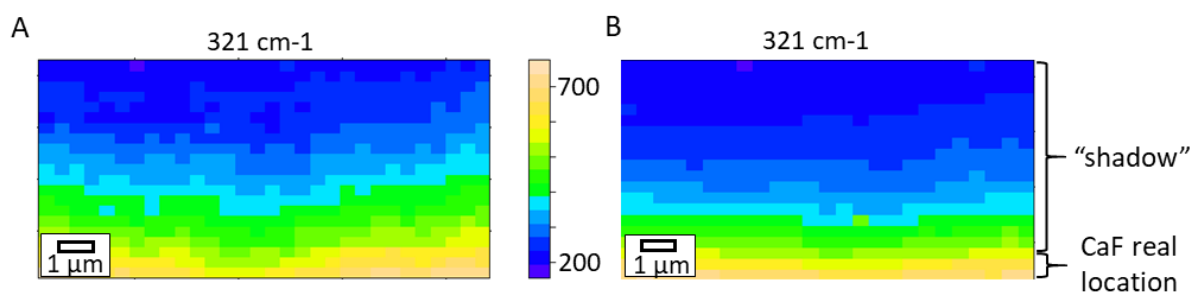


**Figure 6.10.** The heat maps constructed based on the  $321\text{ cm}^{-1}$  peak is assigned to  $\text{CaF}_2$ . Both heatmaps obtained with (A) confocal and (B) 4Pi Raman microscopes show the presence of the shadow effect when the signal originating from the  $\text{CaF}_2$  peak is visible, while focusing the microscope at a location of  $6\text{ }\mu\text{m}$  above the physical location of the  $\text{CaF}_2$  slide casts a "shadow" on the image. Colors in molecular images correspond to counts in arbitrary units.

The fact that different molecules have different signal intensities, but the same overlapping peaks, makes the deconvolution of 4Pi Raman microscopy data a challenging and interesting topic for further research.

### 6.3.4 Analysis of Raman scattering data

The hierarchical clustering analysis was used to obtain molecular fingerprints of *C. psittaci*, localize its position inside a BGM cell and separate the data points corresponding to *C. psittaci* from the cellular cytoplasm. The average spectrum was calculated for each resulting cluster, Figure 6.11 (A). Next, the intensities of the following peaks:  $1004\text{ cm}^{-1}$ ,  $1453\text{ cm}^{-1}$  and  $1662\text{ cm}^{-1}$  were compared between the *C. psittaci* and the BGM cytoplasm. The intensity value of the  $1004\text{ cm}^{-1}$  peak was similar for both *C. psittaci* and its surrounding cellular cytoplasm. The  $1453\text{ cm}^{-1}$  and  $1662\text{ cm}^{-1}$  peaks were found to be more intense in *C. psittaci* spectra by  $\approx 47\%$  and  $\approx 24\%$ , Figure 6.11 (B).

The  $1453\text{ cm}^{-1}$  and  $1662\text{ cm}^{-1}$  peaks can be used as markers to localize *C. psittaci* inside of the host cell. It is essential to mention that higher peak intensities in *C. psittaci* spectra versus the those in spectra of the host cell cytoplasm were previously reported<sup>209</sup>. In that study, a higher intensity was observed for all peaks, including the  $1004\text{ cm}^{-1}$  protein peak. However, it was suggested that such differences in intensities were the result of a cellular deformation caused, for example, by sample preparation. Using data analysis, we have also observed an increase

in intensity of Raman scattering peaks associated with *C. psittaci*. Nevertheless, the number of peaks there, including the 1004  $\text{cm}^{-1}$  protein peak, had similar scattering intensity in both *C. psittaci* and the host cell cytoplasm. This prompts to suggest that a deformation of the sample did not cause the difference in intensity of the observed lipid peaks.

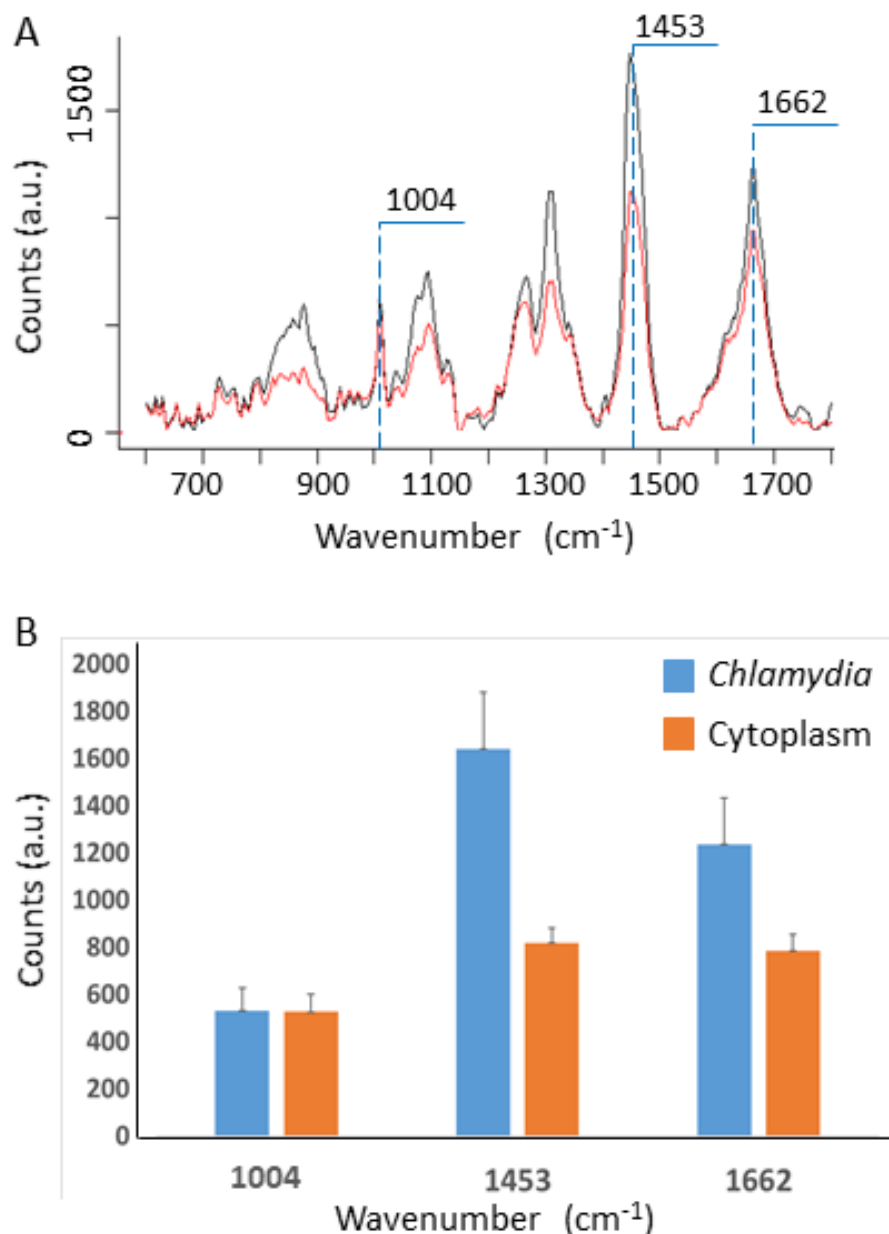


**Figure 6.11.** Analysis of 4Pi Raman microscopy data. (A) The average spectra of data points assigned to *C. psittaci* (the black curve) and to the host cell cytoplasm (the red curve). (B) A comparison of 1004  $\text{cm}^{-1}$ , 1453  $\text{cm}^{-1}$  and 1662  $\text{cm}^{-1}$  peak intensities in the cytoplasm of the host cell and *C. psittaci*. Each column is calculated based on the spectral points allocated to the cytoplasm (221 datapoints) or *Chlamydia* (26 datapoints) by the hierarchical clustering analysis. Error bars represent the standard deviation between the data points.

A strong Raman scattering signal can be explained by the fact that a dense lipid membrane may cover *C. psittaci* or that bacteria change the lipid composition and/or density of cellular membrane inclusion. Those changes may be utilized by *C. psittaci* to protect it from the host cellular defense mechanisms.

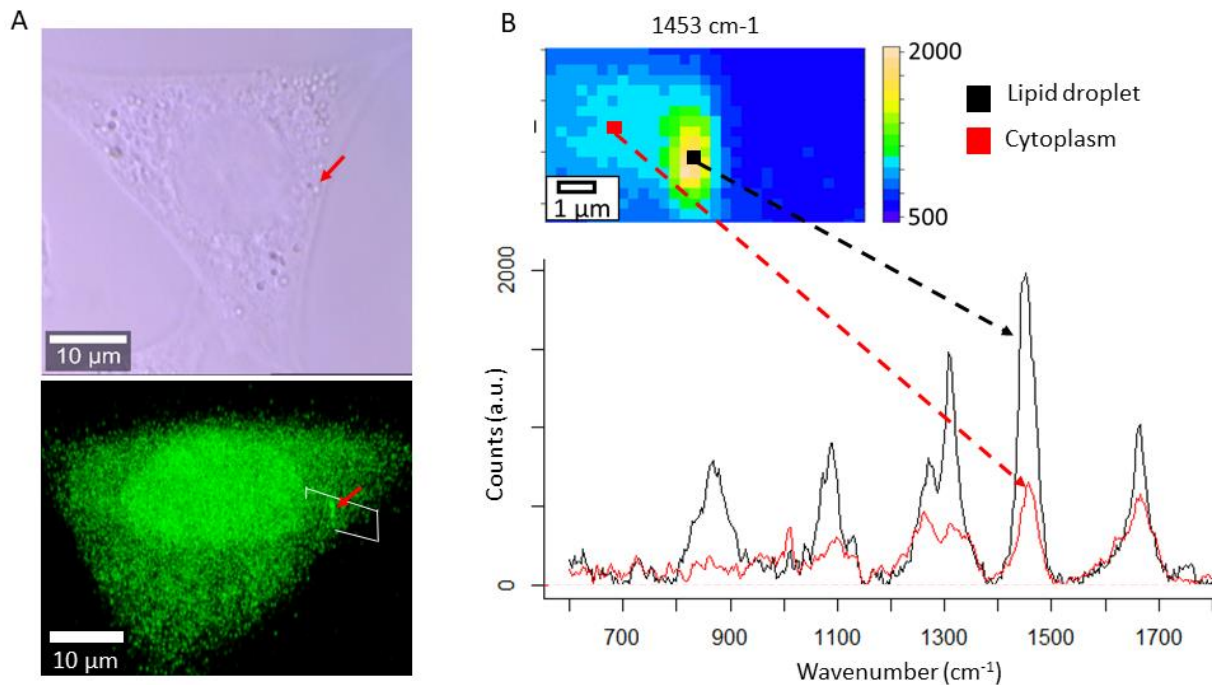


**Figure 6.12.** (A) Transmission and fluorescent microscopy images of the same cell showing lipid droplets inside a HeLa cell. The scanned lipid droplet is marked with the red arrow (top). The area scanned with 4Pi Raman microscopy is marked with the rectangle (bottom). (B) Raman scattering spectra of the lipid droplet and cytoplasm. On the heatmap (insert), the red and black dots point to locations, from which the cytoplasm and lipid droplet spectra were taken. Colors in molecular images correspond to counts in arbitrary units.

We have noticed a similar significant increase in the intensity of the lipid peaks in spectra of a lipid droplet of the HeLa cell, which was measured to test the 4Pi microscopy system, Figure 6.12. A lipid droplet is a subcellular structure composed of densely packed lipids. That is why the presence of intense lipid peaks is expected – and the measured spectra of lipid droplets were similar to lipid droplet molecular fingerprints reported in literature<sup>213 214</sup>.

To obtain more information about the *C. psittaci* lipid envelope, we have compared its spectrum with that of a lipid droplet. A comparison of the lipid droplet spectrum with the spectrum of the surrounding cytoplasm showed that 1453 cm<sup>-1</sup> and 1662 cm<sup>-1</sup> peaks are more intense in the lipid droplet spectrum, similar to what was observed in BGM cell infected with

*C. psittaci*. However, the intensity of the 1004 cm<sup>-1</sup> peak was found to be higher in the lipid droplet compared to that in the *C. psittaci* spectrum. The presence of the intense 1004 cm<sup>-1</sup> peak was expected in lipid droplet molecular fingerprint because it is known that lipid droplet is covered with proteins. These proteins are essential for cellular lipid metabolism regulation. The low 1004 cm<sup>-1</sup> peak intensity in *C. psittaci* may be explained by the lower concentration of proteins in the bacterial outer membrane or inclusion wall compared to the amount of lipids. The ratio of 1662 cm<sup>-1</sup> and 1453 cm<sup>-1</sup> peaks ( $I_{1662}/I_{1453}$ ) can be used to estimate the lipid unsaturation level<sup>214 215</sup>. We have obtained the ratio value of 0.87 for the lipid droplet. However, for *C. psittaci*, it was only 0.53, suggesting that the *C. psittaci* membrane contains fewer unsaturated lipids than the lipid droplet.

It was established in previous studies that lipid droplets are accumulated on the surface and inside the inclusion of *Chlamydia* and it may be a part of the host defense mechanism<sup>216</sup>. But to the best of our knowledge, the study of lipid droplet interaction with *Chlamydia* were only done using *C. trichomonas*, and no research was done on *C. psittaci*<sup>217</sup>. Our finding shows that *C. psittaci* may also accumulate host lipid droplets like *C. trichomonas*. Previous work reported the presence of lipid droplets at the surface or inside of inclusion bodies of *C. trichomonas* as early as 18 hours after the inoculation<sup>216</sup>. However, in our case, *C. psittaci* reticular body spectrum shows the presence of high-density lipids similar to what is found in a lipid droplet in 8 hours after the inoculation. This suggests that the interaction of *C. psittaci* with the host cell lipid droplets may have started at earlier stages of infection, and such interaction may be a part of early mechanism of host defenses evasion. A decrease of intensity of the 1004 cm<sup>-1</sup> peak suggests that the protein part of lipid droplets is modified by *C. psittaci*. The changes in the lipid saturation level hint that *C. psittaci* similar to *C. trichomonas* may use host lipid fatty acids for synthesis of its membrane constituents<sup>218</sup>.

### **6.3.5 AFM topographical imaging**

The lipid-associated peaks on *C. psittaci* molecular fingerprints are 2-3 times more intense than the peaks from the cellular cytoplasm – this makes imaging of the cellular surface with Raman microscopy challenging. To solve this problem, AFM was used as a complementary tool, because it allows obtaining high-resolution topographical images of the cellular membrane. Similar to Raman microscopy, AFM is a label free and non-destructive imaging

technique, where a tip is used for scanning the surface of a sample. Using AFM, we aimed to find morphological surface irregularities in the *C. psittaci* infected cells in comparison to control cells (without *C. psittaci*). The AFM images revealed the presence of the holes/deep cavities in the cellular membrane of the infected cells. Such holes were absent in the control cells, but they were found on infected cells surface, Figure 6.13.

The presence of bacteria inside every cell in the scanned samples was confirmed by both optical and Raman microscopy. We were not able to provide the direct evidence that bacteria were present in the holes using Raman and/or transmission microscopy, because those holes were invisible on normal microscopic images. However, these holes were present only in infected cells and were not observed in any of the control images (Supplementary Information for Chapter 6 (Appendix), Figure S6.3 and Figure S6.4). This strongly suggests a link between bacteria and the holes observed in the membranes.

The observed holes varied in size (diameter) from 0.5  $\mu\text{m}$  to 10  $\mu\text{m}$ , and in depth from 500 nm up to 5  $\mu\text{m}$ . These cavities can be associated with the location, where *C. psittaci* had entered cells. However, the sizes of the holes can be up to 10 times bigger than those associated with an individual *Chlamydia*. An alternative explanation is that the cavities are the result of the cytoplasmic inclusion formation. The holes in the plasma membrane of infected cells were detected both at early (8 hours after inoculation) and late (36 hours) stages of the infection (Supplementary Information for Chapter 6 (Appendix), Figure S6.3 and Figure S6.4). The secondary infection can explain this observation potentially being due to not properly carried out washing away procedure after the inoculation. However, this also raises questions about the speed of the cellular membrane re-sealing, the holes caused by the *C. psittaci* cellular entry, and the duration of the bacteria exposure to the intercellular media after infecting the cell. Such information may be beneficial for a better understanding of the bacteria interaction with the cell and anti-*Chlamydia* drug development. Therefore, it is anticipated that the proposed multimodal method of using the Raman microscopy (to detect infected cells) in a combination with AFM (to obtain surface topography of such cells) will be promising for such applications.

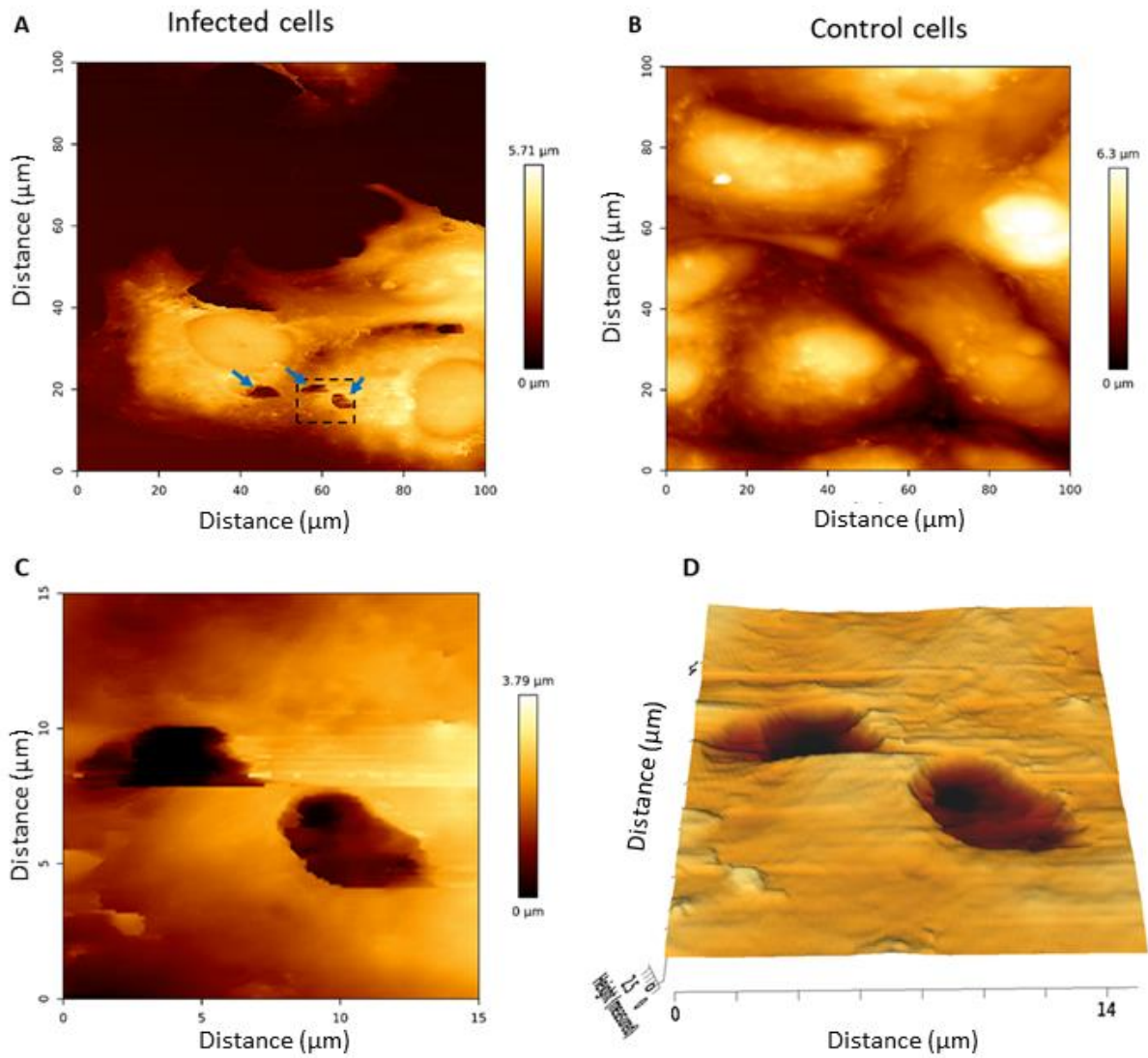


**Figure 6.13.** AFM images of the plasma membrane of BGM cells. (A) Topography image of the surface of cells infected with *C. psittaci*. Holes in the plasma membrane are marked with blue arrows. (B) Topographic image of the surface of control non-infected cells. (C) A high-resolution image of the holes in the plasma membrane of the infected cell. (D) 3D reconstruction based on data presented in the panel (C).



## 6.4 CONCLUSION

In this chapter, we have described the 4Pi Raman setup and have shown how the system can be characterized using well-defined polystyrene nanoparticles. To change the interference between beams, we have used the reflection of one laser beam to stabilize the interference pattern of coherent laser beams at the sample plane and modify the phase relationship between the beams. Next, we have applied 4Pi Raman microscope in a combination with atomic force microscopy to image *C. psittaci* inside Buffalo Green Monkey cells.

The resulting datasets are used to obtain molecular images generated in the form of a two-dimensional (2D) map based on the distribution of the molecules in the sample. The axial profiling of polystyrene nanoparticle showed the possibility of axial resolution improvement, like in 4Pi fluorescence microscopy. However, for high-resolution imaging of biological samples, such as cells and bacteria, the novel deconvolution algorithms must be developed. The analysis of *C. psittaci* associated data points on the resulting non-deconvoluted 4Pi Raman microscopic images revealed the presence of densely packed lipids inside the membrane inclusion, similar to what was observed in intercellular lipid droplets, but with a lower ratio of saturated to unsaturated lipids. The presence of intense lipid-associated peaks in *C. psittaci* molecular fingerprint can be used as a marker for bacteria localization inside the cell. The high-resolution topographic imaging of *C. psittaci* infected cells surface with AFM revealed the presence of irregularly shaped cavities on the cell membrane. Such cavities were absent in non-infection cells. Complementarity of 4Pi Raman microscopy and AFM proved to be a practical approach for the analysis of *C. psittaci* infection. AFM was used to get the topographic image of the cellular surface. It offers the advantage of detecting irregularities, such as pores on the cellular surface. A pore has low contrast and is difficult to detect with light microscopy techniques. AFM, however, can correctly pick up these surface irregularities and therefore has a unique application in this research. But it was not possible to evaluate if the scanned cell was infected with *C. psittaci*. On the other hand, Raman microscopy provided the possibility to localize *C. psittaci* inside cells and to obtain information about the chemical composition, but not cell topography. Therefore, a combination of those two techniques, AFM and Raman microscopy, provided information not accessible if they are used separately. A multimodal approach of Raman microscopy with AFM can also be of interest for the analysis of drug effects on bacteria inside the cell.



# Chapter 7

General discussion, conclusions, and perspectives

# 7 General discussion, conclusions and perspectives

## 7.1. GENERAL DISCUSSION

In this dissertation, complementarity of Raman microscopy is investigated in a combination with other techniques in the context of multimode imaging. Protocols for measurements of biological and medical samples with a Raman microscope and other multimodal imaging approaches are developed and discussed.

General introduction as well as recent developments in Raman microscopy and multimode microscopic biological and macroscopic medical techniques are presented in **Chapter 1**.

The study of mTBI effect on brains of rats, presented in **Chapter 2**, allowed evaluating perspectives of using a combination of Raman microscopy with MRI to study brain tissue damage. The results and future perspectives of this study must be discussed from several different angles. First, we discuss the obtained results and then evaluate perspectives of complimentary use of Raman and MRI for tissue analysis.

The primary motivation for using Raman microscopy for brain tissue analysis is to understand the nature of pathological changes caused by mTBI. The study of brain tissue slices with Raman microscopy revealed a decrease in the ratio of axon proteins to myeloid lipids in the corpus callosum region after mTBI. Raman microscopy generated molecular images showing structural and molecular abnormality inside the corpus callosum region, which is presumably the result of micro-bleeding caused by mTBI. Micro-hemorrhages are common in mTBI<sup>81</sup>. However, blood was found in the corpus callosum area only in one animal. This can be assigned to very thin slices resulting in washing out of blood or to the fact that micro-hemorrhages in mTBI are present only in a limited number of cases<sup>219</sup>. A logical continuation of this research would be to investigate whether changes in the ratios of Raman scattering signal intensities of axon proteins to those of myeloid lipids are influenced by an axon degradation or by an increasing number of myeloid lipids. Recently, a possibility to detect changes in a brain after mTBI was demonstrated using a diffusion tensor MRI approach<sup>220</sup>, where it was found that mTBI causes axon degradation in the corpus callosum. However, even

an advanced form of MRI, used in that study, required histological analysis of brain slices to understand and interpret the diffusion tensor MRI data. Raman microscopy can be particularly attractive for such analysis. And, after scanning with Raman microscopy, brain slices can be subjected to further investigation. For example, axon proteins can be quantified by conventional western blotting<sup>221</sup> or reverse transcription polymerase chain reaction (RT-PCR)<sup>222</sup>. Alternatively, coherent Raman scattering techniques can be used since they were shown to be applicable to neuroscience<sup>223</sup>. Due to high acquisition speeds of recent CARS microscopes<sup>224</sup>, it would be possible to scan a larger number of tissue slices in a shorter time period compared to what is possible with a conventional Raman microscope.

Addition of Raman microscopy for investigation of the brain tissue of rats provides the means of detecting changes in the corpus callosum area, which are otherwise invisible by a conventional MRI. It can be pointed out, however, that the main disadvantage of the used protocol of tissue analysis with Raman microscopy is the need to cut an organ into thin slices to perform such a study. Therefore, this procedure is destructive for organs and cannot be used *in vivo*. However, it does not mean that tissue analysis with Raman is limited to pure laboratory research on animals, because it may be applied in clinics, in post-mortem pathological anatomy studies, or for analysis of biopsy of patients. In this regard, it is important to mention that Raman spectroscopy is nondestructive for tissue slices. After scanning, slices or identified areas can be subjected to further analysis, such as genomic and proteomic sequencing or immunostaining. The main advantage of the used protocol of sample preparation is that it does not contaminate the samples with chemicals, such as paraffin, which may affect Raman scattering measurements. The negative effect of tissue degradation on the quality of molecular images may be solved by embedding samples in a low-density agar layer. Alternatively, a tissue slice can be covered with an ultra-thin CaF<sub>2</sub> slide.

One of the main challenges of tissue analysis with conventional Raman microscopy is that scanning even a single slice is time-consuming. This potential problem may be overcome:

- 1) if analyzed molecules are omnipresent in tissue. Then, scanning any part of the tissue with Raman microscopy would produce desired information; or
- 2) if preliminary information about spatial location of molecules or areas is available. In this case, a combination of Raman microscopy with MRI is particularly attractive for

brain analysis: MRI would facilitate identification of abnormal areas of the brain *in vivo*, which can be then scanned with Raman microscopy.

However, if analyzed molecules are present only in a small area of investigated tissue and no information about the position of this area is known, then identification of such area with Raman microscopy may be extremely challenging, partially due to long scanning times. For example, analysis of the surface of a single brain tissue slice of a rat can take more than 10 hours. And hundreds of such slices must be scanned to image the whole brain or other organs. Progress in this area can be enabled by developments in the area of Raman microscopy based on improvements in software, sensors, and mechanical components. Then, scanning of multiple slices can be effectively performed to generate a detailed 3D image of the whole organ. Such whole organ Raman 3D molecular images are seen to be of great interest in pathological anatomy and life science fields.

After analysing samples at the tissue level (**Chapter 2**), a multimodal approach was applied for sample investigation at the cellular level, where a combination of Raman and fluorescence microscopy was used to localize bovine lactoferrin inside cells (**Chapter 3**). In this study, each Raman spectrum was obtained from an area of around 1.0  $\mu\text{m}$  in diameter, which is close to the resolution limit for a 785 nm laser (using an objective with NA 1.0). Nevertheless, that allowed investigating localization of molecules inside cells and bacteria.

It was found in our studies that bovine lactoferrin molecules translocate to the nuclei of calf rectal epithelial cells. This is a particularly interesting finding, because one of the main roles of secreted forms of lactoferrin and other transferrin molecules is to transport iron to cells from the surrounding medium. After iron delivery, lactoferrin is either degraded in endosomes or released from cells for the next cycle of iron transport. It can be noted that the process of iron delivery, lactoferrin recycling, and degradation occurs in the cytoplasm. Therefore, secreted isoforms of lactoferrin are not typically known to be capable to translocate to the nuclei of cells.

It was also found that the presence of EHEC significantly increases bovine lactoferrin cellular uptake from the growth medium and subsequent translocation to the nuclei of cells. An interesting continuation of this study would be to determine if the bovine lactoferrin translocation is a part of the innate immune response of calf epithelial cells triggered by EHEC.

This can be investigated by repeating experiments with different types of bacterial and viral pathogens. Additionally, it would be interesting to study the effect of bovine lactoferrin translocation on gene expression. This can be done by ribonuclease (RNA) extraction, deoxynucleic (DNA) synthesis and subsequent sequencing.

Conventional fluorescent microscopy proved to be a complementary tool for Raman microscopy. Indeed, application of fluorescent labels significantly simplified identification of the Raman scattering molecular fingerprint of bovine lactoferrin inside cells. However, care must be taken to control that the corresponding molecular fingerprint is originated from the investigated molecule, and not from fluorescent labels or other molecules. Raman microscopy enables identification and intracellular localization of molecules without fluorescent labels, but fluorescent microscopy can be advantageous in comparison to Raman microscopy if:

- 1) localization of specific molecules is desired in a large sample or cell;
- 2) fluorescent labeling of such molecules is technically possible;
- 3) photobleaching would not affect image acquisition.

Fluorescent microscopy allowed imaging of multiple (hundreds) cells in 20 minutes, while it takes approximately 20 minutes to scan a single cell with Raman microscopy. Also, Raman data analysis often requires extensive post-processing and data mining to extract desired information.

Raman microscopy has an essential advantage over conventional fluorescent microscopy by contributing to establishment of molecular compositions of materials and biological objects. Such a situation is discussed in **Chapter 4**. There, the goal was to determine the molecular structure of conductive fibers inside cable bacteria. In such case, it was not possible to use fluorescent labels to localize the fibers inside intact cable bacteria. However, the general location of fibers was known from electron microscopy images of fiber sheaths. Analysis of Raman molecular images of cable bacteria cross-sections revealed the presence of intense peaks at  $371\text{ cm}^{-1}$  and  $492\text{ cm}^{-1}$  in the spectra of the area, where the fibers are expected to be located. Raman microscopy measurements of the chemically extracted fibers allowed to confirm that  $371\text{ cm}^{-1}$  and  $492\text{ cm}^{-1}$  peaks originate from the fibers. The presence of these two peaks revealed that nickel is a part of the fiber structure. This finding was confirmed by subsequent X-ray and mass spectrometry analysis using Nano-SIMS, LEXRF, and STEM-EDX.

Studies described in **Chapter 2** and **Chapter 4** have shown that Raman microscopy is an attractive tool for life science applications under conditions, where information about the nature of molecular changes in samples or molecular structure of investigated molecules is limited. In such cases, Raman microscopy provides the means to obtain general information about the sample, which can be used as a starting point for further investigation using multimodal microscopy approaches.

It is essential to note that in both bLF (**Chapter 3**) and conductive bacteria studies (**Chapter 4**), possibilities to obtain reference spectra of molecules outside of the cell was particularly important for intracellular localization of those molecules. Additionally, localization and subsequent analysis of molecules inside cells and bacteria would be challenging at low concentration of the molecule, particularly if molecules do not have distinct molecular fingerprints. The SERS technique can significantly amplify intensity of the Raman scattering signal, and, therefore, such an approach allows measuring molecules at much lower concentrations.

In **Chapter 5**, we have focused on development of SERS platforms based on modified calcium-carbonate particles. The intriguing property of those particles is their multi-functional nature – they were designed to be used both as drug carriers, controlled by a magnetic field, and as SERS sensors. Such SERS sensors can be applied for detecting low concentrations of an analyte in a solution using 100 times less laser power than that required to detect the same concentration with a conventional Raman microscope. However, the high absorbing capability of the particles made SERS quantification of analyte concentration a challenging task. Another potential disadvantage of using such SERS functionalized particles is that the enhancement takes place only near silver nanoparticles. Therefore, in situations with multiple different molecules in a solution, the sensor might be oversaturated by one type of the molecules because they sediment faster or are absorbed better than other molecules in the solution. In such a case, only those molecules would be detected with a Raman microscope. On the other hand, this property can be used as a foundation for Raman microscopy-based molecular separation system, similar to separation columns in chromatography. The magnetic field can be applied to selectively remove particles when the Raman spectrum would confirm absorption of molecules. This can be performed as a continuation of presented research.



The high absorption capability of the calcium carbonate particles was used in developing a specialized drug delivery system that allows controllable drug release *in vivo*. Calcium carbonate particles were used as cores for the synthesis of alginate drug carriers with SERS functionality. We aimed to use SERS not for biosensing but for localizing particles for implementation of a light-induced drug release mechanism. This mechanism is based on the fact that SERS signal enhancement is linked with local temperature increase. Localized temperature increase results in alginate capsule destruction and drug release. Subsequently, the described above SERS drug carrier was successfully tested *in vivo* in *C. elegans* worms. We have demonstrated detection and induction of drug release from an alginate capsule using a Raman microscope. The capsules cannot be used as biosensors inside *C. elegans* worms, because alginate molecules located around silver nanoparticles generate a strong SERS background. This makes the detection of most organic molecules challenging. However, a strong background can be an advantage. We have demonstrated that it can be used for fast particle detection inside a nematode worm. Detection is based on the principle that the Raman signal originates only from the SERS functionalized alginate capsule, while the rest of the measured nematode tissue acts as a “dark” field (does not produce any signal). In such a situation, the detection of a particular peak is not necessary to localize the particle.

The main challenge of applying the presented drug delivery system in humans is that laser radiation must reach particles through the tissue, and then the scattered light must reach a detector. In nematodes, we were able to obtain Raman scattering using 1 mW of laser power with 0.1 second integration time. With longer integration times, the Raman scattering signal may be detected using even lower laser powers. However, the experiment was only done in *C. elegans* worms – small and transparent nematodes. Therefore, an interesting continuation of the research would be to determine whether the presented drug delivery system can be used *in vivo* in larger eukaryotic organisms. It was found that at 10 W, around 2 % or 20 mW of near-infrared light can penetrate 3 cm of tissue<sup>225</sup>. We have shown that 10 mW is sufficient to induce drug release. This suggests a possibility to use alginate capsules for targeted subcutaneous drug delivery.

In addition to developing and extending the range of biological applications, one further goal of this dissertation was to find the means to improve the resolution of a Raman microscope. To achieve this goal, we have developed a 4Pi Raman microscope. We have shown that under

certain conditions, 4Pi Raman microscopy can confirm structure of a coating with thicknesses in the range of around 6 nm<sup>199</sup>. The construction of a 4Pi Raman microscopy setup is described in **Chapter 6**. There, polystyrene nanoparticles were used for characterization of the built 4Pi Raman microscope.

Subsequently, the developed 4Pi Raman microscope was applied to study Buffalo Green Monkey (BGM) cells infected with *C. psittaci*. The results showed that the presented Raman 4Pi system could compensate the phase fluctuations originated from such complex heterogeneous biological samples as BGM cells with intracellular bacteria. It is not possible yet to demonstrate an increase in the axial resolution of 4Pi Raman microscopy images of BGM cells. But this can be partially addressed by scanning with higher numerical aperture objectives and applying dedicated deconvolution algorithms, which facilitate removal of the secondary lobes from the PSF. But such algorithms should take into account the complex nature of Raman molecular images. The main difference with fluorescent microscopy is that in Raman molecular images there is no “dark field,” and every pixel in the image acts as a light source. The presence of a particularly intense peak at some points along the excitation laser pathway may add additional image distortions.

The second essential challenge with Raman 4Pi microscopy was a long measurement time. It took multiple hours to obtain a single axial image from an area of 20 x 25 pixels. Such a long scanning time was the result of low laser powers of the beams (due to coupling losses), and, therefore, 10 seconds (or more) of the integration time per single measurement was needed to resolve all peaks. A more powerful laser and improved hardware may solve or at least alleviate this problem. The main advantage of 4Pi Raman microscopy is a better resolution and an increase in the strength of the measured signal intensity due to better power concentration. Therefore, it is not particularly useful to apply 4Pi Raman microscopy to study tissues, organs, and other relatively large samples without the need for high resolution imaging. However, for samples like cable bacteria, 4Pi Raman microscopy could be particularly interesting since it may facilitate avoiding image artifacts described in **Chapter 4**.

Additionally, we were interested in applying a multimodal approach to study cells using 4Pi Raman in a combination with AFM. The analysis of *C. psittaci* associated data points revealed the presence of densely packed lipids in the inclusion membrane. Those molecular fingerprints of lipids were similar to those of intercellular lipid droplets, but with a lower ratio of saturated

to unsaturated lipids. High-resolution imaging of *C. psittaci* infected cells with AFM revealed the presence of irregularly shaped protrusions or cavities on the cell membrane.

Multimodal (Raman and AFM) approach opens possibilities to retrieve relevant information about the state of infected cells, their topography, and their chemical composition. It is plausible to obtain information about the molecular structure of bacteria inside the cytoplasm using Raman microscopy. However, it is challenging to obtain information about the cellular surface topography at the same resolution as that in AFM. Specifically, surface irregularities, such as pores, have a low contrast and are difficult to detect with light microscopy techniques. AFM, on the other hand, proved to be capable of detecting these surface irregularities, and, therefore, has a unique application potential in this research. Therefore, a combination of those two techniques allows obtaining information not accessible if they were to be used separately. A possibility of non-destructive analysis of intercellular bacteria, for example, *Chlamydia*, would allow advancing research and understanding of the interaction of such bacteria with cells.

## 7.2. GENERAL CONCLUSIONS

During this dissertation work, Raman microscopy has been combined with various multimodal nanoscopic, microscopic and macroscopic medical imaging modalities to investigate diverse applications in bioengineering, life science, and biology. The results obtained in that research can be concluded as follows.

Conclusions are presented here according to the goals set for this work in Chapter 1.

- 1) Brain tissues: complementarity of Raman microscopy with magnetic resonance imaging (MRI) is explored on an example of pathological changes in brain tissues after mild traumatic injury (mTBI), Chapter 2.

The analysis of brain slices with a Raman microscope **revealed the decrease in the ratio of axon proteins to myeloid lipids in corpus callosum** region after mTBI. A combination of MRI with Raman microscopy appears to be highly promising. MRI can be used to identify the regions inside the tissue. Then, high-resolution molecular images of this region can be obtained with a Raman microscope – thus allowing to obtain information and details otherwise not accessible to MRI.

- 2) Molecular transport in cells: application of Raman microscopy as a label-free technique with fluorescence microscopy for intracellular detection of bovine lactoferrin inside calf rectal epithelial cells in the presence/absence of bacteria, Chapter 3.

It was found that **bovine lactoferrin molecules translocate to nuclei of cells**. Such translocation is not typical for secreted forms of the transferrin family of molecules. The rate of bovine lactoferrin uptake and translocation to the nucleus was increased by the presence of EHEC bacteria. The combined use of conventional fluorescence microscopy with Raman microscopy is beneficial only in specific cases. Fluorescent labels enable precise localization of molecules inside the cell. This can be used to identify the Raman molecular fingerprint of a molecule inside cells.

- 3) Intra-bacterial molecular substructures: application of Raman microscopy along-side X-ray microscopy and mass spectrometry for establishing the molecular composition of conductive fibers inside the so-called cable bacteria, Chapter 4.

**Nickel has been identified as the key element responsible for long-range conductance of fibers in cable bacteria.** This finding suggests the existence of a yet unknown mechanism of a long-distance electron transport in these bacteria. A combination of Raman microscopy with mass spectrometry and X-ray analytical tools has the following benefits. Mass spectrometry and X-ray microscopy techniques allowed obtained information on an atomic level. But they cannot be used *in vivo* and often cannot penetrate deep inside the sample. Raman microscopy allowed obtaining axial cross-section molecular images of the sample, is non-destructive, and can be used *in vivo*. Therefore, Raman microscopy can be applied to obtain general information about the sample, which can be used as a starting point for further investigation with X-ray microscopy and/or mass spectrometry. Additionally, information about molecular bonds obtained from Raman spectrum is complimentary with information about atomic composition provided by X-ray methods.

- 4) Tracing microparticles as drug delivery carriers in worms: test a possibility to localize microparticles *in vivo* by surface enhanced Raman scattering (SERS) and induce a drug release from those microparticles inside *C. elegans* worms, Chapter 5.

Elaborate drug delivery systems based on calcium carbonate particles were developed. Raman microscopy and its combination with SERS modality allowed, on the one hand, detection of particles inside *C. elegans* worms, while, on the other hand, it permitted for controllable induction of drug release. **The proposed approach facilitated particle localization** inside worms, but it was not based on detection of a particular molecular fingerprint. Instead, it is demonstrated here that the presence of the background, due to the SERS signal amplification, can be utilized for detection of the particle position inside worms.

5) Development of a 4Pi Raman confocal microscope and its application, together with atomic force microscopy (AFM), to study *Chlamydia psittaci* infected cells, Chapter 6. The 4Pi Raman microscope was successfully developed during this dissertation work. We have achieved this by combining the 4Pi technique with a confocal Raman microscope to build a 4Pi Raman microscope with an improved axial resolution. The resulting microscope was characterized using nanoparticles. A possibility of applying 4Pi Raman microscopy to study complex samples is shown, and advantages and potential challenges in such an analysis are identified. While a significant distinction of ultra-thin layers of an inorganic sample was achieved, significant improvements of the axial resolution of cell images have not yet been demonstrated. In fluorescence 4Pi superresolution microscopy, the labels act as sources of very strong and distinct fluorescence, while the rest of the sample is dark. In Raman scattering, every point of the sample acts as a source of a scattering signal, and development of novel deconvolution algorithms is required.

Application of Raman 4Pi microscopy in biological sciences is carried out on an example of cells infected with *C. psittaci*. This analysis **revealed the presence of densely packed lipids inside the membrane inclusion**, similar to what was observed in intercellular lipid droplets, but with a lower ratio of saturated to unsaturated lipids. The high-resolution topographic imaging of *C. psittaci* infected cells surface with AFM showed **the presence of irregularly shaped cavities on the cell membrane**. Complimentary application of Raman microscopy with atomic force microscopy (AFM) has excellent potential. AFM can be used to obtain the surface topography or mechanical properties of the samples, which can be then combined with Raman axial or lateral molecular images to obtain information otherwise not accessible for each of these techniques.

Overall, the results of this thesis work reveal that multimodal imaging involving Raman microscopy is a very promising approach for a broad range of applications in bioscience engineering, biomedical and biological sciences.

## 7.3. PERSPECTIVES AND FUTURE DIRECTIONS

### I. Development of multimodal imaging – industrial perspectives

The multimodal imaging approach is envisioned to play an increasingly important role in analysis of biological processes. Therefore, industrial companies are trying to develop new instruments, where multimodal scanning is incorporated in one device, as it was done, for example, by adding atomic force microscopy (AFM) modality to a Raman microscope by WITec (Ulm, Germany): <https://www.witec.de/techniques/afm/> (accessed 10.01.2021). Other industrial companies are using a similar approach. Bruker (Billerica, MA, U.S.A.) and NT-MDT (Zelenograd, Russia) have been teaming-up with Renishaw (Wotton-under-Edge, U.K.): <https://www.renishaw.com/en/renishaws-invia-confocal-raman-microscope-connects-to-brukers-dimension-icon-afm--37345> (accessed 10.01.2021) and Horiba (Edison, NJ, USA): [https://www.horiba.com/en\\_en/products/by-segment/scientific/surface-characterization/afm-raman-publications/](https://www.horiba.com/en_en/products/by-segment/scientific/surface-characterization/afm-raman-publications/) (accessed 10.01.2021), to add AFM capabilities to Raman microscopy.

As it was described in **Chapter 1** and from results obtained in this thesis, Raman microscopy is foreseen to play a very important role in multimodal image acquisition. Therefore, it is essential to discuss emerging trends in Raman microscopy and spectroscopy.

### II. The following emerging trends are identified for Raman microscopy and spectroscopy

**(1) Reproducibility and analysis of obtained data.** For advancing Raman microscopy further, a strong need exists for standardization in sample preparations, measurements, and data analyses. This has not been left without attention by the Raman community, where the European initiative “Raman4Clinics”: [www.raman4clinics.eu](http://www.raman4clinics.eu) (accessed 10.01.2021) aims to address the issues of standardization and promotes the application of Raman in clinical diagnostic <sup>226</sup>.

Regarding the data analysis: the main challenge here is not the complexity of Raman spectrum analysis, but the availability of databases for interpreting the data shown on the spectrum.

For example, while analyzing the brain tissue, we have used the ratios of axon and myelin related peaks, because it was experimentally established that these peaks are related to axon proteins and myelin. However, limited information was available, which could help to understand the changes in other peak intensities, their ratios, or shapes in corpus callosum after mTBI. Therefore, there is a clear need to establish open-source databases, like the National Center for Biotechnology Information Sequence Read Archive (NCBI SRA) used in bioinformatics, which would link changes in Raman spectra with experimentally observed changes in molecular composition of samples. After such databases would be established, the specialized data mining tools are expected to be developed for analysis of Raman datasets and their interpretation. It was demonstrated that precisely controlled and standardized scanning conditions in a combination with high-quality reference database allow not only qualitative but also quantitative molecular analysis of cellular components <sup>30</sup>.

**(2) Increasing stability and sensitivity of SERS.** Raman measurements are highly susceptible to small changes in sample composition, its surrounding, and equipment used for acquiring spectra. The problem of stability and reproducibility is particularly relevant for SERS because of the nature of the surface enhancement effect. In this regard, a comparison of free-space (nanoparticle and nanostructure-based ones) and waveguide-based SERS structures <sup>227</sup> has revealed the potential of waveguides to increase stability, reproducibility, and sensitivity of Raman measurements. Waveguide-based SERS approaches enhance the stability of signal acquisition and that represents a particularly promising area for biological applications, for example, in toxicology <sup>228</sup>. SERS platforms based on biocompatible and biodegradable polymer-based waveguides <sup>229</sup> are seen to be of importance for decreasing potential costs in medical diagnostics.

**(3) High-throughput screening and analysis of biological samples.** Raman spectroscopy is used to obtain information about the molecular composition of samples. It is label-free, non-destructive, and, therefore, it can be used *in vivo*. Its application for high-throughput analysis of biological samples seems extremely promising. However, it is still challenging to analyze a large number of cells or bacteria in a short time frame using conventional Raman microscopes. This problem can be solved by developing specialized high-throughput Raman spectroscopy and microscopy approaches. Such a high-throughput Raman platform was



recently presented and was used for rapid screening of eukaryotic cells <sup>230</sup>. A combination of Raman scattering techniques and microfluidics <sup>231 232</sup> is seen as interesting and promising advance, and development of high-throughput screening platforms based on Raman scattering is expected to be continued. Such platforms are envisioned to play an increasingly important role both in research and in clinics.

**(4) Improving the resolution of Raman microscopy.** There is an ongoing effort to increase the resolution in Raman microscopy and a number of techniques is proposed to achieve this goal. For example, on-chip applications can be used to improve the resolution. The total internal reflection (TIRF) superresolution on-chip approach serves as a good example of such a development <sup>233</sup>. However, TIRF-based approaches are limited to the surface, in this case to the surface of the chip, where the evanescent wave of the waveguide excites molecules. Also, application of the principles used in fluorescence superresolution microscopy can help to achieve superresolution in Raman microscopy <sup>234</sup>.

For improving resolution in 4Pi Raman microscopy and applying this technique further in biology, the following steps can be taken: higher numerical aperture objectives on both arms and faster scanning capabilities are desirable, while for facilitating alignment of the interacting beams – waveguides can be employed. Furthermore, a dedicated 4Pi Raman microscopy deconvolution algorithm is expected to improve images and open full potential of a resolution improvement in the 4Pi Raman scattering microscopy mode. Here, measurement standardization in combination with reference databases, similar to the approach discussed earlier <sup>30</sup>, would be useful for development of such deconvolution algorithms.



## REFERENCES

- 1 McCutchen, C. W. Superresolution in Microscopy and the Abbe Resolution Limit. *J. Opt. Soc. Am.* **57**, 1190-1192, doi:10.1364/JOSA.57.001190 (1967).
- 2 Abbe, E. Beiträge zur Theorie des Mikroskops und der mikroskopischen Wahrnehmung. *Archiv für Mikroskopische Anatomie* **9**, 413-468, doi:10.1007/BF02956173 (1873).
- 3 in *Studies in Physical and Theoretical Chemistry* Vol. 85 (ed P. L. Polavarapu) 61-79 (Elsevier, 1998), doi: [https://doi.org/10.1016/S0167-6881\(98\)80040-2](https://doi.org/10.1016/S0167-6881(98)80040-2).
- 4 in *Confocal Raman Microscopy* Vol. 158 (eds Dienes T., Hollricher O., & Toporski J.) 22-27 (Springer, 2010),doi: 10.1007/978-3-642-12522-5.
- 5 Wong, M.-L. Polarizability and tensor ellipsoid in the Raman effect. *Vibrational Spectroscopy* **7**, 197-199, doi:[https://doi.org/10.1016/0924-2031\(94\)85031-3](https://doi.org/10.1016/0924-2031(94)85031-3) (1994).
- 6 Beć, K. B., Huck, C. W. Breakthrough Potential in Near-Infrared Spectroscopy: Spectra Simulation. A Review of Recent Developments. *Frontiers in Chemistry* **7**, 48, doi: 10.3389/fchem.2019.00048 (2019).
- 7 Holtom, G. R., Thrall, B. D., Chin, B. Y., Wiley, H. S. & Colson, S. D. Achieving molecular selectivity in imaging using multiphoton Raman spectroscopy techniques. *Traffic (Copenhagen, Denmark)* **2**, 781-788, doi:10.1034/j.1600-0854.2001.21106.x (2001).
- 8 Moura, C. C., Tare, R. S., Oreffo, R. O. C. & Mahajan, S. Raman spectroscopy and coherent anti-Stokes Raman scattering imaging: prospective tools for monitoring skeletal cells and skeletal regeneration. *J R Soc Interface* **13**, 20160182, doi:10.1098/rsif.2016.0182 (2016).
- 9 Woodbury, E. J. & Ng, W. K. Ruby Laser Operation in the Near IR. *Proc. Inst. Radio Eng.* **50**, 2367 **50**, 2367 (1962).
- 10 Freudiger, C. W. *et al.* Label-free biomedical imaging with high sensitivity by stimulated Raman scattering microscopy. *Science (New York, N.Y.)* **322**, 1857-1861, doi:10.1126/science.1165758 (2008).
- 11 Svenningsson, L., Lin, Y.-C., Karlsson, M., Martinelli, A. & Nordstierna, L. Molecular Orientation Distribution of Regenerated Cellulose Fibers Investigated with Polarized Raman Spectroscopy. *Macromolecules* **52**, 3918-3924, doi:10.1021/acs.macromol.9b00520 (2019).
- 12 John, N. & George, S. in *Spectroscopic Methods for Nanomaterials Characterization* (eds Sabu Thomas, Raju Thomas, Ajesh K. Zachariah, & Raghvendra Kumar Mishra) 95-127 (Elsevier, 2017).
- 13 Efremov, E. V., Ariese, F. & Gooijer, C. Achievements in resonance Raman spectroscopy review of a technique with a distinct analytical chemistry potential. *Analytica chimica acta* **606**, 119-134, doi:10.1016/j.aca.2007.11.006 (2008).
- 14 Krafft, C. *et al.* Label-Free Molecular Imaging of Biological Cells and Tissues by Linear and Nonlinear Raman Spectroscopic Approaches. *Angewandte Chemie International Edition* **56**, 4392-4430, doi:<https://doi.org/10.1002/anie.201607604> (2017).
- 15 D'Acunto, M., Trombi, L., D'Alessandro, D. & Danti, S. Raman spectroscopy of osteosarcoma cells. *Physical biology* **16**, 016007, doi:10.1088/1478-3975/aaefbf (2018).
- 16 Alraies, A., Canetta, E., Waddington, R. J., Moseley, R. & Sloan, A. J. Discrimination of Dental Pulp Stem Cell Regenerative Heterogeneity by Single-Cell Raman Spectroscopy. *Tissue engineering. Part C, Methods* **25**, 489-499, doi:10.1089/ten.TEC.2019.0129 (2019).
- 17 Hsu, C. C. *et al.* A single-cell Raman-based platform to identify developmental stages of human pluripotent stem cell-derived neurons. *Proceedings of the National Academy of Sciences of the United States of America* **117**, 18412-18423, doi:10.1073/pnas.2001906117 (2020).
- 18 Pahlow, S. *et al.* Isolation and identification of bacteria by means of Raman spectroscopy. *Advanced drug delivery reviews* **89**, 105-120, doi:10.1016/j.addr.2015.04.006 (2015).

- 19 García-Timmermans, C. *et al.* Label-free Raman characterization of bacteria calls for standardized procedures. *Journal of microbiological methods* **151**, 69-75, doi:10.1016/j.mimet.2018.05.027 (2018).
- 20 Querido, W., Ailavajhala, R., Padalkar, M. & Pleshko, N. Validated Approaches for Quantification of Bone Mineral Crystallinity Using Transmission Fourier Transform Infrared (FT-IR), Attenuated Total Reflection (ATR) FT-IR, and Raman Spectroscopy. *Applied Spectroscopy* **72**, 1581-1593, doi:10.1177/0003702818789165 (2018).
- 21 Surmacki, J., Brozek-Pluska, B., Kordek, R. & Abramczyk, H. The lipid-reactive oxygen species phenotype of breast cancer. Raman spectroscopy and mapping, PCA and PLSDA for invasive ductal carcinoma and invasive lobular carcinoma. Molecular tumorigenic mechanisms beyond Warburg effect. *Analyst* **140**, 2121-2133, doi:10.1039/c4an01876a (2015).
- 22 Bergholt, M. S. *et al.* Raman Spectroscopy Reveals New Insights into the Zonal Organization of Native and Tissue-Engineered Articular Cartilage. *ACS central science* **2**, 885-895, doi:10.1021/acscentsci.6b00222 (2016).
- 23 Helal, K. M. *et al.* Raman spectroscopic histology using machine learning for nonalcoholic fatty liver disease. *FEBS letters* **593**, 2535-2544, doi:10.1002/1873-3468.13520 (2019).
- 24 Hosu, C. D. *et al.* Raman spectroscopy applications in rheumatology. *Lasers in medical science* **34**, 827-834, doi:10.1007/s10103-019-02719-2 (2019).
- 25 Rygula, A. *et al.* Raman imaging highlights biochemical heterogeneity of human eosinophils versus human eosinophilic leukaemia cell line. *British journal of haematology* **186**, 685-694, doi:10.1111/bjh.15971 (2019).
- 26 Long, R. *et al.* Two-color vibrational imaging of glucose metabolism using stimulated Raman scattering. *Chemical Communications* **54**, 152-155, doi:10.1039/C7CC08217G (2018).
- 27 Lee, H. J. *et al.* Assessing Cholesterol Storage in Live Cells and *C. elegans* by Stimulated Raman Scattering Imaging of Phenyl-Diyne Cholesterol. *Scientific reports* **5**, 7930, doi:10.1038/srep07930 (2015).
- 28 Fu, D. *et al.* Imaging the intracellular distribution of tyrosine kinase inhibitors in living cells with quantitative hyperspectral stimulated Raman scattering. *Nature Chemistry* **6**, 614-622, doi:10.1038/nchem.1961 (2014).
- 29 Turk, N. *et al.* Waveguide-based surface-enhanced Raman spectroscopy detection of protease activity using non-natural aromatic amino acids. *Biomedical optics express* **11**, 4800-4816, doi:10.1364/boe.398038 (2020).
- 30 Kuzmin, A. N., Pliss, A. & Prasad, P. N. Ramanomics: New Omics Disciplines Using Micro Raman Spectrometry with Biomolecular Component Analysis for Molecular Profiling of Biological Structures. *Biosensors (Basel)* **7**, 52, doi:10.3390/bios7040052 (2017).
- 31 Morita, S.-i. *et al.* Raman and autofluorescence spectrum dynamics along the HRG-induced differentiation pathway of MCF-7 cells. *Biophys. J.* **107**, 2221-2229, doi:10.1016/j.bpj.2014.10.002 (2014).
- 32 Ivan, A. B. *et al.* Combined Raman and autofluorescence *ex vivo* diagnostics of skin cancer in near-infrared and visible regions. *J. Biomed. Opt.* **22**, 1-10, doi:10.1117/1.JBO.22.2.027005 (2017).
- 33 De Gelder, J., De Gussem, K., Vandenabeele, P. & Moens, L. Reference database of Raman spectra of biological molecules. *J. Raman Spectrosc.* **38**, 1133-1147, doi:https://doi.org/10.1002/jrs.1734 (2007).
- 34 de Veij, M., Vandenabeele, P., De Beer, T., Remon, J. P. & Moens, L. Reference database of Raman spectra of pharmaceutical excipients. *J. Raman Spectrosc.* **40**, 297-307, doi:https://doi.org/10.1002/jrs.2125 (2009).
- 35 Jensen, L. & Schatz, G. C. Resonance Raman Scattering of Rhodamine 6G as Calculated Using Time-Dependent Density Functional Theory. *The Journal of Physical Chemistry A* **110**, 5973-5977, doi:10.1021/jp0610867 (2006).

- 36 Bratashov, D. N. *et al.* Raman imaging and photodegradation study of phthalocyanine containing microcapsules and coated particles. *J. Raman Spectrosc.* **42**, 1901-1907, doi:<https://doi.org/10.1002/jrs.2938> (2011).
- 37 Wang, Y. & Schlücker, S. Rational design and synthesis of SERS labels. *Analyst* **138**, 2224-2238, doi:[10.1039/C3AN36866A](https://doi.org/10.1039/C3AN36866A) (2013).
- 38 Langer, J. *et al.* Present and Future of Surface-Enhanced Raman Scattering. *ACS Nano* **14**, 28-117, doi:[10.1021/acsnano.9b04224](https://doi.org/10.1021/acsnano.9b04224) (2020).
- 39 Yang, M. *et al.* SERS-active gold lace nanoshells with built-in hotspots. *Nano letters* **10**, 4013-4019, doi:[10.1021/nl101946c](https://doi.org/10.1021/nl101946c) (2010).
- 40 D'Hollander, A. *et al.* Development of nanostars as a biocompatible tumor contrast agent: toward in vivo SERS imaging. *International journal of nanomedicine* **11**, 3703-3714, doi:[10.2147/ijn.s91340](https://doi.org/10.2147/ijn.s91340) (2016).
- 41 Rycenga, M. *et al.* Surface-Enhanced Raman Scattering: Comparison of Three Different Molecules on Single-Crystal Nanocubes and Nanospheres of Silver. *The Journal of Physical Chemistry A* **113**, 3932-3939, doi:[10.1021/jp8101817](https://doi.org/10.1021/jp8101817) (2009).
- 42 Slesiona, N. *et al.* DNA-Biofunctionalization of CTAC-Capped Gold Nanocubes. *Nanomaterials (Basel, Switzerland)* **10**, doi:[10.3390/nano10061119](https://doi.org/10.3390/nano10061119) (2020).
- 43 Yamakoshi, H. *et al.* Imaging of EdU, an Alkyne-Tagged Cell Proliferation Probe, by Raman Microscopy. *Journal of the American Chemical Society* **133**, 6102-6105, doi:[10.1021/ja108404p](https://doi.org/10.1021/ja108404p) (2011).
- 44 Cui, L., Yang, K. & Zhu, Y. G. Stable Isotope-Labeled Single-Cell Raman Spectroscopy Revealing Function and Activity of Environmental Microbes. *Methods in molecular biology (Clifton, N.J.)* **2046**, 95-107, doi:[10.1007/978-1-4939-9721-3\\_8](https://doi.org/10.1007/978-1-4939-9721-3_8) (2019).
- 45 Berry, D. *et al.* Tracking heavy water (D<sub>2</sub>O) incorporation for identifying and sorting active microbial cells. *Proceedings of the National Academy of Sciences of the United States of America* **112**, E194-E203, doi:[10.1073/pnas.1420406112](https://doi.org/10.1073/pnas.1420406112) (2015).
- 46 Schermelleh, L. *et al.* Super-resolution microscopy demystified. *Nature Cell Biology* **21**, 72-84, doi:[10.1038/s41556-018-0251-8](https://doi.org/10.1038/s41556-018-0251-8) (2019).
- 47 Hell, S. W., Stelzer, E. H., Lindek, S. & Cremer, C. Confocal microscopy with an increased detection aperture: type-B 4Pi confocal microscopy. *Optics letters* **19**, 222, doi:[10.1364/ol.19.000222](https://doi.org/10.1364/ol.19.000222) (1994).
- 48 Gustafsson, M. G. Nonlinear structured-illumination microscopy: wide-field fluorescence imaging with theoretically unlimited resolution. *Proceedings of the National Academy of Sciences of the United States of America* **102**, 13081-13086, doi:[10.1073/pnas.0406877102](https://doi.org/10.1073/pnas.0406877102) (2005).
- 49 Hell, S. W. & Wichmann, J. Breaking the diffraction resolution limit by stimulated emission: stimulated-emission-depletion fluorescence microscopy. *Optics letters* **19**, 780-782, doi:[10.1364/ol.19.000780](https://doi.org/10.1364/ol.19.000780) (1994).
- 50 Betzig, E. *et al.* Imaging intracellular fluorescent proteins at nanometer resolution. *Science (New York, N.Y.)* **313**, 1642-1645, doi:[10.1126/science.1127344](https://doi.org/10.1126/science.1127344) (2006).
- 51 Axelrod, D. Cell-substrate contacts illuminated by total internal reflection fluorescence. *The Journal of cell biology* **89**, 141-145, doi:[10.1083/jcb.89.1.141](https://doi.org/10.1083/jcb.89.1.141) (1981).
- 52 Stöckle, R. M., Suh, Y. D., Deckert, V. & Zenobi, R. Nanoscale chemical analysis by tip-enhanced Raman spectroscopy. *Chemical Physics Letters* **318**, 131-136, doi:[https://doi.org/10.1016/S0009-2614\(99\)01451-7](https://doi.org/10.1016/S0009-2614(99)01451-7) (2000).
- 53 Schmid, T., Yeo, B.-S., Leong, G., Stadler, J. & Zenobi, R. Performing tip-enhanced Raman spectroscopy in liquids. *J. Raman Spectrosc.* **40**, 1392-1399, doi:<https://doi.org/10.1002/jrs.2387> (2009).
- 54 He, Z. *et al.* Tip-Enhanced Raman Imaging of Single-Stranded DNA with Single Base Resolution. *J Am Chem Soc* **141**, 753-757, doi:[10.1021/jacs.8b11506](https://doi.org/10.1021/jacs.8b11506) (2019).
- 55 Silva, W. R., Graefe, C. T. & Frontiera, R. R. Toward Label-Free Super-Resolution Microscopy. *ACS Photonics* **3**, 79-86, doi:[10.1021/acsp Photonics.5b00467](https://doi.org/10.1021/acsp Photonics.5b00467) (2016).

- 56 Watanabe, K. *et al.* Structured line illumination Raman microscopy. *Nat Commun* **6**, 10095 (2015), doi:https://doi.org/10.1038/ncomms10095.
- 57 Coccato, A., Moens, L. & Vandenabeele, P. On the stability of mediaeval inorganic pigments: a literature review of the effect of climate, material selection, biological activity, analysis and conservation treatments. *Heritage Science* **5**, 12, doi:10.1186/s40494-017-0125-6 (2017).
- 58 Rousaki, A. *et al.* On-field Raman spectroscopy of Patagonian prehistoric rock art: Pigments, alteration products and substrata. *TrAC Trends in Analytical Chemistry* **105**, 338-351, doi:https://doi.org/10.1016/j.trac.2018.05.011 (2018).
- 59 Pilot, R. SERS detection of food contaminants by means of portable Raman instruments. *J. Raman Spectrosc.* **49**, 954-981, doi:https://doi.org/10.1002/jrs.5400 (2018).
- 60 Gukowsky, J. C., Xie, T., Gao, S., Qu, Y. & He, L. Rapid identification of artificial and natural food colorants with surface enhanced Raman spectroscopy. *Food Control* **92**, 267-275, doi:https://doi.org/10.1016/j.foodcont.2018.04.058 (2018).
- 61 Mandrile, L. *et al.* Migration study of organotin compounds from food packaging by surface-enhanced Raman scattering. *Talanta* **220**, 121408, doi:https://doi.org/10.1016/j.talanta.2020.121408 (2020).
- 62 Madela, K. *et al.* A simple procedure to analyze positions of interest in infectious cell cultures by correlative light and electron microscopy. *Methods Cell Biol* **124**, 93-110, doi:10.1016/b978-0-12-801075-4.00005-7 (2014).
- 63 Janel, S., Werkmeister, E., Bongiovanni, A., Lafont, F. & Barois, N. CLAFEM: Correlative light atomic force electron microscopy. *Methods Cell Biol* **140**, 165-185, doi:10.1016/bs.mcb.2017.03.010 (2017).
- 64 Yamada, Y., Konno, H. & Shimabukuro, K. Demonstration of correlative atomic force and transmission electron microscopy using actin cytoskeleton. *Biophysics and physcobiology* **14**, 111-117, doi:10.2142/biophysico.14.0\_111 (2017).
- 65 Stachnik, K. *et al.* Multimodal X-ray imaging of nanocontainer-treated macrophages and calcium distribution in the periacicular bone matrix. *Scientific reports* **10**, 1784, doi:10.1038/s41598-020-58318-7 (2020).
- 66 Massoud, T. F. & Gambhir, S. S. Molecular imaging in living subjects: seeing fundamental biological processes in a new light. *Genes & development* **17**, 545-580, doi:10.1101/gad.1047403 (2003).
- 67 Coccato, A. *et al.* Micro-Raman spectroscopy and complementary techniques (hXRF, VP-SEM-EDS,  $\mu$ -FTIR and Py-GC/MS) applied to the study of beads from the Kongo Kingdom (Democratic Republic of the Congo). *J. Raman Spectrosc.* **48**, 1468-1478, doi:https://doi.org/10.1002/jrs.5106 (2017).
- 68 Guentsch, A. *et al.* Effect of biomimetic mineralization on enamel and dentin: A Raman and EDX analysis. *Dental Materials* **35**, 1300-1307, doi:https://doi.org/10.1016/j.dental.2019.05.025 (2019).
- 69 Panizzi, P. *et al.* Multimodal imaging of bacterial-host interface in mice and piglets with *Staphylococcus aureus* endocarditis. *Sci Transl Med* **12**, doi:10.1126/scitranslmed.aay2104 (2020).
- 70 Kniggendorf, A. K. *et al.* Confocal Raman microscopy and fluorescent in situ hybridization - A complementary approach for biofilm analysis. *Chemosphere* **161**, 112-118, doi:10.1016/j.chemosphere.2016.06.096 (2016).
- 71 Thurman, D. J. in *Head trauma: Basic, preclinical, and clinical directions* (ed L. Miller & R. Hayes) 324-347 (NY: Wiley, 2001).
- 72 Leibson, C. L. *et al.* Medical Care Costs Associated with Traumatic Brain Injury over the Full Spectrum of Disease: A Controlled Population-Based Study. *J. Neurotrauma* **29**, 2038-2049, doi:10.1089/neu.2010.1713 (2012).
- 73 Teasdale, G. & Jennett, B. Assessment of coma and impaired consciousness - practical scale *Lancet* **2**, 81-84 (1974).

- 74 CDC. Injury, prevention, & control: traumatic brain injury. Center for Disease Control and Prevention. <http://www.cdc.gov/traumaticbraininjury/statistics.html> (2010).
- 75 Daneshvar, D. H. *et al.* Long-Term Consequences: Effects on Normal Development Profile After Concussion. *Phys. Med. Rehabil. Clin. N. Am.* **22**, 683+, doi:10.1016/j.pmr.2011.08.009 (2011).
- 76 Tax, C. M. W. *et al.* Quantifying the brain's sheet structure with normalized convolution. *Med. Image Anal.* **39**, 162-177, doi:10.1016/j.media.2017.03.007 (2017).
- 77 Katti, G., Ara, S. & Shireen, A. Magnetic Resonance Imaging (MRI)@ A Review. *International Journal of Dental Clinics* **3** (2011).
- 78 Mittl, R. L. *et al.* Prevalence of MR evidence of diffuse axonal injury in patients with mild head-injury and normal head CT findings *Am. J. Neuroradiol.* **15**, 1583-1589 (1994).
- 79 Shenton, M. E. *et al.* A review of magnetic resonance imaging and diffusion tensor imaging findings in mild traumatic brain injury. *Brain Imaging Behav.* **6**, 137-192, doi:10.1007/s11682-012-9156-5 (2012).
- 80 Matsushita, M., Hosoda, K., Naitoh, Y., Yamashita, H. & Kohmura, E. Utility of diffusion tensor imaging in the acute stage of mild to moderate traumatic brain injury for detecting white matter lesions and predicting long-term cognitive function in adults Clinical article. *J. Neurosurg.* **115**, 130-139, doi:10.3171/2011.2.jns101547 (2011).
- 81 Park, J. H. *et al.* Detection of Traumatic Cerebral Microbleeds by Susceptibility-Weighted Image of MRI. *J. Korean. Neurosurg. Soc.* **46**, 365-369, doi:10.3340/jkns.2009.46.4.365 (2009).
- 82 Krafft, C. & Popp, J. The many facets of Raman spectroscopy for biomedical analysis. *Anal. Bioanal. Chem.* **407**, 699-717, doi:10.1007/s00216-014-8311-9 (2015).
- 83 Braeckman, K., Descamps, B. & Vanhove, C. Advanced Diffusion Imaging in The Hippocampus of Rats with Mild Traumatic Brain Injury. *Journal of visualized experiments : JoVE*, doi:10.3791/60012 (2019).
- 84 Braeckman, K., Descamps, B., Vanhove, C. & Caeyenberghs, K. Exploratory relationships between cognitive improvements and training induced plasticity in hippocampus and cingulum in a rat model of mild traumatic brain injury: a diffusion MRI study. *Brain Imaging Behav* **14**, 2281-2294, doi:10.1007/s11682-019-00179-4 (2020).
- 85 Chung, S. *et al.* White Matter Tract Integrity: An Indicator of Axonal Pathology after Mild Traumatic Brain Injury. *J. Neurotrauma* **35**, 1015-1020, doi:10.1089/neu.2017.5320 (2018).
- 86 Morisaki, S. *et al.* Application of Raman spectroscopy for visualizing biochemical changes during peripheral nerve injury in vitro and in vivo. *J. Biomed. Opt.* **18**, 8, doi:10.1117/1.jbo.18.11.116011 (2013).
- 87 Surmacki, J. M. *et al.* Label-free monitoring of tissue biochemistry following traumatic brain injury using Raman spectroscopy. *Analyst* **142**, 132-139, doi:10.1039/c6an02238c (2017).
- 88 Köhler, M., Machill, S., Salzer, R. & Krafft, C. Characterization of lipid extracts from brain tissue and tumors using Raman spectroscopy and mass spectrometry. *Anal Bioanal Chem* **393**, 1513-1520, doi:10.1007/s00216-008-2592-9 (2009).
- 89 Rickard, J. J. S. *et al.* Rapid optofluidic detection of biomarkers for traumatic brain injury via surface-enhanced Raman spectroscopy. *Nature Biomedical Engineering* **4**, 610-623, doi:10.1038/s41551-019-0510-4 (2020).
- 90 Tomaiuolo, F. *et al.* Gross morphology and morphometric sequelae in the hippocampus, fornix, and corpus callosum of patients with severe non-missile traumatic brain injury without macroscopically detectable lesions: a T1 weighted MRI study. *J. Neurol. Neurosurg. Psychiatry* **75**, 1314-1322, doi:10.1136/jnnp.2003.017046 (2004).
- 91 Marmarou, A. *et al.* A new model of diffuse brain injury in Rats. Part 1: Pathophysiology and biomechanics. *J. Neurosurg.* **80**, 291-300, doi:10.3171/jns.1994.80.2.0291 (1994).
- 92 Thavarajah, R., Mudimbaimannar, V. K., Elizabeth, J., Rao, U. K. & Ranganathan, K. Chemical and physical basics of routine formaldehyde fixation. *Journal of oral and maxillofacial pathology : JOMFP* **16**, 400-405, doi:10.4103/0973-029x.102496 (2012).

- 93 Beleites, C. S., V. hyperSpec: A Package to Handle Hyperspectral Data Sets in R. R package version 0.98-20130516. URL <http://hyperspec.R-Forge.R-project.org> (2013).
- 94 Eilers, P. H. C. Baseline Correction with Asymmetric Least Squares Smoothing. *Anal. Chem* **75**, 3631–3636 (2003).
- 95 Gibb, S. & Strimmer, K. MALDIquant: a versatile R package for the analysis of mass spectrometry data. *Bioinformatics* **28**, 2270–2271, doi:10.1093/bioinformatics/bts447 (2012).
- 96 Bergner, N. *et al.* Hyperspectral unmixing of Raman micro-images for assessment of morphological and chemical parameters in non-dried brain tumor specimens. *Anal Bioanal Chem* **405**, 8719–8728, doi:10.1007/s00216-013-7257-7 (2013).
- 97 Kirsch, M., Schackert, G., Salzer, R. & Krafft, C. Raman spectroscopic imaging for in vivo detection of cerebral brain metastases. *Anal Bioanal Chem* **398**, 1707–1713, doi:10.1007/s00216-010-4116-7 (2010).
- 98 Lorincz, A. *et al.* Raman spectroscopy for neoplastic tissue differentiation: a pilot study. *Journal of Pediatric Surgery* **39**, 953–956, doi:https://doi.org/10.1016/j.jpedsurg.2004.02.043 (2004).
- 99 Jermyn, M. *et al.* Intraoperative brain cancer detection with Raman spectroscopy in humans. *Sci. Transl. Med.* **7**, 9, doi:10.1126/scitranslmed.aaa2384 (2015).
- 100 Aisen, P., Leibman, A. & Zweier, J. Stoichiometric and site characteristics of the binding of iron to human transferrin. *J Biol Chem* **253**, 1930–1937 (1978).
- 101 Gkouvatzos, K., Papanikolaou, G. & Pantopoulos, K. Regulation of iron transport and the role of transferrin. *Biochimica et biophysica acta* **1820**, 188–202, doi:10.1016/j.bbagen.2011.10.013 (2012).
- 102 Siqueiros-Cendón, T. *et al.* Immunomodulatory effects of lactoferrin. *Acta Pharmacologica Sinica* **35**, 557–566, doi:10.1038/aps.2013.200 (2014).
- 103 Park, J.-H. *et al.* An antimicrobial protein, lactoferrin exists in the sweat: proteomic analysis of sweat. *Experimental Dermatology* **20**, 369–371, doi:10.1111/j.1600-0625.2010.01218.x (2011).
- 104 Masson, P. Lactoferrin in milk from different species. *Comp Biochem Physiol B* **39**, 119–129 (1971).
- 105 González-Chávez, S. A., Arévalo-Gallegos, S., Rascón-Cruz, Q. Lactoferrin: structure, function and applications. *International Journal of Antimicrobial Agents* **33**, 301.e1–8., doi:https://doi.org/10.1016/j.ijantimicag.2008.07.020 (2009).
- 106 Birgens, H. S. Lactoferrin in plasma measured by an ELISA technique: Evidence that plasma lactoferrin is an indicator of neutrophil turnover and bone marrow activity in acute leukaemia. *Scandinavian Journal of Haematology* **34**, 326–331, doi:10.1111/j.1600-0609.1985.tb00757.x (1985).
- 107 Rybarczyk, J. *et al.* Effects of lactoferrin treatment on Escherichia coli O157:H7 rectal colonization in cattle. *Veterinary Microbiology* **202**, 38–46, doi:https://doi.org/10.1016/j.vetmic.2015.12.013 (2017).
- 108 Grauke, L. J. *et al.* Gastrointestinal Tract Location of Escherichia coli O157:H7 in Ruminants. *Applied and Environmental Microbiology* **68**, 2269, doi:10.1128/AEM.68.5.2269-2277.2002 (2002).
- 109 Naylor, S. W. *et al.* Lymphoid Follicle-Dense Mucosa at the Terminal Rectum Is the Principal Site of Colonization of Enterohemorrhagic Escherichia coli O157:H7 in the Bovine Host. *Infection and Immunity* **71**, 1505, doi:10.1128/IAI.71.3.1505-1512.2003 (2003).
- 110 Griffin, P. M. & Karmali, M. A. Emerging Public Health Challenges of Shiga Toxin–Producing Escherichia coli Related to Changes in the Pathogen, the Population, and the Environment. *Clinical Infectious Diseases* **64**, 371–376, doi:10.1093/cid/ciw708 (2016).
- 111 Sperandio, V. & Nguyen, Y. Enterohemorrhagic E. coli (EHEC) pathogenesis. *Frontiers in Cellular and Infection Microbiology* **2**, doi:10.3389/fcimb.2012.00090 (2012).



- 112 Liu, D., Wang, X., Zhang, Z. & Teng, C. T. An intronic alternative promoter of the human lactoferrin gene is activated by Ets. *Biochemical and Biophysical Research Communications* **301**, 472-479, doi:https://doi.org/10.1016/S0006-291X(02)03077-2 (2003).
- 113 Siebert, P. D. & Huang, B. C. B. Identification of an alternative form of human lactoferrin mRNA that is expressed differentially in normal tissues and tumor-derived cell lines. *Proceedings of the National Academy of Sciences* **94**, 2198-2203, doi:10.1073/pnas.94.6.2198 (1997).
- 114 Mariller, C. *et al.* Delta-lactoferrin, an intracellular lactoferrin isoform that acts as a transcription factor. *Biochemistry and cell biology = Biochimie et biologie cellulaire* **90**, 307-319, doi:10.1139/o11-070 (2012).
- 115 Iafisco, M., Foltran, I., Foggia, M., Bonora, S. & Roveri, N. Calorimetric and Raman investigation of cow's milk lactoferrin. *Journal of Thermal Analysis and Calorimetry* **103**, 41-47, doi:10.1007/s10973-010-1084-2 (2011).
- 116 Dziva, F. *et al.* EspP, a Type V-secreted serine protease of enterohaemorrhagic *Escherichia coli* O157:H7, influences intestinal colonization of calves and adherence to bovine primary intestinal epithelial cells. *FEMS Microbiology Letters* **271**, 258-264, doi:10.1111/j.1574-6968.2007.00724.x (2007).
- 117 Mahajan, A. *et al.* An investigation of the expression and adhesin function of H7 flagella in the interaction of *Escherichia coli* O157:H7 with bovine intestinal epithelium. *Cellular Microbiology* **11**, 121-137, doi:10.1111/j.1462-5822.2008.01244.x (2009).
- 118 Macartney, K. K., Baumgart, D. C., Carding, S. R., Brubaker, J. O. & Offit, P. A. Primary Murine Small Intestinal Epithelial Cells, Maintained in Long-Term Culture, Are Susceptible to Rotavirus Infection. *Journal of Virology* **74**, 5597-5603, doi:10.1128/jvi.74.12.5597-5603.2000 (2000).
- 119 Sheng, H. *et al.* Internalization of *Escherichia coli* O157:H7 by Bovine Rectal Epithelial Cells. *Frontiers in Microbiology* **2**, doi:10.3389/fmicb.2011.00032 (2011).
- 120 Rybarczyk, J. *et al.* Lactoferrin translocates to the nucleus of bovine rectal epithelial cells in the presence of *Escherichia coli* O157:H7. *Veterinary Research* **50**, 75, doi:10.1186/s13567-019-0694-3 (2019).
- 121 Dibb-Fuller, MP., Best, A., Stagg, DA., Cooley, WA., Woodward, MJ. An in-vitro model for studying the interaction of *Escherichia coli* O157:H7 and other enteropathogens with bovine primary cell cultures. *Journal of Medical Microbiology* **50**, 759-769, doi:https://doi.org/10.1099/0022-1317-50-9-759 (2001).
- 122 Blondelle, S. E., Takahashi, E., Houghten, R. A., & Pérez-Payá, E. Rapid identification of compounds with enhanced antimicrobial activity by using conformationally defined combinatorial libraries. *Biochemical Journal* **313**, 141-147, doi:10.1042/bj3130141 (1996).
- 123 De Luca, A. C. *et al.* Label-free biochemical characterization of bovine sperm cells using Raman microscopy. Vol. 8938 PWB (SPIE, 2014).
- 124 Nielsen, L. P., Risgaard-Petersen, N., Fossing, H., Christensen, P. B. & Sayama, M. Electric currents couple spatially separated biogeochemical processes in marine sediment. *Nature* **463**, 1071-1074, doi:10.1038/nature08790 (2010).
- 125 Bjerg, J. T. *et al.* Long-distance electron transport in individual, living cable bacteria. *Proceedings of the National Academy of Sciences* **115**, 5786-5791, doi:10.1073/pnas.1800367115 (2018).
- 126 Pfeffer, C. *et al.* Filamentous bacteria transport electrons over centimetre distances. *Nature* **491**, 218-221, doi:10.1038/nature11586 (2012).
- 127 Meysman, F. J. R. Cable Bacteria Take a New Breath Using Long-Distance Electricity. *Trends in microbiology* **26**, 411-422, doi:10.1016/j.tim.2017.10.011 (2018).
- 128 Cornelissen, R. *et al.* The Cell Envelope Structure of Cable Bacteria. *Frontiers in Microbiology* **9**, doi:10.3389/fmicb.2018.03044 (2018).

- 129 Jiang, Z. *et al.* In vitro single-cell dissection revealing the interior structure of cable bacteria. *Proceedings of the National Academy of Sciences of the United States of America* **115**, 8517-8522, doi:10.1073/pnas.1807562115 (2018).
- 130 Meysman, F. J. R. *et al.* A highly conductive fibre network enables centimetre-scale electron transport in multicellular cable bacteria. *Nat Commun* **10**, 4120-4120, doi:10.1038/s41467-019-12115-7 (2019).
- 131 Thiruvallur Eachambadi, R. *et al.* A Highly-ordered and Fail-safe Electrical Network in Cable Bacteria. *bioRxiv*, 866319, doi:10.1101/866319 (2019).
- 132 El-Naggar, M. Y. *et al.* Electrical transport along bacterial nanowires from *Shewanella oneidensis* MR-1. *Proceedings of the National Academy of Sciences* **107**, 18127-18131, doi:10.1073/pnas.1004880107 (2010).
- 133 Wang, F. *et al.* Structure of Microbial Nanowires Reveals Stacked Hemes that Transport Electrons over Micrometers. *Cell* **177**, 361-369.e310, doi:10.1016/j.cell.2019.03.029 (2019).
- 134 Talari, A. C. S., Movasaghi, Z., Rehman, S. & Rehman, I. u. Raman Spectroscopy of Biological Tissues. *Applied Spectroscopy Reviews* **50**, 46-111, doi:10.1080/05704928.2014.923902 (2015).
- 135 Lasch, P. N., D. in *Encyclopedia of Analytical Chemistry*, 1-32, doi:10.1002/9780470027318.a01117.pub2 (2000).
- 136 Barth, A. Infrared spectroscopy of proteins. *Biochimica et biophysica acta* **1767**, 1073-1101, doi:10.1016/j.bbabi.2007.06.004 (2007).
- 137 Nakamoto, K. in *Handbook of Vibrational Spectroscopy*, doi:10.1002/0470027320.s4104 (2006).
- 138 Petrenko, T., Ray, K., Wieghardt, K. E. & Neese, F. Vibrational Markers for the Open-Shell Character of Transition Metal Bis-dithiolenes: An Infrared, Resonance Raman, and Quantum Chemical Study. *Journal of the American Chemical Society* **128**, 4422-4436, doi:10.1021/ja0578451 (2006).
- 139 Horch, M. *et al.* Resonance Raman Spectroscopy on [NiFe] Hydrogenase Provides Structural Insights into Catalytic Intermediates and Reactions. *Journal of the American Chemical Society* **136**, 9870-9873, doi:10.1021/ja505119q (2014).
- 140 Fiedler, A. T., Bryngelson, P. A., Maroney, M. J. & Brunold, T. C. Spectroscopic and Computational Studies of Ni Superoxide Dismutase: Electronic Structure Contributions to Enzymatic Function. *Journal of the American Chemical Society* **127**, 5449-5462, doi:10.1021/ja042521i (2005).
- 141 Boschker, H. T. S. *et al.* Efficient long-range conduction in cable bacteria through nickel protein wires. *bioRxiv*, 2020.2010.2023.351973, doi:10.1101/2020.10.23.351973 (2020).
- 142 Hu, F., Wei, L., Zheng, C., Shen, Y. & Min, W. Live-cell vibrational imaging of choline metabolites by stimulated Raman scattering coupled with isotope-based metabolic labeling. *Analyst* **139**, 2312-2317, doi:10.1039/C3AN02281A (2014).
- 143 Slater, T. J. A., Lewis, E. A. & Haigh, S. J. Energy Dispersive X-ray Tomography for 3D Elemental Mapping of Individual Nanoparticles. *Journal of visualized experiments : JoVE*, 52815, doi:10.3791/52815 (2016).
- 144 Kaulich, B. *et al.* Low-energy X-ray fluorescence microscopy opening new opportunities for bio-related research. *J R Soc Interface* **6 Suppl 5**, S641-647, doi:10.1098/rsif.2009.0157.focus (2009).
- 145 Guerquin-Kern, J. L., Wu, T. D., Quintana, C. & Croisy, A. Progress in analytical imaging of the cell by dynamic secondary ion mass spectrometry (SIMS microscopy). *Biochimica et biophysica acta* **1724**, 228-238, doi:10.1016/j.bbagen.2005.05.013 (2005).
- 146 Nuñez, J., Renslow, R., Cliff, J. B. & Anderton, C. R. NanoSIMS for biological applications: Current practices and analyses. *Biointerphases* **13**, 03B301, doi:10.1116/1.4993628 (2017).
- 147 Cornelissen, R. *et al.* The Cell Envelope Structure of Cable Bacteria. *Frontiers in Microbiology* **9**, 3044, doi:10.3389/fmicb.2018.03044 (2018).

- 148 Yun, Y. H., Lee, B. K. & Park, K. Controlled Drug Delivery: Historical perspective for the next generation. *Journal of controlled release : official journal of the Controlled Release Society* **219**, 2-7, doi:10.1016/j.jconrel.2015.10.005 (2015).
- 149 Erdoğar, N., Akkin, S. & Bilensoy, E. Nanocapsules for Drug Delivery: An Updated Review of the Last Decade. *Recent patents on drug delivery & formulation* **12**, 252-266, doi:10.2174/1872211313666190123153711 (2018).
- 150 Sercombe, L. *et al.* Advances and Challenges of Liposome Assisted Drug Delivery. *Frontiers in Pharmacology* **6**, doi:10.3389/fphar.2015.00286 (2015).
- 151 Bharti, C., Nagaich, U., Pal, A. K. & Gulati, N. Mesoporous silica nanoparticles in target drug delivery system: A review. *Int J Pharm Investig* **5**, 124-133, doi:10.4103/2230-973X.160844 (2015).
- 152 Parakhonskiy, B. V. *et al.* Macromolecule loading into spherical, elliptical, star-like and cubic calcium carbonate carriers. *Chemphyschem : a European journal of chemical physics and physical chemistry* **15**, 2817-2822, doi:10.1002/cphc.201402136 (2014).
- 153 Vidiyasheva, I. V. *et al.* Transfer of cells with uptaken nanocomposite, magnetite-nanoparticle functionalized capsules with electromagnetic tweezers. *Biomaterials Science* **6**, 2219-2229, doi:10.1039/C8BM00479J (2018).
- 154 Müderrisoğlu, C. *et al.* Nanostructured Biointerfaces Based on Bioceramic Calcium Carbonate/Hydrogel Coatings on Titanium with an Active Enzyme for Stimulating Osteoblasts Growth. *Advanced Materials Interfaces* **5**, doi:10.1002/admi.201800452 (2018).
- 155 Saveleva, M. S. *et al.* Hybrid PCL/CaCO<sub>3</sub> scaffolds with capabilities of carrying biologically active molecules: Synthesis, loading and in vivo applications. *Materials science & engineering. C, Materials for biological applications* **85**, 57-67, doi:10.1016/j.msec.2017.12.019 (2018).
- 156 Koo, K.-T., Polimeni, G., Qahash, M., Kim, C. K. & Wikesjö, U. M. Periodontal repair in dogs: guided tissue regeneration enhances bone formation in sites implanted with a coral-derived calcium carbonate biomaterial. *Journal of Clinical Periodontology* **32**, 104-110, doi:10.1111/j.1600-051X.2004.00632.x (2005).
- 157 Gopi, S., Subramanian, V. K. & Palanisamy, K. Aragonite–calcite–vaterite: A temperature influenced sequential polymorphic transformation of CaCO<sub>3</sub> in the presence of DTPA. *Materials Research Bulletin* **48**, 1906-1912, doi:https://doi.org/10.1016/j.materresbull.2013.01.048 (2013).
- 158 Rodriguez-Blanco, J. D., Shaw, S. & Benning, L. G. The kinetics and mechanisms of amorphous calcium carbonate (ACC) crystallization to calcite, viavaterite. *Nanoscale* **3**, 265-271, doi:10.1039/CONR00589D (2011).
- 159 Voronin, D. V. *et al.* In Vitro and in Vivo Visualization and Trapping of Fluorescent Magnetic Microcapsules in a Bloodstream. *ACS applied materials & interfaces* **9**, 6885-6893, doi:10.1021/acsami.6b15811 (2017).
- 160 Li, W. R. *et al.* Antibacterial activity and mechanism of silver nanoparticles on Escherichia coli. *Applied microbiology and biotechnology* **85**, 1115-1122, doi:10.1007/s00253-009-2159-5 (2010).
- 161 Gharibshahi, L., Saion, E., Gharibshahi, E., Shaari, A. H. & Matori, K. A. Structural and Optical Properties of Ag Nanoparticles Synthesized by Thermal Treatment Method. *Materials (Basel)* **10**, 402, doi:10.3390/ma10040402 (2017).
- 162 Mock, J. J., Barbic, M., Smith, D. R., Schultz, D. A. & Schultz, S. Shape effects in plasmon resonance of individual colloidal silver nanoparticles. *The Journal of Chemical Physics* **116**, 6755-6759, doi:10.1063/1.1462610 (2002).
- 163 Fleischmann, M., Hendra, P. J. & McQuillan, A. J. Raman spectra of pyridine adsorbed at a silver electrode. *Chemical Physics Letters* **26**, 163-166, doi:https://doi.org/10.1016/0009-2614(74)85388-1 (1974).

- 164 Prochazka, M. Medical Applications of SERS. In: Surface-Enhanced Raman Spectroscopy. Biological and Medical Physics, Biomedical Engineering. Springer, Cham. [https://doi.org/10.1007/978-3-319-23992-7\\_7](https://doi.org/10.1007/978-3-319-23992-7_7) (2016)
- 165 Muehlethaler, C., Leona, M. & Lombardi, J. R. Review of Surface Enhanced Raman Scattering Applications in Forensic Science. *Analytical Chemistry* **88**, 152-169, doi:10.1021/acs.analchem.5b04131 (2016).
- 166 Pérez-Pineiro, R., Correa-Duarte, M., Salgueiriño, V. & Alvarez-Puebla, R. SERS assisted ultra-fast peptidic screening: A new tool for drug discovery. *Nanoscale* **4**, 113-116, doi:10.1039/c1nr11293g (2011).
- 167 Vo-Dinh, T. SERS chemical sensors and biosensors: new tools for environmental and biological analysis. *Sensors and Actuators B: Chemical* **29**, 183-189, doi:https://doi.org/10.1016/0925-4005(95)01681-3 (1995).
- 168 Zopf, D. *et al.* Plasmonic Nanosensor Array for Multiplexed DNA-based Pathogen Detection. *ACS sensors* **4**, 335-343, doi:10.1021/acssensors.8b01073 (2019).
- 169 Gühlke, M., Selve, S. & Kneipp, J. Magnetic separation and SERS observation of analyte molecules on bifunctional silver/iron oxide composite nanostructures. *J. Raman Spectrosc.* **43**, 1204-1207, doi:10.1002/jrs.4039 (2012).
- 170 Raza, A. *et al.* ALD assisted nanoplasmonic slot waveguide for on-chip enhanced Raman spectroscopy. *APL Photonics* **3**, 116105, doi:10.1063/1.5048266 (2018).
- 171 Parakhonskiy, B. V., Abalymov, A., Ivanova, A., Khalkenkov, D. & Skirtach, A. G. Magnetic and silver nanoparticle functionalized calcium carbonate particles—Dual functionality of versatile, movable delivery carriers which can surface-enhance Raman signals. *Journal of Applied Physics* **126**, 203102, doi:10.1063/1.5111973 (2019).
- 172 Volodkin, D. V., Larionova, N. I. & Sukhorukov, G. B. Protein Encapsulation via Porous CaCO<sub>3</sub> Microparticles Templating. *Biomacromolecules* **5**, 1962-1972, doi:10.1021/bm049669e (2004).
- 173 Kamyshinsky, R. *et al.* Composite materials based on Ag nanoparticles in situ synthesized on the vaterite porous matrices. *Nanotechnology* **30**, 035603, doi:10.1088/1361-6528/aaea38 (2019).
- 174 Kosuda, K. M., Bingham, J. M., Wustholz, K. L., Van Duyne, R. P. & Groarke, R. J. in *Comprehensive Nanoscience and Nanotechnology (Second Edition)* (eds David L. Andrews, Robert H. Lipson, & Thomas Nann) 117-152 (Academic Press, 2016),doi: <https://doi.org/10.1016/B978-0-12-803581-8.00611-1>
- 175 Parakhonskiy, B. V. *et al.* Size controlled hydroxyapatite and calcium carbonate particles: Synthesis and their application as templates for SERS platform. *Colloids and Surfaces B: Biointerfaces* **118**, 243-248, doi:https://doi.org/10.1016/j.colsurfb.2014.03.053 (2014).
- 176 Wu, C., Chen, E. & Wei, J. Surface enhanced Raman spectroscopy of Rhodamine 6G on agglomerates of different-sized silver truncated nanotriangles. *Colloids and Surfaces A: Physicochemical and Engineering Aspects* **506**, 450-456, doi:https://doi.org/10.1016/j.colsurfa.2016.07.020 (2016).
- 177 del Mercato, L. L. *et al.* LbL multilayer capsules: recent progress and future outlook for their use in life sciences. *Nanoscale* **2**, 458-467, doi:10.1039/B9NR00341J (2010).
- 178 De Geest, B. G. *et al.* Intracellularly Degradable Polyelectrolyte Microcapsules. *Advanced Materials* **18**, 1005-1009, doi:https://doi.org/10.1002/adma.200502128 (2006).
- 179 Carregal-Romero, S. *et al.* NIR-light triggered delivery of macromolecules into the cytosol. *Journal of controlled release : official journal of the Controlled Release Society* **159**, 120-127, doi:10.1016/j.jconrel.2011.12.013 (2012).
- 180 Skirtach, A. G. *et al.* Laser-induced release of encapsulated materials inside living cells. *Angewandte Chemie (International ed. in English)* **45**, 4612-4617, doi:10.1002/anie.200504599 (2006).

- 181 Wu, Z., Gao, C., Frueh, J., Sun, J. & He, Q. Remote-Controllable Explosive Polymer Multilayer  
Tubes for Rapid Cancer Cell Killing. *Macromolecular Rapid Communications* **36**, 1444-1449,  
doi:10.1002/marc.201500207 (2015).
- 182 Pankhurst, Q. A., Connolly, J., Jones, S. K. & Dobson, J. Applications of magnetic nanoparticles  
in biomedicine. *Journal of Physics D: Applied Physics* **36**, R167-R181, doi:10.1088/0022-  
3727/36/13/201 (2003).
- 183 Shchukin, D. G., Gorin, D. A. & Möhwald, H. Ultrasonically Induced Opening of Polyelectrolyte  
Microcontainers. *Langmuir* **22**, 7400-7404, doi:10.1021/la061047m (2006).
- 184 Rwei, A. Y., Wang, W. & Kohane, D. S. Photoresponsive nanoparticles for drug delivery. *Nano  
Today* **10**, 451-467, doi:10.1016/j.nantod.2015.06.004 (2015).
- 185 Galaev, I. & Mattiasson, B. Thermoreactive water-soluble polymers, nonionic surfactants, and  
hydrogels as reagents in biotechnology. *Enzyme Microb Technol* **15**, 354-366,  
doi:10.1016/0141-0229(93)90122-i (1993).
- 186 Marturano, V., Cerruti, P., Giamberini, M., Tylkowski, B. & Ambroggi, V. Light-Responsive  
Polymer Micro- and Nano-Capsules. *Polymers (Basel)* **9**, 8, doi:10.3390/polym9010008  
(2016).
- 187 Skirtach, A. G. *et al.* The Role of Metal Nanoparticles in Remote Release of Encapsulated  
Materials. *Nano Letters* **5**, 1371-1377, doi:10.1021/nl050693n (2005).
- 188 Skirtach, A. G., Antipov, A. A., Shchukin, D. G. & Sukhorukov, G. B. Remote activation of  
capsules containing Ag nanoparticles and IR dye by laser light. *Langmuir* **20**, 6988-6992,  
doi:10.1021/la048873k (2004).
- 189 Yao, C. *et al.* Gold Nanoparticle Mediated Phototherapy for Cancer. *Journal of Nanomaterials*  
**2016**, 5497136, doi:10.1155/2016/5497136 (2016).
- 190 Kaletta, T. & Hengartner, M. O. Finding function in novel targets: *C. elegans* as a model  
organism. *Nature Reviews Drug Discovery* **5**, 387-399, doi:10.1038/nrd2031 (2006).
- 191 Meneely, P. M., Dahlberg, C. L. & Rose, J. K. Working with Worms: *Caenorhabditis elegans* as  
a Model Organism. *Current Protocols Essential Laboratory Techniques* **19**, e35,  
doi:10.1002/cpet.35 (2019).
- 192 Trojanowski, N. F., Raizen, D. M. & Fang-Yen, C. Pharyngeal pumping in *Caenorhabditis  
elegans* depends on tonic and phasic signaling from the nervous system. *Scientific reports* **6**,  
22940-22940, doi:10.1038/srep22940 (2016).
- 193 Cherkas, A. *et al.* Label-free molecular mapping and assessment of glycogen in *C. elegans*.  
*Analyst* **144**, 2367-2374, doi:10.1039/c8an02351d (2019).
- 194 Barros, A. G., Liu, J., Lemieux, G. A., Mullaney, B. C. & Ashrafi, K. Analyses of *C. elegans* fat  
metabolic pathways. *Methods Cell Biol* **107**, 383-407, doi:10.1016/b978-0-12-394620-  
1.00013-8 (2012).
- 195 Wang, P. *et al.* Imaging lipid metabolism in live *Caenorhabditis elegans* using fingerprint  
vibrations. *Angewandte Chemie (International ed. in English)* **53**, 11787-11792,  
doi:10.1002/anie.201406029 (2014).
- 196 Lengert, E. *et al.* Hollow silver alginate microspheres for drug delivery and surface enhanced  
Raman scattering detection. *RSC Advances* **6**, 20447-20452, doi:10.1039/C6RA02019D  
(2016).
- 197 De Los Santos, C., Chang, C.-W., Mycek, M.-A. & Cardullo, R. A. FRAP, FLIM, and FRET:  
Detection and analysis of cellular dynamics on a molecular scale using fluorescence  
microscopy. *Mol Reprod Dev* **82**, 587-604, doi:10.1002/mrd.22501 (2015).
- 198 Jahr, W., Velicky, P. & Danzl, J. G. Strategies to maximize performance in STimulated Emission  
Depletion (STED) nanoscopy of biological specimens. *Methods* **174**, 27-41,  
doi:10.1016/j.ymeth.2019.07.019 (2020).
- 199 Diaz Tormo, A., Khalenkow, D., Saurav, K., Skirtach, A. G. & Le Thomas, N. Superresolution  
4pi Raman microscopy. *Optics letters* **42**, 4410-4413, doi:10.1364/ol.42.004410 (2017).

- 200 Liu, J. *et al.* Synthesis of Mo<sub>2</sub>N nanolayer coated MoO<sub>2</sub> hollow nanostructures as high-performance anode materials for lithium-ion batteries. *Energy & Environmental Science* **6**, 2691-2697, doi:10.1039/C3EE41006D (2013).
- 201 Yoo, S., Gwon, T., Eom, T., Kim, S. & Hwang, C. S. Multicolor Changeable Optical Coating by Adopting Multiple Layers of Ultrathin Phase Change Material Film. *ACS Photonics* **3**, 1265-1270, doi:10.1021/acsp Photonics.6b00246 (2016).
- 202 Choi, M. *et al.* Multilayered Graphene Nano-Film for Controlled Protein Delivery by Desired Electro-Stimuli. *Scientific reports* **5**, 17631 (2015), doi:https://doi.org/10.1038/srep17631.
- 203 Lee, K. *et al.* Quantitative phase imaging techniques for the study of cell pathophysiology: from principles to applications. *Sensors (Basel)* **13**, 4170-4191, doi:10.3390/s130404170 (2013).
- 204 Dautry-Varsat, A., Subtil, A. & Hackstadt, T. Recent insights into the mechanisms of Chlamydia entry. *Cell Microbiol* **7**, 1714-1722, doi:10.1111/j.1462-5822.2005.00627.x (2005).
- 205 Bastidas, R. J., Elwell, C. A., Engel, J. N. & Valdivia, R. H. Chlamydial intracellular survival strategies. *Cold Spring Harbor perspectives in medicine* **3**, a010256, doi:10.1101/cshperspect.a010256 (2013).
- 206 Gitsels, A., Sanders, N. & Vanrompay, D. Chlamydial Infection From Outside to Inside. *Front Microbiol* **10**, 2329, doi:10.3389/fmicb.2019.02329 (2019).
- 207 Balsamo, G. *et al.* Compendium of Measures to Control Chlamydia psittaci Infection Among Humans (Psittacosis) and Pet Birds (Avian Chlamydiosis), 2017. *Journal of avian medicine and surgery* **31**, 262-282, doi:10.1647/217-265 (2017).
- 208 Rohde, G., Straube, E., Essig, A., Reinhold, P. & Sachse, K. Chlamydial zoonoses. *Dtsch Arztebl Int* **107**, 174-180, doi:10.3238/arztebl.2010.0174 (2010).
- 209 Szaszak, M. *et al.* Characterizing the intracellular distribution of metabolites in intact Chlamydia-infected cells by Raman and two-photon microscopy. *Microbes and infection* **15**, 461-469, doi:10.1016/j.micinf.2013.03.005 (2013).
- 210 Piontek, M. C. & Roos, W. H. Atomic Force Microscopy: An Introduction. *Methods in molecular biology (Clifton, N.J.)* **1665**, 243-258, doi:10.1007/978-1-4939-7271-5\_13 (2018).
- 211 Vanrompay, D., Ducatelle, R., Haesebrouck, F. & Hendrickx, W. Primary pathogenicity of an European isolate of Chlamydia psittaci from turkey poults. *Vet Microbiol* **38**, 103-113, doi:10.1016/0378-1135(93)90078-l (1993).
- 212 Matthäus, C. *et al.* Chapter 10: Infrared and Raman microscopy in cell biology. *Methods in cell biology* **89**, 275-308, doi:10.1016/S0091-679X(08)00610-9 (2008).
- 213 Czamara, K. *et al.* Unsaturated lipid bodies as a hallmark of inflammation studied by Raman 2D and 3D microscopy. *Scientific reports* **7**, 40889, doi:10.1038/srep40889 (2017).
- 214 Szafraniec, E. *et al.* Raman spectroscopy-based insight into lipid droplets presence and contents in liver sinusoidal endothelial cells and hepatocytes. *J Biophotonics* **12**, e201800290, doi:10.1002/jbio.201800290 (2019).
- 215 Czamara, K. *et al.* Raman spectroscopy of lipids: A review. *J. Raman Spectrosc.* **46**, doi:10.1002/jrs.4607 (2014).
- 216 Cocchiario, J. L., Kumar, Y., Fischer, E. R., Hackstadt, T. & Valdivia, R. H. Cytoplasmic lipid droplets are translocated into the lumen of the Chlamydia trachomatis parasitophorous vacuole. *Proceedings of the National Academy of Sciences of the United States of America* **105**, 9379-9384, doi:10.1073/pnas.0712241105 (2008).
- 217 Elwell, C., Mirrashidi, K. & Engel, J. Chlamydia cell biology and pathogenesis. *Nat Rev Microbiol* **14**, 385-400, doi:10.1038/nrmicro.2016.30 (2016).
- 218 Yao, J., Dodson, V. J., Frank, M. W. & Rock, C. O. Chlamydia trachomatis Scavenges Host Fatty Acids for Phospholipid Synthesis via an Acyl-Acyl Carrier Protein Synthetase. *J Biol Chem* **290**, 22163-22173, doi:10.1074/jbc.M115.671008 (2015).

- 219 Khalenkow, D., Donche, S., Braeckman, K., Vanhove, C. & Skirtach, A. G. Added Value of  
Microscale Raman Chemical Analysis in Mild Traumatic Brain Injury (TBI): A Comparison with  
Macroscopic MRI. *ACS Omega* **3**, 16806-16811, doi:10.1021/acsomega.8b02404 (2018).
- 220 San Martín Molina, I. *et al.* In Vivo Diffusion Tensor Imaging in Acute and Subacute Phases of  
Mild Traumatic Brain Injury in Rats. *eNeuro* **7**, ENEURO.0476-0419.2020,  
doi:10.1523/ENEURO.0476-19.2020 (2020).
- 221 Bell, G. Quantifying western blots: none more black. *BMC Biol* **14**, 116-116,  
doi:10.1186/s12915-016-0339-1 (2016).
- 222 Merianda, T. T., Vuppalachchi, D., Yoo, S., Blesch, A. & Twiss, J. L. Axonal transport of neural  
membrane protein 35 mRNA increases axon growth. *Journal of Cell Science* **126**, 90,  
doi:10.1242/jcs.107268 (2013).
- 223 Saar, B. G. *et al.* Coherent Raman tissue imaging in the brain. *Cold Spring Harbor protocols*  
**2014**, doi:10.1101/pdb.top081695 (2014).
- 224 Camp Jr, C. H. *et al.* High-speed coherent Raman fingerprint imaging of biological tissues.  
*Nature Photonics* **8**, 627-634, doi:10.1038/nphoton.2014.145 (2014).
- 225 Henderson, T. A. & Morries, L. D. Near-infrared photonic energy penetration: can infrared  
phototherapy effectively reach the human brain? *Neuropsychiatr Dis Treat* **11**, 2191-2208,  
doi:10.2147/NDT.S78182 (2015).
- 226 Guo, S. *et al.* Comparability of Raman Spectroscopic Configurations: A Large Scale Cross-  
Laboratory Study. *Analytical Chemistry* **92**, 15745-15756, doi:10.1021/acs.analchem.0c02696  
(2020).
- 227 Turk, N. *et al.* Comparison of Free-Space and Waveguide-Based SERS Platforms.  
*Nanomaterials (Basel, Switzerland)* **9**, doi:10.3390/nano9101401 (2019).
- 228 Liu, Q. *et al.* SERS using two-photon polymerized nanostructures for mycotoxin detection.  
*RSC Advances* **10**, 14274-14282, doi:10.1039/D0RA01909G (2020).
- 229 Gierej, A. *et al.* Poly(D,L-Lactic Acid) (PDLLA) Biodegradable and Biocompatible Polymer  
Optical Fiber. *Journal of Lightwave Technology* **37**, 1916-1923,  
doi:10.1109/JLT.2019.2895220 (2019).
- 230 Schie, I. W. *et al.* High-Throughput Screening Raman Spectroscopy Platform for Label-Free  
Cellomics. *Anal Chem* **90**, 2023-2030, doi:10.1021/acs.analchem.7b04127 (2018).
- 231 Zhang, X., Yin, H., Cooper, J. M. & Haswell, S. J. Characterization of cellular chemical dynamics  
using combined microfluidic and Raman techniques. *Anal. Bioanal. Chem.* **390**, 833-840,  
doi:10.1007/s00216-007-1564-9 (2008).
- 232 Lyu, Y. *et al.* Automated Raman based cell sorting with 3D microfluidics. *Lab on a chip* **20**,  
4235-4245, doi:10.1039/d0lc00679c (2020).
- 233 Jayakumar, N., Helle, Ø. I., Agarwal, K. & Ahluwalia, B. S. On-chip TIRF nanoscopy by applying  
Haar wavelet kernel analysis on intensity fluctuations induced by chip illumination. *Opt.*  
*Express* **28**, 35454-35468, doi:10.1364/OE.403804 (2020).
- 234 Graefe, C. T. *et al.* Far-Field Super-Resolution Vibrational Spectroscopy. *Analytical Chemistry*  
**91**, 8723-8731, doi:10.1021/acs.analchem.9b01731 (2019).
- 235 Beć, K. B., Futami, Y., Wójcik, M. J. & Ozaki, Y. A spectroscopic and theoretical study in the  
near-infrared region of low concentration aliphatic alcohols. *Physical Chemistry Chemical*  
*Physics* **18**, 13666-13682, doi:10.1039/C6CP00924G (2016).





# APPENDIX

## **Supplementary Information for Chapter 1**

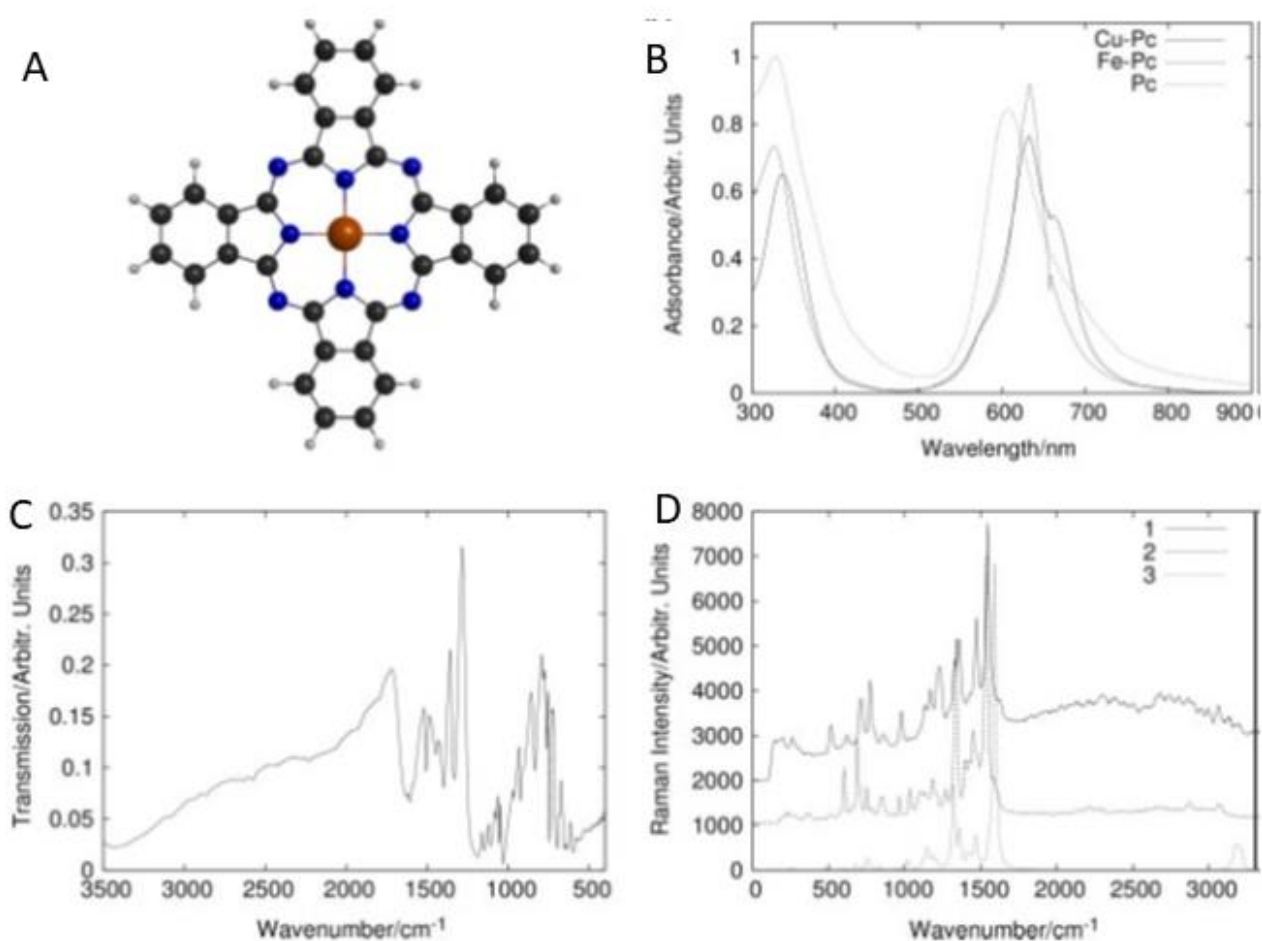


**Figure S1.1.** (A) Molecular structure of Cu-phthalocyanine tetrasulfonic acid tetrasodium salt (Cu-Pc). The sulfonate groups and sodium ions are omitted for clarity. (B) UV-vis spectra of Pc, Cu-Pc and Fe-Pc molecules. (C) FTIR absorption spectra of Cu-Pc molecules measured as a dry KBr pellet. (D) Experimentally measured resonance (line 1); experimentally measured non-resonance (line 2); and theoretically calculated (line 3) spectra of Cu-Pc. Adapted from: Bratashov, D. N. et al. <sup>36</sup>

Although the structure of phthalocyanine is known, Figure S1.1, modeling its Raman vibrations can be useful. On the one hand, modeling allows to assure that proper peak assignment is made. And it allows to investigate the influence of surrounding atoms and environment, in which these atoms are located.

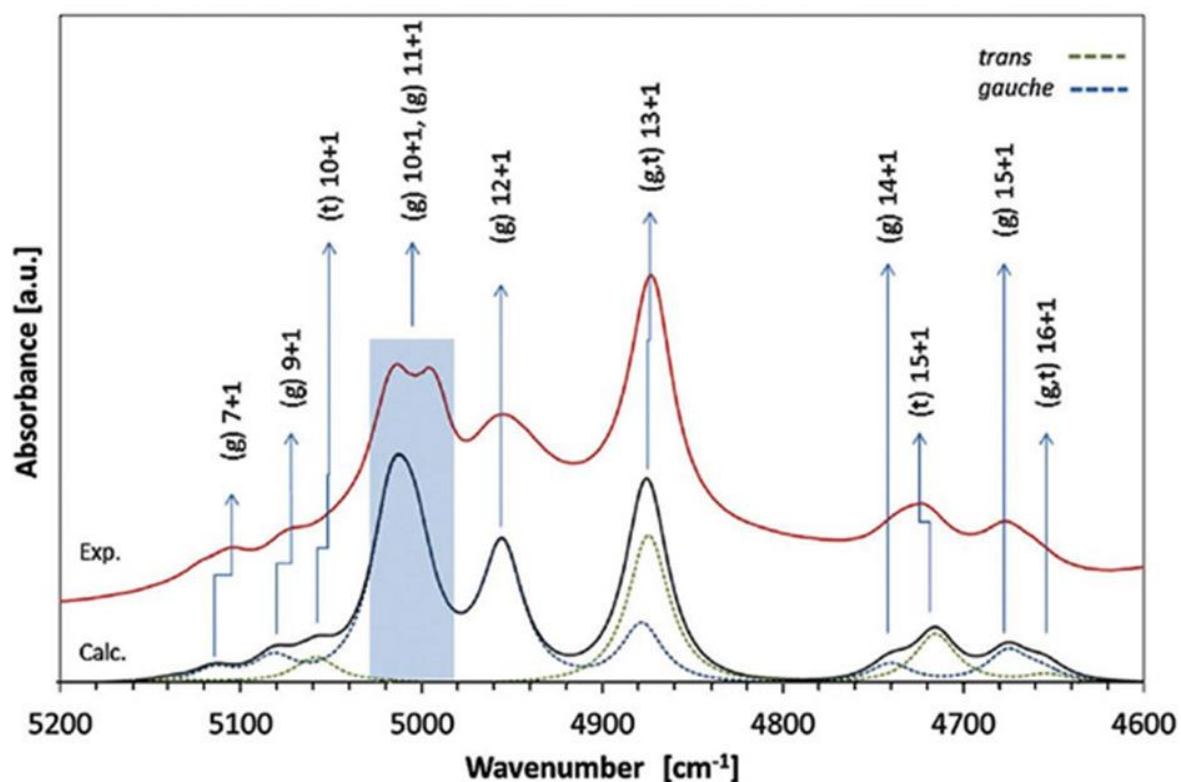


**Figure S1.2.** Band assignments in the experimental and calculated near-IR spectra of low concentration ( $5 \cdot 10^{-3}$  M  $\text{CCl}_4$ ) ethanol. The calculated NIR spectrum is based on the CPCM-B2PLYP-D/SNST level of theory. Details of the 5200–4600  $\text{cm}^{-1}$  region, adapted from Bec et al.

235

As it is shown in Figure S1.2, peak or band assignments can be also facilitated by simulation of the peaks in Raman scattering spectra. Tracing the influence of a solvent or other molecules is often enabled by simulation of scattering spectra.

## **Supplementary Information for Chapter 2**

## **S2.1 Basics of Raman data processing and analysis**

Raw Raman datasets must be preprocessed before further analysis or image generation<sup>s1</sup>. Pre-processing is done to remove the outliers, improve the signal-to-noise ratio, reduce the dimensionality and complexity of data. This leads also to the improvement of the accuracy and robustness of downstream data analysis. It was also found that preprocessing significantly enhances the performance of data mining techniques<sup>s2 s3</sup>.

### **S2.1.1 Pre-processing of Raman spectra**

#### **Smoothing of the spectral curve**

The pre-processing can be started with the smoothing of the spectral curve. The goal of this operation is to remove the low intensity noise from the measured spectra. It is caused by small fluctuations in laser power and thermal and shot noise in the detector. Typically, smoothing algorithms rely on the fact that data points are changing gradually from point to point in a real peak, while the noisy spectral points tend to change their values quickly. Therefore, the signal-to-noise ratio can be improved by replacing each spectral intensity value with the average value calculated from the surrounding data points. There are multiple smoothing algorithms, such as the Savitzky-Golay filter, moving average filter, weighted average, wavelet transformation. However, our tests show that smoothing can lead to slight changes in intensity of some peaks. Also, sometimes small peaks can be lost. Such alternation may result in false positive or false negative conclusions when two different spectra are compared. Therefore, we decided to exclude the smoothing from our pre-processing pipeline. Instead, it was found that the effects of the thermal and shot noise, and laser power fluctuation can be removed by increasing the measurement time or by acquiring several spectra and calculating the mean spectrum. The spectrum becomes smoother over time because counts from the real peaks are accumulating faster than counts from the false peaks caused by noise. It is also possible to remove the noise by taking multiple spectra from the same point of the sample and calculate the mean spectrum.

#### **Background removal**

We start the spectrum pre-processing with the background removal. A CCD camera used to detect Raman signal continuously generates a low intensity background signal. It can be

removed by, first, taking the measurements with excitation laser off so that the resulting spectrum will contain only background noise from the CCD camera, and then subtracting this spectrum from the spectrum of the sample. The other, more problematic, source of background is fluorescence of the sample itself. The strong fluorescence background is nearly always present in biological samples. However, excitation with a laser operating at 785 nm results in a lower background signal than that with lower excitation wavelengths<sup>54</sup>.

There are several ways to remove the background from the measured spectra. The first method, which we have tested, was polynomial background subtraction. Here, a polynomial curve is fitted to the spectrum and subtracted. The high order polynomials tend to follow the spectrum relatively accurate but often introduce the wave-like artifacts around zero. On the other hand, the curve, resulted from low order polynomial fitting, poorly subtracts the background from complex spectra with many peaks. Therefore, we aimed to find a more optimal method of background removal. Among the tested algorithms<sup>55</sup>, we have chosen the asymmetric least square (*als*) method for the background curve fitting<sup>56</sup>. Here, a background curve, also called – the baseline, is estimated via smoothing of the raw Raman spectrum. The function describing the baseline curve can be found using the least-squared method. The function is iteratively estimated, aiming to minimize the squared difference between the original Raman spectrum and the baseline. In the conventional least-square method, negative and positive residual errors have similar weights. However, the preference is given to positive residual square errors in the asymmetric least-square algorithm. It is done to keep the Raman peaks intact. The curve is additionally smoothed by adding the second-order derivative as another term to the estimated function. The *als* algorithm is accurate and fast, and we have confirmed that it can be applied for a broad range of biological spectra.

Additionally, after optimization of the *als* algorithm parameters for complex spectra, the same set of parameters can be used for any spectral data with lesser complexity. This removes the need to re-adjust algorithm parameters for every new dataset. An example of background removal with *als* is shown in Figure S2.1.

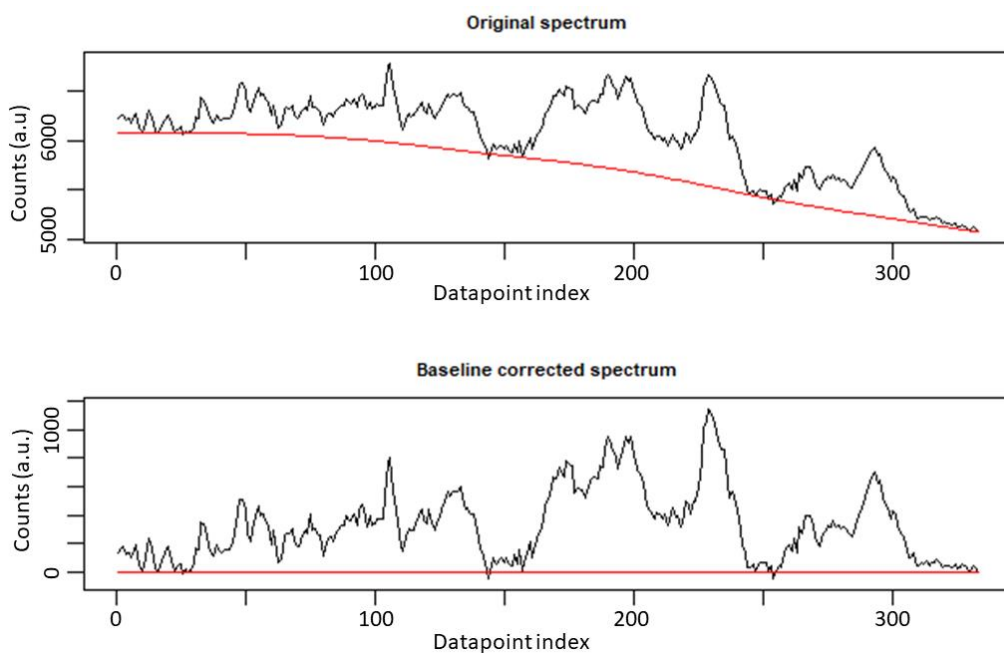


**Figure S2.1.** Background subtraction. The baseline curve, drawn in red, is estimated with a background subtraction algorithm, implemented in the baseline package for R.3.4.

### Cosmic-ray removal

Cosmic rays are highly energetic particles that originated from the sun or from outside of the solar system. When they hit atoms in the Earth atmosphere, the impact produces a cascade of charged mesons, which, subsequently, degrade to muons. The interaction of muon with CCD camera resulted in a sharp, intense peak on the Raman spectrum, Figure S2.2.

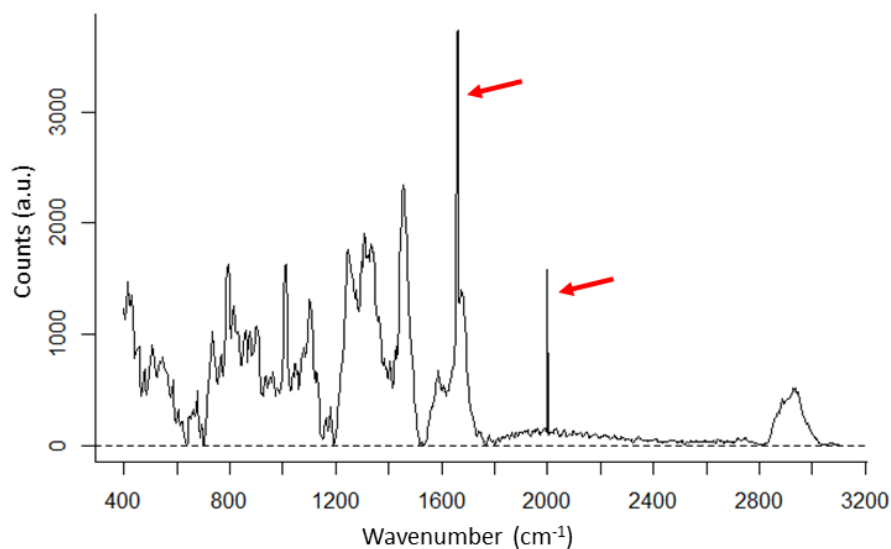


**Figure S2.2.** Raman spectrum of a bacterium. The peaks marked with red arrows originate from cosmic rays.



We have developed several methods for cosmic ray removal. In the first method, all single spectra are taken in triplets. Measurements must be done in the same spot, with the same objective and excitation laser power. Then cosmic ray in one spectrum can be filtered out by substitution with the average intensity values at this point from the other two spectra. Alternately, it is possible to solve the cosmic ray problem by merely discarding the affected spectrum and taking the new measurement.

However, none of the mentioned above approaches can be applied for area scans. Re-measuring a single datapoint in an area scan can be challenging because of possible software and hardware limitations. Taking multiple area scans in the same spot is extremely time-consuming. Also, pixels from different scans may not perfectly match, due to small changes in sample position caused by stage instability or motions of the sample. The identification of the affected spectra can also cause problems, because it may require to visually inspect hundreds of spectra from which the common area scan dataset comprises. This can be solved by constructing the heatmaps for peaks of interest. The principles of heatmap generation will be discussed in detail later in this section. The spectra with cosmic rays can be identified by looking for the most color intense pixels on the heatmap image. Then, spectra associated with those pixels can be manually inspected to confirm the presence of cosmic rays. Next, the affected part of the spectrum is substituted with the averaged intensity values calculated from the spectra of 2, 4, 6, or 8 direct neighbors. The exact number of data points used for averaging is dependent on a particular situation. For example, if the affected pixel is found at the edge of the cell membrane, it is probably not the most efficient way to calculate the substitution datapoint using the neighboring pixels associated with the cytoplasm or intracellular space. Therefore, only two neighbors may be taken into account. At the same time, if the affected pixel is in the middle of a homogeneous region of a sample, then taking the maximum number of direct neighbors would produce the most optimal result.

## **Normalization**

Normalization is an essential step in pre-processing. Even measuring the same homogeneous sample at different points or on different days may result in significant variations in peak intensity across recorded spectra. This bias in intensity has two sources. The first is the hardware conditions, such as instrument alignment and changes in laser power. The second

is caused by differences in microscope focus across the scanned points. In the area scans, the bias can be additionally introduced by fluctuations in microscope Z-stage (vertical stage) position over time, variations in the sample thickness, and by tilts of the sample.

Normalization is the transformation of data, wherein each point is divided by the largest value on the curve. In literature, there are descriptions of various normalization methods<sup>55</sup>. Depending on the nature of samples and the goal of the measurements, one normalization technique may be more suitable than another. Some of the methods developed in this thesis work are discussed below.

### **Peak normalization**

This method is applicable if a particular peak is present in all spectra in the dataset. The molecule, which produces such a peak must have the same concentration in all measured samples. Additionally, such a peak must not overlap with the peaks from other molecules in samples. If both conditions are satisfied, then the normalized spectrum is calculated by dividing the intensity of each data point in the spectrum by intensity of this peak.

Let us represent a single spectrum as a vector  $Sp = (I_1, I_2, I_3, \dots, I_n)$ ; where  $I$  is the intensity of a single spectral data points and  $n$ - the total number of data points. Then, normalized spectrum  $SpN$  can be defined as follows:

$SpN = (IN_1, IN_2, IN_3, \dots, IN_n)$ ;  $IN$ - normalized intensity of a single data point.  $n$ - the total number of data points.

$IN_i = I_i/PN$ ;  $i=1\dots n$ , where  $PN$  intensity of the peak used for normalization.

### **The min-max normalization**

In this method, the minimum and maximum intensities among the data points of the spectrum are calculated<sup>55</sup>. Then, the normalized spectrum is obtained by subtracting from each spectral point the minimum and dividing the result by the difference between the maximum and the minimum.

$$Sp_{max} = \max ((I_1, I_2, I_3, \dots, I_n))$$

$$Sp_{min} = \min ((I_1, I_2, I_3, \dots, I_n))$$

$$IN_i = (I_i - Sp_{min}) / (Sp_{max} - Sp_{min}); i=1\dots n$$

It is essential to note that in the case of the spectrum with subtracted background, the minimum intensity would be zero. Therefore, the min-max normalization *de facto* becomes the peak normalization, where the peak used for normalization is the most intense one in the spectrum. If the wavelength of the peak with the maximum intensity is different between the normalized spectra – the min-max normalization may introduce a significant bias in the dataset.

### Vector normalization

Here, the norm of the spectrum, *SpNorm*, is calculated by taking the square root of the sum of the squared intensities of the spectrum:

$$SpNorm = \sqrt{I_1^2 + I_2^2 + I_3^2 + \dots + I_n^2}$$

Then, the normalized spectrum is obtained by dividing each spectral data point by the norm:  
 $IN_i = I_i / SpNorm; i=1\dots n.$

### Peak detection and reduction of data complexity

While each peak consists of many spectral points, often only the peak's position and maximum intensity values are required for the downstream analysis. In this case, the rest of the points may be discarded, leading to a significant reduction of spectrum complexity. This reduction not only simplifies the spectral analysis but also increases the accuracy of data mining algorithms. The peak identification can be made manually by visual analysis of the plotted spectrum. However, a dataset may contain hundreds or thousands of spectra. In this case, a manual approach would be time consuming and may have a negative effect on the emotional state of the data analyst. Additionally, a possibility of human errors may introduce bias in the dataset. Therefore, it may be beneficial to make the peak identification in multi-spectral datasets using the data mining approach.

We have developed the following algorithm for peak detection and data complexity reduction, (Supplementary Information for Chapter 2 (Appendix), S2.2). It is implemented in R 3.4. The script is designed to be used inside the *hyperspec* package<sup>93</sup> data frame but can be effortlessly adjusted to be used with any data structures.

Our algorithm is based on the fact that the highest point of the peak is always the local maximum of signal intensities in the subset of data points, which forms this peak. Therefore, the task of peaks identification can be reduced to the task of finding all local maxima higher than a certain threshold defined by the user. This can be implemented with a sliding window approach. The window, defined by *lower\_window\_bound* and *upper\_window\_bound*, is moved across the dataset, and at each step, the local maximum is calculated. When the position of the local maximum inside the window overlaps with the current center of the window – then, this position is considered to be the position of the peak. The algorithm returns two vectors. First, named *wavelength* stores the wavelengths of the found peaks, and *second\_table\_of\_peaks* contain the corresponding maximum intensities of the found peaks. The input parameter *threshold* allows the user to set the minimum intensity that the datapoint must have to be considered the peak. This allows filtering out the background noise.

The complexity of the algorithm is approximately  $O(N^2)$ , where  $N$  is the size of the dataset. That is faster than brute force approaches, such as iterative least square fit based on the Gaussian or Lorentzian functions. Additionally, in contrast to peak identification algorithms, which are using neural-network-based image recognition for peak identification, the presented algorithm does not require any training sets. The results of applying the algorithm for peak identification and data complexity reduction are illustrated in Figure S2.3.

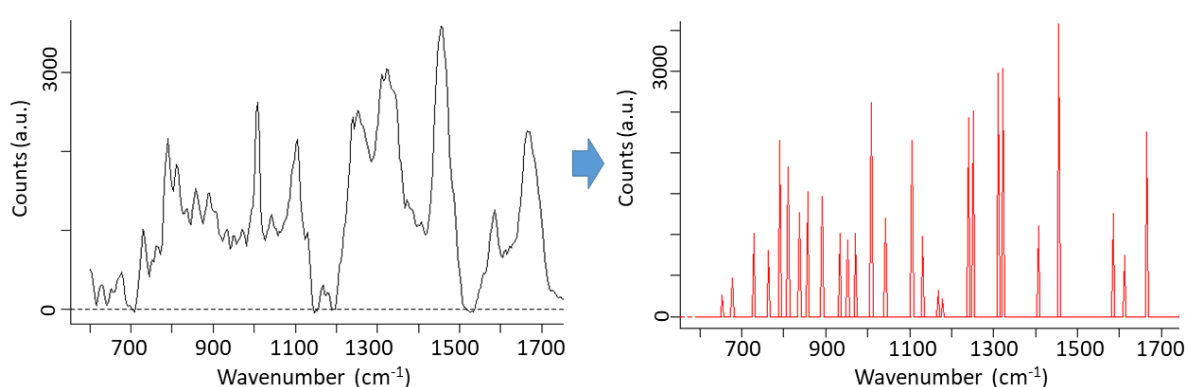


**Figure S2.3.** Spectral data complexity reduction. The reduction is made by identifying the point with maximum intensity for each peak and removal the rest of the data point.

### S2.1.2 Raman data analysis

In this section, a brief description is given on how information can be extracted from Raman spectra.

#### The single spectrum analysis

Analysis at the single spectrum level will be illustrated on an example of the spectrum taken from the spine of a fish, Figure S2.4.

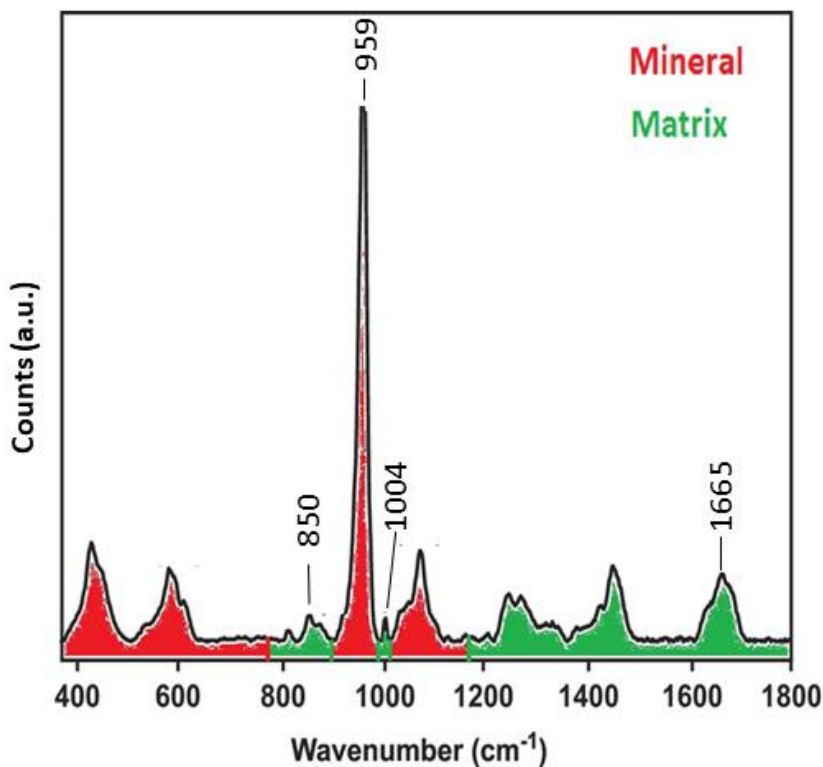


**Figure S2.4** Raman spectrum of a fish spine.

This spectrum has the following information content.

1. The peak at a specific position indicates the presence of a molecular bond, and, therefore, the molecule, associated with this position. The peak at 1665 cm<sup>-1</sup>, assigned to the amide I bonds in a protein, indicates the presence of peptides in a sample. The peaks at 1004 cm<sup>-1</sup> and 850 cm<sup>-1</sup> show the presence of amino acids phenylalanine and proline, respectively.

2. The width at half maximum of the peak can be used as a measure of crystallinity and structural orientation relative to the laser polarization. In this example, the width at half maximum of the  $959\text{ cm}^{-1}$  peak, associated with the phosphate ( $\text{PO}_4$ ) group in bone, can be used to evaluate the crystallinity of the bone mineral matrix<sup>57</sup>.

3. Intensity of a Raman peak is directly proportional to the concentration of molecules in a sample. However, without taking multiple spectra and estimating the calibration curve, it is challenging to quantify the concentration of the molecule of interest in the sample. This information can be accessed indirectly by comparing the peak ratios. For example, the phosphate to amide I peak ratios in the spectrum shown in Figure S2.4 allows making a qualitative estimation of the mineral content of the bone.

### **The analysis of the multiple spectrum dataset**

There are two types of multiple spectra datasets. The first type consists of single spectra taken from different samples and/or under various experimental conditions. Here, the dataset can be represented as a two-dimensional (2D) matrix, where each row is the intensity vector from a single spectrum.

The second type is the dataset resulted from the area scan. This data can be also stored in the form of a matrix, similar to the first type. However, the spectra positions on the scanned area are adding the extra dimensions to the matrix.

### **Clustering analysis**

Multispectral analysis can be started with sorting spectra inside the subsets according to their similarity. This can be achieved with clustering analysis. The separation, or clustering, is done using the distance between the spectra. Single Raman spectrum obtained using a Alpha300R+ Raman confocal microscope (WITec) typically consists of 1024 recorded intensities of the corresponding wavelengths. Therefore, the Raman spectrum can be represented as a single point, or vector, in the 1024-dimensional space, where each spectral point is one axis, and point intensity is the value along this axis. The spectra, which have a high degree of similarity, will be close in the 1024-dimensional space. Clustering algorithms can use the distance

between spectra in multi-dimensional space to separate spectra in clusters. After testing various basic clustering algorithms<sup>s8</sup>, such as the hierarchical clustering, fuzzy mean, and k-means, it was found that the hierarchical clustering is the most suited approach for analysis of Raman multi spectra datasets. However, before discussing its advantages and disadvantages, it is essential to describe the working principles of hierarchical clustering<sup>s8</sup>. Application of this method to the multispectral dataset results in a set of linked clusters represented in the form of a tree, Figure S2.5.

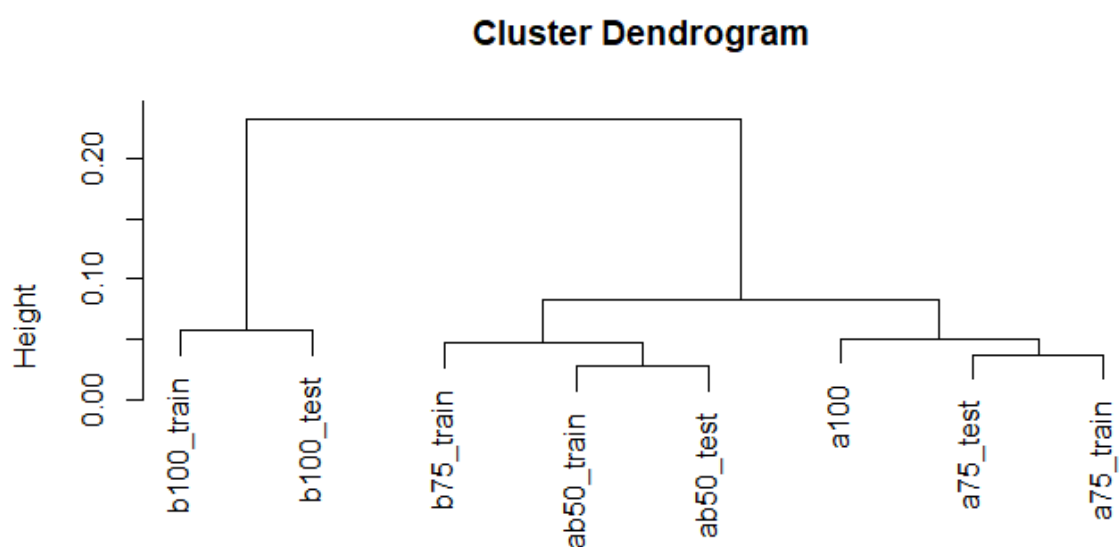


**Figure S2.5.** Example of a tree generated by the hierarchical clustering analysis.

There are two ways to generate such a tree. The divisive clustering starts from the stem – the central cluster, which contains all data points. Next, this cluster is split up into smaller data subsets, or branches. The separation is performed according to the datapoints similarity. Data subsets are divided further into smaller branches. The separation process continues until each branch contains only one data point. In the agglomerative clustering, the order is reversed. Here, one starts from individual spectra and merges them in small branches. Then, they are merged in larger branches and so on, till the arrival to the stem. In both methods, the final number of clusters can be obtained by cutting the tree at the chosen level. It should be noted that there are various methods in hierarchical clustering analysis to estimate the similarity

between the datapoints<sup>59</sup>. For, example, it is possible to use the Euclidian distance between the points in a multidimensional space (as it was discussed above in this section). Alternatively, it is possible to use such a non-Euclidian distance, such as the Bray-Curtis method, as a measure of the datapoints (dis)-similarity<sup>510</sup>. In the latter case, the counts stored in Raman spectra are used to calculate the dissimilarity coefficient, which shows how (dis)-similar two spectra are.

The advantage of hierarchical clustering is that this is a semi-unsupervised method. The datapoint separation is calculated only once, and the number of final clusters can be changed by simply cutting the tree at different levels. In other basic clustering methods, it is often necessary to define the desired number of clusters before the clustering analysis. This often requires the data analyst to make an educated guess on how many subsets can exist in such a dataset. The quality of a guess may depend on the amount of known information about the dataset. Then, the resulted clusters must be examined, evaluated, and in case of non-satisfactory result – the clustering analysis is repeated with a different number of clusters. In hierarchical clustering, it is also necessary to make such a guess. However, the structure of the tree provides an additional level of information about how the spectra are related to each other, helping to select the optimal number of clusters.

Clustering analysis can be used for sample identification and outlier removal. This concept is illustrated in Figure S2.6. The spectrum from the sample of interest, marked sample1, was grouped together with spectra from *Escherichia coli* (*E. coli*) on the lowest level of the hierarchy. This indicates the high similarity between the spectra and is a strong indication that the unknown sample of interest is an *E. coli* bacterium. It may be beneficial to include a few outliers in the dataset to increase the degree of certainty. In this example, outliers are spectra from a *HeLa* cell and silica. It should be noticed that the spectrum from a *HeLa* cell is also clustered together with spectra from an *E. coli* bacterium but at a higher hierarchical level. It is however expected, because bacteria and cells share a certain degree of similarity in their biochemical composition. At the same time, the spectrum from silica was set entirely apart from organic spectra on the hierarchical tree. Interestingly, according to the hierarchical tree in Figure S2.6, the spectrum from *E. coli* bacterium is more similar to an eukaryotic cell than to a *Bacillus* bacteria. This example illustrates the fact that the hierarchical tree based on Raman spectra does not always correlate with the phylogenic tree.



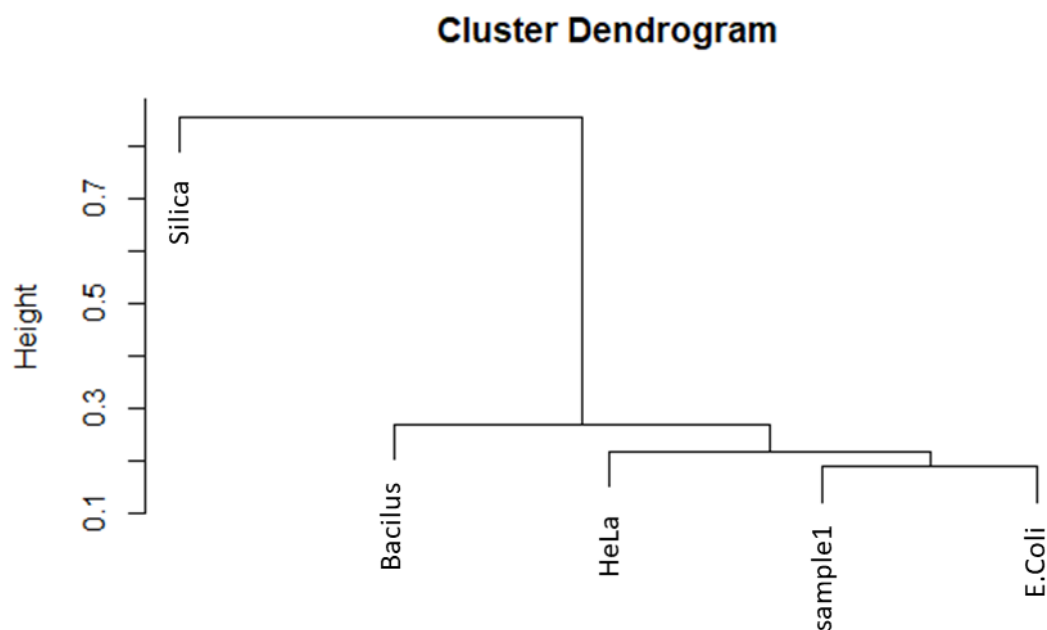


**Figure S2.6.** Sample identification using hierarchical clustering.

### Generation of molecular images

An image can be represented as a two-dimensional matrix, where the column and row indexes of the matrix cell correspond to the coordinate point of a pixel on the image. The value stored inside the matrix cell corresponds to the color of this pixel. The area scan dataset can be depicted in a similar manner. The matrix column and row indexes would also correspond to the position on the scanned area. However, here matrix cell would contain the spectrum taken at this point. These spectra are vectors in a multidimensional space. Therefore, the task of generating images from the Raman area scan is reduced to the task of transforming the multidimensional spectral vectors to the form that can be visualized on a two-dimensional image. There are two main approaches to the Raman molecular imaging problem: univariate and multivariate. In an univariate approach, the image is generated as a heatmap based on intensity of a single peak. The higher the intensity of the peak in a specific position on the area scan is – the brighter the corresponding pixel on the molecular image is. The peak selected for heatmap generation may be associated with a molecule of interest. In such a case, the resulted image allows estimating the concentration of this molecule in various points of the scanned area. The disadvantage of such an approach is that most of spectral data points are discarded.

In multivariate approaches, the image is generated based on multiple peaks. As it is mentioned above, it is challenging to represent multidimensional information on a two-dimensional image. Therefore, the complexity of the Raman dataset must be reduced. This can be done by dividing the analyzed Raman spectrum into groups based on their similarity. Then, each spectrum in the area scan matrix is substituted by the identifier of the group, to which this spectrum belongs. By assigning to each similarity group an unique pseudo color, the molecular image can be generated. It allows visualization of the distribution of various molecules of interest in the scanned area. At the same time, it does not always allow estimating the concentration, like in the univariate approach.

An example of implementation of basic pre-processing and imaging pipeline in *R* can be found in Supplementary Information for Chapter 2 (Appendix), S2.2.

## **S2.2. Raman data preprocessing in R**

### **Single spectrum dataset**

The script presented in this section is designed for pre-processing the single Raman spectra in *.spc* format, generated by *WITec Control4* software.

The pre-processing includes background subtraction, normalization, intensity values adjustments, data labeling. The results are then converted into the table text file, which can then be imported into Excel or Matlab.

```
#loading required libraries
```

```
library("hyperSpec") # hyperSpec package
```

```
library("baseline") # Contains all kinds of functions for baseline removal
```

```
library(MALDIquant) #library used for vector normalization
```

```
#set working directory where raw spectra are stored
```

```
setwd('d://test')
```

```
files=list.files(pattern=".spc")
```

*# initialize the variables*

*#variable is used to control whether the meta-data is already stored in a save file. 0-is not stored. 1- is stored*

*header\_of\_saved\_file=0*

*#flags used while combining the single spectral datasets into one dataset. see bellow*

*i2=0*

*total=0*

*#Start loop. It will process spectra in spc format one by one, save the results into a file #and combine single spectra into one dataset named "total", which can be then used #for further analysis*

*#f is the name of spc file currently processed*

*for (f in files)*

*{*

*#read the spectrum from the file and store it in hyperspec format inside the variable c1*

*c1=read.spc(f)*

*#select the region of interest. In example bellow it is the region from 200 till 3200 cm-1*

*c2=c1[,200~3200]*

*#substract the background*

*wavelengths=c2@wavelength*

*b<-baseline(c2\$spc,method="als",lambda = 4, p = 0.001, maxit = 50)*

*c2\$spc=getCorrected(b)*

*#check that all intensity values after background subtraction are positive*

*for(i in 1:length(c2\$spc))*

*{*

*if(c2\$spc[i]<0){c2\$spc[i]=0}*

```
}
```

```
#Normalisation using vector normalization method from MALDIquant package
```

```
hs=c2
```

```
mq <- list()
```

```
for (i in 1:length(hs)){
```

```
mass.spectrum <- createMassSpectrum(mass=wavelengths, intensity=hs@data$spc[i,])
```

```
#metaData(mass.spectrum) <- list(name=cell.name[i])
```

```
mq <- c(mq, mass.spectrum)
```

```
}
```

```
mq.norm <- calibrateIntensity(mq, method="TIC", range=c(200, 3200))
```

```
matrix.spectra <- matrix(nrow= length(mq.norm), ncol = length(wavelengths))
```

```
for (i in 1:length(mq.norm)){
```

```
matrix.spectra[i,] <- intensity(mq.norm[[i]])
```

```
}
```

```
#c2 is hyperspec dataframe which will now contain normalized spectrum with subtracted  
#background
```

```
c2 <- new ("hyperSpec", spc = matrix.spectra, wavelength = wavelengths)
```

```
#alternative normalization methods. They may be used instead of the one presented above
```

```
#####
```

```
#vector normalization
```

```
#a.k1 <- c2$spc - rowMeans(c2$spc) # Centering of intensities
```

```
#a.k2 <- a.k1/sqrt(rowSums(a.k1^2)) # Centered intensities divided by the length of the  
#spectrum (as vector)
```

```
#rowSums(a.k2^2) # This should be 1
```

```
#c2.norm=c2
```

```
#c2.norm$spc=a.k2
```

```
#c2=c2.norm
```

```
## min-max normalization- extremely simple-just one line of code
```

```
# can be used only if all spectra have the same max peak
```

```
#make sure that all minimum points are equal or greater than 0
```

```
#c2.norm=c2
```

```
#c2.norm$spc=(c2$spc-min(c2$spc))/(max(c2$spc)-min(c2$spc))
```

```
#c2=c2.norm
```

```
#####
```

```
#label the spectrum. Here the label is automatically generated based on the name of the  
#processed spc file
```

```
f=gsub(" ","_",f)
```

```
f=gsub(".spc","",f)
```

```
c2$label=f
```

```
#Multiply normalized intensities by 1000 because intensity values after normalization are  
#very low. This step is not mandatory and does not affect the data in any way. The reason to  
#do this is to make it easier to read final spectra
```

```
c2$spc=c2$spc*1000
```

```
#Combine all the normalized spectra into a single hyperspec dataframe
```

```
#if variable i2 is 0 then we initialize the dataframe named "total," where we want to store all  
#our spectra, by storing the current spectrum inside it
```

```
#if i2 equals to 1; then we simply add the next spectrum to it
```

```
if (i2==1)
```

```
{
total=rbind(total,c2)
}
```

```
if (i2==0)
```

```
{
total=c2
```

```
i2=1
```

```
}
```

*#Save as text file, one string at a time. The string contains the Raman intensities of the resulting #pre-processed spectrum*

*#First, we write the header. The flag variable header\_of\_saved\_file is used to make sure that #header will be written only once*

```
if (header_of_saved_file!=1) {
```

*# Header format: Row title "Wavelength", followed by all the wavelengths in this example #by wavelength from 200 till 3200 cm-1.*

```
a=c("wavelength",wl(c2))
```

```
write(a,"test2.txt", append=TRUE,ncol=length(c2$spc)+1)
```

```
header_of_saved_file =1
```

```
}
```

*#write the raman intensities of pre-processed file*

*a=c(f,c2\$spc) ## Row title 'name of the current file', followed by all the intensities.*

```
write(a,"test2.txt", append=TRUE,ncol=length(c2$spc)+1)
```

```
}
```

### **Pre-processing area scan dataset**

The script is written to process data stored in *spc* format and produced by WITec Control-4 software package. The pre-processing of the area scan is similar to single spectrum pre-processing. The only difference is that in order to generate a molecular image of the scanned area the spatial coordinates must be assigned to each data point. A potential challenge with

the used software package (WITec Control-4) is that it stores the area scan as a single vector of multiple single spectra. No metadata such as spatial coordinates is stored. This can be solved by calculating the coordinate axis using data provided by an user such as the number of scanned points per line, the number of lines, and the resolution. Then, a label containing the spatial coordinates is assigned to each point of the spectral vector.

The script will store the pre-processed file in a table text file, which is compatible with Excel and Matlab.

```
#area scan pre-processing
```

```
library("hyperSpec") # hyperSpec package
```

```
library("baseline") # Contains all kinds of functions for baseline removal
```

```
library(MALDIquant) #contains function for vector normalization
```

```
#make the list of all files in spc format in the working directory
```

```
files=list.files(pattern=".spc")
```

```
print(files)
```

```
#choose file you want to process – here we choose the 4th spc file in the list
```

```
f=files[4]
```

```
print(f)
```

```
#read file and store it in hyperspec dataframe
```

```
hs=read.spc(f)
```

```
#select the spectral range of interest. Here it is from 600 to 1800 cm-1
```

```
hs=hs[,600~3200]
```

```
wavelengths <- hs@wavelength
```

```
#it is necessary to manually set the size of the scanned area so that the coordinates vectors  
#can be calculated.
```

```
#ppl scanned points per line or the size of X-axis,
```

```
#lines- how many lines were scanned or Y-axis of the image,
```

*#pxl.um- is the resolution- how many points are scanned per um. The correct settings of this parameter are necessary to correctly display the dimensions on all generated molecular images*

```
ppl <- 40
```

```
lines <- 30
```

```
pxl.um <- 1
```

*#generate the XY coordinate matrix*

```
XY <- data.frame(cbind(rep((1:ppl)*1/pxl.um,lines),rep((1:lines)*1/pxl.um,each=ppl)))
```

```
colnames(XY) <- c("X","Y")
```

*#and assign the coordinates to the scanned points*

```
hs$x <- XY$X
```

```
hs$y <- sort(XY$Y, decreasing=TRUE)
```

```
labels(hs,"x") <- as.character("x /  $\mu\text{m}$ ")
```

```
labels(hs,"y") <- as.character("y /  $\mu\text{m}$ ")
```

```
plot(hs, "spcprctI5")
```

*#generate the raw molecular image using the averaged intensities of datapoints in the #selected spectral range*

```
plotmap(hs,spc~x*y,func.args = list(na.rm = TRUE),col.regions = topo.colors(100))
```

*#background removal*

```
for (ab in 1:length(hs))
```

```
{
```

```
  b<-baseline(hs[ab]$spc,method="als",lambda = 3, p = 0.001, maxit = 50)
```

```
  hs[ab]$spc=getCorrected(b)
```

```
  for(i in 1:length(hs[ab]$spc))
```

```
  {
```

```
    if(hs[ab]$spc[i]<0){hs[ab]$spc[i]=0}
```



```

}
}
#generate the molecular image after background removal
plotmap(hs,spc~x*y,func.args = list(na.rm = TRUE),col.regions = topo.colors(100))

#normalization
wavelengths <- hs@wavelength
mq <- list()
for (i in 1:length(hs)){
  mass.spectrum <- createMassSpectrum(mass=wavelengths, intensity=hs@data$spc[i,])
  #metaData(mass.spectrum) <- list(name=cell.name[i])
  mq <- c(mq,mass.spectrum)
}
mq.norm <- calibrateIntensity(mq, method="TIC",range=c(2800, 3200))

matrix.spectra <- matrix(, nrow= length(mq.norm), ncol = length(wavelengths))
for (i in 1:length(mq.norm)){
  matrix.spectra[i,] <- intensity(mq.norm[[i]])
}
hs <- new ("hyperSpec", spc = matrix.spectra, wavelength = wavelengths)
hs$x <- XY$X
hs$y <- sort(XY$Y, decreasing=TRUE)
labels(hs,"x") <- as.character("x /  $\mu$ m")
labels(hs,"y") <- as.character("y /  $\mu$ m")
hs$spc=hs$spc*1000
#after the normalization and background removal
#hs dataframe now contains the final normalized spectra
##saving the data

```

```

c2=hs
#check if the dataset is an area scan
if (length(c2[])>2){

#generate header
a=c("x","y",wl(c2))
f_name="put name of the file where the data must be saved"
write(a,f_name,append=TRUE,ncol=length(c2$spc)+2)
#write_data
x1=1
y1=1
i=1
x=ppl
y=lines
for (x1 in 1:x)
{
for (y1 in 1:y)
{
a=c(x1,y1,c2[i]$spc)
write(a,f_name,append=TRUE,ncol=length(c2[i]$spc)+2)
i=i+1
}
}
}

#heatmap generation
#the peak variable define the peak of interest used for heatmap generation

```

```

peak=1004
plotmap(hs[,,,peak],spc~x*y,func.args = list(na.rm = TRUE),col.regions = topo.colors(100))

#clustering analysis and molecular image generation
#clustering
# Hierarchical Cluster Analysis (HCA)
par(mfrow = c(1,1)) #set to plot in 1 windows
dist <- dist(c2$spc)
dendrogram <- hclust(dist,method="ward")
plot(dendrogram)

#select the height where to cut the dendrogram. Here we cut it into 6 clusters
c2$clusters=as.factor(cutree(dendrogram,6))

#bellow is demonstrated how to examine the clusters and compare their mean spectra
x1=subset(c2,clusters==1)
rownames(x1) #examine which spectra were allocated to cluster 1
x2=subset(c2,clusters==2)
rownames(x2)
x3=subset(c2,clusters==3)
rownames(x3)
#plotting the mean spectra of the clusters 1, 2, 3
plot(mean(x1))
plot(mean(x2),add=TRUE,col="red")
plot(mean(x3),add=TRUE,col="blue")

#plot the molecular image based on clustering analysis
plotmap(c2, clusters~x*y,col.regions= topo.colors(100))

```

## Complexity reduction

The algorithm below will identify all peaks and reduce the complexity of spectral data by keeping only the data points, where the maximum corresponding peak intensities are stored. All other data points will be set to zero. The algorithm uses a sliding window approach. The window is moved (once) through the vector, which contains the measured intensities and will find the local maximum inside the window. If the found maximum is directly in the middle of the window, then this point is the top point of the peak.

```
#function extracts peaks by finding local MAXIMUM in the centre of the window.

#function arguments- spectr- spectrum in hyperspec format. step – defines the sensitivity
#of the algorithm. The smaller the value-the smaller peaks will be resolved. Must be integer
#number and be >1

make_peak_table<-function(spectr,step) {

#initialization of variables. peaktable- vector where the found peaks will be stored.
#wavelength – vector where the wavelengths of the found peaks will be stored

peaktable=0

wavelength=0

#c3 - temporary variable to store the analyzed spectrum.

c3=spectr

a1=0

for (i in (step+1):(length(c3$spc)-step))

{c=i-step

b=i+step

d=max(c3$spc[c:b])

#if local maximum is in the middle of the window- store its intensity inside the peaktable
#vector and wavelength inside the wavelength[] vector

if (d==c3$spc[i]) {peaktable[a1]=d

wavelength[a1]=wl(c3)[i]

a1=a1+1}

}

#return the results in the form of hyperspec format dataframe
```

```
#set intensities of all data points in analyzed spectrum to 0 and fill the dataframe with found  
#maximum intensities of the identified peaks
```

```
c3$spc[]=0
```

```
a1=1
```

```
d=length(wavelength)
```

```
for (i in 1:length(wl(c3)))
```

```
{
```

```
  if(wavelength[a1]==wl(c3)[i]){
```

```
    c3$spc[i]=peaktable[a1]
```

```
    if(a1<d) {a1=a1+1}
```

```
  }
```

```
}
```

```
#return the resulting dataframe to the user
```

```
return(c3)
```

```
}
```

```
#example of usage
```

```
#total dataframe contains multiple pre-processed single spectra. Let's reduce the  
#complexity of the first spectrum in this dataset
```

```
#call function make_peak_table
```

```
a1=make_peak_table(total[1],3)
```

```
#plot the original spectrum
```

```
plot(total[1])
```

```
#plot the transformed spectrum
```

```
plot(a1)
```

### S2.3 Raman molecular images

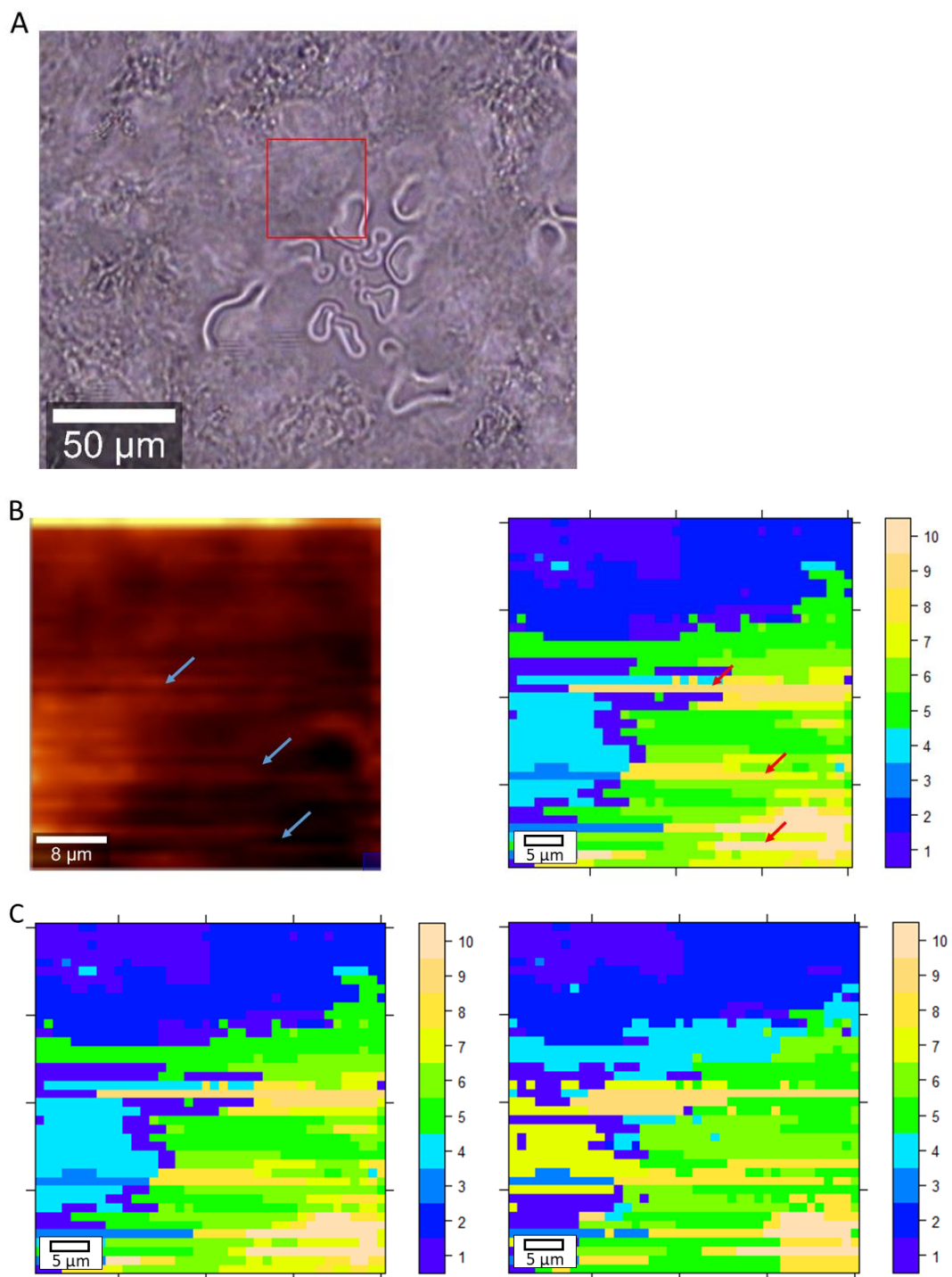


**Figure S2.6.** (A) Light microscope images of rat kidney tissue. The red rectangle marked the area scanned with Raman. (B) Red and blue arrows marked the image artifacts caused by detached tissue debris. (C) Comparison of normalized and non-normalized Raman clustering image.

## References to Supplementary Information for Chapter 2

- S1 Bocklitz, T., Walter, A., Hartmann, K., Rösch, P. & Popp, J. How to pre-process Raman spectra for reliable and stable models? *Analytica chimica acta* **704**, 47-56, doi:10.1016/j.aca.2011.06.043 (2011).
- S2 Martyna, A. *et al.* Improving discrimination of Raman spectra by optimising preprocessing strategies on the basis of the ability to refine the relationship between variance components. *Chemometrics and Intelligent Laboratory Systems* **202**, 104029, doi:https://doi.org/10.1016/j.chemolab.2020.104029 (2020).
- S3 Storey, E. E. & Helmy, A. S. Optimized preprocessing and machine learning for quantitative Raman spectroscopy in biology. *J. Raman Spectrosc.* **50**, 958-968, doi:10.1002/jrs.5608 (2019).
- S4 Yang, S. *et al.* Laser wavelength dependence of background fluorescence in Raman spectroscopic analysis of synovial fluid from symptomatic joints. *J. Raman Spectrosc.* **44**, 1089-1095, doi:10.1002/jrs.4338 (2013).
- S5 Gautam, R., Vanga, S., Ariese, F. & Umapathy, S. Review of multidimensional data processing approaches for Raman and infrared spectroscopy. *EPJ Techniques and Instrumentation* **2**, 8, doi:10.1140/epjti/s40485-015-0018-6 (2015).
- S6 Eilers, P. H. C. Baseline Correction with Asymmetric Least Squares Smoothing. *Anal. Chem* **75**, 3631–3636 (2003).
- S7 Mandair, G. S. & Morris, M. D. Contributions of Raman spectroscopy to the understanding of bone strength. *Bonekey Rep* **4**, 620-620, doi:10.1038/bonekey.2014.115 (2015).
- S8 Miljković, M. *et al.* Label-free imaging of human cells: algorithms for image reconstruction of Raman hyperspectral datasets. *Analyst* **135**, 2002-2013, doi:10.1039/c0an00042f (2010).
- S9 Aljohani, A., Lai, D. T. C., Bell, P. C. & Edirisinghe, E. A. in *Intelligent Computing Methodologies*. (eds De-Shuang Huang, Abir Hussain, Kyungsook Han, & M. Michael Gromiha) 719-731 (Springer International Publishing).
- S10 Tito, R. Y. *et al.* Brief Report: Dialister as a Microbial Marker of Disease Activity in Spondyloarthritis. *Arthritis & rheumatology (Hoboken, N.J.)* **69**, 114-121, doi:10.1002/art.39802 (2017).





## **Supplementary Information for Chapter 4**

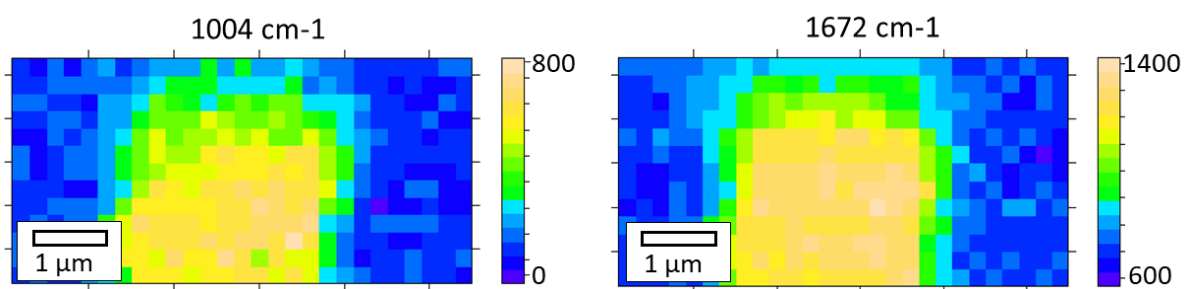


**Figure S4.1.** Raman heatmap images of a cross-section of a cable bacterium.

## **Supplementary Information for Chapter 5**

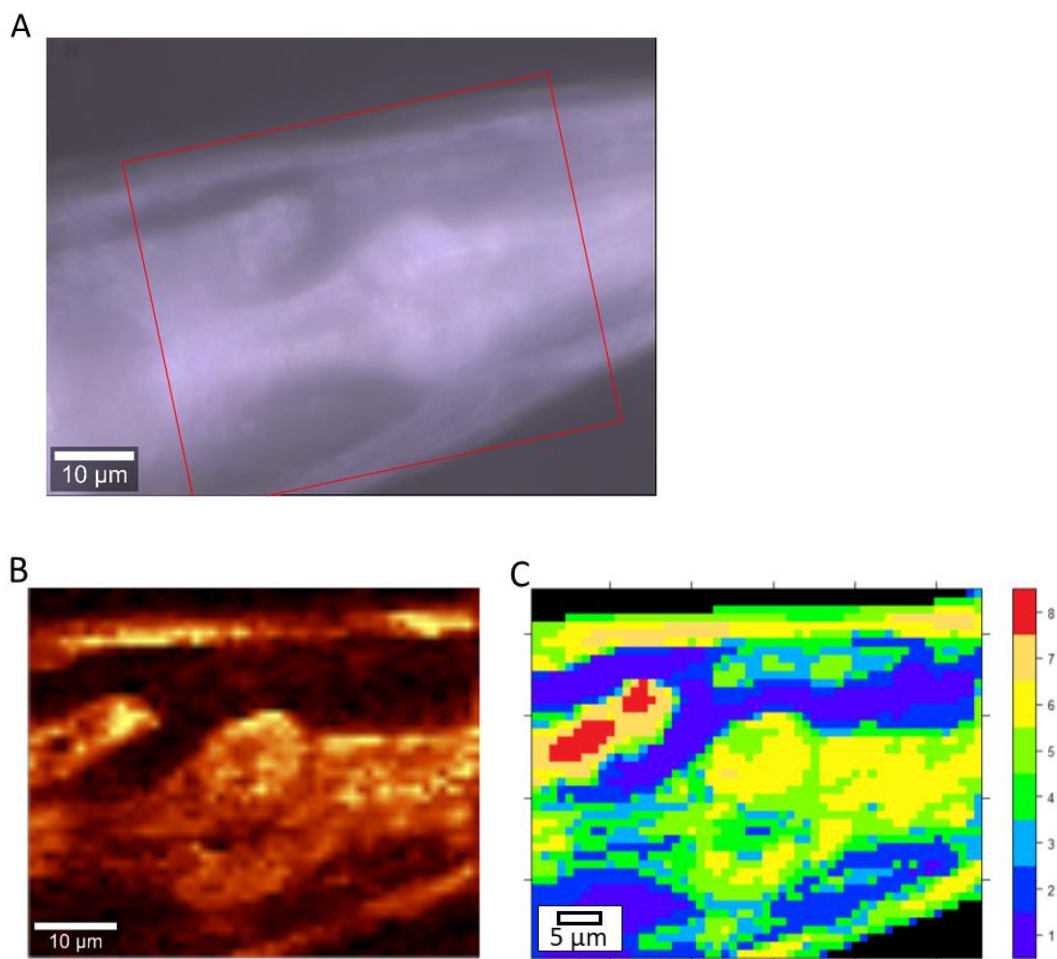


**Figure S5.1.** (A) Optical microscope image of head region of *C. elegans* worm. (B) Raman heatmap constructed based on intensity of  $1665\text{ cm}^{-1}$  peak. It shows the alpha-helix proteins and unsaturated fatty acids distribution. (C) Molecular image is generated by clustering analysis where pixels with a similar molecular fingerprint are depicted with the same false color.

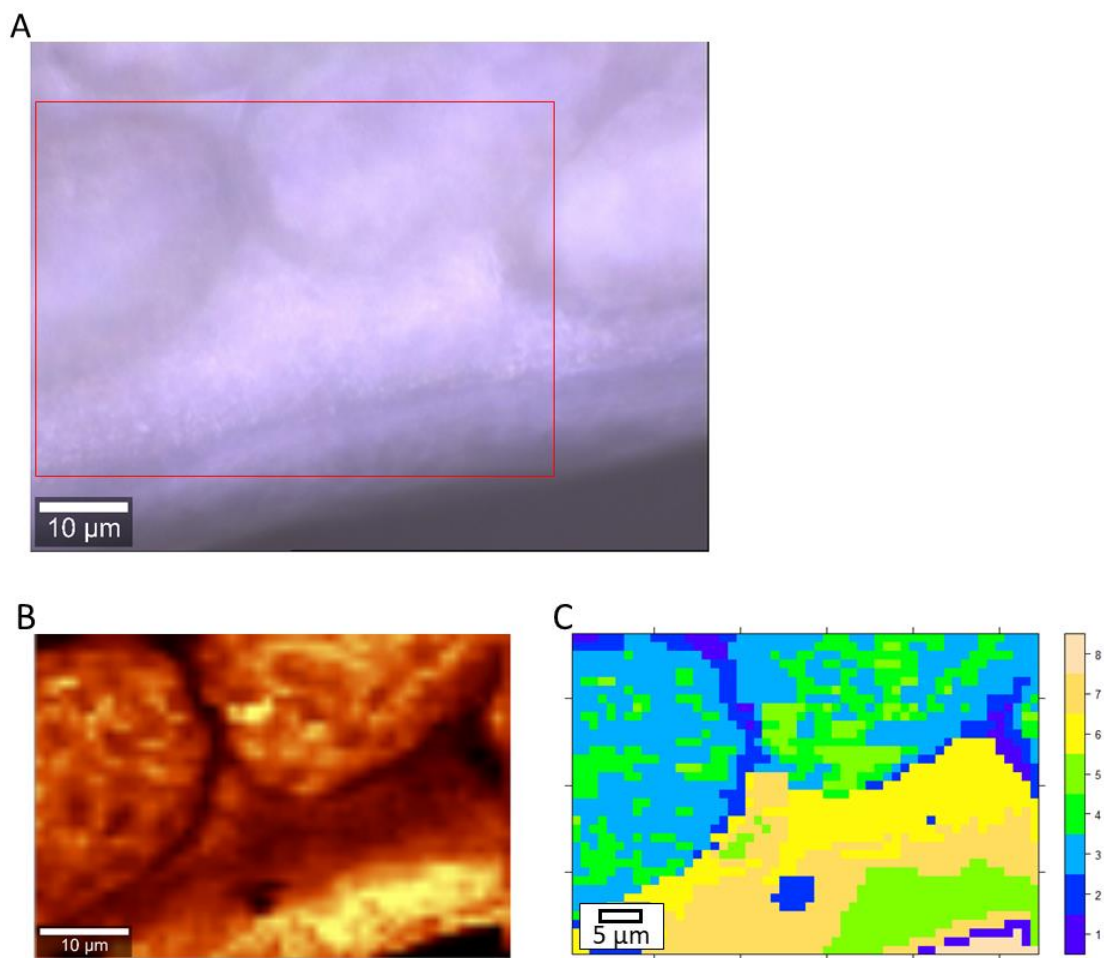


**Figure S5.2.** (A) Optical microscope image of oocytes in the middle section of *C. elegans* worm. (B) Raman heatmap constructed based on intensity of  $1665\text{ cm}^{-1}$  peak. It shows the alpha-helix proteins and unsaturated fatty acids distribution. (C) Molecular image is generated by clustering analysis where pixels with a similar molecular fingerprint are depicted with the same false color.

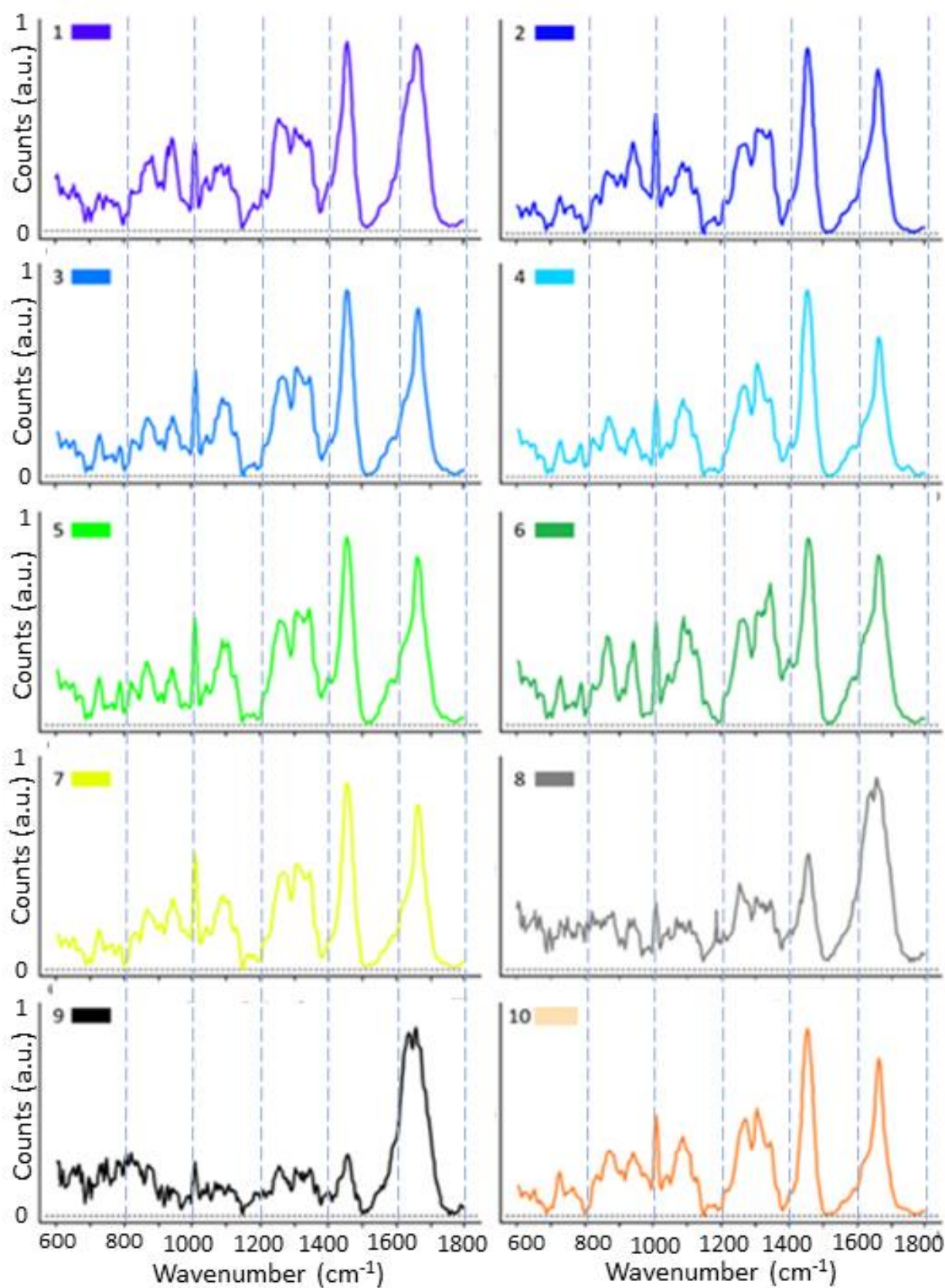


**Figure S5.3** The mean Raman spectra of clusters from Figure 5.7 (C). The color and the number of each spectrum corresponds to the color and the number of the cluster in Figure 5.7 (C).

## **Supplementary Information for Chapter 6**

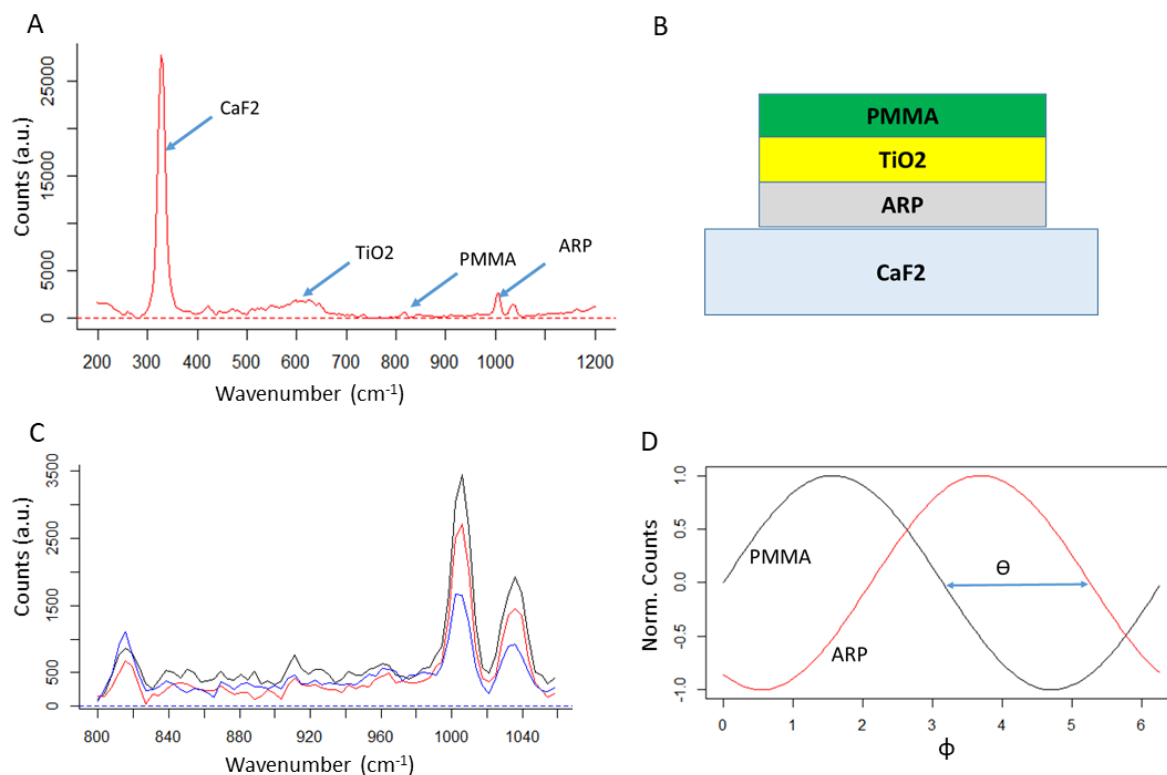


**Figure S6.1.** (A) Raman spectrum of scaffold composed of three nanolayers and deposited on a CaF<sub>2</sub> slide. (B) Schematics of the scaffold composition. (C) PMMA and ARP spectrum under different phase configuration, (D).

The multilayer scaffold was analyzed with Raman 4Pi microscope. Sample was composed of three nanolayers: polymethyl methacrylate (PMMA), amorphous titanium oxide (TiO<sub>2</sub>) and e-beam resist (ARP). Each layer has a distinct peak on Raman molecular fingerprint of the scaffold, Figure S6.1, A. Nanolayers were deposited on an ultra-thin CaF<sub>2</sub> slide, Figure S6.1, B. Next, 4Pi Raman spectra were recorded, each with different phase interactions and, as result, different Raman peak intensities, Figure S6.1, C. In the next step, the profile of the phase interference, which follows the cosine curve, is interpolated for each layer, Figure S6.1, D. The maximum of Raman intensity (the maximum point of the cosine curve) is chosen when the fringe maximum is in the middle of the layers. Therefore, using  $\theta$  - the phase shift between the cosine from different layers and the distance between those layers can be estimated.



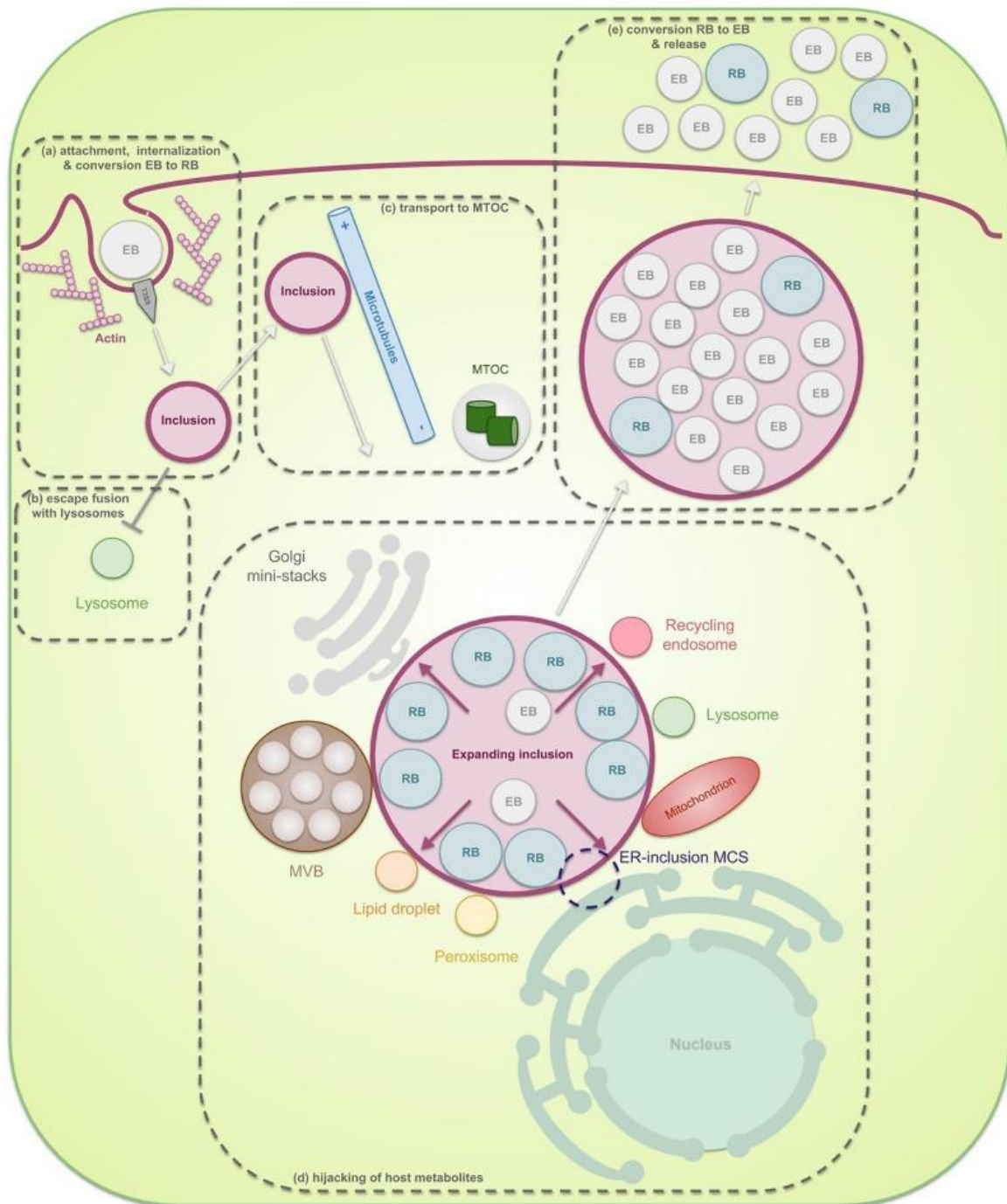


**Figure S6.2.** *Chlamydia* alternates between two morphological forms: Elementary body (EB) and reticulate body (RB). (a) At the start of infection, extracellular infectious EBs use bacterial ligands to bind receptors on the surface of the host cell. The attachment subsequently enables internalization of bacteria into a vesicle inside the host cell, called the inclusion. Internalization can be both dependent or independent of actin, but since the actin-dependent process has been studied more extensively, it is the one depicted in the figure. Herein, EBs inject pre-packed

*T3SS effectors into the host cytoplasm as soon as contact with the host is established, leading to reorganization of actin and uptake of the EBs. Next, the EBs, residing inside the inclusion, are transformed into RBs. RBs are metabolically active particles, which are capable to amplify through binary fission. (b) These RBs immediately produce early effectors, which modify the inclusion membrane in order to prevent lysosomal degradation. (c) Furthermore, the inclusion starts traveling across microtubules away from the periphery and towards the microtubule organizing center (MTOC). (d) Once the inclusion reaches the nutrient-rich peri-Golgi region, the pathogen hijacks host cell metabolites to support its own growth as well as the growth of the inclusion membrane, necessary to allow room for the expanding RBs. Nutrients are obtained through specific interactions of the inclusion with multiple host cell organelles such as fragmented Golgi mini-stacks, the ER, lipid droplets, peroxisomes, lysosomes, recycling endosomes, mitochondria, and multivesicular bodies (MVBs). (e) Finally, the expanded inclusion fills up most of the host cell cytoplasm, after which the RBs are transformed back to EBs. These then exit the host cell to infect new cells. Figure was adapted from Gitsels et al.<sup>206</sup>*

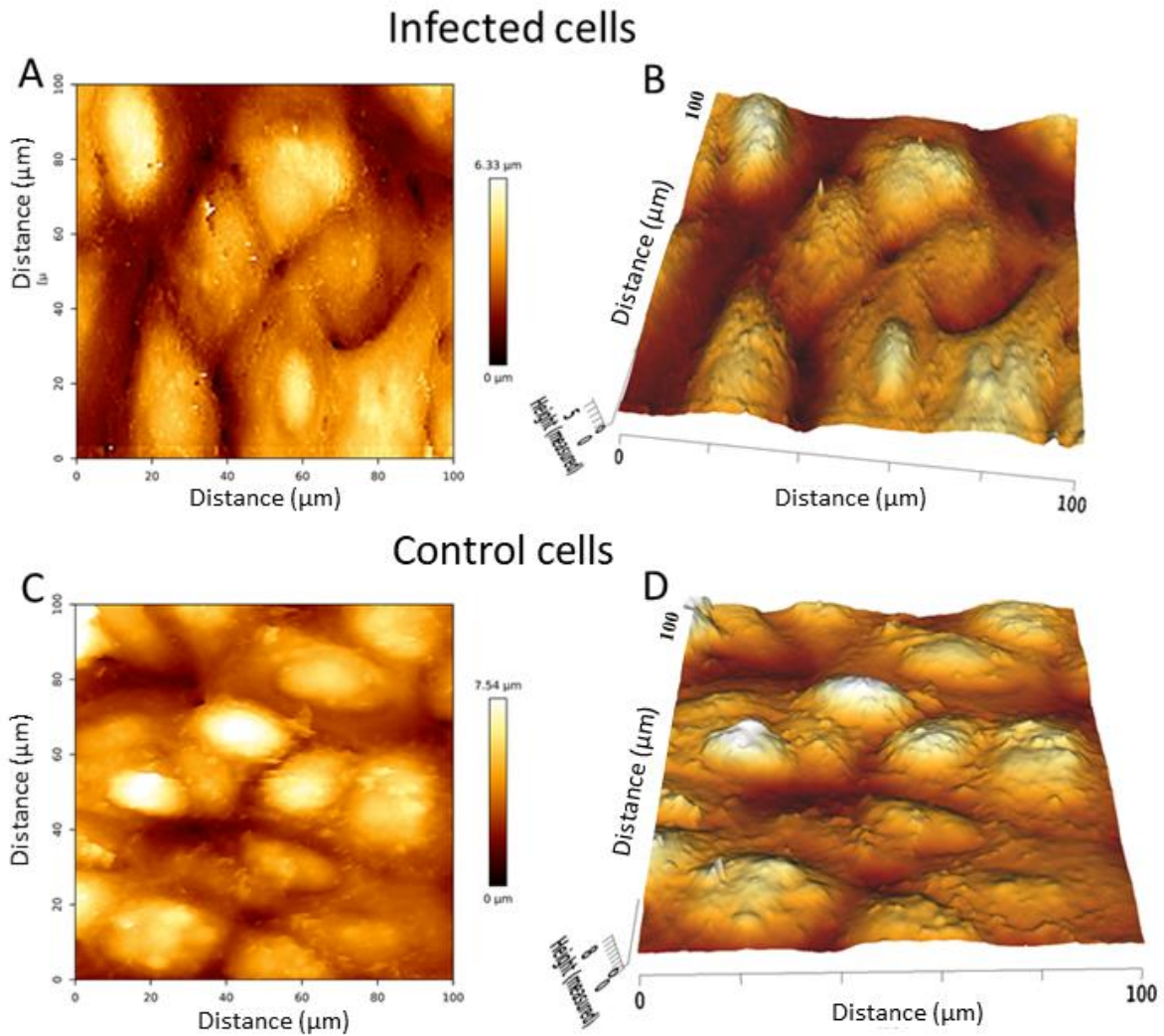


**Figure S6.3.** Imaging of BGM cell plasma membrane with AFM 8 hours after infection. (A) Topographic image of the surface of infected cells, 8 hours after infection. (B) 3D reconstruction of the surface of infected cells based on (A). (C) Topographic image of the surface of control cells. (D) 3D reconstruction of the surface of control cells based on (C). The number of hours is highlighted in this figure caption for distinguishing it from figure caption in Figure S6.3.

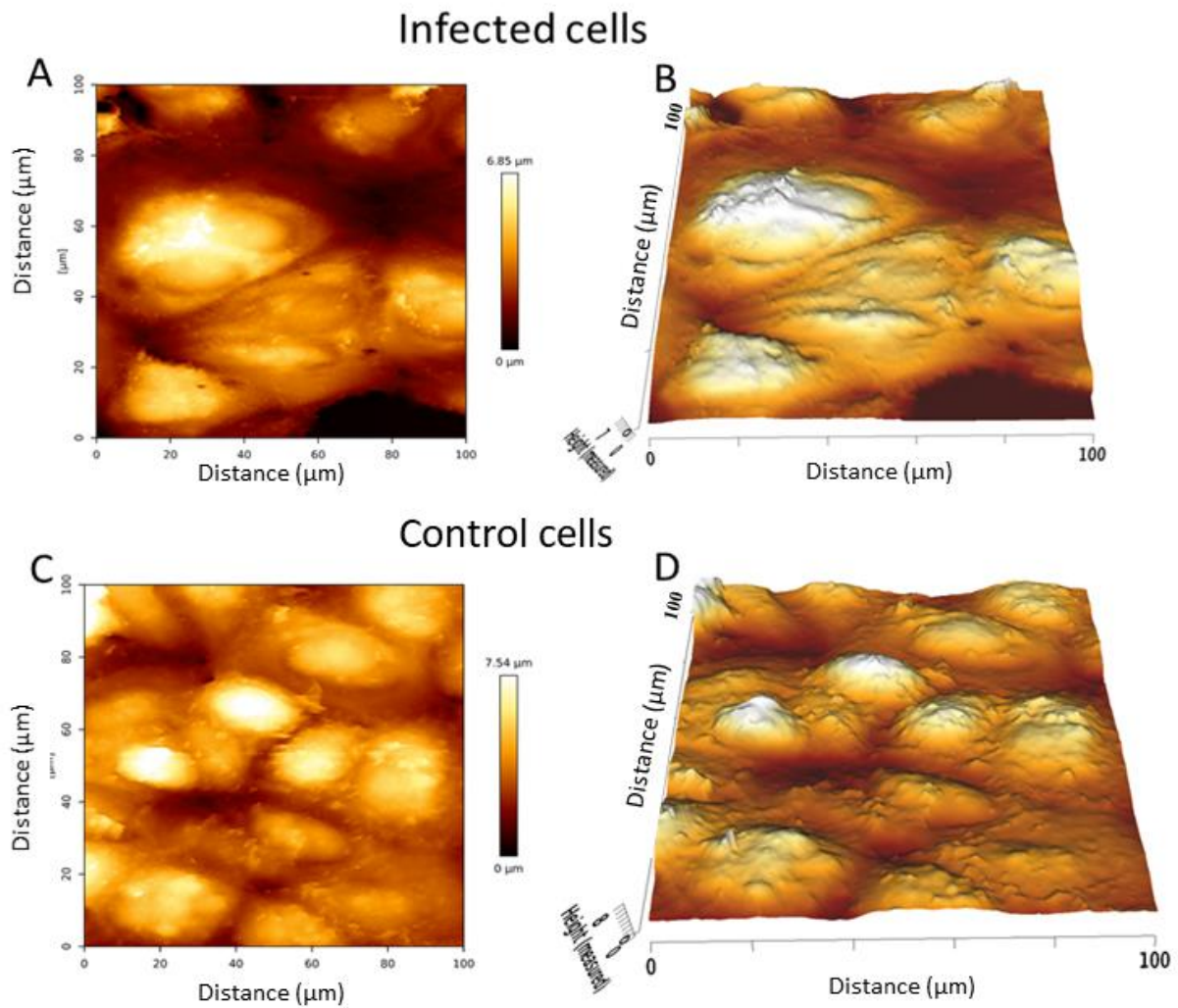


**Figure S6.4. Imaging of BGM cell plasma membrane with AFM 36 hours after infection.** (A) Topographic image of the surface of infected cells, 36 hours after infection. (B) 3D reconstruction of the surface of infected cells based on (A). (C) Topographic image of the surface of the control cells. (D) 3D reconstruction of the surface of control cells based on (C). The number of hours is highlighted in this figure caption for distinguishing it from figure caption in Figure S6.2.

## Summary

Multimodal imaging plays an ever-increasing role in modern microscopy and medicine, while Raman microscopy has an important role due to possibilities of label-free detection of molecules, organisms, and tissues. Raman microscopy is a label-free, optical method based on the inelastic laser light scattering from molecular vibrations inherent to any material. It can be used for a non-destructive analysis and imaging of biological materials with the spatial resolution in the micrometer range. Raman microscopy was successfully used in various areas of life science, such as cancer research, medical diagnostic, tissue engineering, and biomolecule sensing (**Chapter 1**).

In **Chapter 2**, we have investigated how a combination of MRI with Raman molecular imaging can be applied to tissue analysis. Such a combination was used to study the effect of mild traumatic brain injury (mTBI) on macro-(MRI) and micro-(Raman microscopy) scales. MRI can be applied to identify the damaged area inside brain tissue, which can be subsequently analyzed on a molecular level with a Raman microscope. No brain damage in the case of mTBI was detected on the macro-scale with MRI. The analysis of brain tissue on the molecular level with Raman showed a decrease in the ratio of axon proteins to myeloid lipids in the corpus callosum region after mTBI. The Raman molecular imaging-based on the hierarchical clustering analysis allowed detection of structural and molecular abnormality inside the corpus callosum region, which presumed to be the result of a micro bleeding caused by mTBI. The addition of Raman microscopy to the brain analysis pipeline provides the means to track changes in the brain, undetectable by a conventional MRI. However, such analysis is not possible to do *in vivo*, and the scanning of even a single tissue slice is still extremely time-consuming. In **Chapter 2**, the analysis was done at the tissue level and each spectrum in analyzed datasets was recorded from the area of 10  $\mu\text{m}$  in diameter.

In **Chapter 3**, the samples were investigated on a lower microscopic scale. Here, each Raman spectrum was obtained from an area of around 1.0  $\mu\text{m}$  in diameter. Such resolution provided the means to localize and study the molecules of interest inside cells and bacteria. In **Chapter 3**, a combination of Raman and fluorescent microscopies is carried out. Such a combinatory approach was used to study the movement of bovine lactoferrin inside the calf rectal epithelial cell in the presence of EHEC. The molecular composition of bovine lactoferrin was known, but information about its Raman molecular fingerprint inside the cell was not available. Raman

microscopy appears to be a complementary tool to fluorescent microscopy allowing identification of the Raman molecular fingerprint of bovine lactoferrin inside cells. It is established that bovine lactoferrin molecules translocate into the nucleus of calf rectal epithelium cells. Additionally, it was found that the presence of EHEC increased the rate of bovine lactoferrin uptake and its subsequent translocation.

In **Chapter 4**, the molecular structure of conductive fibers inside cable bacteria is investigated. Here, the localization of fibers inside the bacteria was already known, but their molecular composition was unknown. The analysis of Raman scattering spectra of fibers pointed out that the electrical conductivity occurs due to the presence of nickel. This was confirmed by subsequent analysis with STEM-EDX and Nano-SIMS. This work demonstrated the need for complementary tools to confirm the information obtained from the analysis of the Raman spectrum.

Research conducted in **Chapter 3** and **Chapter 4** showed that analysis and localization of molecules inside cells and bacteria are challenging if the concentration of the molecule of interest is low and it does not have a distinct molecular fingerprint. Such a problem can be solved with SERS. In **Chapter 5**, we have developed and characterized the calcium-carbonate based particles with dual functionality: drug carriers, controlled by a magnetic field, and SERS biosensors. Such SERS biosensors showed to be able to detect the low concentration of the analyte in a solution using 100 times less laser power than what is required to detect the same concentration with conventional Raman. However, the high absorbing ability of the particles made the quantification of analyte concentration with SERS challenging. However, the high absorbing ability of calcium carbonate particles was used to create the alginate drug carriers with SERS functionality. Such functionality provides the means of controllable light-induced drug release. The resulting drug carrier was tested *in vivo* in *C. elegans*. The SERS was used for the induction of drug release and precise localization of the shells inside the *C. elegans*. Because of the SERS functionality, the shells ultra-fast detection *in vivo* was possible with Raman using only 1 mW of laser power. The presented detection method was based on measuring the SERS background and not on the signal intensity of a particular Raman peak.

Subsequently, Raman 4Pi microscope was developed. Such a system has a better axial resolution and enhanced Raman signal compared to standard Raman. It was shown that under certain conditions 4Pi Raman microscope can have the resolution of 6 nm. **Chapter 6** describes

the Raman 4Pi setup and shows how the system can be characterized using polystyrene nanoparticles. Next, a 4Pi Raman microscope in a combination with atomic force microscopy (AFM) was applied to study the Buffalo Green Monkey (BGM) cells infected with *C. psittaci*. The complementary use of 4Pi Raman and AFM proved to be a practical approach for analysis of *C. psittaci* infection. The combination of those two techniques grants us information not accessible if they were to be used separately. The application of Raman 4Pi allowed us to identify the presence of dense-packed lipids in the *C. psittaci* inclusion membrane. These lipids had molecular fingerprint similar to intercellular lipid droplets, but with a lower ratio of saturated to unsaturated lipids. The high-resolution imaging of *C. psittaci* infected cells with AFM revealed the presence of irregularly shaped cavities on the cell membrane surface. Additionally, axial imaging of *C. psittaci* infected cells allowed identifying the sources of interference that influence the data points on the 4Pi Raman molecular image. Such information will be essential for development of the Raman 4Pi deconvolution algorithm, necessary to open the full potential of resolution improvement in the 4Pi mode.



## **Samenvatting**

Multimodale beeldvorming speelt een steeds grotere rol in de moderne microscopie en geneeskunde, terwijl Raman-microscopie een belangrijke rol speelt vanwege de mogelijkheden van labelvrije detectie van moleculen, organismen en weefsels. Ramanmicroscopie is een labelvrije, optische methode die gebaseerd is op de inelastische laserlichtverstrooiing door moleculaire trillingen die inherent zijn aan elk materiaal. Het kan worden gebruikt voor een niet-destructieve analyse en beeldvorming van biologisch materiaal met ruimtelijke resoluties in het micrometerbereik. Ramanmicroscopie werd succesvol gebruikt in kankeronderzoek, medische diagnostiek, weefselengineering en biomolecuul detectie, zoals het geschreven in **hoofdstuk 1**.

In **hoofdstuk 2** onderzoeken we hoe de combinatie van MRI met de Ramans moleculaire beeldvorming op de weefselanalyse kan worden toegepast. De combinatie werd gebruikt om het effect van licht traumatisch hersenletsel (mTBI) op macro- en microschaal te bestuderen. De MRI kan worden toegepast om het beschadigd gebied in de hersenen te lokaliseren en te identificeren, om deze vervolgens met behulp van een Ramanmicroscopie op moleculair niveau te kunnen analyseren. Er werd geen hersenbeschadiging gedetecteerd op de macroschaal met de MRI. De analyse van het hersenweefsel op moleculair niveau met Raman toonde na het mTBI een afname in de verhouding tussen de axon-eiwitten en de myeloïde lipiden in het corpus callosum gebied. De Ramans moleculaire beeldvorming, op basis van hiërarchische clusteranalyse, stelde ons in staat om structurele en moleculaire afwijkingen in het corpus callosum te detecteren, die vermoedelijk het gevolg zijn van microbloedingen, veroorzaakt door het mTBI. De toevoeging van Raman aan de pijplijn van de hersenstudie biedt de mogelijkheid om veranderingen in de hersenen op te sporen, die niet met behulp van conventionele MRI kunnen worden gedetecteerd. Een dergelijke analyse kan echter niet *in vivo* worden uitgevoerd en het scannen van zelfs maar één enkel stukje weefsel is uiterst tijdrovend.

In **hoofdstuk 2** werd de analyse gedaan op weefselniveau en werd elk spectrum in de geanalyseerde datasets opgenomen uit het gebied van 10  $\mu\text{m}$  in diameter. In **hoofdstuk 3** werden de monsters onderzocht op een lagere microscopische schaal. Hier werd elk Raman spectrum verkregen uit het gebied van ongeveer 1,0  $\mu\text{m}$  in diameter. Een dergelijke resolutie bood de mogelijkheid om de betrokken moleculen in de cellen en bacteriën te lokaliseren en

te bestuderen. In **hoofdstuk 3** hebben we geprobeerd de Raman en de fluorescentiemicroscopie te combineren. Een dergelijke combinatie werd gebruikt om de beweging van bovine lactoferrine in de rectale epitheelcel van het kalf in aanwezigheid van EHEC te bestuderen. De moleculaire samenstelling van bovine lactoferrine was bekend, maar informatie over de Ramans moleculaire vingerafdruk in de cel ontbrak. De fluorescentiemicroscopie werd een levensvatbare aanvulling op de Raman, waardoor we de Ramans moleculaire vingerafdruk van cellulaire bovine lactoferrine konden identificeren. Er werd vastgesteld dat bovine lactoferrine zich kon verplaatsen naar de kern van de rectale epitheelcellen van het kalf. Bovendien werd er vastgesteld dat de aanwezigheid van EHEC de opname van bovine lactoferrine en de daaropvolgende translocatie verhoogde.

In **hoofdstuk 4** werd de moleculaire structuur van de geleidende vezels in de kabelbacterie onderzocht. Hier stond het probleem in contrast met hetgeen dat in het eerste deel van het hoofdstuk werd besproken. De lokalisatie van de vezels in de bacterie was al gevonden, maar hun moleculaire samenstelling was onbekend. De analyse van de vezelspectra suggereerde de aanwezigheid van metaalionen. Dit werd bevestigd door latere analyse met STEM-EDX en Nano-SIMS. Dit werk toonde de essentie aan van aanvullende instrumenten om de informatie die werd verkregen uit de analyse van het Raman spectrum te bevestigen.

Het onderzoek in **hoofdstuk 3** en **hoofdstuk 4** toonde aan dat analyse en lokalisatie van moleculen in cellen en bacteriën een uitdaging vormen als de concentratie van het betrokken molecuul laag is en het niet over een duidelijke moleculaire vingerafdruk beschikt. Een dergelijk probleem kan met behulp van SERS worden verholpen. In **hoofdstuk 5** ontwikkelen en karakteriseren we de calciumcarbonaat gebaseerde deeltjes met een dubbele functionaliteit: medicijndragers, gecontroleerd door een magnetisch veld, en SERS-biosensoren.

Dergelijke SERS-biosensoren bleken in staat te zijn om de lage concentratie aan analyt in een oplossing te detecteren, dat met behulp van een 100 keer zwakker laservermogen dan deze nodig is om dezelfde concentratie te detecteren met conventionele Raman. Echter, het hoge absorptievermogen van de deeltjes maakte de kwantificering van de analytconcentratie met SERS tot een uitdaging. Vervolgens werden calciumcarbonaatdeeltjes gebruikt om alginaatdragers met een SERS-functionaliteit te creëren. Deze functionaliteit biedt de mogelijkheid om lichtgeïnduceerde medicijnafgifte te controleren. De bekomen

medicijndrager werd *in vivo* getest in de *C. elegans*. De SERS werd gebruikt voor het induceren van de loslating van het geneesmiddel en de precieze lokalisering van de schelpen in de *C. elegans*. Vanwege de SERS-functionaliteit, was de ultrasnelle detectie van de schelpen *in vivo* met Raman mogelijk met slechts 1 mW aan laservermogen. De gepresenteerde detectiemethode was gebaseerd op het meten van de SERS-achtergrond en niet op de signaalintensiteit van een bepaalde Raman-piek.

Vervolgens werd een 4Pi Raman microscoop ontwikkeld. Een dergelijk systeem heeft een betere axiale resolutie en een verbeterd Raman signaal in vergelijking met de standaard Raman. Het is aangetoond dat onder bepaalde omstandigheden de 4Pi Raman microscoop een resolutie van 6 nm kan bereiken.

**Hoofdstuk 6** beschrijft de Raman 4Pi opstelling en laat zien hoe het systeem met behulp van polystyreen nanodeeltjes kan worden gekarakteriseerd. Vervolgens werd de 4Pi Raman microscoop in combinatie met atoomkrachtmicroscopie (AFM) toegepast op de *Buffalo Green Monkey (BGM)* cellen, geïnfecteerd met *C. psittaci*, ter bestudering. Het complementair gebruik van 4Pi Raman en AFM bleek een praktische aanpak voor de analyse van de *C. psittaci* – infectie te zijn. De combinatie van deze twee technieken leverde ons informatie op die niet toegankelijk zou zijn, indien de technieken elk afzonderlijk zouden worden toegepast. De toepassing van Raman 4Pi stelde ons in staat om de aanwezigheid van dicht opeengeplakte lipiden in de *C. psittaci* inclusiemembraan te identificeren. Deze lipiden hadden een moleculaire vingerafdruk vergelijkbaar met deze van de intercellulaire lipidedruppels, maar met een lagere verhouding tussen verzadigde en onverzadigde lipiden. De hoge-resolutie beeldvorming van *C. psittaci* geïnfecteerde cellen met AFM onthulde de aanwezigheid van onregelmatige gevormde holtes op het oppervlak van de celmembraan. Bovendien, liet de axiale beeldvorming van *C. psittaci* geïnfecteerde cellen ons toe de bronnen van de interferentie te identificeren, die de datapunten op de 4Pi Raman moleculaire beeld beïnvloeden. Dergelijke informatie zal essentieel zijn voor de ontwikkeling van het Raman 4Pi deconvolutiealgoritme, dat nodig zal zijn om het volledig potentieel van de resolutieverbetering in de 4Pi-modus te vrijwaren.

## **CV and the publication list of the author**

## *CURRICULUM VITAE*

### Personalia

Full name: Dmitry Nicolaevich Khalenkow

Date and place of birth: 28 December 1983, Grodno, Belarus

Nationality: Belgian / Belarussian

E-mail: [Dmitry.Khalenkow@ugent.be](mailto:Dmitry.Khalenkow@ugent.be)

[Dmitry.Khalenkow@gmail.com](mailto:Dmitry.Khalenkow@gmail.com)

Phone: +32 484 73 73 34

*Affiliation:*

Nano-Biotechnology Laboratory, Faculty of Bioscience Engineering, Ghent University

Workplace address: Coupure Links 653, 9000 Ghent, Belgium



### Education

- Ph.D. studies in Bioscience Engineering, Ghent University, Belgium
- Master of Science in Biomedical Sciences and Bioinformatics, Ghent University, Belgium
- Bachelor of Science in Biochemistry, Ghent University, Belgium
- Bachelor of Science in Informatics, Grodno State University, Belarus

### Skiles and experience

Raman data acquisition, preparation of complex biological samples, cell culture maintenance, computer processing of data

## Publications and Conference presentations

### I) Peer-reviewed publications used in this thesis, (Web-of-Science database).

1. **Added value of microscale Raman chemical analysis in mild traumatic brain injury (TBI): A comparison with macroscale MRI.**

Khalenkow D, Donche S, Braeckman K, Vanhove C, Skirtach AG.

*ASC Omega* **2018**, 3, 12.

*Contribution: took part in designing the experiment, developed the protocol for tissue samples measurement with Raman, supervised the master student, who performed the experiment, wrote the paper.*

2. **Complementary multimodal microscopy study of *Chlamydia psittaci* infected cells: 4Pi Raman and atomic force microscopy.**

Khalenkow D, Diaz Tormo A, Rybarczyk J, Verduijn J, Van Der Meeren L, Vanrompay D, Le Thomas N, Skirtach AG.

*(submitted).*

*Contribution: designed and performed the experiment, conducted Raman measurements and data analysis, wrote the manuscript.*

3. **Superresolution 4 $\pi$  Raman microscopy.**

Diaz Tormo A, Khalenkow D, Saurav K, Skirtach AG, Le Thomas N.

*Opt Lett.* **2017**, 42, 4410-4413.

*Contribution: took part in designing the experiment and conducting the measurements, contributed to writing the paper.*

4. **Lactoferrin translocates to the nucleus of bovine rectal epithelial cells in the presence of *Escherichia coli* O157:H7.**

Rybarczyk J (\*), Khalenkow D (\*), Kieckens E, Skirtach AG, Cox E, Vanrompay D.

*Veterinary Research* **2019**, 50, 75. (\* - equal first-author contribution).

*Contribution: made fluorescent microscopy and Raman measurement part of the experiment, contributed to writing the paper.*

**5. Laser-induced remote release *in vivo* in *C. elegans* from novel silver nanoparticles-alginate hydrogel shells.**

Lengert E, Parakhonskiy B, Khalekow D, Zečić A, Vangheel M, Monje Moreno JM, Braeckman BP, Skirtach AG.

*Nanoscale* **2018**, 10, 17249-17256.

*Contribution: took part in experimental design, made the protocol for *C. elegans* analysis with Raman, helped with fluorescent microscopy part of the experiment, done drug release *in vivo* part of the project, contributed to writing the paper.*

**6. Magnetic and silver nanoparticle functionalized calcium carbonate particles—Dual functionality of versatile, movable delivery carriers which can surface-enhance Raman signals.**

Parakhonskiy BV, Abalymov A, Ivanova A, Khalekow D, and Skirtach AG.

*J. Appl.Phys.* **2019**, 126, 203102.

*Contribution: took part in the experimental design, made the protocol for functionalized particles measurement with Raman, helped with functionalization of magnetic properties of the particles, conducted Raman measurements of the particles and helped with data analysis, contributed to writing the paper.*

**7. Efficient long-range conduction through microbial nickel protein wires.**

Boschker HTS, Cook PLM, Polerecky L, Thiruvallur Eachambadi R, Lozano H, Hidalgo-Martinez S, Khalekow D, Spampinato V, Claes N, Kundu P, Wang DA, Bals S, Sand KK, Cavezza F, Hauffman T, Tataru Bjerg J, Skirtach AG, Kochan K, McKee M, Wood B, Bedolla D, Gianoncelli A, Geerlings NMJ, Van Gerven N, Remaut H, Geelhoed JS, Millan-Solsona R, Fumagalli L, Nielsen L-P, Franquet A, Manca JV, Gomila G, Meysman FJR.

*Nat. Commun. (under revision).*

*Contribution: created the protocol for measurement of intact cable bacteria and extracted fibers with near-IR Raman, performed the near-IR Raman measurements, contributed to writing the paper.*



**II) Other peer-reviewed publications contributed to by the author, but which are not linked to this thesis work, (Web-of-Science database).**

**8. Label-free Raman characterization of bacteria calls for standardized procedures.**

García-Timmermans C, Rubbens P, Kerckhof FM, Buyschaert B, Khalekow D, Waegeman W, Skirtach AG, Boon N.

*J. Microbiol. Methods* **2018**, 151, 69-75.

*Contribution:* took part in designing of the experiment and performing the measurement of bacteria samples, made the protocol for bacteria measurement with Raman, took part in creating the data analysis pipeline, contributed to writing the paper.

**9. Raman and quantitative-phase microscope with counter-propagating beams demonstrated on HeLa cells.**

Diaz Tormo A, Khalekow D, Skirtach AG, Le Thomas N.

*OSA Continuum* **2019**, 2, 797.

*Contribution:* took part in designing and conducting the measurements, done the cell sample preparation, contributed to writing the paper.

**10. Modulating the crystallization of phytosterols with monoglycerides in the binary mixture systems: mixing behavior and eutectic formation.**

Bin Sintang MD, Danthine S, Khalekow D, Tavernier I, Tzompa Sosa DA, Julmohammad NB, Van de Walle D, Rimaux T, Skirtach A, Dewettinck K.

*Chem Phys Lipids*. **2020**, 230, 104912.

*Contribution:* designed the protocol for sample measurement with Raman, done Rama measurement and helped with data analysis, contributed to writing the paper.

**11. Loading capacity versus enzyme activity in anisotropic and spherical calcium carbonate microparticles.**

Donatan S, Yashchenok A, Khan N, Parakhonskiy B, Cocquyt M, Pinchasik BE, Khalekow D, Möhwald H, Konrad M, Skirtach A.

*ACS Appl. Mater. Interfaces* **2016**, 8, 14284–14292.

*Contribution: took part in experimental design, measured the particles with Raman, contributed to writing the paper.*

**12. Transfer of cells with uptaken nanocomposite, magnetite-nanoparticle functionalized capsules with electromagnetic tweezers.**

Vidiasheva IV, Abalymov AA, Kurochkin MA, Mayorova OA, Lomova MV, German SV, Khalenkow D, Zharkov MN, Gorin DA, Skirtach AG, Tuchin VV, Sukhorukov GB.  
*Biomater Sci.* **2018**, 6, 2219-2229.

*Contribution: assisted with designing and performing the experiment, maintaining the cell culture and the cell viability testing, contributed to writing the paper.*

**13. Novel self-gelling injectable hydrogel/alpha-tricalcium phosphate composites for bone regeneration: Physiochemical and microcomputer tomographical characterization.**

Douglas TEL, Schietse J, Zima A, Gorodzha S, Parakhonskiy BV, Khalenkow D, Shkarin R, Ivanova A, Baumbach T, Weinhardt V, Stevens CV, Vanhoorne V, Vervaeet C, Balcaen L, Vanhaecke F, Slośarczyk A, Surmeneva MA, Surmenev RA, Skirtach AG.  
*J. Biomed Mater. Res. A* **2018**, 106, 822-828.

*Contribution: designed the protocol for hydrogel analysis with Raman and done the measurement of hydrogel, contributed to writing the paper.*

**14. Ca:Mg:Zn:CO<sub>3</sub> and Ca:Mg:CO<sub>3</sub>-tri- and bi-elemental carbonate microparticles for novel injectable self-gelling hydrogel-microparticle composites for tissue regeneration.**

Douglas TEL, Sobczyk K, Łapa A, Włodarczyk K, Brackman G, Vidiasheva I, Reczyńska K, Pietryga K, Schaubroeck D, Bliznuk V, Voort PV, Declercq HA, Bulcke JVD, Samal SK, Khalenkow D, Parakhonskiy BV, Van Acker J, Coenye T, Lewandowska-Szumieł M, Pamuła E, Skirtach AG.

*Biomed. Mater.* **2017**, 12, 025015.

*Contribution: measured the hydrogel-microparticle composites with Raman, contributed to writing the paper.*

**15. Plasmonic hybrid biocomposite as an effective substrate for detection of biomolecules by surface-enhanced Raman spectroscopy.**

Chernozem RV, Surmeneva MA, Atkin V, Krause B, Baumbach T, Parakhonskiy BV, Khalekow D, Skirtach AG, Surmenev RA.

*Rus. Phys. J.* **2018**, 61, 1288-1293.

*Contribution: helped with experimental design and done the Raman measurements of plasmonic biocomposite sample, assisted with Raman data analysis, contributed to writing the paper.*

**16. Water-stable plasma-polymerized N,N-Dimethylacrylamide coatings to control cellular adhesion.**

Egghe T, Cools P, Van Guyse JFR, Asadian M, Khalekow D, Nikiforov A, Declercq H, Skirtach AG, Morent R, Hoogenboom R, De Geyter N.

*ACS Appl. Mater. Interfaces* **2020**, 12, 2, 2116–2128.

*Contribution: performed the coating measurements with Raman, contributed to writing the paper.*

### III) Conferences and other presentations, (not only Web-of-Science database).

- 1) Khalenkow D. Invited presentation at the user group meeting, Eindhoven **2020**.
- 2) Khalenkow D., Tormo Diaz A., Le Thomas N., Skirtach A.G. WITec presentation in Ulm, Germany **2019**.
- 3) Study of bacterial inner structures with 4 Pi Raman microscopy. Tormo Diaz A., Khalenkow D., Skirtach A.G., Le Thomas N. Conference: Conference on Lasers and Electro-Optics (CLEO) Location: San Jose, CA Date: MAY 13-18, **2018**. Sponsor(s): IEEE 2018 CONFERENCE ON LASERS AND ELECTRO-OPTICS (CLEO) Book Series: Conference on Lasers and Electro-Optics.
- 4) Khalenkow D. Raman4Clinics presentation, Ghent University, Ghent (Belgium), **2017**.